Kinetics of Lipid-Based RNA Delivery in Mammalian Cells

Judith Anna Müller

München 2024

Kinetiken von lipidbasiertem RNA Transfer in Säugetierzellen

Judith Anna Müller

Dissertation
an der Fakultät für Physik
der Ludwig-Maximilians-Universität München

vorgelegt von
Judith Anna Müller
aus Rheinfelden

München, den 24.10.2024

Erstgutachter: Prof. Dr. Joachim O. Rädler
Zweitgutachter: Prof. Dr. Sophia Rudorf
Tag der mündlichen Prüfung: 09.12.2024

Zusammenfassung

In den letzten Jahren wurde das immense Potenzial von Lipidnanopartikel (LNP) basierten mRNA-Therapien deutlicher, sowohl bei der Behandlung genetischer Erkrankungen, zur Umprogrammierung von Immunzellen in der Krebsforschung und als molekularbiologisches Forschungsinstrument. Biophysikalische Forschung erlaubt es, die aktuellen Herausforderungen für die präzise Kontrolle des biologischen Outputs, wie die heterogene Verteilung und das Fehlen von geeigneten Modellen zur Vorhersage, zu adressieren.
Im Fokus dieser Arbeit steht die Erforschung der Kinetik des LNP-mRNA Transfers mithilfe von Live-Cell-Imaging auf Einzelzell-Arrays (LISCA). Um den Durchsatz und das Signal-zu-Rauschverhältnis zu verbessern wurde zunächst die Mikrostrukturierung optimiert. Zusätzlich wurden mehrere Fluoreszenzreporter eingesetzt, um parallel den intrazellulären Weg von LNPs in Einzelzellen und die daraus resultierende Expressionskinetik der Reporterproteine und deren onset-Zeiten zu verfolgen. Mithilfe von Ratengleichungen wurde die Dynamik des lipidbasierten mRNA-Transportprozesses - von der Aufnahme der Nanopartikel bis hin zur Proteinsynthese - quantitativ modelliert. Diese Modelle erklären die beobachteten Kinetiken und erlauben die Messung von Systemparametern, wie beispielsweise der mRNA Lebensdauer.
Im ersten Teil der Arbeit wurden die konzentrationsabhängigen Unterschiede zwischen Lipofectamine und LNPs als mRNA Transportvektor, sowie der Einfluss des LNP Transfektionsserums und der inneren LNP Struktur auf die zeitabhängige Proteinexpression untersucht. Es wurde dann gezeigt, dass im Fall von "Codelivery", bei denen mehrere RNA-Spezies in LNPs verpackt werden, die Dosierungsabhängigkeit eine gegenseitige Abhängigkeit durch Konkurrenz um die verfügbaren Ribosomen ergeben kann.
Im dann folgenden Teil der Arbeit wurde untersucht, wie sich die Ribosomendichte auf der kodierenden Region der mRNA auf deren Lebenszeit auswirkt. Um diese subtilen Lebenszeitveränderungen zu messen, wurde eine Referenz-Reporter-mRNA cotransfiziert, durch die sich das inhärente zelluläre Rauschen herausfiltern lässt. Es wurde festgestellt, dass das Einfügen von langsam translatierten Codonabschnitten eine positionsabhängige Kontrolle der mRNA-Stabilität ermöglicht, mit entgegengesetzten Effekten in Anwesenheit oder Abwesenheit von spezifischer siRNA.
Im letzten Teil der Arbeit wurde ein Ansatz zur Implementierung eines genetischen Regelkreises verfolgt. Durch Verwendung des regulatorischen Motifs einer inkohärenten "Feed-Forward" Schleife, wurde eine dynamische Anpassung der mRNA-LNP Proteinexpressionskinetik ermöglicht. Es wurde gezeigt, dass das ratiometrische Verhältnis von mRNA und siRNA die Proteinproduktion kontrolliert, zu einer Reduktion von Fluktuationen in den Expressionsniveaus führt und die Reaktionszeit der Expression verkürzt. Das Verhalten dieses Systems wurde durch ein enzymatisches Modell des RNA-Interferenz-abhängigen mRNA-Zerfalls beschrieben, welches eine quantitative Beschreibung der Reaktionszeiten und Expressionslevel erlaubt.
Dieser hier beschriebene interdisziplinäre Ansatz der Einzelzell-Expressionskinetiken mit Konzepten der Kontrolltheorie aus der Systembiologie, trägt dazu bei, komplexe kombinatorische LNP-mRNA Anwendungen für präzise quantitative und zeitliche Kontrolle transienter Genexpression zu etablieren und so in der Zukunft robustes Expressionsverhalten für therapeutische und zellbiologische Herausforderungen zu adressieren.

Abstract

In recent years, the immense potential of lipid nanoparticle (LNP)-based mRNA applications has become increasingly evident in treating genetic diseases, reprogramming immune cells for cancer research, and serving as valuable research tools. Biophysics addresses challenges of LNP-mRNA delivery, such as heterogeneous biodistribution and insufficient predictive models, which complicate the control of biological output. Therefore, a deeper understanding of the physical principles governing mRNA delivery, distribution, and kinetics is essential for developing precise and dynamic control strategies.

This work focused on investigating the kinetics of LNP-mRNA transfer using live-cell imaging on single-cell arrays (LISCA). To enhance throughput and signal-to-noise ratio, microstructuring of the arrays was first optimized. Additionally, multiple fluorescence reporters were employed to simultaneously track the intracellular pathway of LNPs in single cells, along with the resulting expression kinetics of the reporter proteins and their onset times. By using kinetic rate equations, the dynamics of the lipid-based mRNA delivery process - from nanoparticle uptake to protein synthesis - were quantitatively modeled, providing insights into time-resolved expression dynamics. These models explain the observed kinetics and allow for the measurement of system parameters, such as mRNA lifetime.

In the first part of this thesis, the concentration-dependent differences between Lipofectamine and LNPs as mRNA transport vectors were examined, along with the influence of LNP transfection serum and internal LNP structure on time-dependent protein expression. Co-delivery strategies involving multiple mRNA species encapsulated in LNPs were also explored, revealing that such co-delivery can lead to coupling of translation due to competition for ribosome resources.

In the next part of this work, the impact of ribosome density along the coding region of the mRNA on its lifetime was investigated. To measure these subtle lifetime changes, a reference reporter mRNA was co-transfected, enabling the filtering of inherent cellular noise. The insertion of slow-translated codon windows was shown to provide position-dependent control of mRNA stability, with opposite effects observed in the presence or absence of targeting siRNA.

In the last part of this thesis, an approach for implementing a genetic regulatory motif was explored. By employing an artificial incoherent feed-forward loop, dynamic adjustment of mRNA-LNP protein expression kinetics was achieved. It was demonstrated that ratiometric encapsulation of siRNA and mRNA allowed control over protein production, reduced fluctuations in expression levels, and accelerated expression response. The behavior of this system was captured using an enzymatic model of RNA interference-dependent mRNA decay, offering a quantitative description of both response times and expression levels.

This interdisciplinary approach of single-cell expression kinetics with concepts of control theory from systems biology, contributes to the establishment of complex combinatorial LNP-based mRNA applications for precise quantitative and temporal control of transient gene expression, addressing robust expression behavior in therapeutic and cell biology contexts.

"I had always imagined paradise
as a kind of library."

Jorge Luis Borges

Contents

Associated Publications and Manuscripts

[**P1**] **Judith A. Müller**, Gerlinde Schwake, Anita Reiser, Daniel Woschée, Zahra Alirezaeizanjani', Joachim O. Rädler, Sophia Rudorf. Less is more: Slow-codon windows enhance eGFP mRNA resilience against RNA interference, *BioRxiv*, doi.org/10.1101/2024.09.27.615338 (2024), *Royal Society Interface, under revision* (2024)

[**P2**] **Judith A. Müller**, Nathalie Schäffler, Thomas Kellerer, Gerlinde Schwake, Thomas S. Ligon, Joachim o. Rädler. Kinetics of RNA-LNP delivery and protein expression. *European Journal of Pharmaceutics and Biopharmaceutics* 197, 114222 (2024)

[**P3**] **Judith A. Müller**, Gerlinde Schwake, Joachim O. Rädler. Einzelzellmikroskopie im Hochdurchsatz auf Mikrostrukturen. *Biospektrum* 28, 723–725 (2022)

[**M1**] **Judith A. Müller**, Nathalie Schäffler and Joachim O. Rädler. Stoichiometric siRNA/mRNA lipid nanoparticles mediate self-regulated protein expression via incoherent feed-forward loop, *to be submitted to Nature Communications* (2024)

[**M2**] Cristina Carucci, Julian Philipp, **Judith A. Müller**, Akhil Sudarsan, Nadine Schwierz, Drew F. Parsons, Andrea Salis, Joachim O. Rädler. Buffer specificity of ionizable lipid nanoparticle transfection efficiency and bulk phase transition, *ACS Nano, under revision* (2024)

[**M3**] Thomas Kellerer, Tanja Grawert, Florian Schorre, **Judith A. Müller**, Cole D. Green, Joachim O. Rädler, and Thomas Hellerer. Spectrally Encoded Multiphoton Particle Tracking (SEMPA-Track): A Real-Time 4D-Single Particle Fluorescence Lifetime Imaging Microscope, *submitted to Nature Communications* (2024)

[**M4**] **Judith A. Müller**, Manuel S. Torres Matsumoto, Nathalie, Schäffler, Konstantin Steppe, and Joachim O. Rädler. Ribosomal Competition in mRNA Co-Delivery, *in prepa-*

ration

[**M5**] Bernhard Kirchmair, Daria Maksutova, **Judith A. Müller**, Carola Bartels, and Joachim O. Rädler. mRNA Payload of Lipid Nanoparticles *in preparation*

[**M6**] Thomas Kellerer, Lukas Moser, **Judith A. Müller**, Cole D. Green, Joachim O. Rädler, and Thomas Hellerer. Speed Up Phase Resolved Fluorescence Lifetime Imaging (SUPER-FLIM) for Real-Time Microenvironmental Sensing, *to be submitted to Nature Light: Science and Applicatoins* (2024)

Contributions to Conferences

[**DPG Annual Meeting, Regensburg**] **Judith A. Müller**, Gerlinde Schwake, Anita Reiser, Daniel Woschée, Zahra Alirezaeizanjani', Joachim O. Rädler and Sophia Rudorf. Live-imaging on single-cell arrays (LISCA) to study mRNA codon optimization based on ribosome modeling, *Poster* (2022)

[**DPG Annual Meeting, Dresden**] **Judith A. Müller** and Joachim O. Rädler. Stoichiometric siRNA/mRNA lipid nanoparticles mediate self regulated protein expression via incoherent feed-forward loop, *Poster* (2023)

[**ASGCT Annual Meeting, Los Angeles**] **Judith A. Müller**, Gerlinde Schwake, Joachim O. Rädler and Sophia Rudorf. Live-Imaging on Single-Cell Arrays LISCA) as a Platform to study Dynamics of mRNA Expression in Mammalian Cells, *Talk* (2023)

[**CeNS/SFB1032 Workshop, Venice**] **Judith A. Müller**, Gerlinde Schwake, Anita Reiser, Daniel Woschée, Zahra Alirezaeizanjani', Joachim O. Rädler and Sophia Rudorf. Ribosome jams protect mRNA from RNAi, *Poster* (2023)

[**ASGCT Annual Meeting, Baltimore**] **Judith A. Müller**, Gerlinde Schwake, Joachim O. Rädler and Sophia Rudorf. Exploring mRNA Expression Dynamics in Mammalian Cells through Live-Imaging of Single-Cells, *Talk* (2024)

1. Introduction

There is an old wisdom saying "*It's about the journey, not the destination*". While this applies to many aspects of everyday life, it also holds a certain truth in scientific investigations. Beyond the intrinsic scientific curiosity, knowledge about the journey provides evidence about underlying mechanisms of for example the processes that shaped our universe, the formation of galaxies, evolution of life, chemical reactions, or biological processes. This is particularly relevant when studying living systems, where there is often no clearly defined endpoint of a process, rather, the outcome of the measurement is determined by its timepoint. Consequently, the "correct" timepoint of measurement depends on the specific research question, and the answer may lie within the pathway itself. For a comprehensive understanding, it is therefore crucial to monitor key parameters over the whole timescale of an experiment. The aim of this thesis was to measure and quantitatively describe the time-dependent kinetics of lipid-mediated mRNA- and siRNA-based applications and to develop tools to systematically control their dynamics.

Beyond the significant role of mRNA during the COVID-19 pandemic [1], RNA therapies hold great promise in addressing the health challenges of our generation, particularly in areas such as personalized medicines, infectious diseases, and cancer treatment [2–5]. In addition to these therapeutic advances, RNA is also emerging as a valuable tool in synthetic biology, with mRNA enabling transient expression of exogenous proteins and siRNA facilitating temporary knockdown of targeted protein expression. Together, these tools allow constructing synthetic networks or encoding machines for genetic engineering [6–10]. In the context of genetic engineering, it is crucial to enable the precise control of gene expression. However, the success of RNA applications is often measured solely by the the final protein level while the dynamics of the system are frequently overlooked. This narrow focus misses valuable insights into the trafficking processes and expression dynamics that are crucial for a profound understanding that is required for an optimal design of mRNA applications [11].

For successful RNA delivery, a vector is required to transport the RNA to the cell and to overcome the cell membrane to deliver the RNA into the cytosol. Lipid-based delivery systems have emerged as the most promising non-viral vectors [12, 13], offering reduced toxicity, increased cargo capacity, and less complex manufacturing compared to

other delivery methods such as viral or polymer-based vectors [14–16]. Therefore, this work aimed to analyze the kinetics of lipid-based RNA delivery from both a physics and synthetic biology perspective, with the goal of improving the understanding of the RNA delivery and translation process in mammalian cells. Such insights are essential for predictive modeling of RNA kinetics and pave the way for the rational design of future RNA applications. The combination of physics and synthetic biology offers a powerful framework for studying these complex processes. Physics provides the tools to describe the soft matter of biology and enables predictive insights through theoretical modeling [17] while the field of synthetic biology focuses on the development of innovative tools to explore and understand life [18, 19].

A profound understanding of the RNA delivery is particularly important due to the inherent stochasticity of the multistep process [20, 21]. As outlined in **Fig. 1.1**, the process begins with administration, where the LNP encounters abundant proteins that may exchange with its outer lipid layer forming a protein corona [22–24]. This corona can mediate the cellular uptake, typically through receptor mediated endocytosis [25, 26]. However, after the uptake, the LNP remains trapped inside the endosome, and its escape from this compartment is the rate-limiting step of the entire delivery process [27]. If the endosome is not degraded or recycled, the lipid nanoparticle (LNP) can escape, and once its cargo - the RNA - is unpacked, becomes available for further processing, such as mRNA translation.

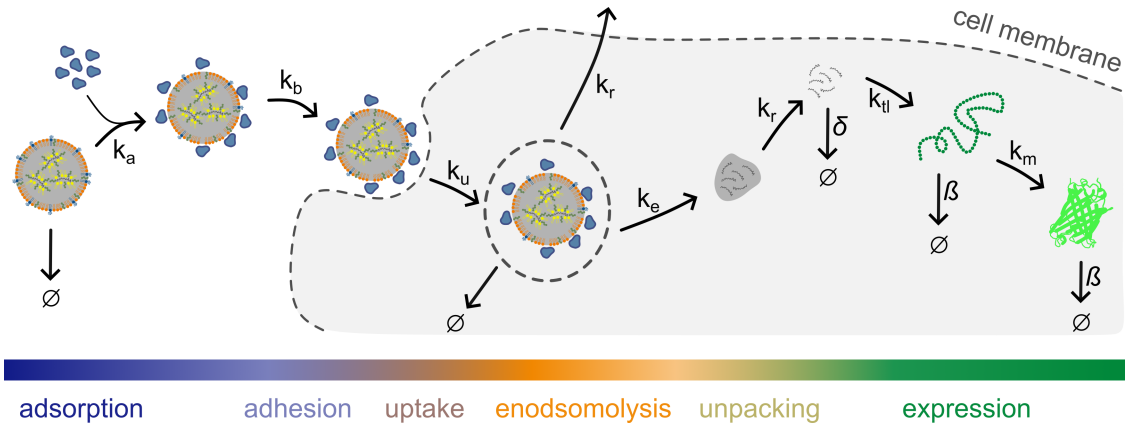

Figure 1.1.: RNA/LNP delivery is a cascade of stochastic processes: The delivery of an mRNA-loaded LNP to a mammalian cell starts with administration and protein adsorption that mediates adhesion to the cell surface. After uptake, successful escape from the endosome and unpacking from remaining lipids can result in translation and protein expression. Adapted from [**P1**].

In cell populations, the average often fails to reflect the true picture due to the inher-

ent heterogeneity and noise within cell populations may distort the result [28]. Single-cell analysis allows to analyze the isolated delivery processes to an individual cell together with its separation from its physiological context, where cells are constantly interacting with their surroundings further increasing complexity of the complex. Various methods have been developed for single-cell analysis [29], but many lack the temporal resolution needed to effectively capture dynamics of RNA delivery. Hence, the live-cell imaging on single-cell arrays (LISCA) platform was developed [30], enabling the simultaneous observation of hundreds of individual cells over time. Fluorescence reporters were used to monitor single cells placed on micropatterned structures, and high-throughput automated image analysis enabled to quantify the underlying gene expression kinetics. Theoretical modeling of protein expression following mRNA transfection allowed independent assessment of degradation and production rates, which is essential for understanding and designing RNA applications.

In this work, a single-cell based experimental approach was employed to understand the distinct steps of the stochastic RNA delivery cascade using lipid-based carriers and to develop tools for precise manipulation of gene expression.
Chapter 2 discusses fundamental scientific concepts relevant within this thesis, explaining gene expression and the scientific relevance of exogenous RNA delivery. It also covers the biophysical methods for characterization of LNPs *ex vivo* and the analysis of its *in vivo* pathways using the in-house developed LISCA platform. Additionally, the foundation of theoretical modeling for both mRNA and siRNA delivery is established together with the theoretical concept of network motifs.
In **Chapter 3**, the trafficking and expression kinetics dependent on carrier type, composition of the protein corona, and LNP structure were analyzed, focusing on the impact on uptake, endosomal escape and protein expression.
Building on this, **Chapter 4** presents a single-cell investigation of the co-delivery of different mRNA species with an emphasis on coupled protein expression and delivery timing. Further, different co-delivery strategies of mRNA with siRNA were analyzed, focusing on the impact of RNA interference (RNAi) efficacy and timing. Finally, co-delivery-based quantification of is performed.
In **Chapter 5**, this analysis is then used to explore how codon manipulation affects the translation kinetics of co-delivered mRNAs in absence and presence of RNAi, demonstrating how such manipulation can systematically tune mRNA stability. This is achieved by stochastic simulations of ribosome movement in combination with single-cell experiments involving co-delivery of two mRNA species alongside with a targeting siRNA. This approach contributes to the disentanglement of the complex interplay between ribosome

movement, translation, RNA interference (RNAi), and mRNA stability.
Finally, in **Chapter 6**, co-delivery systems are utilized to design small LNP-based biological circuits to improve noise in mRNA transfections and to tune response times. The implementation of incoherent feed-forward loops (icFFLs) is shown to provide a precise tool for synthetic biology, enabling control over noise, response time.
Chapter 7 concludes with a general discussion, summarizing how these investigations enhance our understanding of the underlying mechanisms of lipid-based RNA delivery and offer various strategies for refining RNA therapeutic approaches as well as for designing tools for synthetic biology applications.

2. Fundamental Concepts

2.1. Gene Expression

2.1.1. Central Dogma of Molecular Biology

Life, as we know, is governed by the central dogma of molecular biology, as illustrated in **Fig. 2.1**. All genetic information is encoded on the desoxy ribonucleic acid (DNA). When a specific piece of information is required, the DNA is transcribed into messenger ribonucleic acid (mRNA) by polymerases. The resulting mRNA is then transported out of the nucleus into the cytosol, where it becomes accessible for ribosomes, the key transnational enzymes. Ribosomes move along the mRNA, matching each codon of the open reading frame (ORF) with the correct transfer RNA (tRNA), which carries the corresponding amino acid encoded by the codon. Each codon encodes a specific amino acid, but different codons can encode the same amino acid, known as synonymous codons. The ribosome then adds the amino acid to the growing peptide chain, ultimately leading to protein synthesis.

2.1.2. Relevance of mRNA: Therapeutic Approaches and Synthetic Biology

Since its discovery in 1961 [31], mRNA has been the focus of numerous investigations, not only for therapeutic applications but also as a tool in synthetic biology. Beyond the well-known mRNA-LNP based COVID-19 vaccine, researchers are exploring mRNA therapeutics to treat other infectious diseases, develop cancer vaccines [32, 33], or address conditions arising from the absence of functional proteins, which can be introduced through mRNA therapy [34–36]. A comprehensive review on therapeutic applications of mRNA and its discovery can be found in the review by Sahin *et al.* [2]. In addition to its therapeutic potential, mRNA has proven to be a valuable tool in synthetic biology, with applications in stem cell engineering, the design of biological networks, and the study of protein functions [2, 37].
The extensive research on mRNA is driven by several factors. First, mRNA translation

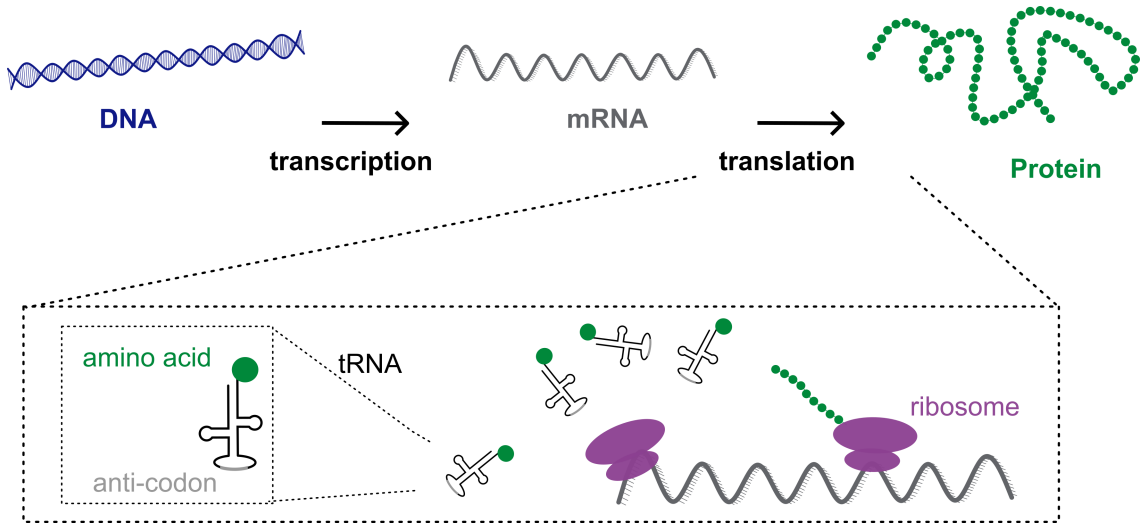

Figure 2.1.: The central dogma of molecular biology: DNA is transcribed into mRNA (nucleus), which is subsequently translated into protein (cytosol). Ribosomes facilitate translation by pairing codons in the mRNA with the tRNA with the matching anti-codon, each the corresponding amino acid.

happens in the cytosol, allowing it to bypass the need to enter the nucleus, which enhances both efficiency and speed compared to DNA-based applications. Additionally, because mRNA does not integrate into the genome, the risk of mutagenesis is significantly reduced. The transient nature of mRNA translation and protein expression enables controlled gene expression within a defined time window after application. However, challenges remain, particularly in improving mRNA efficiency, extending its relatively short half-life compared to DNA, addressing its immunogenicity, precision, and biodistribution [2, 38, 39].

2.1.3. RNA Interference: Mechanism and Applications

In biology, pathways are rarely straight-forward; rather, life operates as a complex network of interfering mechanisms. In 1998, Mello and Fire discovered a specific form of interference known as RNAi, which was awarded the Nobel Prize in 2006 [40]. RNAi is a post-transcriptional gene silencing mechanism wherein small, non-coding double-stranded RNAs, such as small interferring RNA (siRNA) and micro RNA (miRNA) (whose discovery was just awarded with the Nobel Prize in medicine) interfere with mRNA [41, 42]. This interference reduces the levels of target mRNA either through translational repression or cleavage, dependent on the sequence specificity of the interfering RNA [43, 44].
In nature, long double-stranded RNA molecules are cut into 21-23 nucleotide (nt) fragments, by an enzyme called Dicer [45]. Synthetic RNAi can be induced in mammalian cells by directly delivering siRNA targeting a specific sequence [46]. These synthetic

double-stranded RNA fragments are already delivered after the Dicer stage [47]. Unlike the majority of miRNAs, which are not fully complementary to their target sequences, most siRNAs are typically designed to fully match their target sequence for maximum efficiency [42].

The kinetic of translation repression by synthetic RNAi is illustrated in **Fig. 2.2**. Upon reaching the cytosol, siRNA complexes with RNAi-associated proteins to form the RNA-induced silencing complex (RISC). This protein complex includes argonaute protein 2 (Ago2), together with the *trans*-activation RNA binding protein 2, and DICER1 [42]. The anti-sense strand of the interfering RNA binds to Ago2, unwinding the guide strand and serving as a template to recognize the complementary mRNA sequence through Watson-Crick base paring [41]. This interaction ultimately triggers mRNA cleavage. Following mRNA degradation, the RISC/siRNA complex and cleaved mRNA dissociate, allowing the recycled RISC to engage with another target mRNA [48]. This cycle leads to a reduction in target mRNA levels and, consequently, a decrease in the corresponding protein levels.

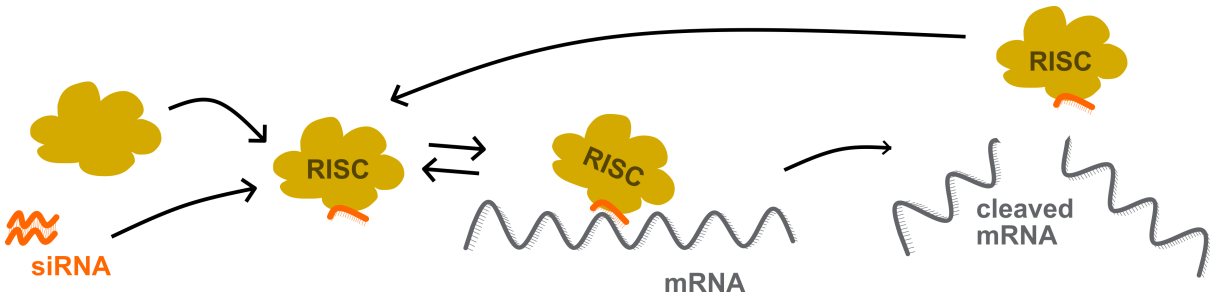

Figure 2.2.: Kinetics of RNA interference: siRNA complexes with RISC proteins, which then locate the complementary binding site on the mRNA. Successful binding leads to mRNA cleavage and recycling of the RISC.

Like mRNA, siRNA holds significant potential as a therapeutic agent. In contrast to mRNA therapeutics, which introduce specific proteins, siRNA therapeutics function by knocking down target mRNA thereby inhibiting its translation. The first successful proof-of-concept for siRNA therapeutics was demonstrated in mice in 2002, targeting hepatitis C [49]. In 2018, the first FDA-approved siRNA-based therapy for human use was filed for Patisiran (Alnylam), targeting hereditary transthyretin amyloidosis [50]. As of today, five additional siRNA therapeutics (though not LNP-based) have received approval for clinical use [42]. Beyond its vast potential in medicine, RNAi serves as a powerful tool in synthetic biology, enabling applications such as the construction of tunable oscillators in cells [51], the manipulation of cell motility [52], the creation of genetic switches [53], and the buffering of noise in gene expression [54, 55].

2.2. Gene Delivery

The effective utilization and investigation of the aforementioned genetic toolbox requires the successful delivery of nucleic acids into mammalian cells. However, naked RNA and DNA are rapidly degraded in biological fluids and are unable to penetrate cells [12] due to their size and negative charge [45]. Additionally, the immune system is primed to target and eliminate any exogenous genetic material [32, 56], further complicating the delivery of unprotected nucleic acids. As a result, alternative strategies are essential for efficient gene delivery.

Over the past few decades, various approaches for gene delivery have been developed. One of the most straight-forward approaches is electroporation, which employs short electrical pulses to temporarily perforate the cell membrane, allowing small molecules to enter. Although this technique can facilitate gene delivery, it also causes cell damage and is limited in therapeutic applications due to difficulties accessing tissues [57]. Viral vectors are widely used to deliver genetic material due to their high transduction efficiency. However, concerns about their safety, including potential immune responses and limited cargo capacity, remain substantial obstacles [32, 58].

Non-viral alternatives such as polyplexes with polyethyleneamine (PEI) as former benchmark candidate and, more recently, poly(ß-Aminoesters) (PBAE) [59] offer stable and customizable RNA complexation. These polymers facilitate cellular uptake and endosomal escape through electrostatic interaction with the cell membrane [60]. However, many polymers exhibit cellular toxicity that needs to be addressed [61].

Currently, the most common delivery method aside from viral vectors, is lipid-based systems. Before lipid nanoparticles (LNPs) dominated the field, liposomes composed of membrane lipids such as phosphatidylcholine (PC), which spontaneously form of bilayer structures, were widely used for gene delivery [62]. However, post-loading of nucleic acids into these liposomes is inefficient and complex, which led to the development of cationic liposomes, which complex with nucleic acids based on charge [63]. A popular and commercially available reagent is Lipofectamine^{TM} 2000, Invitrogen^{TM} (L2000), which is based on cationic lipids [64]. Despite its widespread use in gene delivery research, its application *in vivo* is limited due to the large and heterogeneous size of the particles, their instability, positive charge, and associated toxicity [61]. Later, ionizable lipids such as 1,2-dioleoyl-3-dimethylammonium propane (DODAP) [65] or DLin-MC3-DMA (MC3) [66] were developed, which are positively charged at low pH and can encapsulate negatively charged nucleic acids. Upon transfer to a buffer with physiological pH, these lipids become neutral, thereby reducing toxicity [65]. Further approaches such es cell-penetrating peptides, exosomes, dendrimers, microparticles, or hydrogel-based delivery methods [32],

are interesting but are beyond the scope of this work. Here, mainly LNPs, as the leading technology for non-viral delivery of RNA and gene-editing applications [12], will be used and described in the following sections.

2.2.1. Ionizable Lipid Nanoparticles

In 2017, the first LNP-based drug, Patisiran (Onpattro, Alynylam Pharmaceuticals), was approved for clinical application for the siRNA-based treatment of transthyretin induced amyloidoisis [12, 66]. Since then, the LNP technology has advanced rapidly, contributing to the development of vaccines for the global COVID-19 pandemic [67, 68], and, more recently, to the development of several cancer vaccines [3, 69, 70].
LNPs typically consist of four lipids: an ionizable lipid, a phospholipid, cholesterol, and a polyethylene glycol (PEG)-ylated lipid, whose structures and functions will be discussed in the following section. RNA encapsulation requires rapid mixing, while the molar composition of lipids and nitrogen to phosphate (N/P) ratio (defining the ionizable lipid to mRNA ratio) dictate the properties of the LNP. The ionizible lipid forms a core with nucleic acids and cholesterol, surrounded by an outer shell composed of phospholipids and PEG-lipids [12, 71]. These structural arrangements have been studied for example through molecular modeling [72], small angle X-ray scattering (SAXS) [73], and cryogenic transmission electron cryomicroscopy (CryoTEM) [74].

Lipid Components

Each of the four main lipid classes in an LNP serves a distinct function, and variations in these components lead to changes in LNP structure, size, and cellular processing. Exemplary chemical structures of commonly used lipids from each class are shown in **Fig. 2.3**. The ionizable lipid, such as DODAP or MC3 [75], complexes with the nucleic acid payload. The activity of an LNP is highly dependent on the choice of ionizable lipid [76], particularly its pKa, as a protonation at endosomal pH facilitates endosomal escape [12]. The phospholipid supports the endosomal escape based on its fusiogenic properties [32, 77] and plays a role in circulation time [78] and biodistribution [79]. Cholesterol modulates the nanostructure and thereby contributes to *in vivo* stability. Notably, Patel *et al.* (2020) demonstrated how cholesterol analogs, such as ß-sitosterol, can significantly enhance LNP formulation efficiency [80].
PEGylation of LNPs greatly improves stability and circulation time by shielding the particle [81, 82]. After administration, PEGs lipids exchange with proteins to form a protein corona, which interacts with the cell membrane and influences LNP potency [83, 84]. However, PEG lipids also reduce interactions with the endosomal membrane [85]. Since

PEG lipids reside at the outer shell of the LNP, varying their molar ratio alters the surface-to-volume ratio, making this an important tool for modulating LNP size [74, 86]. Beyond the individual function of each lipid, the overall composition determines efficiency, circulation time, and organ tropism when LNPs are applied *in vivo* [78, 87, 88]. Typically, the lipid ratio of the *Onpattro* formulation is used for LNP applications: ionizable-lipid:phospholipid:cholesterol:PEG-lipid 50:10:38.5:1.5 molar ratio [50].

Nucleic Acid Load

In chapter 2.1.1, DNA and mRNA were introduced as the basic building blocks of life. Additionally, regulatory processes such as RNA interference, which are mediated by molecules like miRNA or siRNA [40, 89], were discussed. LNPs offer the potential to encapsulate not just a single type of nucleic acid but, but multiple species simultaneously. Regardless of the nucleic acid species encapsulated, a key characteristic of LNPs is the nucleic acid to ionizable lipid ratio, commonly referred to as the N/P ratio. This ratio is defined as the number of protonable amine groups on the lipid headgroup (N) to the negatively charged phosphate groups on the nucleic acid backbone (P). Detailed instructions for calculating the N/P ratio can be found in Appendix A.1.3.
Nucleic acids are composed of a phosphate group, a sugar (desoxyribose for DNA and ribose for RNA) and a base. The sugar and the phosphate form the backbone while the specific sequence of bases defines the function. The bases in DNA are adenine (A), guanine (G), cytosine (C) and thymine (T). In RNA, adenine, cytosine and thymine are also present, but thymine is replaced by uracil (U). Through Watson-Crick base pairing [90], where A pairs with T (or U in RNA) and C pairs with G, the DNA's characteristic double helix is formed, and mRNA - tRNA interactions are mediated during translation. The focus of this thesis is to study transient protein expression dynamics through the encapsulation and delivery of mRNA and siRNA. Beyond their biological properties and functions, also the biophysical differences between siRNA and mRNA must also be considered. mRNA is a single-stranded molecule typically ranging from 500 to several thousand nucleotides, whereas siRNA is much shorter double-stranded molecule, consisting of 21-23 nucleotides [45]. These difference result in molecular weights of different orders of magnitude (approximately 10^6 g/mol for mRNA and 10^4 g/mol for siRNA) [2, 45], which has implications for their behavior during the LNP self-assembly and delivery. For instance, previous studies have shown that the co-encapsulation of mRNA with non-functional siRNA can alter the mRNA protein expression, likely due to structural changes within the LNP [91].

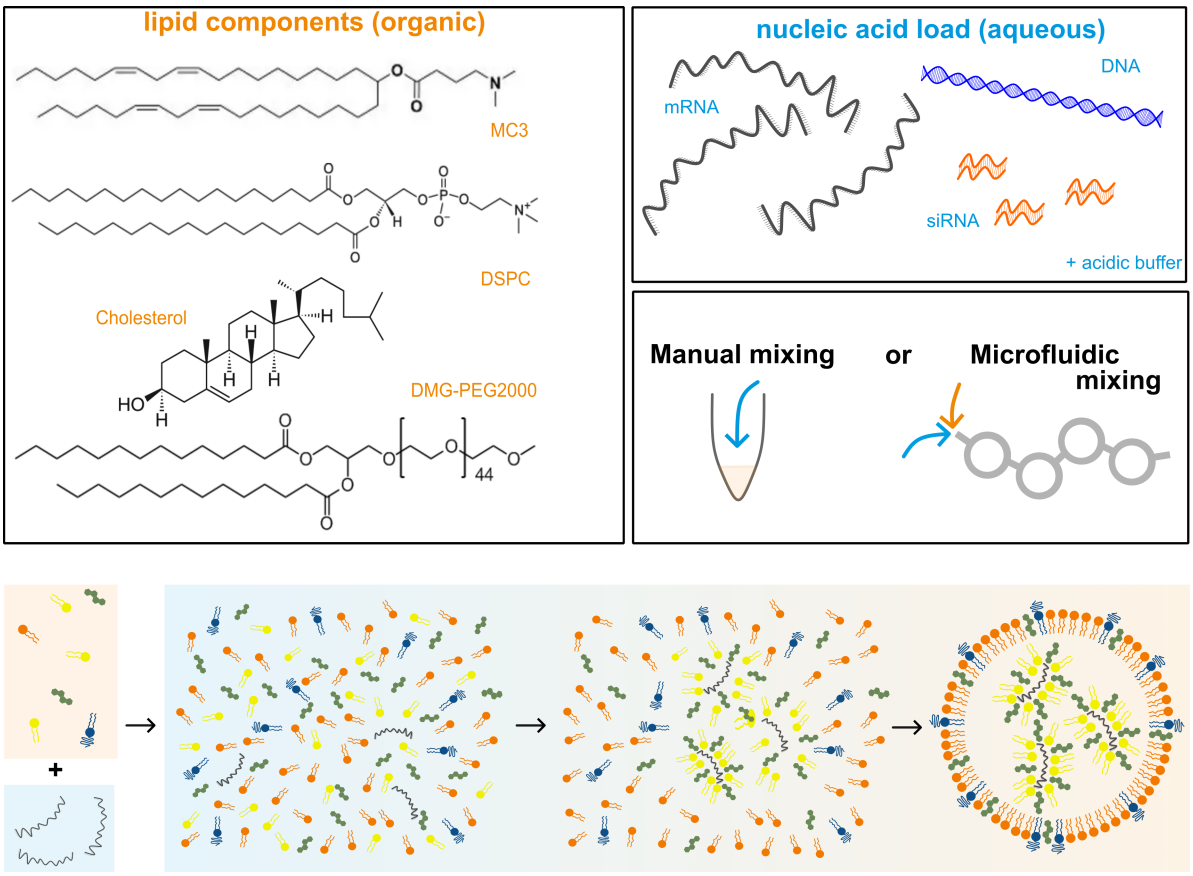

Figure 2.3.: Overview of the LNP production process: Lipid components are combined and dissolved in an organic phase, while nucleic acid components are diluted in water and the respective acidic buffer to form the aqueous phase. The two phases are then rapidly combined, either manually or through microfluidic mixing, leading to the self-assembly of LNPs. Gradient from blue to orange indicating increasing solvent polarity.

2.2.2. Microfluidic Mixing

A defined size and low polydispersity index (PdI) are crucial for precise LNP applications [92] and the preparation method has been shown to determine efficacy [12, 93]. However, simple mixing by pipetting or pouring the organic and aqueous phase together does not result in a homogeneous particle distribution. LNP formation relies on a self-assembly process, driven by electrostatic interactions between the ionizable lipid and the RNA that form inverted micelles containing the RNA. Through the fast increase of lipid solvent polarity (as organic and aqueous phase mix), this micellear aggregation is guided through hydrophobic interactions followed by the formation of the outer shell (**Fig. 2.3**). Therefore, the formation of equilibrium structures is dependent on the rapidity of mixing of the organic and aqueous phases, as it directly influences the local concentration and ratios of the components [94].

To achieve rapid, efficient and controllable mixing, microfluidic mixing - using turbulent

or chaotic flow - is typically employed [86, 95]. Various types of microfluidic mixers are available, with the simplest being a T-junction, featuring two input streams and one perpendicular output stream. To enhance turbulence during microfluidic mixing, more advanced designs have been developed, such as herringbone structures, baffles or torodial channels [86, 96]. With the increasing use of LNPs, numerous mixing technologies and platforms have emerged. However, many of these come with limitations, such as large minimum batch sizes and high dead volumes, which reduce yields [97].
For research applications, lab scale volumes - typically low - and high reproducibility are demanded. One microfluidic mixing platform that meets these requirements is the NanoAssemblr® Spark™, which utilizes microfluidic cartridges with ring mixers as sketched in **Suppl. Fig. A.1**. These bifurcating mixers split the channels into separate paths that merge back together after varying path lengths, creating both chaotic advection through differing paths and turbulent flow at the junctions. This technology enables scalable and reproducible LNP mixing with high encapsulation efficiency despite the low volumes used for mixing [98].

2.2.3. Downstream Processing

Even if the mixing process of the LNP were ideal - so that all initial components form perfectly uniform LNPs - they would still be in a mixture of water, ethanol and acidic buffer, which needs to be exchanged with a physiologic buffer. This is to reverse the ionization of the ionizible lipids and to reduce toxicity in *in vitro* and *in vivo* applications. Additionally, the concentration of LNPs might require adjustment, and - as the process is most likely not ideal - any aggregates formed during processing would need to be removed. Tangential flow filtration (TFF) is a technology capable of addressing all these tasks [99]. However, this technique is not feasible for lab scale production. Fortunately, there are other methods that can be employed to achieve buffer exchange, remove aggregates and adjust concentration. First, buffer exchange can be facilitated with dialysis, using a membrane susceptible to small molecules while retaining the LNPs. Second, aggregates, due to their size and weight difference from LNPs, can be removed by centrifugation. Adjustment of the concentration can either be reached by dilution in the appropriate buffer, while increasing the concentration typically requires vacuum evaporation at room temperature, providing low-stress conditions. A detailed description of the methods, along with corresponding protocols, is provided in section A.1.4.

2.2.4. Size Determination of Lipid Nanoparticles

When discussing the size of an LNP, the property that is most likely referred to is the hydrodynamic radius (R_H) or the hydrodynamic diameter (D_H). The hydrodynamic radius is not necessarily the actual radius of the particle but rather the description of a theoretical sphere that diffuses in the same way as the particle [100].
In this work, two techniques were used to measure the size of an LNP: fluorescence correlation spectroscopy (FCS), which measures fluorescence intensity, and dynamic light scattering (DLS), which measures the intensity of the scattered light. Both methods then calculate the auto-correlation of signals, enabling determination of the hydrodynamic radius.

Fluorescence Correlation Spectroscopy

FCS is a quantitative single-molecule technique that collects photons emitted by fluorescent particles in a liquid sample within a defined volume over time. By calculating the auto-correlation of these signals, FCS enables the analysis of particle concentration, diffusion constant, and thereby particle size, kinetics and other photophysical parameters [101]. To achieve this, a confocal setup is required in order to get a defined detection volume (see Appendix A.1.5). This detection volume can then be approximated as a Gaussian ellipsoid, characterized by its axes ω_z and ω_r. When the fluorescent particles are sufficiently diluted, allowing the detection of only one particle at a time within the detection volume, time-resolved intensity profiles are recorded. These are then used to calculate the auto-correlation function (ACF):

$$G(\tau) = \frac{\langle I(t)I(t+\tau)\rangle}{\langle I(t)\rangle^2} \tag{2.1}$$

Quantitative FCS relies on knowledge of the detection volume and the diffusive properties of the analyte. This information is used to fit the data and obtain both the diffusion time of particles and the amplitude of the ACF. The diffusion time (τ_D) is given by:

$$\tau_D = \frac{\omega_r^2}{4D} \tag{2.2}$$

where D is the translational diffusion coefficient. The particles investigated in this study were assumed to be spherical and were measured in fluids with low Reynolds numbers. Hence, the diffusion time and hydrodynamic diameter are connected by the Stokes-

Einstein equation:

$$D = \frac{k_B T}{6\pi\eta R_H} \tag{2.3}$$

where k_B is the Boltzman constant, T is the temperature, η is the solvent's viscosity, and R_H is the hydrodynamic radius of the spherical particle.
Another important fit parameter is the amplitude of the ACF, which provides information about the number of particles (N) in the detection volume:

$$\frac{1}{G_d(0)} = \langle N \rangle \tag{2.4}$$

When FCS is performed using two spectrally separated fluorophores, a spatial correlation can be introduced into the analysis. The cross-correlation function for two species G_1 and G_2 is defined as:

$$G_{CC}(\tau) = \frac{\langle I_1(t) * I_2(t+\tau) \rangle}{\langle I_1(t) \rangle * \langle I_2(t) \rangle} \tag{2.5}$$

DespiteFCS requiring the incorporation of fluorescence species to the LNP, it enables to study loading efficiency of single or multiple species [102], as well as the ability to monitor LNP-related dynamics, such as self-assembly [103] and formation of the protein corona [104].

Dynamic Light Scattering

DLS, similar to FCS, measures the intensities of diffusing particles in solution with subsequent calculation and analysis of the ACF to determine the diffusion coefficient. In contrast to FCS, DLS does not require fluorophore encapsulation, as it relies on the scattering intensities of the particles instead of fluorescence. Since scattering depends on particle size (and shape), this allows the determination of particle size and size distribution. When particles are illuminated by a laser, elastic electromagnetic scattering occurs, inducing oscillating dipoles resulting in spherical scattering in all directions. For particles smaller than the wavelength of the laser, Rayleigh scattering dominates [105], while for larger particles, Mie scattering dominates [106]. Since these two scattering mechanisms have different proportionalities to particle size and intensity, it can be challenging to quantitatively analyse mixtures of small and large particles.
In addition to providing information about the distribution of hydrodynamic radii, DLS generates information on the polydispersity of the particle solution. The characteristic parameter used to describe this is the PdI, defined as the ratio of the standard deviation

to the mean particle size [100].

2.2.5. Cascade of Cellular LNP Processing

Cellular delivery of nucleic acids through LNPs can be described as a cascade of stochastic processes. An overview of the distinct steps involved is provided in **Fig. 1.1**. This section will explain the single steps from administration to endosomal release [107].

Administration

For LNP transfection experiments, the RNA-LNP is applied systemically, either in *in vivo* applications, or in cell- or tissue cultures for research purposes. Following application, the LNP is exposed to a variety of proteins leading over time to the dissociation of the PEG lipid and the subsequent adsorption of proteins, forming a protein corona around the LNP [22, 85]. This naturally occurring process has been shown to serve as natural targeting mechanism, with the most prominent adsorbed protein being apolipoprotein E (ApoE), which leads to enhanced uptake by liver cells [23].

Uptake

After application, when the LNP reaches a cell, the internal processing, and thus the fate of the particle, is determined by the route of entry into the cell [26, 108]. The dominant uptake mechanism for LNPs has been shown to be endocytosis [23]. Endocytosis encompasses a family of pathways, divided into receptor-mediated (caveolin- or clathrin-dependent) and receptor-independent (micropinocytosis and phagocytois) pathways [109–111]. Most LNPs are internalized via clathrin-mediated endocytosis (CME) [112], facilitated by the particle's protein corona. Various proteins have been shown promote CME [23–25, 113], and, consequently, uptake modulation is possible by adjusting LNP parameters such as its size, lipid ratios, the type of PEG lipid anchor, or the PEG chain size, which in turn affect the type and amount of adsorbed proteins [88, 114]. Additionally, decorating LNPs with targeting ligands allows for the selective transfection of certain cell types [115–117].
However, the numerous parameters influencing particle uptake make accurate quantification of the dynamics challenging. For instance, the timing of uptake is strongly depends on the pathways, ranging from 0.5 to 1.5 hours for CME, and 2 to 6 hours for micropinocytosis [109]. Furthermore, the specific uptake pathway is not only influenced by the protein corona, but has been shown to be determined by particle size, shape and cell-type [118–122]. This variety of factors is reflected in the wide range of uptake times observed, from

rapid uptake within minutes [21, 25, 85] to slower uptake occurring over several hours [80, 123, 124].

Endosomal Escape

After uptake, the particle is trapped inside the endosome, a vesicle composed of the double-layered cell membrane surrounding the LNP(s). As illustrated in **Fig. 1.1**, the endosome can either undergo recycling, degradation, or it can release the LNP into the cytosol, where the cargo becomes accessible for further processing, such as translation. Endosomal escape has been identified as both a major source of LNP-related toxicity [125] and the primary bottleneck in delivery efficiency [126]. In RNA-LNP transfections, only 2 to 15% of the nucleic acid cargo is successfully released into the cytosol [97, 109, 127–129], while the remainder is degraded or undergoes exocytosis [130–132].
Hence, investigating the underlying mechanism is crucial for improving LNP-based nucleic acid delivery. One key factor is endosomal acidification, which starts in early endosomes at pH 5.5 - 6.5 and progresses to late endosomes at pH 5.0 - 5.5 [124, 133, 134]. This acidification induces structural changes in the LNP as a function of the pH [73, 135, 136] that destabilize the endosomal membrane, facilitating escape. Specifically, the transition from an inverse micellar (L_{II}) phase to an inverse hexagonal (H_{II}) phase [73] aids endosomal destabilization through fusion of protonated lipids and endogenous endosomal lipids, allowing the release of the cargo. Different types of lipids possess different curvature profiles that depend on their shape and contribute to the formation of lamellar or inverted phase, has been confirmed through CryoTEM [13, 65, 112, 137–139].
The window of opportunity for endosomal escape is narrow [126], and faster endosomal trafficking has been correlated with higher expression levels [134]. Therefore, understanding the timing of these events is critical, as the speed of trafficking influences the likelihood of escape [140, 141]. Reported time scales for escape vary widely, from minutes up to 15 hours, and are further influenced by factors such as endosomal size [114] and the lipid composition of the LNP [128, 142]. Beyond the contribution of the ionizable lipid, cholesterol also plays a role by stabilizing the curvature region of the endosomal opening during release [143, 144]. Close interaction between the LNP and the endosomal membrane is necessary for membrane fusion, and therefore, partial removal of the protein corona is required for this interaction [145]. Thus, the design of the protein corona also impacts the efficiency of LNP escape. Interestingly, the number of LNPs within a single endosome can affect the probability of release, likely due to the buffering effect of the ionizable lipid [24, 114]. An overview of the reported timescales for endosomal escape is provided in publication [**P2**].

After escape into the cytosol, the linear delivery model presented in **Fig. 1.1** suggests that an additional step is required, in which mRNA is released from residual lipids. This step determines the time frame from endosomal release to the initiation of translation [145].

2.2.6. Co-delivery strategies

The increased loading capacity of LNPs compared to viral vectors [146] facilitates the co-delivery of several and different nucleic acids. For example, the co-delivery of siRNA and mRNA has been tested for cancer therapy to deliver tumor suppressors together with siRNA mediated knock down of oncogenes [91], as well as to enhance chimeric antigen receptor T-cell (CAR-T) cell therapy [147]. In synthetic biology, co-delivery has gained particular relevance with the advent of CRISPR/Cas engineering, which requires the delivery of Cas9 protein - either as a protein or encoded in mRNA or plasmid DNA (pDNA) - alongside single guide RNA (sgRNA) [6, 7, 148–150].
For packaging in co-delivery of two species, three different strategies are available. The two different species can either be co-encapsulated and delivered together (**Fig. 2.4a**), encapsulated separately but be co-delivered (**Fig. 2.4b**), or encapsulated separately and be delivered sequentially at different timepoints (**Fig. 2.4c**). Depending on the chosen approach and the encapsulated species, the expression levels [91, 129, 151] and kinetics [152] of the delivered nucleic acids may vary.

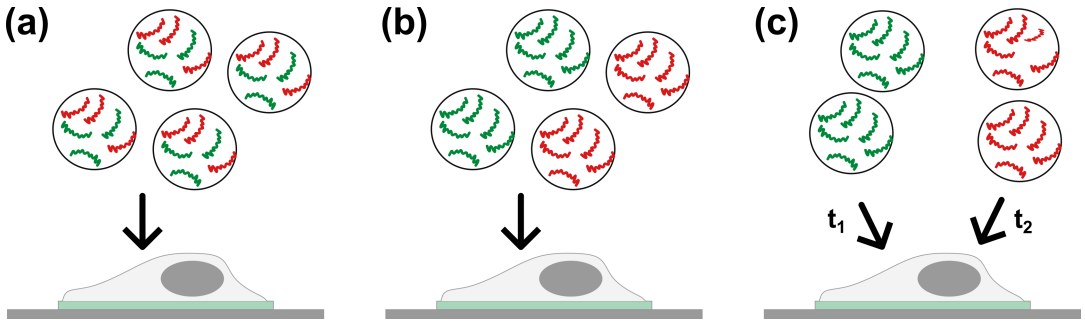

Figure 2.4.: Co-Delivery Strategies: (a) Co-encapsulation of two species within the same particle. (b) Separate encapsulation and simultaneous delivery, or (c) separate encapsulation with successive delivery at different timepoints.

2.3. Single-Cell Experiments

2.3.1. The Role of Single-Cell Experiments in Biophysics

For a long time, information regarding how cells respond to perturbations and process information was gathered primarily through ensemble measurements or as averaged data points [153, 154]. While population analysis might be sufficient to answer certain scientific questions, others require more detailed insights. These insights are crucial because a population is not necessarily representative of its individual members. Cellular heterogeneity manifests in various features, such as metabolic state, cell cycle, gene expression, and cell differentiation status [72, 153]. Together with cell history and microenvironment, these factors contribute to phenotypic differences. As discussed by Snijder and colleagues in 2011, these differences often arise from deterministic processes [154]. Every biochemical reaction carries a certain level of noise, and each pathway consists of cascades of biochemical reactions with inherent noise levels. Additionally, any treatment applied in solution to a cell population leads to a distribution of molecules that reach the cells. Every step of uptake and processing is thus a stochastic process, resulting in heterogeneity of a populations response.
In this work, the implications of both intrinsic and extrinsic noise are studied. The importance of single-cell experiments for precision measurements is highlighted, along with how these measurements can be utilized to measure, understand and control noise.
Noise can be conceptualized as a statistical property of cell populations [72, 153]. Intrinsic noise is primarily caused by variations within molecular networks and biochemical reactions, while extrinsic noise is associated with differences in protein levels resulting from upstream influences, such as the environment or treatment conditions. [155–157]. Consequently, a fundamental challenge in population experiments is presented by the separation of stochasticity from deterministic effects at the phenotypic level [154, 158].
Reflecting on the phenomenon of noise, it could be questioned, how the complexity of a mammalian cell, with all its regulations and stochastic variations, can remain functional. A partial answer to this lies in regulatory mechanisms and networks, which will be discussed later in this work [159]. However, the investigation of regulatory networks is also hindered by several of the aforementioned factors. In particular, the lack of cell synchronization in the ensemble can mask subpopulations [154] or wash out important information about dynamics [72]. This makes single-cell imaging indispensable for the analysis of biological circuits [160]. Additionally, single-cell analysis enables to simultaneous measurement of multiple coupled parameters [153], facilitating multivariate analysis, as demonstrated by Murschhauser *et al.* [161]. However, isolating cells may lead to ad-

verse effects, as it has been shown that processes such as endocytosis can be influenced by cell-cell contact [154].
Various techniques are available to capture single-cell properties, including flow cytometry, PCR analyses, and single-cell sequencing methods. However, these methods typically do not provide temporal resolution.
Other methods, particularly newer (fluorescence) microscopy techniques, allow the acquisition of temporal information, enabling the study of molecular dynamics and kinetics [162]. Recently, a broader range of super-resolution microscopy techniques have been developed, allowing the tracking of single molecules or compartments within a cell. Prominent examples include Stochastic Optical Reconstruction Microscopy (STORM), Stimulated Emmission Depletion Microscopy (STED), and Structured Illumination Microscopy (SIM), which have significantly contributed to the understanding the fate of LNPs inside eukaryotic cells [163–165]. To capture information about the microenvironment, methods such as fluorescence lifetime imaging microscopy (FLIM) [111, 166, 167] or förster resonance energy transfer (FRET) [168–171] are commonly employed for observations at the nanometer scale.
The focus here is on a time-lapse fluorescence microscopy method that enables the recording of trajectories of thousands of single cells in parallel over time periods up to 72 hours: live-cell imaging on single-cell arrays (LISCA) [30, 107, 172–174]. In addition to temporal resolution of up to 48 hours, this technique provides sufficient statistics for high-precision measurements. The LISCA workflow is illustrated in **Fig. 2.5** and will described further in the following sections. In brief, micro-patterned substrates are prepared to allow adhesion of one cell per spot (**Fig. 2.5a**). Transfection of cells with fluorescent reporters allows the uptake and expression kinetics of each cell to be tracked via live-cell microscopy under physiologic conditions (**Fig. 2.5b**). Automated image analysis produces hundreds of trajectories per experiment (**Fig. 2.5c**), which serve as the basis for analyzing underlying kinetics, fitting mathematical models, and investigating noise.
This technique enables the identification of subpopulations, rare events, and correlations between activities. Additionally, genetic circuits, which may otherwise be washed out due to the lack of cellular synchronization, can be analyzed. The kinetic data allow to quantitative comparisons with dynamic models [72, 107, 174].

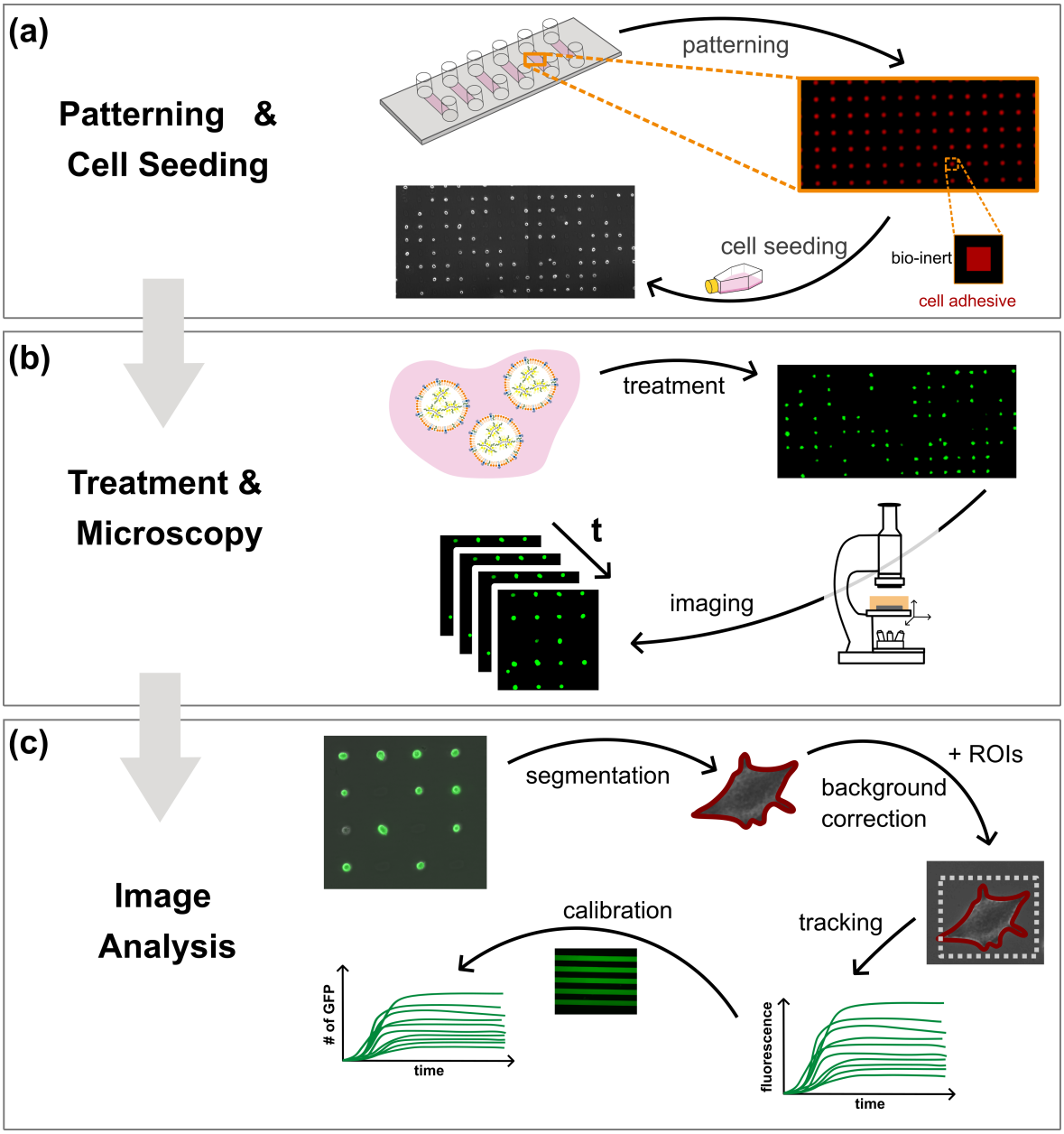

Figure 2.5.: Live-cell imaging on single-cell arrays: (a) Microscope slides are patterned, followed by cell seeding to allow self-assembly, (b) Cells are treated, and time-lapse imaging is performed under physiological conditions, (c) Image analysis is conducted to generate trajectories.

2.3.2. Subtractive or Additive Preparation of Single-Cell Microarrays

High-throughput measurement of single-cell gene delivery and protein expression requires separation of cells. To prevent the formation of a cell layer, substrates with cell-adhesive spots with an area in the order of magnitude of a single cell are prepared, surrounded by a bio-inert surface. This ensures a standardized confinement of cells and maintains a

rather uniform cellular surface across all observed cells, which is particularly important for quantitative uptake studies.

A variety of micro-patterning techniques can be applied to achieve this. In earlier work, methods such as selective microscale plasma-initiated protein patterning (µPiPP) [175], photo-lithography for the production of microstructured gold squares [176], and hydrogel-based micromolding [177, 178] have been tested. In this work, selective UV-illumination was chosen to pattern a bio-inert PVA surface using either an additive or a subtractive approach. Both methods are illustrated in **Fig. 2.6**.

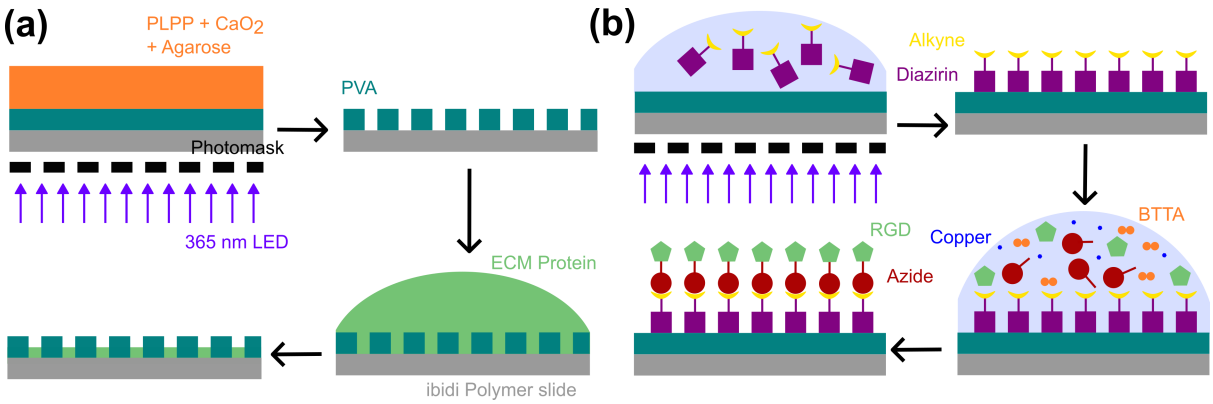

Figure 2.6.: Single cell micropatterning techniques: (a) Selective removal of PVA, (b) Photopatterning

Both approaches are based on selective illumination through a silica wafer photo mask with 20x20µm squares that are susceptible for UV-light. The subtractive approach illustrated in **Fig. 2.6a** employs a catalytic mixture based on the photoactivatable reagent PLPP (Enamine) to remove the PVA layer at the illuminated spots. Consequently, the slide surface is uncovered and can be coated with proteins. Laminin, a protein commonly found in the extracellular matrix (ECM) of epithelial cells, was primarily used to facilitate cell adhesion at the patterned squares.

The additive approach, shown in **Fig. 2.6b**, utilizes selective UV illumination to couple a diazirine alkyne to the PVA surface. This selectively modified surface served as a basis for the coupling of the cell-adhesive peptide cyclo-Arg-Gly-Asp (cRGD) via a $CuSO_4$ click reaction. For detailed materials and experimental methods, refer to Chapter A.1.

2.3.3. Time-Lapse Microscopy

Single-cell analysis as described here, requires a fast imaging technique that allows for the tracking hundreds of single cells in parallel and capture reporter dynamics. Light microscopy is considered the most fundamental tool for investigating biological samples

[179]. The simplest application of light microscopy is brightfield imaging, which utilizes the density differences in biological samples that lead to variations in absorption, generating contrast. A slightly more advanced set-up is required for phase contrast imaging, where the contrast is enhanced compared to brightfield imaging. Here, the phase shift generated by different compartments within a cell is converted to amplitude differences, visualizing the contrast.
The most important light microscopy technique in the context of this work is fluorescence microscopy. This method is based on the property of certain molecules to emit photons upon excitation with a specific wavelength, and the emission is captured to generate contrast [180]. For this work, an epifluorescence microscope was employed to collect brightfield images (for identifying and tracking cells) and fluorescence images (to follow the kinetics of fluorescent reporters). To enable long-term live imaging, an incubation chamber for physiological conditions was built around the microscope.
In the next section, different classes of fluorescence reporters relevant to this work will be discussed.

2.3.4. Fluorescence Reporters

To follow protein expression over time, fluorescence reporters provide a direct readout. Fluorescence is a photo luminescent process in which excitation of matter with photons of a distinct wavelength leads to emission of photons of longer wavelength (Stokes shift) after relaxation to the ground state. This process is characterized by the transition from the excited singlet state to the ground state within nanoseconds, resulting in the emission of a photon. During fluorescence microscopy, the emitted photons are then converted into electronic information that allows for their quantification. [162]
To assess the fate of an LNP during a transfection, two different types of reporters are utilized here: fluorescent proteins that are encoded within the delivered mRNA and fluorescent molecules that are covalently coupled to the mRNA or lipid components.

2.3.5. Fluorescent Proteins

The fluorescent property of fluorescent proteins is encoded in their peptide sequence. Fluorescence is then based on the specific microenvironment given by protein structure that relies on correct folding. Such sequences can be encoded in mRNA or plasmid vectors, presenting the opportunity for studying the kinetics of gene expression.
The most famous fluorescent protein is the green fluorescent protein (GFP), which was discovered in 1962 [181, 182]. Here, fluorescence arises from three adjacent amino acids -

serine, tyrosine, and glycine - that are located in the center of the beta-sheet cylinder of the folded protein. This configuration creates a hydrophobic environment for the carboxyl group of the serine and the amino group of the glycine to react, forming a imidazolinone ring system that - in an oxidation step, reacts with the tyrosine to form a fluorophore with an emission peak at around 509 nm [183].
Significant effort has been dedicated to engineering GFP for improved brightness, stability, and efficiency. Numerous variants of GFP with color-shifted fluorescence now exist [184], allowing for multiplexing in live-cell experiments. Over the last few years, a variety of other fluorescence proteins, beyond the GFP family, have been discovered and improved, including the recently developed mScarlet 3[185] and mGreenLantern [186].

Direct Labelling of RNA-LNPs

Transfection with endogenous reporters in endogenous vehicles may require tracking their fate during the experiment [80, 122, 187]. Due to their unique photophysical properties and biocompatibility, the cyanine dye family is commonly used for the labeling of biomolecules [188]. Their fluorescent properties arise from an electron-accepting methine (quaternary amine) group connected through a spacer with a tertiary amine group, forming a π-conjugated system [189]. In this work, cyanine 3 (Cy3) and cyanine 5 (Cy5) dyes are primarily employed, as they can easily be coupled to RNA or lipid molecules [190, 191].

2.3.6. High-Throughput Automated Image Analysis

A typical time-lapse scanning microscopy experiment captured 100-150 view field positions, with one image taken per timepoint and position. For a 30-hour experiment with a 10-minute capturing interval, this resulted in in $1.8 * 10^4$ to $2.7 * 10^4$ images. **Fig. 2.6** shows exemplary snapshots from one field of view after transfection. Apart from the need for effective data storage management, this large volume of data required an advanced image analysis platform.
The in-house developed python-based automated microscopy analysis (PyAMA) provides a workflow that enables the time-lapse data to be analyzed in a semi-automated manner [30, 174, 192]. In a first step, segmentation of cells based on the deviation of the pixel gray scale values of bright field images was performed, yielding the shape and coordinates for individual cells. Additionally, a background correction based on the algorithm, developed by Schwarzfischer *et al.*, was applied. This algorithm, designed for the analysis of time-lapse data, accounts for the decrease in background signal of the poly(vinyl alcohol) (PVA) slide over time due to photo bleaching, and was applied separately for each time stack

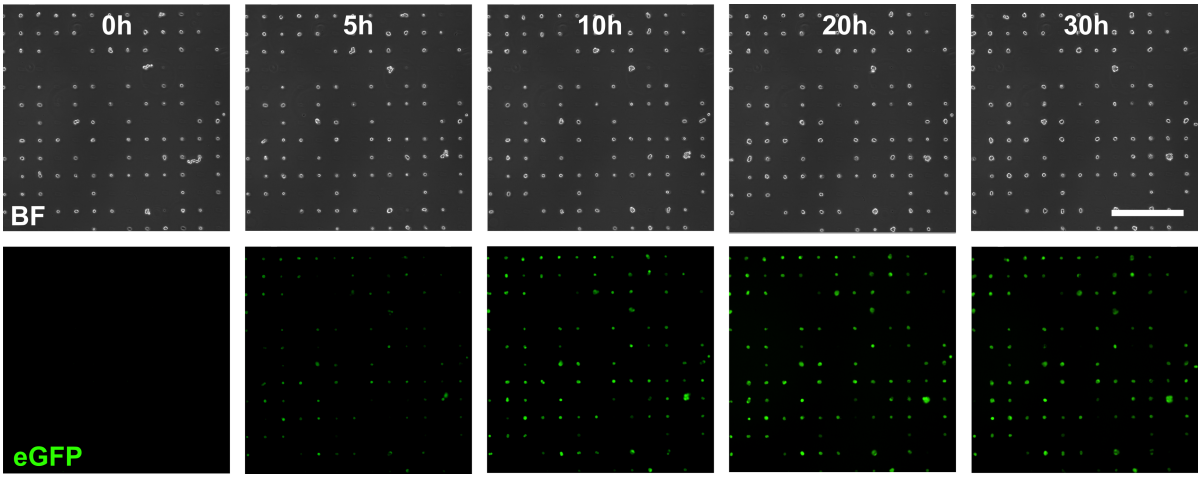

Figure 2.7.: Snapshots from time lapse imaging: HuH7 cells were transfected with GFP mRNA and imaged for 30h. One exemplary field of view is shown for different timepoints as indicated. Top row shows brightfield images, bottom row shows GFP fluorescence.

[193]. Segmentation and background correction were fully automated for the analysis of an entire nd2 (a Nikon specific file format) file. Following this, manual intervention is required to ensure that automated cell selection adheres to the selection criteria. Classical exclusion criteria included: double or multiple occupancy per spot, cell not attached to a spot, cell death during the observation period, or - depending on the experimental scope - cell division during observation. More advanced segmentation algorithms, such as cellpose [194] were tested and certainly, artificial intelligence will further improve the analysis workflow in the future.
After segmentation, background correction and manual selection, a region of interest (ROI) was defined. The ROI can be the cell shape itself or, as employed in this work, a square around the cell, as indicated in **Fig. 2.5c**. This ROI significantly reduced the fluctuations in the fluorescence trajectories without altering the protein expression signal. By loading the segmentation with ROIs, background-corrected fluorescence stacks, and tracking data of each cell over time, fluorescence trajectories were generated, forming the basis for most of the results presented in this work.

2.4. Mathematical Modelling of RNA Delivery

2.4.1. LNP Delivery as a Cascade of Stochastic Processes

In **Fig. 1.1**, the complexity of LNP delivery to mammalian cells is depicted. Based on this dissection into smaller sub-processes, quantitative modelling becomes possible [21, 137, 195, 196]. As described previously, these steps include administration and corona

formation, binding to the cell surface, followed by uptake via endocytosis and endosomal processing inside the cell, which can lead to either recycling, degradation or mRNA release. From there, the mRNA is unpacked from the lipids, enabling translation initiation through ribosome binding, followed by translation and eventual protein maturation. Each of these steps involves distinct forward and degradation rates. Naturally, this simplification of a biological process is accompanied by complications, such as the varying number and loading of endosomes, cell-type specificity of certain rates, and rare events that may interfere with the cascade [161].
By overcoming those challenges, quantification of gene delivery is enabled, offering a valuable tool to improve understanding, predict gene delivery, and support the development of new therapeutic applications or investigative tools for biotechnology. However, only a few rates have been quantified in the past. Time-resolved single-cell microscopy experiments provide the opportunity to access specific rates with high statistical significance and to further explore correlations between events [72]. In this work, fluorescence trajectories monitor protein production following RNA transfection and, therefore, allow the underlying rates to be determined, as discussed in the following sections.

2.4.2. Translation Modelling

In a simple approach, where protein is produced with k_p and degraded at rate k_d, the change in protein P over time is expressed as:

$$\frac{\partial P(t)}{\partial t} = k_p - k_d * P(t) \tag{2.6}$$

Solving this differential equation results in:

$$P(t) = P_{st} * (1 - e^{-k_d * t}) \tag{2.7}$$

where P_{st} represents the steady-state level of protein. This model was developed for DNA-based protein expression, where the level of mRNA can be approximated as constant over time. The steady-state level of protein expression is defined as:

$$\frac{\partial P(t)}{\partial t} = 0 = k_p - k_d * P_{st} \tag{2.8}$$

leading to:

$$P_{st} = \frac{k_p}{k_d} \tag{2.9}$$

This shows that the steady-state level is the ratio of the production rate to the degradation rate.
Another characteristic parameter in gene delivery is the response time $t_{1/2}$, defined as the time after which half of the steady-state level is reached. Using equation 2.7, this is calculated as:

$$P(t_{1/2}) = \frac{1}{2} * P_{st} = P_{st} * (1 - e^{-k_d * t_{1/2}}) \tag{2.10}$$

and therefore:

$$t_{1/2} = \frac{ln(2)}{k_d} \tag{2.11}$$

This demonstrates that the response time is solely dependent on the general decay rate defined as defined in this simple model [197].
In the mRNA-LNP-based transfection experiments conducted in this work, protein expression is transient. However, within the observed time frame and due to high protein stabilities, a steady-state level can be approximated with the maximum expression level (**Fig. 2.8**).

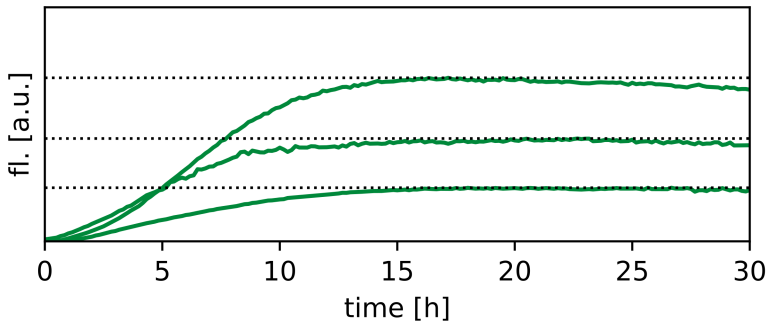

Figure 2.8.: Approximation of steady-state level with maximum expression level: In transient protein expression experiments, when protein stability is high, the steady-state level observed in stable protein expression experiments can be approximated by the maximum protein expression level. Exemplary single-cell traces (green) following LNP transfection of GFP mRNA are shown, with the maximum expression level indicated by black dotted lines.

From this general model for protein production, a more specific model for mRNA translation following transfection, described as a biochemical reaction, has been proposed [21].

In this model, the translation rate is denoted as k_{tl}, the protein degradation rate as β, and $mRNA(t)$ represents the number of mRNA molecules available for translation at time t:

$$\frac{\partial P(t)}{\partial t} = k_{tl} * mRNA(t) - \beta * P(t) \tag{2.12}$$

In contrast to the simple model described above, the mRNA level is not constant over time but is also subject to degradation at a rate δ. Therefore, this decay must be implemented via an additional differential equation:

$$\frac{\partial mRNA(t)}{\partial t} = -\delta * mRNA(t) \tag{2.13}$$

This set of differential equations 2.12 and 2.13 yields an analytical expression for the number of proteins, with m_0 representing the number of mRNA molecules available at time t_0:

$$P(t) = \frac{m_0 * k_{tl}}{\delta - \beta} * (1 - e^{-(\delta-\beta)(t-t_0)}) * e^{-\beta(t-t_0)} \tag{2.14}$$

This formula predicts the time-dependent amount of protein within a cell. In this work, protein production is monitored via protein fluorescence, as exemplified in **Figs. 2.5b, c, 2.7**. As described previously, fluorescent proteins must fold correctly - or in other words: mature - to become fluorescent. To account for this in the translational model, a term for protein maturation, with maturation rate k_m, was included [172]. The resulting three-stage model for mRNA translation into immature protein (P^*), maturing into functional - fluorescent - protein (P), is sketched in **Fig. 2.9a**. This process is described by the following set of ordinary differential equations (ODEs):

$$\frac{\partial mRNA(t)}{\partial t} = -\delta * mRNA(t) \tag{2.15}$$

$$\frac{\partial P^*(t)}{\partial t} = k_{tl} * mRNA(t) - k_m * P^*(t) - \beta * P^*(t) \tag{2.16}$$

$$\frac{\partial P(t)}{\partial t} = k_m * P^*(t) - \beta * P(t) \tag{2.17}$$

with the solution:

$$P(t) = m_0 * k_{tl} * (\frac{1}{\delta + k_m} * e^{-(\beta + k_m)(t-t_0)} - \frac{1}{\beta - \delta} * e^{-\beta(t-t_0)} + \frac{k_m}{(\beta - \delta)(\beta - \delta + k_m)} * e^{-\delta(t-t_0)}) \tag{2.18}$$

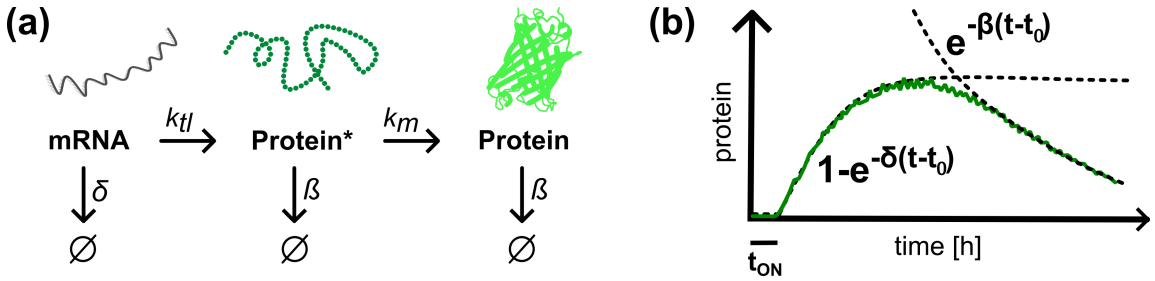

Figure 2.9.: Three-stage maturation model for mRNA translation (a) A schematic presentation of the model illustrates mRNA being translated at rate k_{tl} into the amino acid chain, which matures at rate k_m into functional protein. Both mRNA and protein are subject to degradation at rates δ and β, respectively. (b) The solution of the ODEs describing the model indicates that the initial phase of the fluorescence trajectory - after a distinct onset time - is primarily influenced by mRNA stability, while the second phase is dependent on protein stability. Approximations are indicated with dashed lines. Figure adapted from **[P2]**

For GFP, a valid approximation is that $\beta << \delta$, allowing the initial incline to be described by an exponential function solely dependent on the mRNA degradation rate δ, running into a steady-state level. Consequently, the response time is proportional to the inverse of the mRNA degradation rate. Accordingly, the decline is only dependent on the protein stability, at long time-scales. Both approximations are illustrated in **Fig. 2.9b**. It is important to note that the degradation rates mentioned are not the total degradation rates at which no more mRNA or protein is detected; rather, the mRNA degradation rate indicates the point at which mRNA is no longer intact enough for successful translation, while the protein degradation rate indicates where the protein denatured so that no more fluorescence is generated. To enhance the precision of fitting, protein degradation and maturation can be quantified using an experimental approach where cycloheximide, a translational suppressor, is added during a LISCA experiment. After addition, every translation is halted. Apart from the toxic side effects, fluorescence trajectories from this timepoint onward are shaped solely by protein degradation and maturation [172].

2.4.3. RNA Interference Modelling

In addition to translation, this work examines the interference of mRNA with siRNA. Therefore, it is crucial to not only investigate the mathematical modeling of mRNA translation but also to analyze the kinetics of this RNA interference (RNAi).
To quantitatively describe RNAi, various models have been proposed in the past. Cuccato *et al.* [47] summarized common models, including a stoichiometric model with and without co-cooperativity (simultaneous binding of more than one siRNA), an enzymatic approach based on Michaelis-Menten kinetics and a Hill-kinetic model derived from phenomenological observations. They aim to capture the dependence of the mRNA decay rate with the siRNA/RISC and mRNA concentration.
In **Fig. 2.10**, schematic mRNA decay rates for different modeling approaches are presented for varying siRNA concentrations. The first attempt assumes a stoichiometric reaction between mRNA and siRNA-associated RISC, followed by mRNA cleavage and subsequent degradation of both components. Based on this model and following mass-action kinetics, the RNAi-induced mRNA degradation (δ_{RNAi}) is proportional to the concentrations of siRNA/RISC and mRNA:

$$\delta_{RNAi}([mRNA],[siRNA/RISC]) \sim [mRNA] * [siRNA/RISC] \tag{2.19}$$

Within this framework, co-cooperativitiy can be included, which accounts for the presence of multiple siRNA binding sites (n) on the mRNA. This leads to:

$$\delta_{RNAi}([mRNA],[siRNA/RISC]) \sim [mRNA] * [siRNA/RISC]^n \tag{2.20}$$

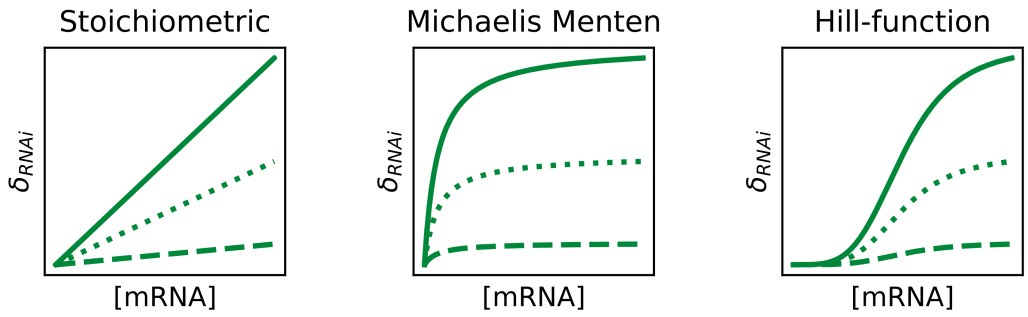

Figure 2.10.: Modelling of RNA interference: Three mathematical approaches to describe RNAi dependent mRNA degradation ($delta_{RNAi}$) are illustrated here. Example graphs represent a stoichiometric approach, Michaelis-Menten kinetics, and Hill-function enzyme kinetics. Bold, dotted and, dashed line indicate varying concentrations of siRNA from high to low, respectively.

However, the stoichiometric approach does not account for siRNA/RISC recycling after

cleavage, making it insufficient for modeling mammalian RNAi dynamics [198]. A more intuitive model for describing RNAi kinetics employs classical Michaelis-Menten enzyme kinetics, as previously described by Malphettes *et al.* in 2006 [199]. This model incorporates the recycling of RISC and describes the reaction in two steps. In a first step, the siRNA associated with RISC and the mRNA reversibly form a complex at rate k_{comp}:

$$[siRNA/RISC] + [mRNA] \overset{k_{comp}}{\rightleftharpoons} [mRNA - siRNA/RISC] \tag{2.21}$$

In a second step, this complex is dissolved at a specific cleavage rate k_{cleav}. Non-reversibly, the mRNA is cleaved and the siRNA/RISC dissociates, becoming available for the next reaction.

$$[mRNA - siRNA/RISC] \xrightarrow{k_{cleav}} \text{cleaved } mRNA + [siRNA/RISC] \tag{2.22}$$

In the publication by Malphettes *et al.*, the authors demonstrate that the degradation rate in this dynamic can be expressed as:

$$\delta_{RNAi}([mRNA], [siRNA/RISC]) = \frac{k_{cleav} * k_{comp}}{k_{cleav} + k_{comp} * [mRNA]} * [mRNA] * [siRNA/RISC] \tag{2.23}$$

Assuming constant siRNA/RISC concentrations (which is a valid assumption due to its high stability [42, 200]), this follows classical Michaels-Menten kinetics with a maximum reaction speed (v_m):

$$v_m = k_{cleav} * [siRNA/RISC] \tag{2.24}$$

and Michaelis Menten constant:

$$k_m = \frac{k_{cleav}}{k_{comp}} \tag{2.25}$$

leading to:

$$\delta_{RNAi}([mRNA], [siRNA/RISC]) = v_m * \frac{[mRNA]}{k_m + [mRNA]]} \tag{2.26}$$

Naturally, this model can also be expanded to include co-cooperativity by accounting for multiple siRNA binding sites on the mRNA. In this case, an intermediate step is included, where additional siRNA/RISCs can bind to the mRNA depending on the number of

binding sites. When the mRNA is cleaved, the corresponding number of siRNA/RISC would be released.
Lastly, a Hill-function approach, often applied to describe ligand-receptor dynamics, can be adapted to RNAi. The basic assumption here is, that one substance (siRNA/RISC) is present in high (respectively constant) concentrations, while the concentration of the other is present in lower concentration [201]. Phenomenological studies suggest, that RNAi dynamics are well-captured by this approach [47]. By adapting the general Hill-equation for RNAi, the degradation rate becomes:

$$\delta_{RNAi}([mRNA],[siRNA/RISC]) = \delta_{RNAi,max} * \frac{[mRNA]^h}{\theta^h + [mRNA]^h} * [siRNA/RISC] \quad (2.27)$$

where h is the Hill coefficient, $\delta_{RNAi,max}$ is the maximum degradation rate caused by RNAi, and θ the concentration of siRNA/RISC required to reach half of $\delta_{RNAi,max}$, assuming that the ligand (mRNA) concentration is variable and the receptor (siRNA/RISC) concentration constant.

2.5. Biological Circuits

When approaching a biological issue from a physics point of view, one prominent question often arises: in a population of genetically identical cells of the same type, where every cell is confined in the same way and has access to the same nutrients, why doesn't every cell produce the exact same amount of protein [202]? Even if each cell is exposed to the exact same input signals, large fluctuations are still observed, resulting in heterogenoeity of protein expression. This variability, often referred to as noise, can stem from various internal and external factors. The intricate processes required for the health and function of mammalian cells are inherently subject to stochastic noise, which may have driven the evolution of regulatory motifs [154, 203, 204]. A major objective in systems biology is to understand such regulatory processes on the single-gene level [72]. By studying simple network motifs, those insights contribute to the understanding of more complex interactions. Single-cell analysis with temporal resolution enables the study of genetic circuits, by capturing cell-to-cell variability [72].

2.5.1. Gene Expression Noise

Cell-to-cell variability can arise from different cellular states or from stochastic fluctuations inherent in every molecular reaction within a cell [205]. This is particularly pronounced when small numbers of molecules are involved in biochemical reactions, where fluctua-

tions in molecular concentrations dominate. Such biochemical noise eventually results in phenotypic differences even within isogenic populations [206].
A mathematical explanation for noise of single-cell protein levels can be derived from the simple model for protein production presented in Equation 2.6, where the steady-state level is derived as the ratio of the production and decay rate. A rate analysis, as illustrated in **Fig. 2.11**, demonstrates how the steady-state level is influenced by fluctuations in those rates and how their intersection defines the steady-state level. In gene transcription networks, the production rate is assumed to be constant due to continuous gene transcription. However, the removal or degradation rate increases steadily over the cell cycle, as dilution from cell growth is considered. (**Fig. 2.11a**). Variations in the production rate, with a constant removal rate, result in different steady-state levels (**Fig. 2.11b**), and similarly, variations in the removal rate yield comparable effects (**Fig. 2.11c**. Both removal and production rate are complex biological processes subject to intrinsic fluctuations, resulting in noise.

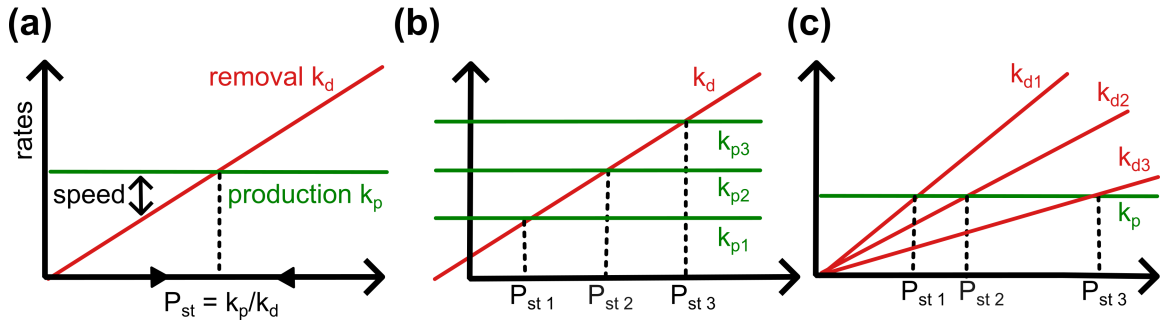

Figure 2.11.: Origin of noise explained by a simple protein production model: (a) Protein is produced with a constant k_p, while the decay rate k_d increases over time. The intersection of these rates defines the steady-state level as derived in Equation 2.9. (b) Variations in the production rate result in different steady-state levels, leading to noise. (c) Similarly, fluctuations in the decay rate lead to variability in the steady-state level, also contributing to noise.

2.5.2. Gene Expression Networks

Nature's strategy for controlling noise involves complex regulatory networks. While much is known about transcription networks [197], this work focuses on translation networks. Transcription networks regulate gene expression and typically consist of interaction patterns between genes and transcription factors. In contrast, translation networks are primarily regulated by miRNAs, the predominant post-transcriptional regulator [89]. Notably, miRNAs control approximately 60% of the human genome through RNAi, as discussed in section 2.1.3 [43].

The combination of transcription and translation networks creates complex regulatory systems, such as the well-characterized miRNA200c network involved in numerous cellular processes, such es proliferation, motility, apoptosis, and epithelial-mesenchymal transition (EMT) [52, 207, 208]. Many of these systems can be reduced to a set of fundamental network motifs [209, 210], which are essential building blocks of gene regulation. These motifs will be explored in the following section.

The most straightforward regulatory motif is simple regulation, where a factor X, activated by an input signal, regulates transcription of a gene Y or the translation of mRNA Y (**Fig. 2.12**). The product of Y increases and eventually saturates into a steady-state level (for a mathematical description, see section 2.4.2). Thus, the level of Y product is directly dependent on the amount of X and its own degradation rate.

Another motif is negative autoregulation (NAR), in which a gene or an mRNA Y represses the production of its own product. This occurs, for example, when a transcription factor inhibits the transcription of its own gene. In *E.coli*, this is a common network motif [211] characterized by shorter response times and reduced cell-to-cell variability. In such a network, the overall degradation rate of Y is higher compared to an unregulated system, reducing variability in output levels, as the sensitivity to fluctuations is reduced (compare to **Fig. 2.11**).

Positive autoregulation (PAR) represents the logical opposite, where a gene Y promotes its own production. For low levels of Y, the production is slow, causing high response times, and if Y is high, production is also high. This sensitivity on Y concentration causes high cell-to-cell variability [197].

Figure 2.12.: Building blocks of gene regulation: Simple regulation, along with positive and negative autoregulation.

Simple regulation, along with negative and positive autoregulation, involve only one or two nodes. Introducing a third node creates a feed-forward loop (FFL), which will be discussed in the following section. Naturally, all these networks can be expanded by incorporating multiple inputs and/or outputs, or by adding bidirectional interactions between the components. In this work, the focus will be placed on networks with single interactions [204, 209, 210, 212].

2.5.3. Feed-Forward Loops

In addition to the network patterns depicted in **Fig. 2.12**, FFL are another fundamental building block. This motif, prevalent in numerous gene networks across various organisms, involves three nodes: The regulator X, a controlled entity Y, and a third element Z that both regulates and is regulated simultaneously. The regulator X is activated by an input signal, such as changes in nutrition, mRNA delivery, or a signalling cascade. The interactions between these three components can either be activating (activator) or inhibitory (repressor), resulting in eight possible architectures as shown in **Fig. 2.13**. Two paths are present, the direct pathway with the connection from X to Y, and the indirect path, where X regulates Y via Z. Based on this, FFLs are categorized into coherent loops - where the overall sign of the direct and the indirect path is the same - and incoherent loops - where the sign of both paths is opposite. The most common types in nature are the coherent type I (shown on the left in **Fig. 2.13**) and the icFFL type I (on the left in the incoherent column of **Fig. 2.13**), with the latter referred to as icFFL readability.

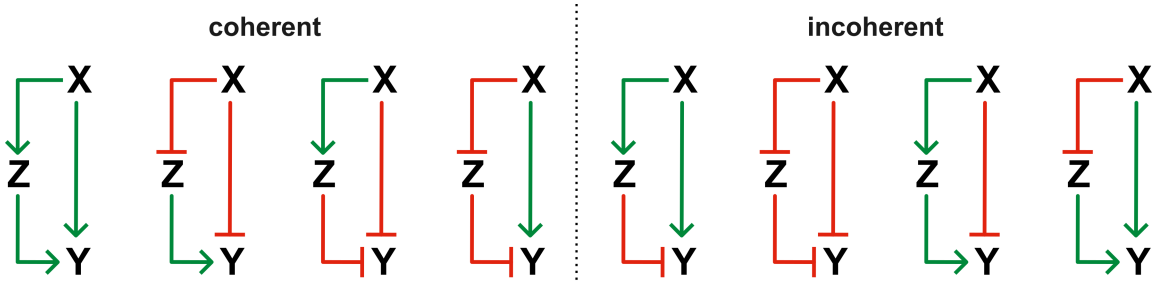

Figure 2.13.: Feed-forward loop architectures: Regulator X controls Y and Z, with Z also regulating Y. Green indicates activating interactions, while red indicates repressive functions. Left: Coherent FFLs exhibit the same overall sign on both the direct and indirect path. Right: icFFLs display opposite signs on the two paths. Adapted from [197]

.

Later, this work aims to employ icFFLs for the controlled expression of exogenous genes. Therefore, the icFFL type I deemed most suitable due to its inherent characteristics, which will be the focus of the following paragraphs.
A prominent biological implementation of an icFFL motif involves a transcription factor X that activates the production of a target Y while simultaneously activating the production of miRNA that downregulates Y. Such icFFL motifs have been found to buffer fluctuations in gene expression, thereby reducing noise [213–215]. To illustrate this noise-buffering property, exemplary protein expression trajectories are shown in **Fig. 2.14a-c**.

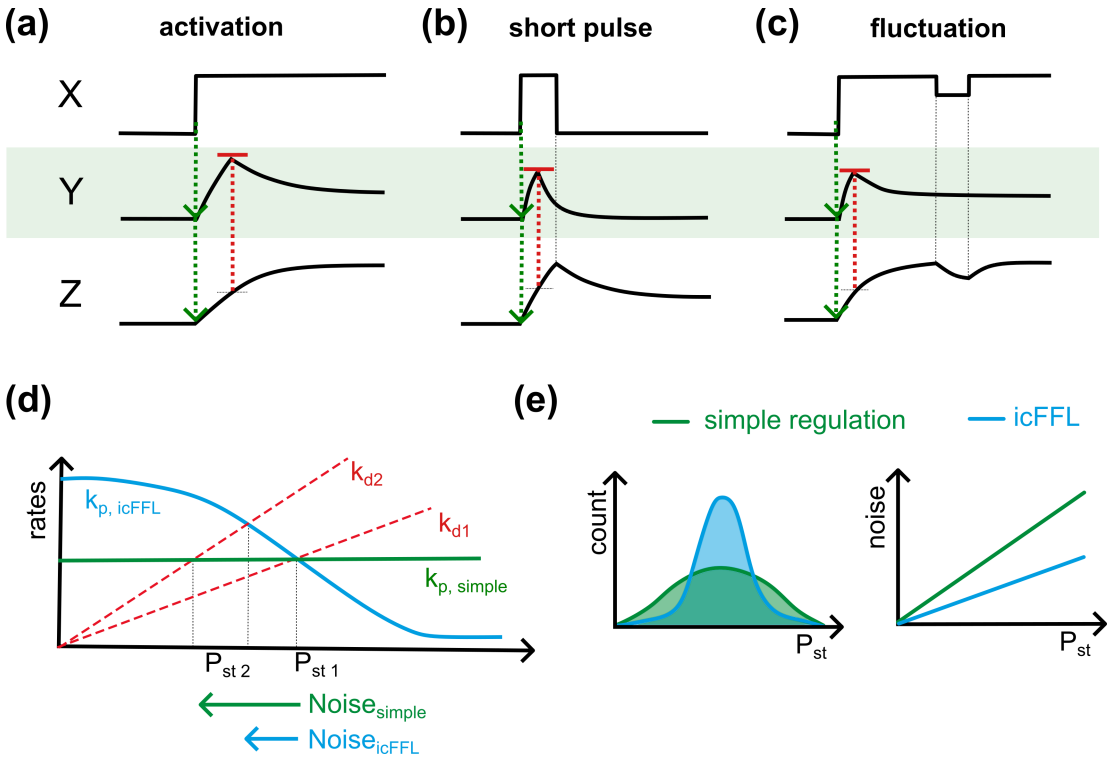

Figure 2.14.: Noise analysis in icFFL regulations: (a) Stable activation of X leads to an increase in the levels of Y and Z. Upon reaching a certain threshold, the level of Z causes repression of Y production. (b) A short pulse of X results in a short pulse of Z and Y. (c) Small fluctuations in X are buffered by Z, preventing significant influence on the level of Y. (d) The adapted production rate in the regulated system (light blue) leads to smaller fluctuations in the steady-state level across varying degradation rates. (e) This results in a narrower distribution of steady-state levels, thereby reducing noise. Adapted from [216].

Following stable activation of X, the production of Y begins to increase, concurrently with the rise in repressor (Z) production. Upon reaching a certain threshold level, Z starts to repress the production of Y, leading to decrease in Y until a steady state level is reached. In response to a short pulse of X, short pulses for Y and Z are observed. If the level of X is subject to small fluctuations, the steady-state level of Z is ultimately buffered against fluctuations through Y. When applying this concept to the rate analysis depicted in **Fig. 2.11**, the production rate k_p can be adapted as shown in **Fig. 2.14d**. Assuming fluctuations in the degradation rate k_d, the resulting steady-state level changes less with the icFFL production rate compared to simple regulation. This leads to a narrower distribution of steady-state levels across a range of observed trajectories, indicating reduced noise (**Fig. 2.14e**). In extreme cases, this buffering can be strong enough to render the dose-response relationship nearly independent of the dose.

From this analysis, an additional feature of the icFFL can be derived. When comparing the expression trajectories for the same steady-state level between icFFL and simple

regulation, the response time is found to be shorter for the regulated expression (**Fig. 2.15**). It is important to note that the inherent repression of the icFFL necessitates a higher level of X to achieve the same-steady state level.
Beyond naturally occurring FFL, these characteristic properties have also been confirmed in synthetic FFL [54, 217, 218].

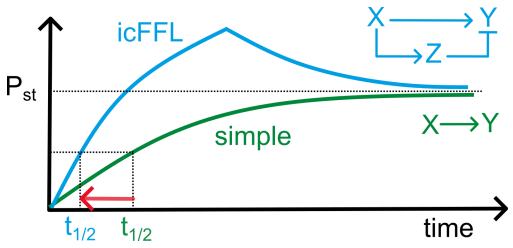

Figure 2.15.: Reduction of response time for icFFLs: A comparison of characteristic production profiles between simple regulated systems and icFFLs for the same steady-state level demonstrates reduction in response time.

3. Physics of Lipid-Based RNA Delivery

In the first phase of the stochastic RNA delivery via LNPs (**Fig. 1.1**), a protein corona forms around the LNPs, influencing cellular uptake. This chapter investigates the role of the delivery vector on expression dynamics, comparing the commonly used lipofectamine 2000 (L2000) with lipid nanoparticles (LNPs). Building on these results, the chapter further examines the impact of the protein corona on LNP intracellular processing dynamics, providing a detailed single-cell analysis of how it alters expression efficiency. Finally, the impact of the LNP's bulk phase structure on protein expression dynamics is studies. The findings presented in this chapter highlight the complex interplay between nanoparticle design and biological outcome.

3.1. Delivery Vector Determines Expression Kinetics

To explore the transfection of nucleic acids *in vitro*, L2000 is a widely used transfection agent known for its high transfection efficiency. However, L2000 lacks functionality *in vivo*, making LNPs the preferred vector. A successful translation from *in vitro* to *in vivo* requires a thorough understanding of the underlying mechanisms of mRNA delivery with either of the two vectors.

Therefore, HuH7 cells were transfected with two different doses of GFP mRNA encapsulated in L2000 or LNPs, and single-cell fluorescence trajectories were collected using time-lapse microscopy to compare kinetic profiles. It is important to note, that the preparation protocols differed for L2000 and LNPs: while serum protein pre-incubation is avoided in liposome transfection to maintain efficiency [219], the LNPs were pre-incubated with serum. **Fig. 3.1a** shows the mean fluorescence traces from the single-cell experiments normalized to their respective maximum expression level. At lower doses, the kinetic profile of LNP and L2000 exhibit differences especially in the incline of expression and the later timepoints where protein mediated degradation dominates ($t > 20$ hours). In contrast, the traces at higher transfected doses were observed to be highly similar. When actual maximum protein levels were examined (**Fig. 3.1b**), the differences between vectors became more pronounced. Interestingly, distribution analysis at lower L2000 doses

reveals two populations of expression levels. The onset time was determined, defined as the timepoint when GFP fluorescence was first detected. Since time-lapse microscopy was initiated only one hour after transfection, onset times earlier than this were approximated with 1 hour. For LNPs, distinct onset time distributions were observed, with earlier onset times at higher doses (**Fig. 3.1b**). In contrast, L2000 onset times were harder to quantify, as expression had already begun in most cells before time-lapse imaging started.
Single-cell analysis also allowed for correlation between onset time and expression level, revealing an anti-correlation: lower expression levels were associated with later onset times, while higher expression levels corresponded to faster onsets (**Fig. 3.1c**). This was more pronounced for LNPs than for L2000.

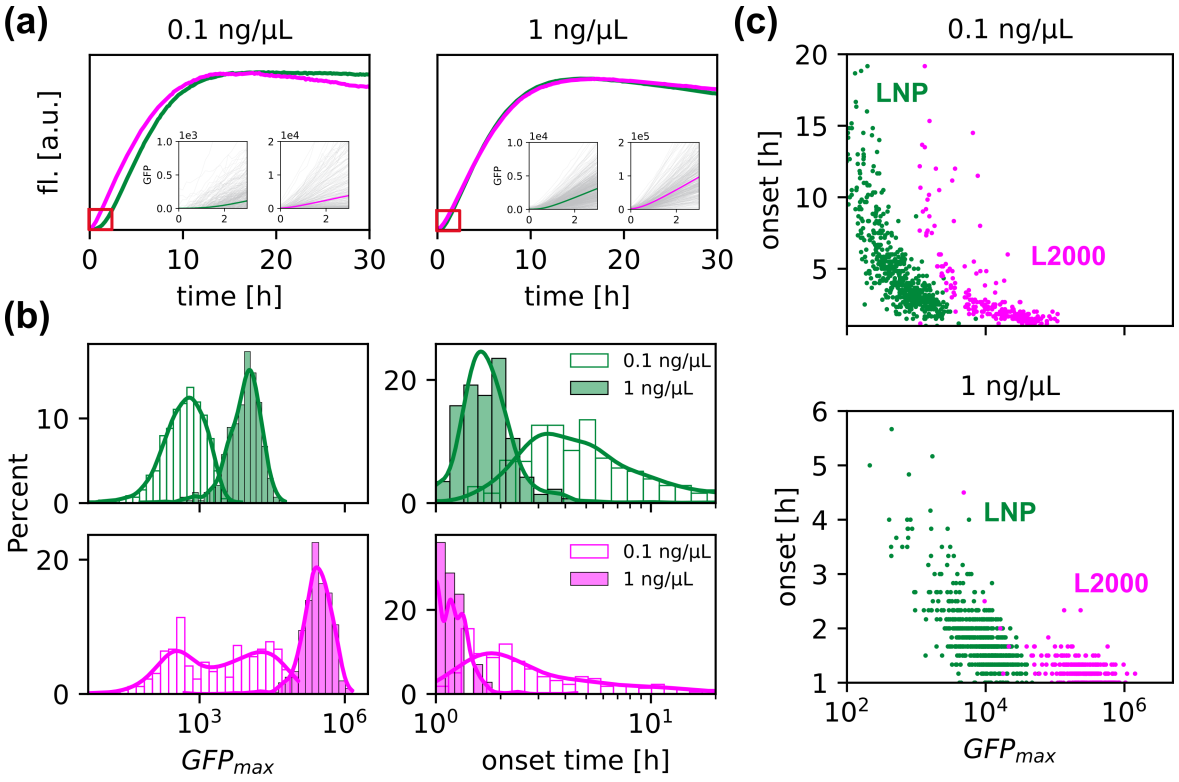

Figure 3.1.: Expression kinetics depend on the delivery vector: (a) Mean fluorescence trajectory following transfection of GFP mRNA with either LNP (green) or L2000 (magenta) in HuH7 cells. The maximum level was normalized for better comparability. The transfected dose is indicated above the graph. Inserts show corresponding single-cell traces for $0 < t < 3$ hours. (b) Distributions of maximum expression levels and onset times for both vectors and doses. (c) Scatter plot correlating onset time with maximum expression level.

Overall, these results highlight the importance of single-cell analysis in investigating differences in protein expression following mRNA transfection. The findings demonstrate that L2000 transfection leads to a faster onset correlated with higher expression levels for

both transfection agents, consistent with previous publications [173]. The broad distribution of expression levels observed at lower doses of L2000 is likely attributable to the less uniform size distribution of the liposomes compared to that of LNPs, as confirmed by DLS measurements.

3.2. Protein Adsorption Influences LNP Uptake and Processing Kinetics

The journey of an LNP after administration - whether systemically for therapeutic purposes or an *in vitro* setup - begins with the adsorption of proteins onto the LNP surface. This adsorption is mediated through the exchange of PEG-lipids with proteins, a dynamic process that allows proteins with the highest affinity for the LNP surface to remain, forming a stable protein corona. Francia *et al.* demonstrated organ tropism *in vivo*, which is influenced by the ability of the LNP to form a specific biomolecular corona [22].
In laboratory settings, the formation of a protein corona is commonly simulated by adding of fetal calf serum (fetal calf serum (FCS)) to the transfection medium. However, variability in FCS protein composition between batches is well-documented [220]. To investigate the impact of this variability on LNP mediated transfections, the following section explores the influence of protein pre-incubation protocols on intracellular processing and protein expression kinetics, aiming to elucidate the relationships between protein corona, uptake, and release.
Therefore, HuH7 cells were transfected with LNPs coated by different protein coronas. Therefore, LNPs encapsulating GFP mRNA (with 20% Cy5-labeled mRNA) were pre-incubated with either 10% BSA or one of two different FCS batches. **Fig. 3.2a** shows the averaged single-cell trajectories of GFP and Cy5 fluorescence, respectively. Pre-incubation with BSA resulted in the highest GFP expression levels compared to both FCS batches, where only minor differences were observed. While GFP fluorescence monitors the protein expression, the Cy5 label on the mRNA provides insights into the amount of the LNPs taken up by the cell. Based on the high electron density in the core of an LNP, the Cy5 signal is expected to be quenched [71] and it was shown that the spectrum of Cy5 is shifted upon release, resulting in higher apparent intensity due to the then improved spectral overlap with the optical filter setup [221]. Therefore, an increase of the Cy5 signal upon mRNA release is expected, followed by a decrease due mRNA degradation and, in addition, due to endosomal recycling or endosomal degradation. Since endosomal release probability has been reported to be low compared to uptake (as discussed in [109] and section 2.2.5), the maximum Cy5 fluorescence correlates with the number of particles

attached or internalized by the cell. As a greater number of particles increases the likelihood of an LNPs reaching the cytosol, the maximum Cy5 fluorescence is also expected to correlate with the maximum protein expression (GFP fluorescence). This was confirmed in **Fig. 3.2b**, where the maximum of both GFP and Cy5 fluorescence is correlated in each single cell, showing a correlation that is slightly shifted for BSA pre-incubation compared to the two FCS samples.

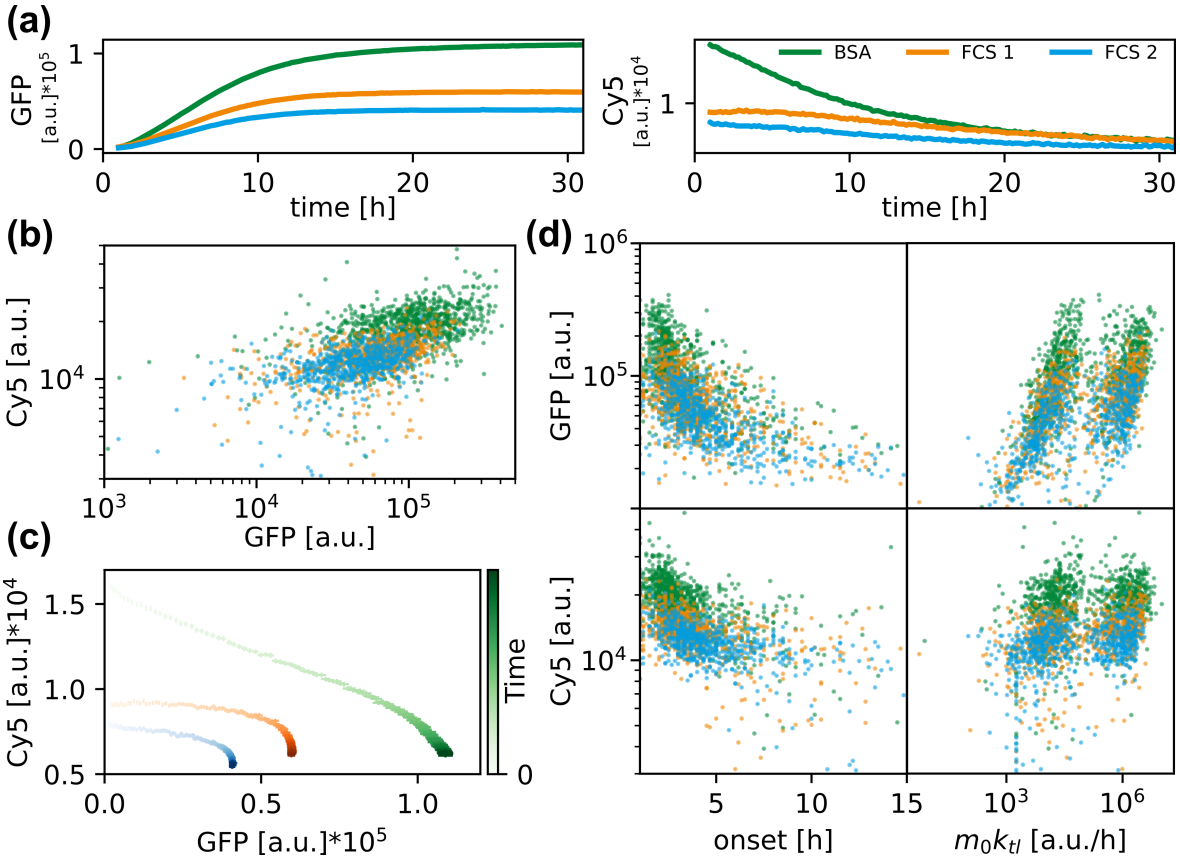

Figure 3.2.: Effect of protein corona on uptake and expression kinetics: (a) Averaged single-cell fluorescence trajectories for HuH7 cells transfected with LNPs with protein coronas (BSA in green, FCS 1 in yellow, FCS 2 in blue). (b) Maximum GFP and Cy5 expression levels show a correlation. (c) Mean Cy5 fluorescence as a function of mean GFP fluorescence at each timepoint (measurement time: 30 hours, 10-minute intervals). Error bars represent the standard error of the mean. (d) Correlation between fluorescence levels (top: GFP, bottom Cy5) and onset time or expression rate ($m_0 k_{tl}$). The expression rate reveals two distinct populations.

To explore the underlying kinetics, the mean of both Cy5 and GFP fluorescence, averaged over all single cells for every timepoint was calculated (**Fig. 3.2c**), revealing distinct kinetic profiles. For BSA, Cy5 fluorescence linearly decreased as GFP fluorescence increased, whereas for FCS LNPs, Cy5 fluorescence remained almost constant, with a sharp decrease at higher GFP levels. To further analyze the kinetics, the kinetic parameters such as onset time and expression rate ($m_0 k_{tl}$) were plotted against the maximum Cy5 and GFP

fluorescence (**Fig. 3.2d**). Both Cy5 and GFP fluorescence correlated with onset time, meaning that cells with high Cy5 and GFP levels showed faster onset times. The expression rate is defined as the product of the initial amount of mRNA molecules available for translation (m_0) and the mRNA translation rate (k_{tl}). Since the same mRNA was used across all experiments (and therefore, k_{tl} is expected to be constant), the expression rate therefore gives information about the number of mRNA molecules that reaches the cytosol. Interestingly, the expression rate divided into two distinct populations with only small correlation with Cy5 or GFP fluorescence.

To further investigate the timing of uptake and release, the peak Cy5 fluorescence was analyzed as a measure of endosomal escape. This was possible, as after the incubation period of LNPs with cells (indicated by the gray area in **Fig. 3.3a**), all excess LNPs were rinsed away before imaging was started. This ensures that any subsequent increase in fluorescence is not due to further LNP accumulation but rather reflects a fluorescence increase caused by endosomal release. Therefore, the later the maximum of Cy5 fluorescence is observed, the later the endosomal release event occurs. The distributions of these timepoints, shown in **Fig. 3.3a** along with their respective median values, reveal that the peak occurs significantly earlier for BSA corona to those with an FCS coating. Interestingly, the opposite trend was observed for the overall maximum Cy5 fluorescence. These single-cell kinetic experiments suggest that not only does the binding affinity of LNPs vary depending on the protein corona composition, but also that the intracellular processing dynamics are affected by these differences.

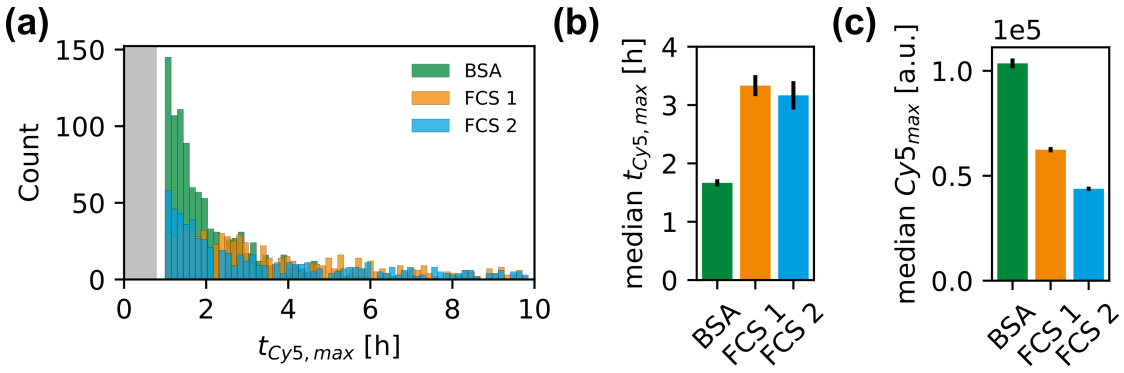

Figure 3.3.: Timing of Cy5 fluorescence as an indicator for uptake and release: (a) Histogram showing the timepoint of Cy5 fluorescence maximum. Gray area indicates the LNP incubation period. Measurements were started at t = 1 hour. (b) Median timepoint of the Cy5 fluorescence peak, and (c) maximum Cy5 fluorescence. Error bars represent the standard error of the mean.

This section explored how different protein coronas influence cellular uptake, endosomal release and protein expression kinetics in HuH7 cells. Through single-cell based analysis, it was shown that LNPs with a BSA coating exhibited higher protein expression, which was

linked to enhanced cellular accumulation and faster processing compared to FCS-coated LNPs.

3.3. Bulk Phase Transition Specific Effects on LNP Kinetics

LNP preparation requires acidic buffers to lower the pH, facilitating protonation of the ionizable lipid headgroup. Most protocols recommend using citrate buffer at pH 3 to 4.5, as it has shown the highest transfection efficiency [68, 222]. However, it has been demonstrated that not only the pH but also the type of buffer used plays a significant role in various biochemical reactions [223–225]. In those studies, LNP bulk phases (composed of MC3 and cholesterol with nucleic acid) prepared in different buffers were analyzed to understand the implications for uptake and endosomal processing pathway. Therefore, structural changes were monitored during pH titration from pH 7 down to pH 3.5. At pH 7, irrespective of the buffer type, an inverse laminar phase (L_{II}) was observed, consistent with the neutral charge of MC3 at that pH. However, for effective endosomal escape, the transition to an inverse cubic (Fd3m) phase, followed by an inverse hexagonal (H_{II}) phase is essential [139]. The inverse cubic phase formed at pH 6.4 for citrate buffer, pH 6.0 for acetate buffer and pH 5.5 for phosphate buffer (the latter forming a mix of Fd3m and P63/mmc phases). Subsequently, the inverse hexagonal phase appeared at pH 6 for citrate-LNPs and at pH 5 for phosphate- and acetate LNPs (for more details refer to [**M2**]).

This study investigates how buffer-specific structural changes in LNPs influence transfection dynamics. LNPs were prepared according to the standard mixing protocol [50] including Cy5-labeled mRNA in either in citrate, phosphate or acetate buffer. The buffer concentration and pH were kept consistent across all preparations. Following mixing, residual buffer was removed by dialysis. The size of the LNPs after dialysis was measured using DLS (Table 3.1). All LNPs had comparable diameters and PdI values, though those prepared in citrate buffer were slightly larger.

	citrate	**phosphate**	**acetate**
diameter [nm]	76 ± 7	70 ± 1	73 ±2
PdI	0.330	0.324	0.304

Table 3.1.: DLS size measurements of LNPs prepared in different mixing buffers.

HuH7 cells were transfected as previously described, with a 45-minute serum pre-incubation,

and GFP and Cy5 fluorescence were recorded. **Fig. 3.4a** shows single-cell and mean fluorescence trajectories for each preparation buffer. Additionally, a mixture of all three LNPs (1:1:1 mix of separately prepared LNPs with each buffer) was tested. The analysis of maximum fluorescence levels revealed distinct distributions (**Fig. 3.4b**), with citrate-LNPs producing the highest expression levels, followed by phosphate- and acetate LNPs. The combinatorial approach resulted in an intermediate expression level. Onset time was determined from single-cell traces. For better comparison, median onset and fluorescence are displayed in **Fig. 3.4c, d**. The earliest onset was observed with citrate buffer, followed by phosphate and acetate buffer. A correlation analysis between onset time and protein fluorescence levels revealed an anti-correlation, where faster onset times corresponded to higher protein expression levels. This correlation aligns with the Hofmeister series [226], as indicated in **Fig. 3.4e**. Interestingly, the 1:1:1 combination of buffers was not located on this line.

The formulation of Cy5-labeled mRNA allowed for the tracking of the mRNA over time. As described previously, a high fluorescence level at t_0 indicates a high accumulation of LNPs at the cell. After endosomal escape, the release of mRNA leads to a slight increase in fluorescence due to unpacking, followed by a decrease as the mRNA degrades and endosomal degradation and/or recycling processes occur. The fluorescence trajectories in **Fig. 3.5a** revealed the highest initial signal for the citrate buffer and the combinatorial LNP mix, followed by acetate and phosphate buffers. For citrate and phosphate, the mean Cy5 fluorescence initially declined before reaching its maximum ($Cy5(t_0) \neq Cy5(t_{Cy5,max})$), which was not observed with acetate buffer except in some individual cells.

The correlation of GFP fluorescence with Cy5 fluorescence revealed distinct scattering profiles, as shown in **Fig. 3.5b**, which were analyzed at 2, 15 and 30 hours post-transfection. At each timepoint, a correlation between Cy5 and GFP signals was evident, though the strength of the correlation varied. At the early timepoint, high Cy5 signals were associated with relatively low GFP signals; however, this relationship inverted over time, with a weak Cy5 signal relative to GFP fluorescence by 30 hours. The high temporal resolution enabled the calculation of median fluorescence for Cy5 and GFP every 10 minutes, as plotted in **Fig. 3.5c**. This plot includes the median values of 180 scatter plots as those shown in **Fig. 3.5b**. For acetate buffer, the Cy5 signal decreased rapidly before a rise in GFP signal was observed, suggesting a high rate of endosomal or mRNA degradation. In contrast, the citrate buffer maintained a higher mRNA signal, indicating more successful endosomal release rather then degradation. Although the initial Cy5 signal for the phosphate buffer was lower, suggesting reduced accumulation or uptake, the decrease in the signal was slower than with acetate. The LNP mix showed an initial Cy5 signal

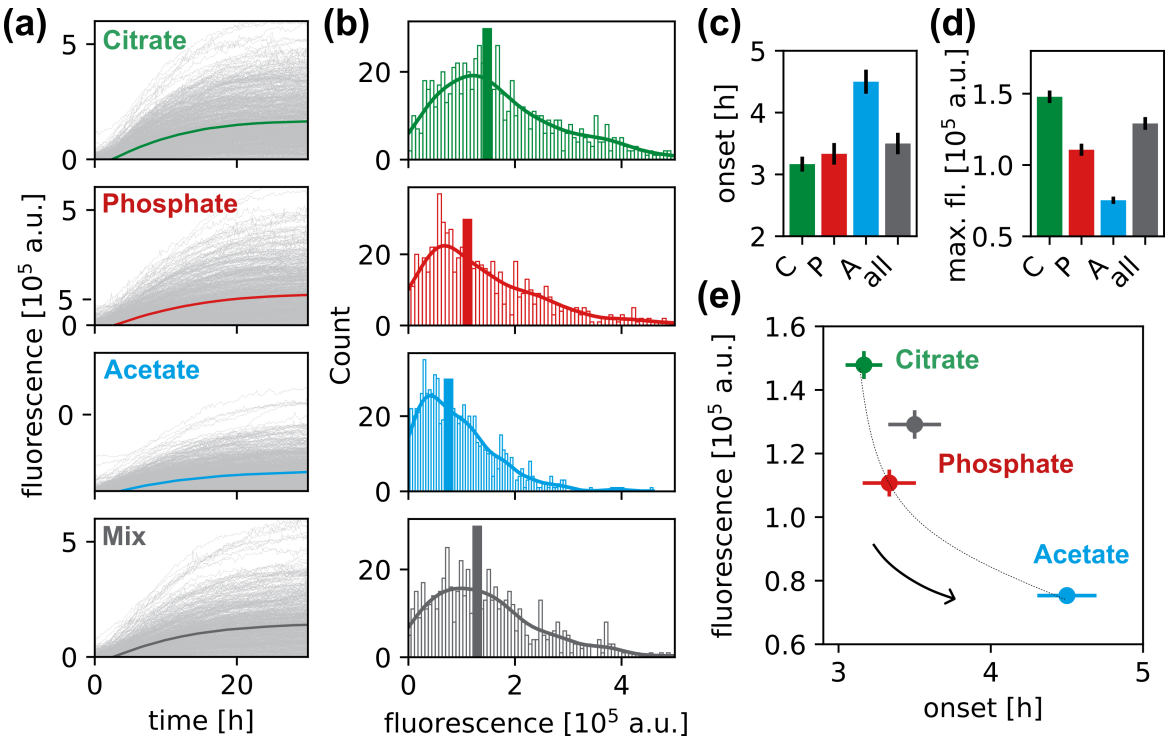

Figure 3.4.: LNP mixing buffer influences transfection dynamics: (a) Single-cell fluorescence traces recorded upon transfection of HuH7 cells with LNPs. Shown are single-cell traces with mean highlighted for the different mixing buffers as indicated. The last graph shows transfection results for LNPs prepared with the different buffers in a 1:1:1 ratio. (b) Distribution of maximum fluorescence levels for each single cell, with the median indicated. (c) Median onset time determined from single-cell traces, and (d) median maximum fluorescence levels. Error bars represent the standard error of the mean. (e) Correlation between onset time and fluorescence level reveals an anti-correlation, with faster onset times associated with higher fluorescence levels, following a conventional Hofmeister series, as indicated by the black arrow. Adapted from [**M2**]

comparable to that of citrate buffered LNPs but degraded more rapidly.

This section demonstrated that the type of mixing buffer significantly influences LNP transfection efficiency and mRNA processing dynamics. The use of citrate buffer resulted in the highest protein expression and experiments hint toward more efficient endosomal escape. Acetate-LNPs were observed to exhibit faster degradation, underscoring the impact of buffer type on intracellular delivery.

3.4. Discussion

This chapter explored the initial phase of lipid-mediated mRNA delivery, comparing L2000 and LNPs in terms of their kinetic profiles. While L2000 is known for higher protein expression *in vivo* [13, 173], this study focused on a detailed kinetic analysis using single-cell

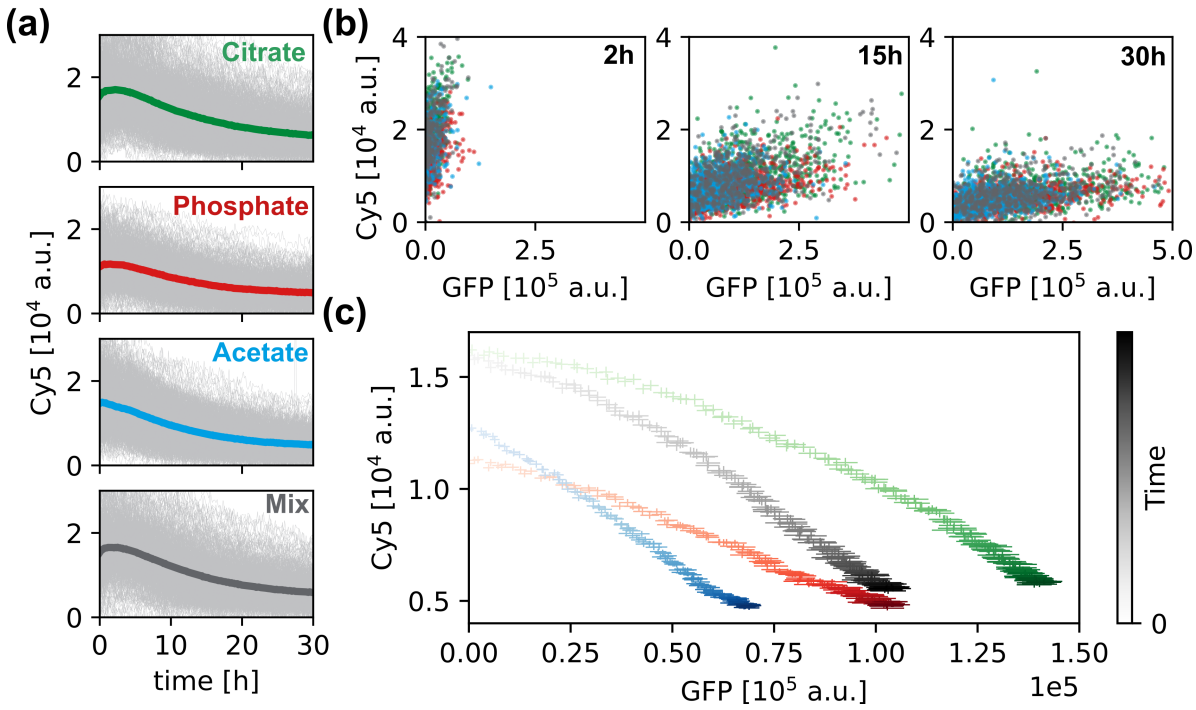

Figure 3.5.: Mixing buffer influences LNP processing dynamics: (a) Cy5-labeled mRNA was used to track the fate of mRNA after transfection in HuH7 cells. Single-cell traces and mean fluorescence are shown. (b) Correlation between Cy5 and GFP signals at different timepoints revealed distinct scatter plot patterns. (c) Median fluorescence of all cells was correlated between GFP and Cy5 at each timepoint. Error bars represent the standard error of the mean. Gradient indicates timepoint.

experiments. Both vectors exhibited similar fluorescence trajectory shapes but differed in onset times, indicating faster uptake and processing, which may be related to differences in uptake pathways [107, 109] or faster endosomal processing [114, 134, 227]. Additionally, low mRNA doses in L2000 transfections revealed two populations of expression levels, likely reflecting differences in particle size populations with varying mRNA loading, especially as this effect was not observed for the more monodispers LNPs. Pre-incubation of LNPs with proteins to form a protein corona facilitated uptake via CME, while for L2000, protein pre-incubation reduced transfection efficiency [219], leading to potential differences in uptake pathways, explaining the differences observed in timing.

The effect of the protein corona on LNP processing and protein expression was further explored, by pre-incubating Cy5-labeled mRNA-encapsulating LNPs with common cell culture additives. HuH7 cells were transfected and differences in total expression level (GFP) and intracellular trafficking (Cy5) were observed. BSA pre-incubation led to higher expression levels compared to FCS. Two different batches of FCS were tested, showing

only minor differences. Nevertheless, further studies are required to confirm a general independence of the FCS batch also taking into account different cell-types. Importantly, size measurements confirmed that LNP size remained relatively unchanged by protein pre-incubation, ruling out size-related interference with uptake and processing dynamics (**Fig. A.6**). A closer look on the individual cells revealed that high GFP levels (indicating protein expression) were associated with high Cy5 levels (indicating mRNA processing). This may suggest a relationship between the number of LNPs (and therefore the number of Cy5 labels) attached to the cell membrane and likelihood for one particle to escape the endosome. Alternatively, this higher Cy5 level could be correlated with the increase of fluorescence upon endosomal escape. Temporal resolution allowed the generation of fluorescence scatter plots at each timepoint,which, when averaged, revealed distinct kinetic profiles for each protein coating. This impact of timing was further investigated and it was found that the onset of protein expression correlated with both, GFP and Cy5 fluorescence. Previous studies have shown that the onset of protein expression correlates with the expression levels [173], likely due to the small window of opportunity for endosomal escape [126]. The correlation between onset and Cy5 fluorescence is thought to result from the higher number of LNPs present or an earlier escape, as discussed above.
Additionally, two distinct populations of expression rates ($m_0 k_{tl}$) were observed, similar to those seen with low doses of L2000. These differences may be caused by variations in protein coating that affects uptake pathways with different timing, or different pH at endosomal escape [24, 25], leading to variations in the number of mRNA molecules delivered to the cytosol.
To differentiate between the effects of LNP quantitiy and endosomal escape, a more detailed analysis on LNP trafficking was conducted by examining the Cy5 fluorescence trajectories. Differences between the different protein coatings became apparent when comparing the timepoint of maximum Cy5 fluorescence. Since no more LNPs accumulate at the cell surface after washing, any subsequenct increase in fluorescence can be attributed to endosomal escape. Therefore, the timepoint of the Cy5 maximum provides insight into the timing of escape. This study shows that the Cy5 maximum is reached earlier for BSA-coated LNPs than for FCS-coated LNPs, indicating faster escape for BSA. Other studies have shown that the protein coronas can shift the endosomal escape to lower pH, and therefore, to later timepoints which overall lowers the probability for escape [24, 25]. That the type of protein also influences this effect is a logical consequence of these findings.

In addition to the type of vector and the type of protein corona, the influence of the internal structure of LNPs on trafficking and protein expression was investigated.
An anti-correlation between onset time and protein expression has been previously de-

scribed [173] and is believed to be linked to the window of opportunity during endosomal escape [107]. Here, it was demonstrated that this anti-correlation pattern is reproduced in LNPs prepared with different buffers. SAXS analysis revealed, that the internal structure and pH-dependent structural changes of LNP bulk phases were influenced by the mixing buffer. Specifically, it was noted that that the transition from L_{II} to H_{II} varied between buffers. However, the order of transfection efficiencies in terms of maximum protein expression (citrate > phosphate > acetate) did not entirely match the order of pH-dependent phase transition (citrate > acetate > phosphate). The analysis of the fate of mRNA during transfection using Cy5 labeling indicated varying initial amounts of mRNA, suggesting differences in the levels of accumulation and/or uptake (which cannot be distinguished in this study) and subsequent differences in the rate of Cy5 signal fading. This points to distinct dynamics in endosomal escape, endosomal degradation and mRNA degradation, as initially hypothesized. As reported in manuscript **[M2]**, the investigation of the nearest-neighbour distance (d_{NN}) during the transition to the inverse hexagonal phase showed a 13% decrease for citrate buffer, 15% for acetate and 6% for phosphate buffer. Interestingly, the highest overall d_{NN} was measured for LNPs prepared with acetate buffer, suggesting that a high nearest-neighbour distance may be unfavorable for endosomal escape. Additionally, when the pH shift was inverted from low to high pH, the d_{NN} decreased for citrate and phosphate buffer but increased for acetate, further highlighting a different behaviour for LNPs prepared with acetate buffer. To explore more factors that might influence this observed behaviour, molecular simulations were conducted by the group of Nadine Schwierz. These simulations considered headgroup area, bending energy, and ion-specific adsorption, suggesting an interplay between headgroup area and ion specificity in the stabilization of L_{II} and H_{II} phases, offering a possible explanation for the observed effects.
Intuitively, for the mix of different buffer-LNPs, one would expect a behavior reflecting the average of the three LNPs. However, since this is not the case but rather a shift towards the behavior of citrate buffer-LNPs is observed, this may suggest similar uptake probabilities but a higher endosomal escape probability for citrate buffer.

In summary, this chapter described different tools that can be employed to modify the processing and protein expression kinetics of lipid-based mRNA delivery. These include the choice of vector, the protein corona, and the internal structure influenced by the type of acidic mixing buffer.

4. Single-Cell Investigation of RNA Co-Delivery

In the previous chapter, the effects of vector modifications on expression kinetics were analyzed. In this chapter, co-delivery experiments were conducted to examine the behavior of multiple RNA species. First, the co-delivery of two different mRNAs was investigated, and the findings were subsequently applied to explore ribosomal competition regimes and coupled translation. Next, internal referencing and co-delivery of mRNA and siRNA were utilized to precisely quantify RNAi dynamics.

4.1. Co-Delivery of Two mRNAs

4.1.1. Coupled Protein Expression on the Single-Cell Level

Cellular functions are defined by their protein expression pattern and the expression of these proteins from genes is a complex process. Studying protein expression in theory or in cell-free systems often failed to predict precise translation rates and protein outputs. The complexity of biological systems, such as mammalian cells, arises from the coupling of various process. When two or more processes share the same (limited) resource, they become coupled [228]. In mammalian cells, there are approximately 10^4 to 10^5 mRNAs while about 10^5 to 10^6 ribosomes are available for translation. Since ribosome biosynthesis is an energetically demanding process [229], this pool of ribosomes can be assumed to remain constant over time. During mRNA translation, multiple ribosomes elongate along a single mRNA, making the pool of available ribosomes smaller. As a result, the specific initiation and elongation rates of an mRNA dictate the number of ribosomes bound to a particular mRNA species, ultimately leading to ribosome competition between mRNAs. Here, the effect of ribosomal competition in A549 cells was investigated following co-delivery of two mRNA species (GFP and CayRFP). While the concentration of one mRNA (the reporter) was varied, the transfected dose of the other mRNA (reference) remained constant in each experiment, as visualized in **Fig. 4.1a**. The reporter - here GFP - exhibited a dose-dependent increase in protein expression corresponding to the transfected

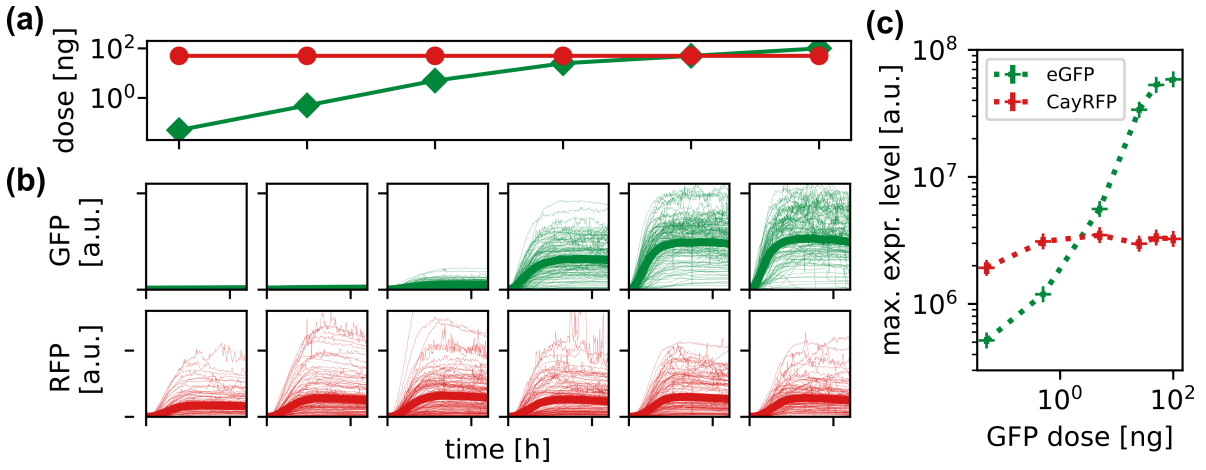

Figure 4.1.: Investigation of ribosomal competition in co-transfection of GFP and CayRFP mRNA: (a) GFP and CayRFP transfection doses (ng/channel) in 50 µL. CayRFP dose remained constant across all experiments, while the GFP dose was varied. (b) Single-cell fluorescence traces for the transfected doses. From left to right: 0.05, 0.5, 5, 25, 50 and 100 ng/channel, with the mean fluorescence trajectory highlighted. (c) Mean maximum expression levels for each experiment. Green represents GFP expression, red represents CayRFP expression. Mean levels with standard error of the mean are shown.

doses, while the expression of CayRFP remained constant (**Fig. 4.1b, c**).

However, when the GFP mRNA was optimized for maximal translation rate by replacing all codons with the fastest available synonymous codons, a coupling effect of GFP and CayRFP expression was observed (**Fig. 4.2a, b**). GFP expression increased in a dose-dependent manner, with saturation at the highest doses. Conversely, the expression of CayRFP, whose transfected dose remained constant across all data points, decreased in correlation with the rise in GFP expression (**Fig. 4.2c**).

This correlation of GFP and CayRFP expression became even more apparent at the single-cell level (**Fig. 4.3**). For each cell, the maximum GFP and CayRFP level were plotted. Since the two signals were expected to be correlated due to co-encapsulation, the number of vehicles reaching the cell and escaping from the endosome should similarly dictate the availability of both GFP and CayRFP mRNA molecules in the cytosol. It is clear that, with the unmutated GFP sequence, GFP fluorescence increased with dose, shifting the population to the right while the CayRFP signal remains unchanged for all GFP levels. This indicates that the translation of the reference mRNA was unaffected by the dose of the reporter mRNA. However, when the translation dynamics of the reporter mRNA were altered by synonymous codon substitution synonymous for faster-translating codons, the pattern changed. The scatter cloud still shifts towards higher GFP fluorescence but despite constant dose, the reference CayRFP signal decreases at higher GFP

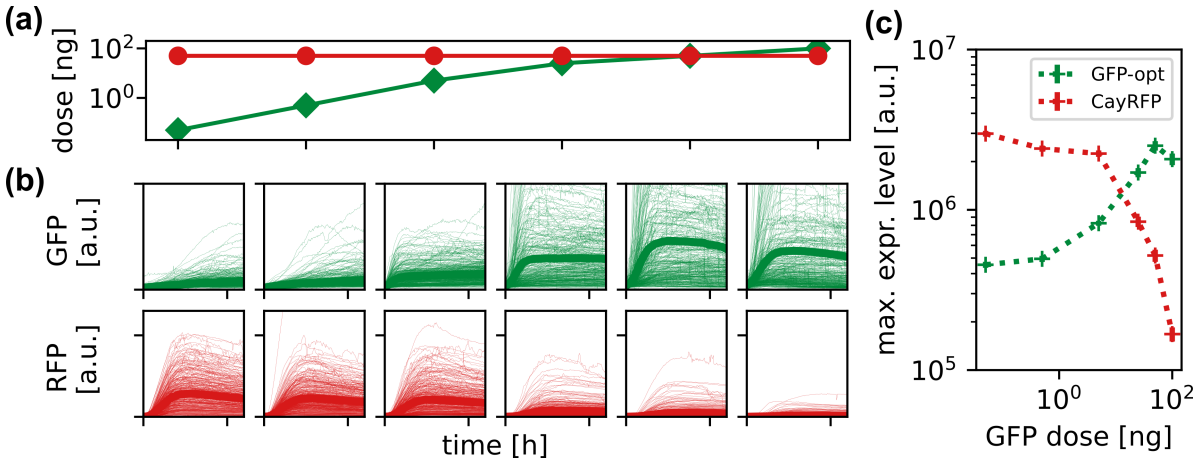

Figure 4.2.: Ribosomal competition in mRNA co-transfection experiments: (a) GFP mRNA dose was varied as previously, while CayRFP dose remained constant at 50 ng/channel. (b) Single-cell fluorescence trajectories with the mean trajectory highlighted. (c) Mean maximum GFP expression level increases in a dose-dependent manner and saturates at highest dose. CayRFP expression decreases co-dependently. Mean levels with standard error of the mean are shown.

doses, suggesting a coupling between the two processes.

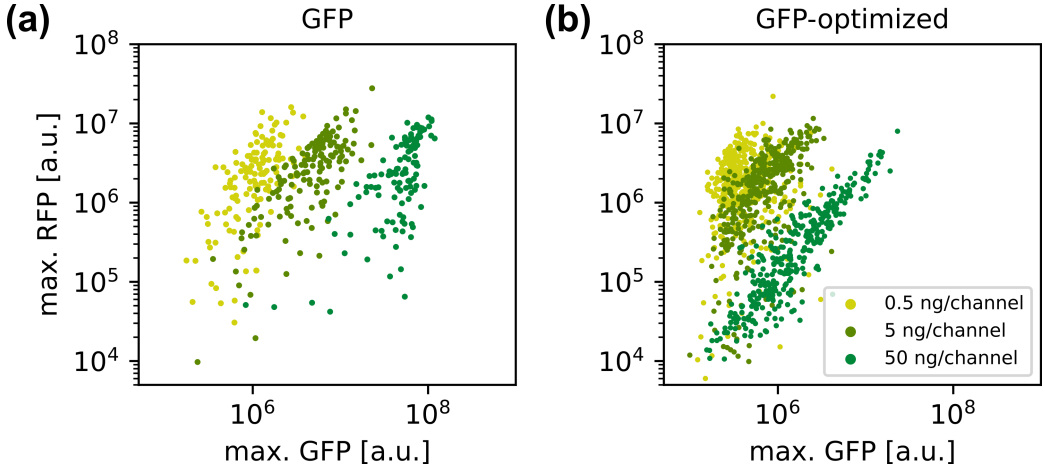

Figure 4.3.: Single-cell dependent coupling of reporter and reference expression based on reporter design: (a) Uncoupled protein expression for unmutated GFP (increasing dose) co-delivered with CayRFP (constant dose). Maximum expression levels for both proteins are shown, with each point representing a single cell. (b) Translation-optimized GFP constructs shows coupling of reporter (GFP) and reference (CayRFP) expression, despite a constant reporter dose.

Next, single-cell traces (see **Fig. 4.1, 4.2**) were fitted to the three-stage maturation model for mRNA translation [172], as shown in **Fig. 4.4**. Ribosomal movement along the mRNA determines the translation rate. The fitting provides information about the expression rate, denoted as $m_0 k_{tl}$. As the dose increases, m_0 (the number of mRNA

molecules available in the cytosol) increases which in turn raises the overall expression rate. However, the translation rate k_{tl} reflects how quickly a ribosome translates a single mRNA into one protein. For a given mRNA in a consistent biological context, this rate is assumed to remain constant. Therefore, with an increasing m_0, a linear increase in the expression rate is expected. In **Fig. 4.4a**, the expression rate for GFP (increasing dose) with co-transfected CayRFP (constant dose) is shown. Since m_0 does not change for CayRFP and k_{tl} is assumed to remain constant, the measured constant expression rate for CayRFP aligns with theoretical predictions. The expression rate of GFP increases linearly with dose, but saturates at higher doses, likely due to limited cellular uptake capacity or toxic side effects of high mRNA and lipid concentrations.
The same fitting was applied to co-delivery experiments with the optimized GFP construct (**Fig. 4.4b**). Here, comparable initial expression rates were observed. Interestingly, the slope of the $m_0 k_{tl}$ rate increased more slowly than the expression rate of unmutated GFP. Simultaneously, the expression rate of the co-delivered CayRFP decreased. While this seems intuitively correct at first glance, some questions remain. The increase of $m_0 k_{tl}$ rate is expected, as m_0 increases with dose. However, for CayRFP, m_0 remains constant, and according to the model, k_{tl} should also remain unchanged, as it describes the rate at which one mRNA is translated into one protein. Therefore, the expression rate should not decrease, regardless of the number of available ribosomes.

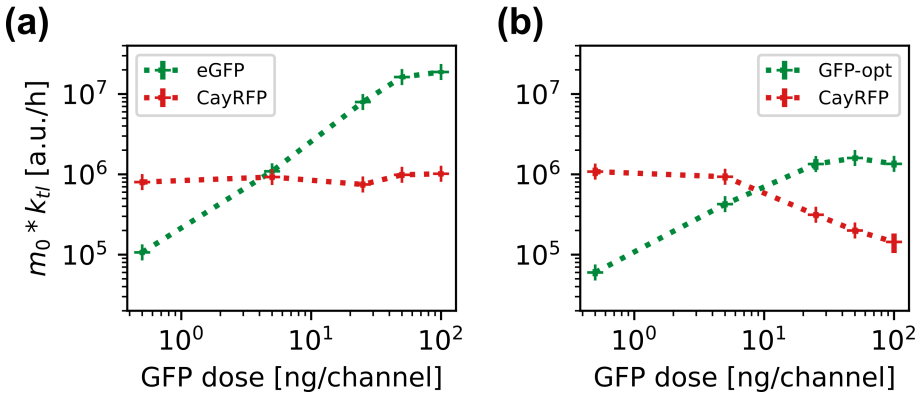

Figure 4.4.: Dependence of expression rates in co-delivery: Single-cell protein expression trajectories were fitted to the three-stage maturation model [172]. Expression rates $m_0 k_{tl}$ were plotted for CayRFP and GFP for different doses of (a) GFP and CayRFP co-transfection, and (b) GFP optimized for maximum translation speed (GFP-opt) and CayRFP co-transfection. The CayRFP mRNA dose was kept constant at 50 ng/channel for all datapoints.

This dependence of translation rates in co-delivery experiments suggests a coupled process, not only in terms of the number of transfection events - where one mRNA is translated into one protein - but also in the translation process itself. Since ribosomes are the central enzymes in translation, their role in co-delivery experiments will be explored further in

the next sections. Quantitative modeling will be employed to gain deeper insights into this coupling mechanism.

4.1.2. Modelling of Ribosomal Competition

To better understand the translational coupling between two mRNAs, a simple kinetic model was developed to capture the interaction between mRNA and ribosomes for more than one translation process at once. As illustrated in **Fig. 4.5**, the two mRNAs share a fixed pool of ribosomes, and translation is initiated by the binding of ribosomes to the 5' UTR of the mRNA. This binding is characterized by a rate constant k_{comp} which is assumed to be specific to each type of mRNA. Once an mRNA forms a complex with a ribosome, translation proceeds at rate k_{tl}, resulting in protein synthesis. After translation (and therefore with the same rate) ribosome and mRNA are released and the ribosome returns to the pool, making the mRNA available for further ribosomal binding. Over time, mRNA is degraded at rate δ and proteins are degraded with rate β. For simplicity, protein maturation is not included in this model. The same set of rates applies to the second mRNA, though they may differ quantitatively. While in living organisms multiple ribosomes can translate a single mRNA simultaneously, this model simplifies the process by assuming only one ribosome translates one mRNA at a time.
Again, this framework can be described by a set of differential equations. The change of mRNA over time can be described as:

$$\frac{\partial mRNA(t)}{\partial t} = -\delta * mRNA(t) - k_{comp} * mRNA(t) + k_{tl} * Rm(t) \tag{4.1}$$

Here, $Rm(t)$ is the concentration of ribosome-mRNA-complex. The change of this complex over time, dependent on mRNA ($mRNA(t)$) and ribosome ($R(t)$) concentration is:

$$\frac{\partial Rm(t)}{\partial t} = k_{comp} * (mRNA(t) + R(t)) - k_{tl} * Rm(t) \tag{4.2}$$

Finally, the protein concentration ($P(t)$) that is measured experimentally is described with:

$$\frac{\partial P(t)}{\partial t} = k_{tl} * Rm(t) - \beta * P(t) \tag{4.3}$$

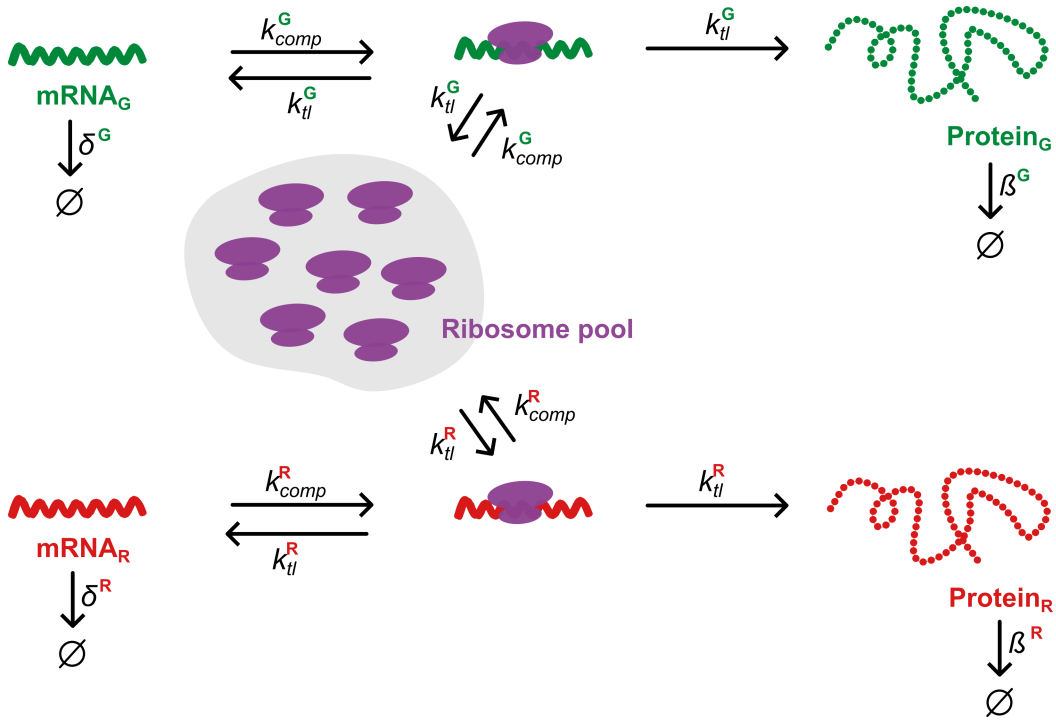

Figure 4.5.: Simple model to explain ribosomal competition in co-delivery experiments.

The rates k_{comp}, k_{tl} and the degradation rates for mRNA δ and protein β are characteristic of each specific type of mRNA and protein. Therefore, for each mRNA, ribosome-mRNA-complex and protein, a distinct set of equation must be defined. These equations are only coupled through the shared ribosomal pool and the number of initially available ribosomes R_0.

Rate estimations based on previous studies [172, 173] along with simulations using Julia [230] of equations 4.1 to 4.3, successfully captured the qualitative dynamics of protein expression (**Fig. 4.6**). This is notable, as this model assumes constant translation rates, which were experimentally shown to vary. Furthermore, the simplification of assuming only one ribosome per mRNA introduces significant differences between the biological observations and the kinetic model.

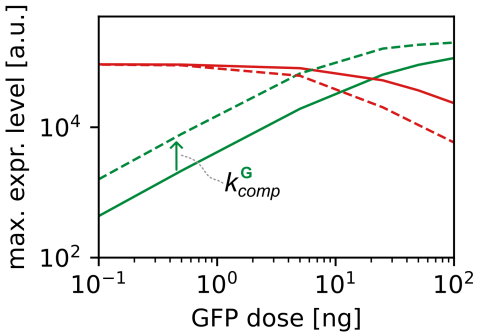

Figure 4.6.: Qualitative modeling of a simple ribosomal competition model captures protein expression dynamics: The solid line and the dashed line differ in the underlying size of the ribosome pool.

4.1.3. Discussion of mRNA Co-Delivery and Ribosome Competition

From the conducted experiments, coupled protein expression following co-delivery of mRNAs, dependent on the design of the mRNA construct, was observed. A simple kinetic model was sufficient to capture expression dynamics and fitting the single-cell fluorescence trajectories revealed co-dependent expression rates in the case of coupled translation. In the three-stage maturation model used to access expression rates, an infinite pool of ribosomes is assumed, meaning ribosome availability does not affect the translation speed. However, with a fixed pool of ribosomes, the probability of mRNA and ribosome crossing paths and complexion decreases, leading to a reduction of the complexion rate k_{comp} for both mRNAs. This mechanism is not accounted for in the three-stage maturation model. Rather - in the regime of limited resources - the effective translation rate becomes a combination of the complexing rate and the translation rate, as described in the ribosomal competition model. This explains the co-dependent expression rates observed in **Fig. 4.4**.

Other models, such as the ribosome flow model [228, 231], may offer additional insight into factors like initiation or elongation rates. Furthermore, it remains to be determined whether the saturation effects observed at higher doses are due to a shortage of resources such as ribosomes, or if they are caused by toxicity effects, either from the high burden of exogenous mRNAs, lipids and proteins, or from reduced endogenous protein expression as exogenous mRNAs dominate ribosomes and tRNA usage.

LISCA measures protein expression trajectories based on fluorescence, but co-translational protein folding can be impeded by ribosomal movement along the mRNA [232]. Therefore, further studies are needed to directly measure the protein concentrations as control. Impaired protein folding could explain why lower fluorescence was observed for the GFP-opt mRNA, despite this mRNA was optimized for rapid translation. Additionally, using other

cell lines besides the A549 cells used here, could shed light on the relationships between translation, metabolism, and cell-specific resource distributions. The data presented in this chapter provides proof of concept for coupled translation of co-delivered mRNAs, laying the groundwork for more detailed studies.

4.2. Co-Delivery of siRNA and mRNA

4.2.1. Kinetics of siRNA Co-Delivery

To study the effect of RNAi on mRNA transfections, it is essential to deliver targeting siRNA to the cell. Co-encapsulation within the same vector allows simultaneous application leading to a more uniform distribution [129, 151]. This co-delivery of siRNA and mRNA is important for investigating biological circuits, as will be discussed in section 6.6. However, in certain applications - such as CRISPR/Cas or those studying RNAi effects and translation dynamics (section 5.5) - it may be preferable to give the mRNA a head start to secure translation initiation. In these cases, the mRNA and siRNA are delivered separately and sequentially, as illustrated in **Fig. 4.7a**. This seemingly minor change leads to significant differences in single-cell fluorescence trajectories. Understanding these differences is crucial for usage of co-delivery in synthetic biology. Here, GFP mRNA and targeting siRNA were co-transfected, and single-cell fluorescence traces were measured (**Fig. 4.7a**), revealing a difference in maximum expression levels. To compare the dynamics, mean traces for each condition were normalized to their respective maximum expression level (**Fig. 4.7b**). Co-delivery resulted in a much faster expression rise compared to successive delivery and quantification of key parameters such as maximum protein level, onset time, response time (time to half-maximum expression), mRNA degradation rate and expression rate are provided in **Fig. 4.7**. Notably, despite delivering the same amount of mRNA and siRNA, maximum expression levels differed between the two approaches. Furthermore, the onset of fluorescence was slightly delayed for successive delivery, as was the response time, while degradation and expression rates were both found to be higher upon co-delivery.

Several factors could explain these observations. First, Zhang *et al.* proposed a 'first-come, first-served' principle in parallel delivery: after the uptake and release of a first particle, the likelihood of a second particle being internalized is lower. In the case of successive delivery of mRNA and siRNA, the mRNA particles may "block" the uptake of siRNA particles delivered later. This aligns with the observation that the mRNA degradation is higher in co-delivery experiments. Additionally, once mRNA is delivered to the cytosol, translation begins. Various studies have shown that the translational machinery interacts

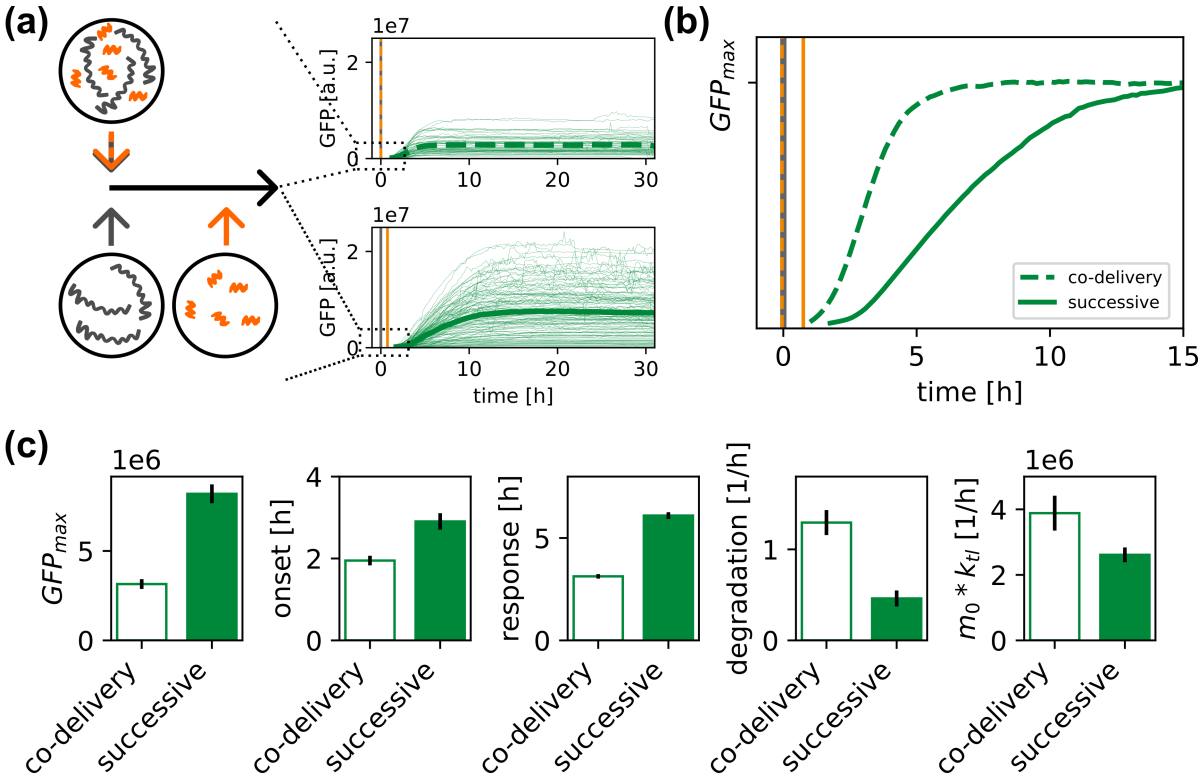

Figure 4.7.: Timing affects siRNA kinetics: (a) siRNA can be co-delivered with the mRNA or applied after the mRNA (successive delivery), resulting in distinct single-cell traces. (b) Normalization to the maximum expression level reveals different protein expression kinetics. (c) Trace analysis shows differences in maximum expression level, onset time, response time, mRNA degradation rate, and expression rate. Bars represent mean with standard error of the mean. Data from transfection of A549 cells.

with the RNAi machinery [233–235], a relationship explored in more detail in chapter 5.5. Most importantly, the high stability of the protein means that when mRNA translation starts before siRNA-mediated cleavage, a significant amount of protein is produced and still present before the siRNA can target the mRNA.

On the other hand, the timing differences are also notable. The faster response in co-delivery points to a regulated expression mechanism, which will be further explored in section 6.6.

4.2.2. Quantification of RNAi

Combining the approaches discussed in sections 4.1 and 4.2.1 enables precise quantification of RNAi mediated mRNA decay. As depicted in **Fig. 4.8**, CayRFP and GFP mRNAs were co-delivered, followed by a GFP-targeting siRNA. This selectively triggered the degradation of GFP mRNA while leaving CayRFP mRNA unaffected, making CayRFP

expression a reliable internal reference to account for cellular noise and improve the accuracy parameter determination. To prevent ribosomal competition, GFP mRNA as in **Fig. 4.1** was used and concentration was maintained constant accross all experiments. The subsequent analysis focused on quantifying RNAi in successive siRNA delivery, a crucial step for later studies on the interaction between translation and RNAi.
To do so, GFP mRNA and CayRFP mRNA were co-encapsulated and co-delivered to either HuH7 or A549 cells. 45 min after mRNA application, siRNA was transfected. Two different siRNAs targeting different positions within the ORF were tested: siRNA 1 and siRNA 2, binding at nucleotide positions 122 and 433, respectively. To account for any non-specific effects caused by the second siRNA transfection, a control experiment with non-binding siRNA (siCtrl) was conducted. Single-cell fluorescence trajectories were recorded, calibrated and fitted to the three-stage maturation model, yielding key parameters such as mRNA stability (inverse of the degradation rate) and expression rate. To confirm the specificity of the siRNAs, stabilities of GFP and CayRFP in presence and absence of GFP-specific siRNA were compared. In **Fig. 4.8**, CayRFP mRNA stability remained constant regardless of siRNA treatment, while GFP mRNA stability significantly decreased in the presence of targeting siRNA.

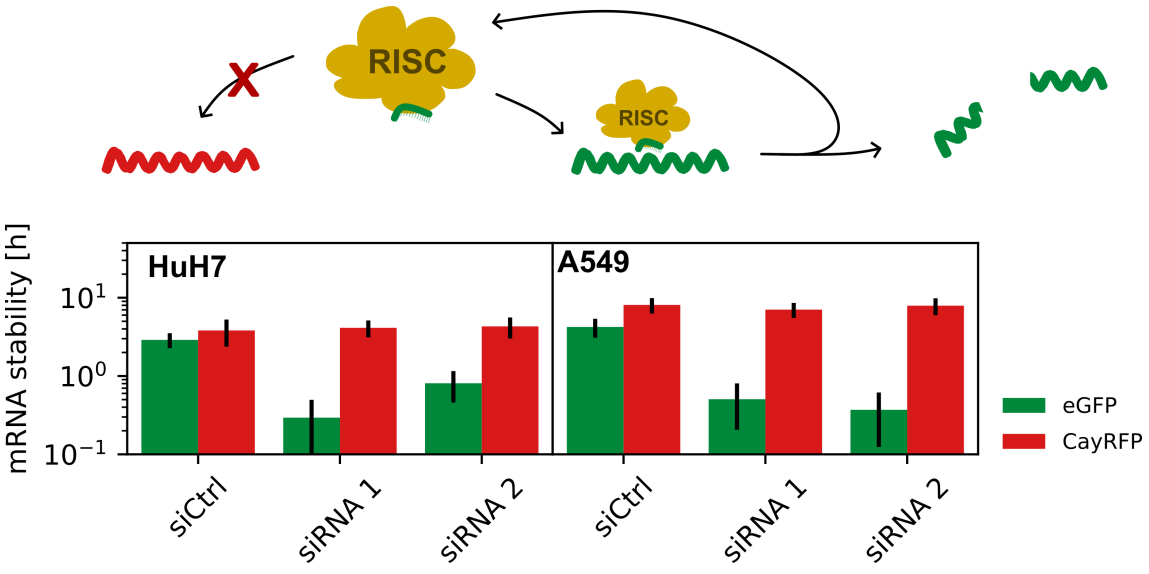

Figure 4.8.: Co-delivery of GFP and CayRFP with specific targeting of GFP mRNA: Top: A sketch of the specific targeting approach is presented. Two mRNAs are co-delivered. Successive delivery of GFP-specific siRNAs leads to cleavage of GFP mRNA but not CayRFP mRNA. Bottom: Single-cell fluorescence trajectories were fitted with the three-stage maturation model. The stability of CayRFP remained constant, whereas the stability of GFP decreased upon siRNA targeting. Experiments were conducted in HuH7 and A549 cells; median values with median absolute deviation (MAD) are shown.

The single-cell nature of the experiment enabled normalization of GFP stability against CayRFP stability within each cell, thereby accounting for cellular noise. The normalized stability was calculated as:

$$\text{normalized stability} = \frac{\text{stability}_{GFP}}{\text{stability}_{CayRFP}} \tag{4.4}$$

To assess the change in stability, the fold change of stability relative to the control experiment was compared, as shown in **Fig. 4.9** for both cell lines. The same approach was applied to the expression rate, which, interestingly, remained constant across conditions. This experimental procedure allowed precise, cell-specific, and siRNA-specific quantification of the destabilization effect. In HuH7 cells, siRNA 1 led to a fold-change reduction in stability of 0.09±0.02, while siRNA 2 resulted in a fold-change of 0.25±0.07. In A549 cell, the effect of the binding site on stability was less pronounced, with reductions of 0.11±0.07 for siRNA 1 and 0.08±0.05 for siRNA 2.

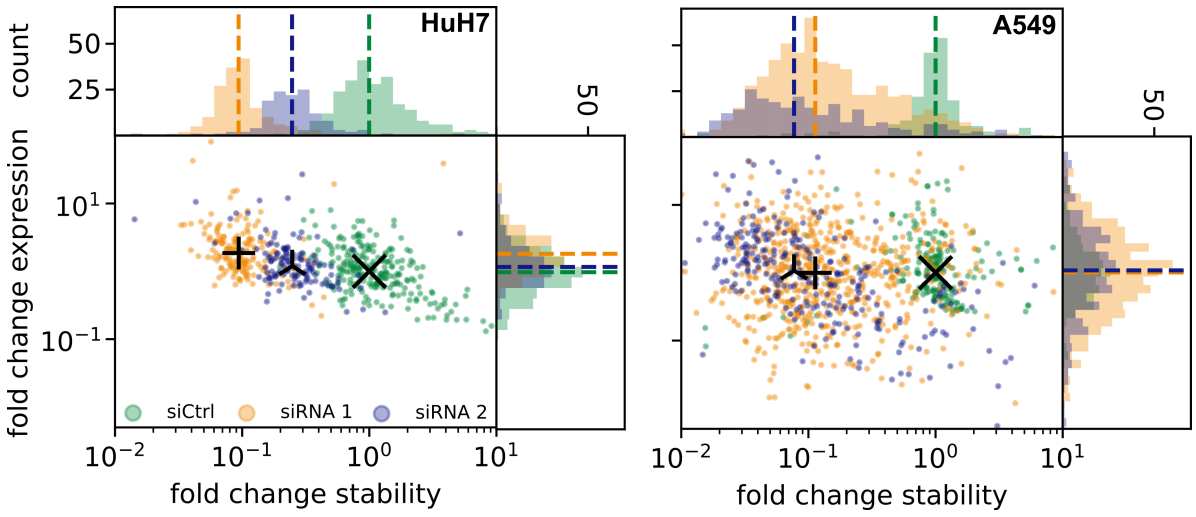

Figure 4.9.: Single-cell fold change of stability and expression rates: Single-cell normalization of the stability and the expression rate (GFP/CayRFP) was measured in HuH7 and A549 cells in the presence of either siCtrl (green), siRNA 1 (orange), or siRNA 2 (blue). Median values are indicated with lines (histograms), or crosses (scatter plots).

4.2.3. Discussion of siRNA/mRNA Co-Delivery

Co-delivery of two RNA species, siRNA and mRNA, has broad applications in synthetic biology, basic research and therapeutic development [91]. While co-encapsulation within the same particle has clear advantages, as previously discussed, siRNA and mRNA exhibit different kinetics, making successive delivery necessary in some cases [152]. In this study,

it was shown, that that siRNA knockdown efficiency is higher when co-delivered with the mRNA, compared to delayed delivery. This finding aligns with the work from Ruijtenberg *et al.*, who demonstrated that 92% of mRNA cleavage by RNAi occurs within the first 10 minutes. Successive delivery, by allowing translation to begin earlier, results in higher protein levels. However, these differences in protein levels cannot be attributed solely to the time advantage of earlier translation. The lower mRNA degradation rate observed in successive delivery suggests additional mechanisms at play. Potential factors include the "first-come, first-serve" principle described by Zhang *et al.* [129] or the interaction between the translational machinery and the RISC, which will be explored in more detail in section 5.5. As a basis for this study, siRNA knockdown efficiency through co-delivery of two mRNAs, followed by successive siRNA delivery was quantified. CayRFP served as internal reference to account for cellular variability, enabling precise quantification of RNAi. These results provide a foundation for investigating RNAi in the context of translation manipulation and control, which will be addressed in the next sections.

5. Manipulation of Translation and mRNA Lifetime through Codon Optimization

The importance of regulating mRNA stability was underscored by the Nobel Prize awarded in 2023 to Katalin Karikó and Drew Weissman for their work on nucleoside modifications that stabilized mRNA, paving its way towards becoming a therapeutic agent [236].
In addition to nucleoside modifications, several other strategies exist to modulate mRNA stability. In this chapter, regulating mRNA stability through synonymous codon exchange will be addressed. Figure 5.1 provides an overview of the key factors, beginning with the capping structure at the 5' end [237], followed by the untranslated region (UTR) design at both ends [238, 239] and the length of the poly(A) tail [240–242]. Within the open reading frame (ORF) - the coding region of the mRNA - further adjustments can be made to fine-tune the mRNA stability. As already mentioned, nucleoside modifications can be introduced to hide the mRNA from the immune system [236, 243] and variations in the UU/UA content have also been shown to influence mRNA stability [244]. Moreover, RNA interference (RNAi) target sites allow for the cell-specific targeting of exogenous mRNAs for degradation [245], therefore impeding mRNA stability. Lastly, codon optimization has been shown to influence stability [246–248] although it has been used more often to increase translational speed and efficiency [249–252].

Codon optimization for therapeutic or biological applications is based on codon bias, a common phenomenon in nature where different organisms exhibit varying frequencies of synonymous codons to regulate translation [253]. This degeneracy of the genetic code allows multiple synonymous codons to encode the same amino acid, with each codon recognized by specific tRNAs that possess distinct decoding rates [254–256]. The choice of codons, therefore, impacts the translation process and thereby the folding dynamics of nascent peptide chains [257]. Based on this, codons can be categorized into two groups: optimal and non-optimal codons. The optimality of codons, which are translated at vary-

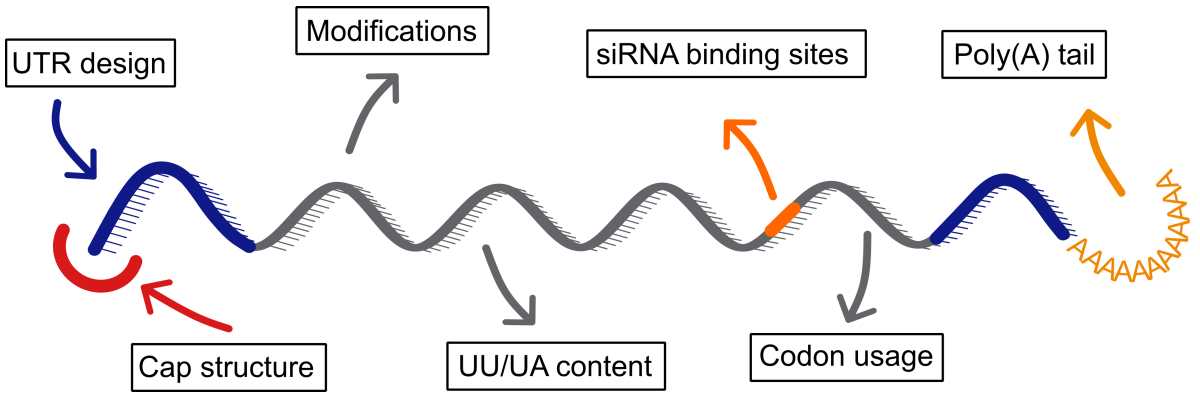

Figure 5.1.: Strategies to influence mRNA stability: Schematic drawing of mRNA with the ORF in gray, UTRs in blue, cap in red, potential RNAi binding sites in orange, and poly(A) tail in yellow.

ing rates and accuracy [258, 259], plays a crucial role in influencing translation by affecting ribosome speed [260–265], translation efficiency [266–268], protein folding [232, 263, 269], and translation fidelity [257, 258].
Initial single-cell experiments with GFP mRNA revealed that full-ORF codon optimization does not lead to increased but rather to decreased fluorescence. Interestingly, the insertion of a patch of de-optimized codons towards the end of the sequence did not compromise protein expression levels (see Appendix, **Fig. A.10**).

In this chapter, the impact of non-optimal slow-codon patches on protein expression dynamics was investigated, with a focus on their effect on mRNA stability in the presence or absence of siRNA. Live-imaging on single-cell arrays (LISCA) was employed to independently measure mRNA translation and degradation. To increase precision through filtering of cellular noise and the implications of the transfection procedure, an internal reference (cayenne red fluorescence protein (CayRFP)) was co-transfected. The comparison of measured single-cell transfection rates with predicted ribosome profiles from stochastic simulations allowed for the investigation of the impact of slow-codon windows on mRNA stability.

5.1. Generation of Predicted Slow-Codon Windows

Aiming for a more detailed understanding of the impact of codon choice on translation, ribosome density along the ORF was simulated based on codon selection. As described by Hanson and Coller in 2018 [257], numerous methods and computer models have been

developed to predict efficient exchanges of synonymous codons [249, 270–274]. Furthermore, Trösemeier *et al.* presented their optimized codon translation for protein synthesis (OCTOPOS) software for stochastic mRNA translation simulations [275]. Utilizing a machine-learning approach, OCTOPOS integrates simulation outcomes with additional mRNA-specific characteristics, such as abundance and length, thereby creating a robust model for predicting protein output. In addition to generating optimized mRNA sequences, OCTOPOS calculates steady-state ribosome density profiles, revealing the ribosome occupancy of individual codons within a sequence.
Here, ribosomal movement was investigated, as depicted in **Fig. 5.2a**, to examine the influence of slow codon windows on the ribosome density profile.

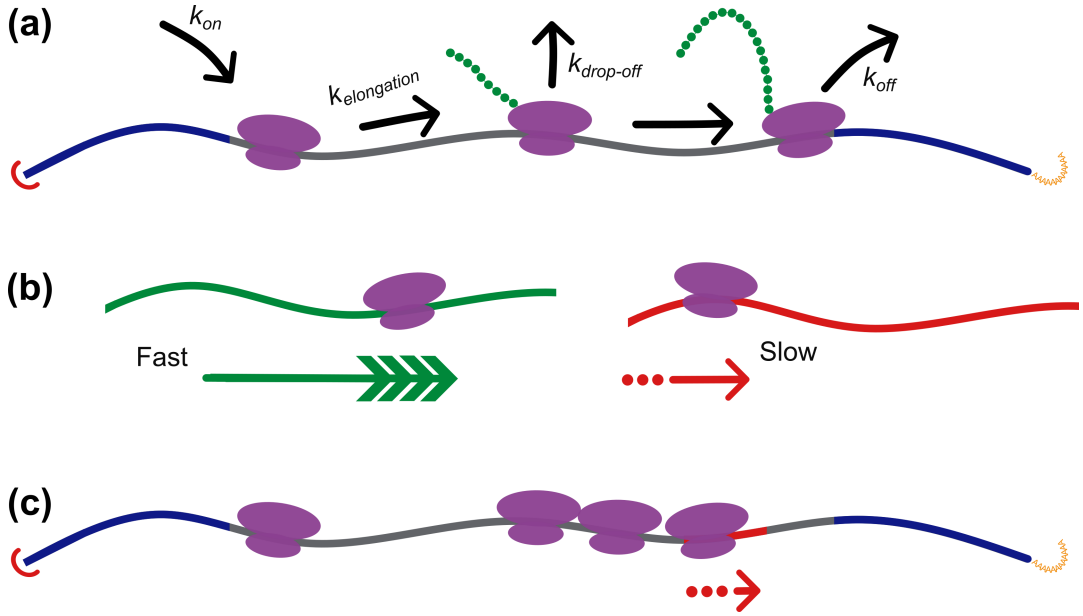

Figure 5.2.: Ribosome movement along the ORF: A sketch of the codon-specific elongation model (COSEM) of ribosome movement along the ORF (adapted from Trösemeier *et al.*) [275]. Ribosomes bind to mRNA with a rate constant k_{on}, elongate with $k_{elongation}$ and complete and finish translation with k_{off}. They may also fall off prematurely with $k_{drop\text{-}off}$. (b) Codon optimality influences the translation speed of ribosomes; optimal codons are translated faster and more accurately, while translation speed of non-optimal codons is reduced. (c) The insertion of non-optimal codon windows in the ORF can cause ribosome accumulations.

The presence of several optimal-codons in succession results in overall fast ribosome movement (**Fig. 5.2b**), while consecutive non-optimal-codons lead to slower ribosome movement. To modulate ribosome density, patches of non-optimal codons were inserted into the otherwise unmutated ORF. Since translation elongation is a stochastic process, such patches then lead to a localized increase in ribosome density, resulting in ribosome jams or even collisions (**Fig. 5.2c**) [246, 276–278].

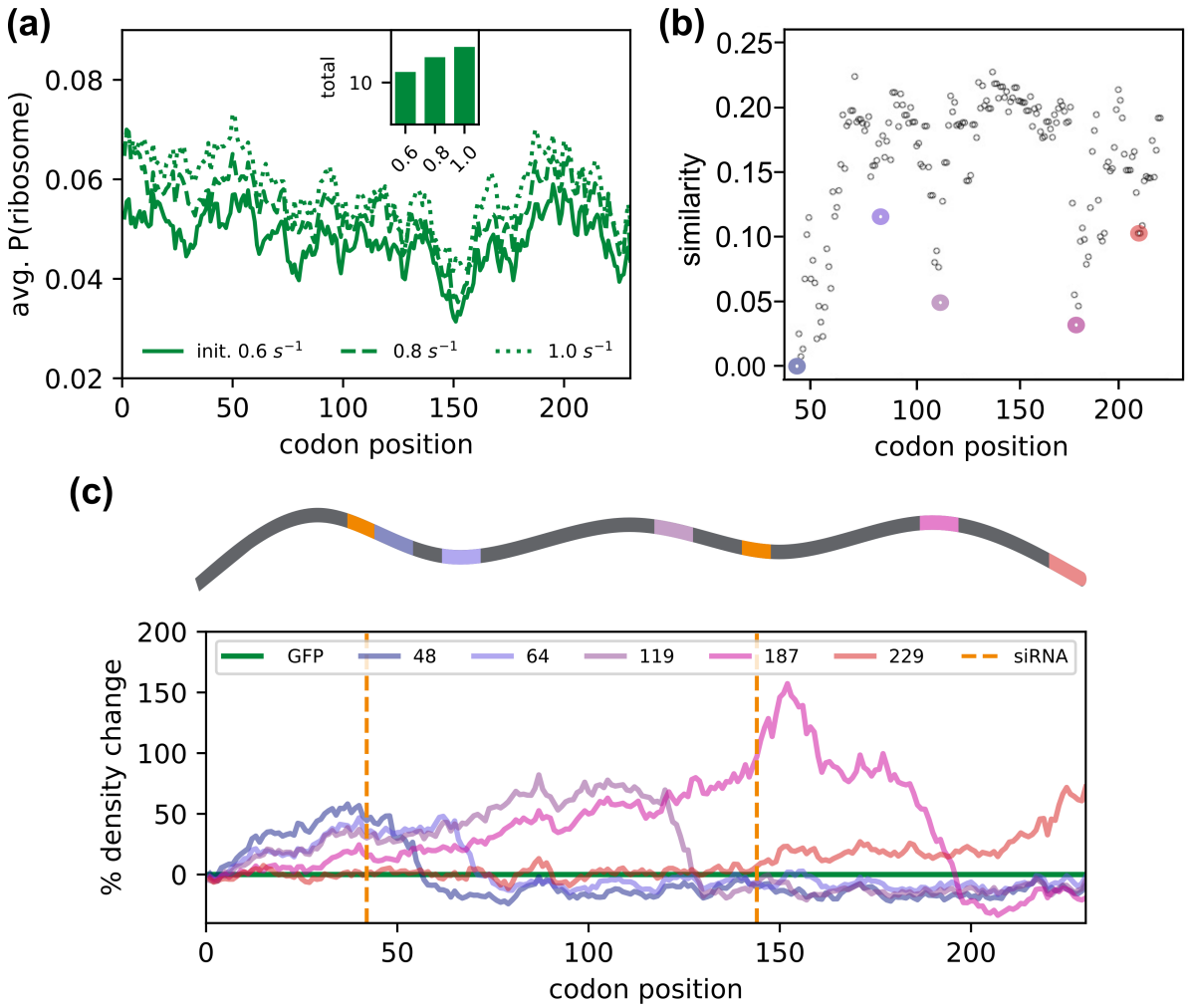

Figure 5.3.: Generation of slow-codon windows along the ORF: (a) Ribosome movement along the ORF was simulated with varying initiation rates, as indicated in the legend. The total ribosome occupancy is depicted in the inser, summing over all codons. (b) 10 adjacent codons were replaced along the ORF, with the first codon iterated for every codon position to determine total protein output. Constructs with the highest similarity to the construct with the slow codon patch at position 48 were selected for further analysis, as highlighted in a gradient from purple to red. (c) Positions of slow-codon windows are indicated in the sketch, with ribosome density profiles normalized to unmutated GFP shown for initiation rate of $0.8s^{-1}$.

To investigate the impact of locally increased ribosome densities on protein expression dynamics, different variants of GFP mRNA were designed by replacing stretches of ten adjacent codons with their non-optimal synonymous codons. The OCTOPUS software was utilized to simulate ribosome movement along the ORF [275, 279]. This simulation yielded density profiles that depended on the chosen translation initiation rates, providing information on the average probability of locating a ribosome at a distinct codon position (**Fig. 5.3a**). As shown in the inset of **Fig. 5.3a**, the initiation rate predominately

influenced total ribosome occupancy. In the following figures, an initiation rate of 0.8 s^{-1} was considered for this study, as it constitutes physiological conditions. In the simulation, 230 different constructs were modeled by iterating over all codon positions for the insertion of the non-optimal codon stretch. For each of these constructs, ribosome movement was simulated and ribosome density profiles were generated. For better comparability, five constructs with similar predicted protein output rates were selected, as highlighted in **Fig. 5.3b**. One slow codon window was inserted per construct, with the positions along the ORF illustrated at the top of **Fig. 5.3c**, alongside the respective ribosome profiles. Increased ribosome densities were observed for all constructs, peaking around the slow-codon window and smearing out towards the 5'-end.

5.2. Slow-Codon Windows Modulate Protein Expression Kinetics

Single-cell analysis allows detailed analysis of the impact on protein expression kinetics, revealing important insights into cellular dynamics. **Fig. 5.4a** shows mean single-cell fluorescence trajectories for two different cell lines, where distinct differences in the dynamics of protein expression were observed between cell lines and mRNA constructs. For simplicity, only three constructs are presented: one with the slow-codon window near the 5'-end ("early"), another construct with the slow-codon stretch in the center of the ORF ("middle"), and the third with the window towards the 3'-end ("late"). Most prominent was the difference of expression levels between the mRNA constructs and cell lines. HuH7 cells tended to generally produce more fluorescent GFP compared to A549 cells (also see **Fig. 5.4b**, top panel). The unmutated GFP mRNA led to high protein production whereas introduction of a slow codon-window led to lower levels. Here, a clear position dependency of the slow-codon-window-position appeared in the HuH7 cells, whereas this trend was not completely reproduced in A549 cells.
The response, i.e. the time where half of the expression maximum is reached, can also be determined for every single cell. Mean values together with standard error of the mean can be found in **Fig. 5.4b**. Interestingly, partially reduced response times were observed.

A closer look on the first hours after mRNA transfection revealed different kinetics for the different constructs (see inserts in **Fig. 5.4a**). As indicated in **Fig. 2.9b**, theoretical models predict this period to be dependent on mRNA stabilities.

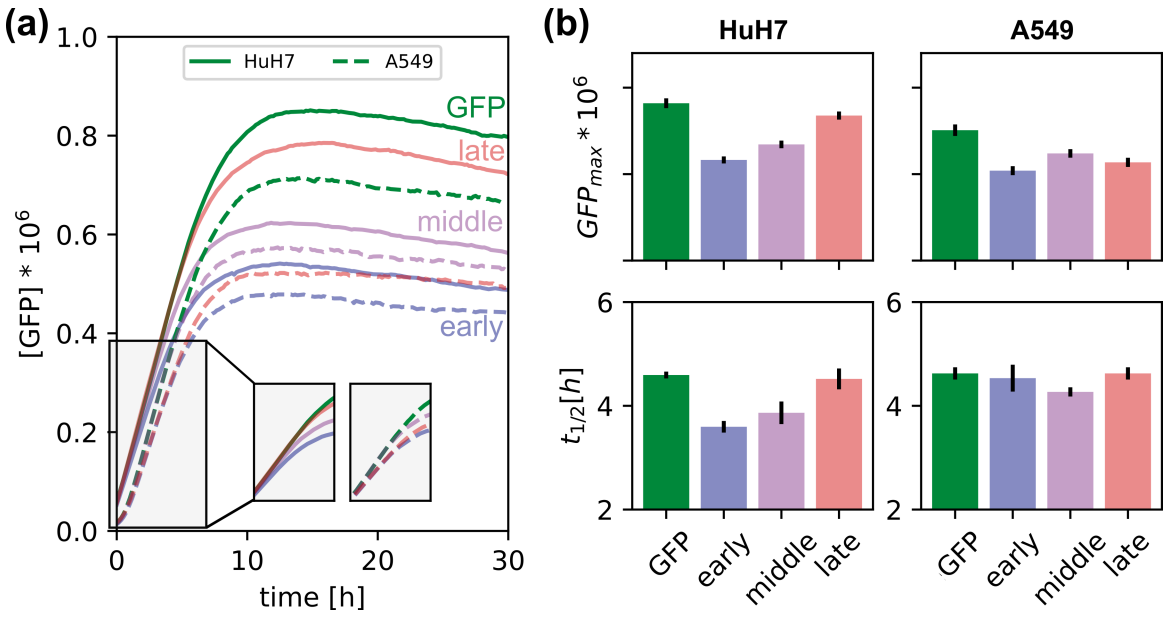

Figure 5.4.: Impact of ribosome movement on expression kinetics: (a) Mean of single cell traces of HuH7 or A549 cells transfected with either unmutated GFP or a construct with a slow codon window towards the 5'-end (early), in the middle of the ORF (middle) or towards the 3'-end (late). Inset shows zoom of the first hours after transfection to highlight influence of degradation rate. (b) Mean GFP level and response time for each construct. Error bars correspond to the standard error of the mean.

5.3. Effect of Slow-Codon Windows on mRNA Stability

The effect of increased ribosome densities and ribosome jams on mRNA stability has been widely discussed in the literature [252, 264, 276]. Given that increased ribosome densities on the ORF were observed in simulations following the insertion of slow-codon windows, their impact on mRNA stability was investigated. Fitting of the single-cell fluorescence trajectories to the previously described three-stage maturation model allowed to for the assessment of mRNA stability and expression rate (initial amount of mRNA multiplied by translation rate, $m_0 k_{tl}$).

Two cell lines were transfected with either unmutated GFP mRNA or one of the five synonymous variants. Co-transfection with CayRFP was performed for internal normalization. For each cell, GFP mRNA stability (τ_{GFP}) and CayRFP mRNA stability (τ_{CayRFP}) were determined. Each τ_{GFP} was normalized to the internal CayRFP control and to the corresponding value measured in the unmutated GFP-transfected cells. This resulted in the fold-change normalized mRNA stabilities that are presented in **Fig. 5.5a**. Generally, reduced mRNA stabilities were observed for the slow-codon-window constructs in both cell lines compared to unmutated GFP mRNA. While stability of the first and last construct showed high similarity between the cell lines, constructs with slow-codon windows

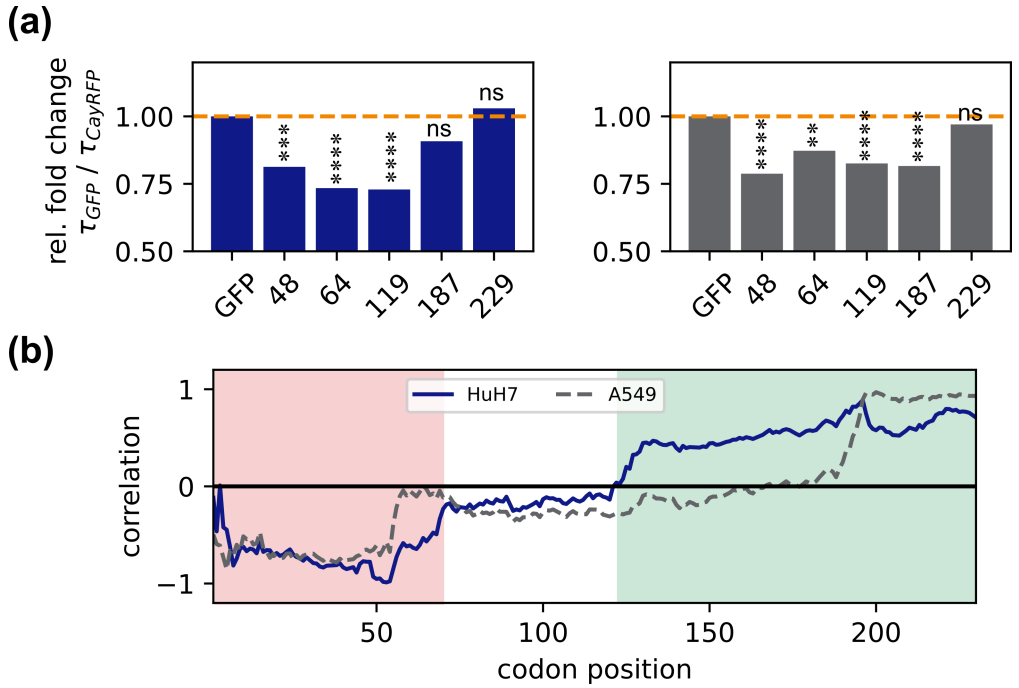

Figure 5.5.: Destabilization of mRNA upon insertion of non-optimal codon patches: Stability of GFP mRNA was determined using LISCA and normalized with equivalent values from the reference CayRFP mRNA for each cell. (a) Constructs with non-optimal codon windows exhibited decreased stability compared to unmutated GFP mRNA in both cell lines. Median stabilities are shown, along with results from the Mann-Whitney-U test. A yellow line indicates the fold-change compared to GFP mRNA. (b) The Pearson's Product Moment Correlation Coefficient was calculated for the measured mRNA stability and predicted ribosome density at every position along the ORF. Figure adapted from **[P1]**.

in the middle of the ORF exhibited slightly different relative stabilities. Mann-Whitney-U tests revealed significant changes in stability for most constructs (exceptions are indicated within the graph). In HuH7 cells, the most substantial change of mRNA stability was observed for the construct with the slow-codon window in position 119, where the relative stability was reduced to 73% ± 11%. In the A549 cells, the construct with the slow-codon window at position 48 had the lowest relative stability of 79% ± 14%.
Protein expression rates $m_0 k_{tl}$ were also measured, but no discernible trend of generally increased or decreased stability was observed. To gain further insight into the correlation of mRNA stability and predicted ribosome density, Pearson's Product Moment Correlation Coefficient was calculated for every position along the ORF:

$$r = \frac{\sum(x_i - \overline{x})(y_i - \overline{y})}{\sqrt{\sum(x_i - \overline{x})^2 * \sum(y_i - \overline{y})^2}} \tag{5.1}$$

A negative r indicates a negative correlation between stability and ribosome density, re-

flecting that an increased ribosome density leads to decreased stability. This finding was particularly evident in the 3'-region, as indicated by the red background in **Fig. 5.5b**. In contrast, towards the 5'-end, an increased ribosome density appeared to positively influence mRNA stability (indicated by green area in **Fig. 5.5b**). For A549 cells, this area was limited to the last 30 codons of the ORF, while it extended further towards the 3'-end in HuH7 cells.
Here, LISCA was employed to determine mRNA stabilities of synonymous GFP variants, in which patches of slow-translated codons were inserted. These constructs exhibited locally increased ribosome densities along the ORF. In accordance with the literature, a destabilizing effect of the slow-codon patches was demonstrated. Correlation analysis revealed a position dependence, with the destabilizing effect being most pronounced towards the 5'end.

5.4. Impact of Codon Optimization on RNAi

In the last chapter, it was shown, that LISCA enables the study of the influence of slow-codon windows on mRNA stability. A disadvantage of slow-codon windows on mRNA lifetime was observed, consistent with previously described findings. As ribosomes and the translational machinery, and the RNAi related RISC (see section 2.1.3) bind to mRNA, the impact of slow-codon windows and related ribosomal densities on the effectiveness of RNAi was investigated. Therefore, targeting siRNAs with binding sites at nucleotide positions 122 (siRNA 1) and 433 (siRNA 2) were transfected 45 minutes after mRNA transfection (see Appendix for experimental details). To account for any impact that the second transfection itself may have on mRNA stability, a control experiment with a non-binding siRNA control was performed. An overall decrease in all mRNA stabilities was observed upon the addition of siRNA, as expected. However, normalization to the respective stability of unmutated GFP mRNA revealed a relative increase in stabilities, as shown in **Fig. 5.6a,b** for both tested cell lines. Except for the construct with the slow-codon window at position 229 in HuH7 cells, all mRNAs exhibited a significant increase in relative stability compared to the siCtrl experiment or at least no significant change compared to the control. In HuH7 cells, a relative fold change of up to 1.4±0.2 was found, and 2.2±0.4 in A549 cells. These findings allow the conclusion that increased ribosome occupancy protects mRNA from RNAi-mediated degradation, or that RNAi mitigates the disadvantageous effect of slow-codon windows. This effect appeared to be more pronounced in A549 cells than in HuH7 cells.
To correct for any effects that might be caused by the second siRNA transfection or any

quality control pathways, relative stabilities were normalized with the respective values from the siCtrl experiment. This isolation of mRNA stability allowed the investigation of whether there is a correlation between the simulated ribosome occupancy at the siRNA binding site and the measured stability. Both values were plotted for each cell line (insets in **Fig. 5.6a,b**, but only weak to no correlation of the stabilities was found. Notably, the stability increase was observed both downstream and upstream of the respective binding sites, underscoring the finding that the ribosome occupancy directly at the binding site was not the driving force of the protective effect.
From this point, the investigation aimed to determine whether there is a general position-dependent effect of ribosome density on mRNA stability. Therefore, the correlation coefficient was calculated again, as described in Equation 5.1. A positive correlation indicates a beneficial effect of ribosome occupancy on the mRNA stability, whereas a negative correlation suggests a destabilizing effect. In contrast to the previous results observed in the absence of RNAi, a positive effect of ribosomal occupancy in the 5'-end of the ORF was noted for both cell lines, while a negative effect was observed at the 3'end. In the center of the ORF, a pronounced difference between both cell lines was evident.

In conclusion, these experiments revealed that under conditions where mRNA is subjected to siRNA-mediated RNAi, regions containing non-optimal codons exhibit a protective effect, despite generally leading to a decrease in mRNA stability. This protective mechanism appears to be largely independent of the specific siRNA cleavage site. Instead, it seems to be influenced by the positioning of the non-optimal codon region within the mRNA sequence. Notably, this effect is positively correlated with ribosome density in the early part of the ORF and negatively correlated in the late part. In the central region, variations were observed depending on the cell type.

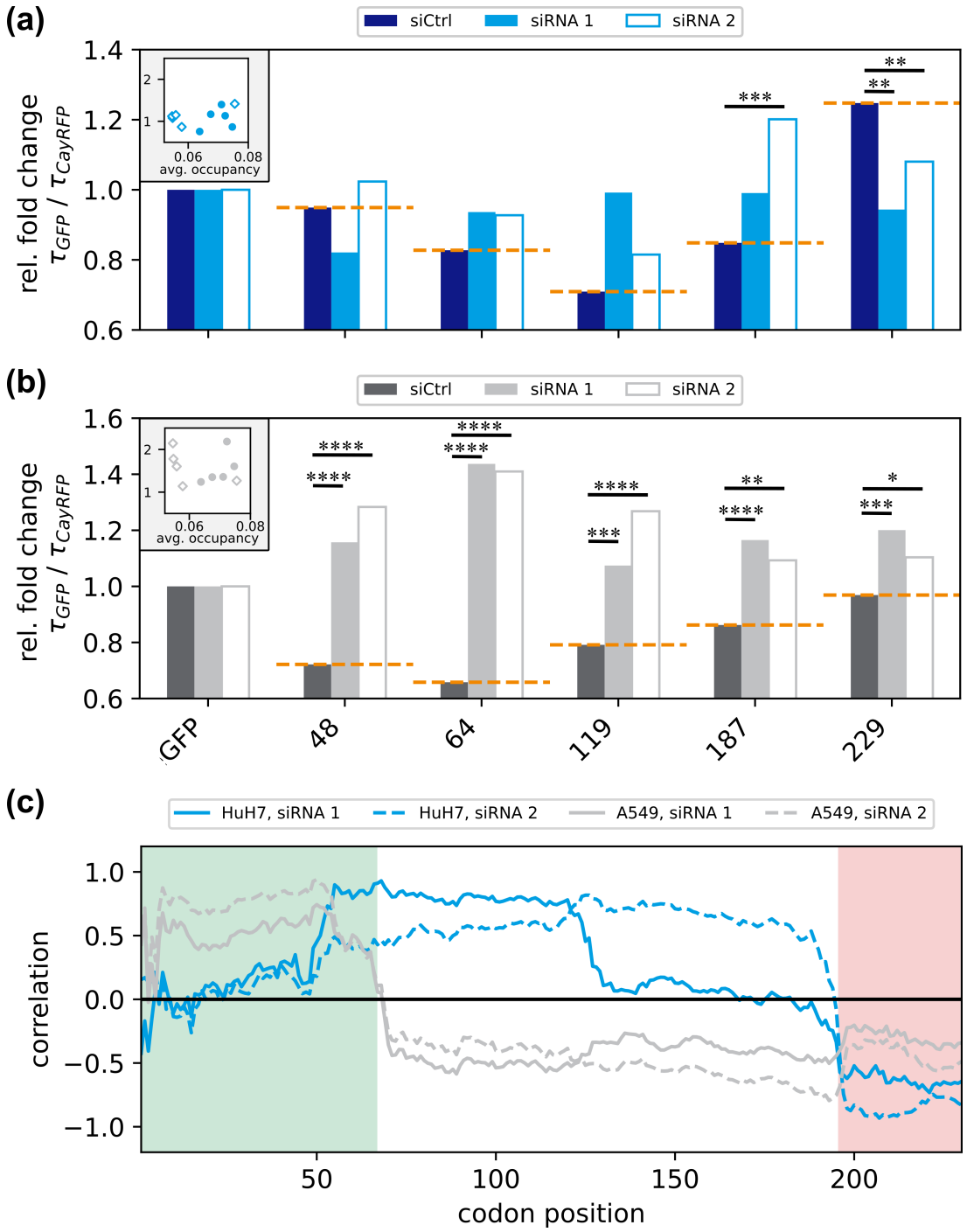

Figure 5.6.: Mitigation of the stability disadvantage of slow-codon windows under RNAi: (a) Stability of slow-codon window constructs transfected to HuH7 cells, normalized to the internal CayRFP reference and median stability of unmutated GFP mRNA. Dark blue bars represent control experiment with non-functional siRNA, while light blue bars indicate stabilities under transfection with functional siRNA 1 or 2. Yellow lines to guide the eye towards the differences compared to the control experiment. Significance values derived from Mann-Whitney-U test. (b) Corresponding data for transfection in A549 cells. (c) Pearson's Product Moment Correlation Coefficient of measured stability with simulated ribosome probability at each codon position along the ORF. Figure adapted from [**P1**].

5.5. Discussion

In this chapter, the complex relationship between codon bias and mRNA stability was studied. Previous experiments revealed a non-trivial correlation between codon optimality and mRNA lifetime, as described in Chapter A.3.2. LISCA facilitated the independent determination of mRNA stability (δ) and expression rate ($m_0 k_{tl}$).
First, the implications of slow-codon patches and ribosome density changes on the expression dynamics of GFP mRNA was investigated. Comparison of the kinetics revealed distinct differences in the maximum expression levels and in the first time frames following transfection. Response times were significantly reduced in HuH7 cells, while almost no significant changes were found in A549 cells. In general, such cell-specific differences may be attributed the metabolic differences between the lung and liver cell lines. Those differences may result in different sized ribosomal pools or the general availability of ribosomes and therefore influences the impact of slow-codon windows. Other cell-type specific differences such as protein kinase R (PKR) dependent translation inhibition [280] that was found increased in A549 cells [281], should be cancelled out here, as such general translation inhibition also applies for the co-transfected reference mRNA.
According to the simple translation model presented in Section 2.4.2, the steady-state level (Equation 2.9) is the ratio of degradation and expression rates, whereas the response time is dependent solely on the degradation rate (equation 2.11). Therefore, this data was the first hint towards decreased mRNA stability, induced by altered codon choice.
This was further investigated through the transfection of the five slow-codon window constructs and a consistently reduced mRNA stability was observed. This effect has been discussed previously in the literature [235, 248, 252, 264, 282] and was attributed to increased ribosome density. Although not fully understood and still a subject of discussion, it has been reported that sequences that stall ribosomes are targeted by a cellular quality control mechanism known as no-go decay (NGD) [234, 277, 278, 282–285]. Therefore, these results support the theoretical assumption derived from simulations indicating increased ribosome density. Moreover, the correlation of predicted ribosome density and measured mRNA stability revealed three areas of correlation in both tested cell lines. Toward the 5' end of the ORF, increased ribosome density resulted in higher mRNA decay, whereas no correlation of density and stability was observed in the center of the ORF. Conversely, toward the 3' end, increased ribosome density seemingly contributes to mRNA stability. Especially near the 5' end, high similarity between both cell lines was observed. It was discussed in literature, that especially the 5' end of the ORF is highly sensitive to changes and differs from the ORF in terms of codon choice [286] to support translation initiation. Therefore, changes in this region as applied in this study

might particularly lead to abnormal ribosomal movement, detected by the cellular control mechanisms [277, 284].

Beyond the destabilizing effect of increased ribosome densities, other studies reported a protective effect of ribosomes against certain decay mechanisms [287–292]. Notably, Ruijtenberg *et al.* described a close interplay between RNAi and translating ribosomes [233]. To contribute to the disentanglement of translation and decay, the effect of slow-codon windows was examined in this study and indeed a stabilizing effect of slow-codon windows on mRNA lifetime under RNAi was reported. Compared to the control experiments, mRNA lifetimes generally increased. While this effect was pronounced in A549 cells for all constructs, significant increases in HuH7 cells were observed only for constructs with slow-codon windows towards the 3' end of the ORF. Nevertheless, it is important to note that even non-significant changes of stability indicate a protective effect against RNAi, as in absence of RNAi, all constructs exhibited a significant decrease in stability.

The correlation between predicted ribosome density from OCTOPOS simulations and measured stability revealed three regions of correlation, which are inverted compared to the experiments without RNAi. Increased ribosome densities at the 5' end of the ORF exhibited a protective effect against siRNA mediated degradation, while ribosomes towards the 3' end seemingly amplified RNA interference. Interestingly, the correlation in the center of the ORF was largely cell-type dependent. A similar ribosomal protection effect in *Saccharomyces cerevisiae* was described in 2021 [293]; however, this protective effect was attributed to controlled translation initiation, which avoids downstream ribosome queues that trigger NGD.

To explain the observed stabilizing effects of ribosomes against RNAi, several factors need to be discussed. Simulations indicated a position-dependent slowdown of ribosomes, and consequently of the entire translational machinery. However, a direct stabilization effect of ribosomes was excluded, as transfection without siRNA showed significant reduction of stability. Yet, a steric effect of ribosomes hindering RISC from reaching its binding sites could exist. If this were the case, it would create a dependence between stability and the distance of the slow-codon window to siRNA binding site. Since in the experiments conducted here, the correlation profile remained highly similar independent of the siRNA binding site, a direct effect cannot be conclusively described. Nevertheless, secondary structure effects, as discussed in the literature [233, 277, 294, 295], could potentially explain the observed effects. Calculations of secondary structures with RNA-fold [296] did not reveal any obvious structural changes that might influence RNAi, such as hairpin structures around binding sites. However, simulations of secondary structure do not accurately reflect cytosolic conditions in terms of pH, viscosity, salt concentrations, or packing density. Hence, further studies are needed to investigate any potential secondary

structure effects. Moreover, secondary structure alone neglects interplay with ribosomes, which can untangle secondary structures during translation and thereby expose RNAi binding sites [233]. Additionally, the first part of the ORF was reported to exhibit low folding [297–299] followed by a highly structured region to slow down ribosomes in order to facilitate smooth translation elongation [298, 300, 301]. While this leads to increased destabilization, the accumulation of regulatory factors in this region might further contribute to hindering RISC of finding its target site. Furthermore, it has been described previously [234, 235] that RISC first binds to a seed region [302, 303], which comprises only a few nucleotides of the full siRNA. Mapping of the seed binding regions of GFP mRNA for the two siRNAs used here revealed increased density of those regions in 5' end (see Appendix **Fig. A.7**). This increased density may explain, why the protective effect of the slow-codon window and increased ribosome density was found to be pronounced in this region.

Additionally, the method described here relies on proper protein folding, as fluorescence is used as a readout. Given that translation speed and ribosome movement may affect fidelity of protein folding, [232, 263, 269], the slow-codon windows inserted here, could disturb correct folding, and would therefore disturb the readout.

In summary, our approach of combining high throughput single-cell experiments and stochastic simulations, allowed for the detection of position-dependent correlations between non-optimal codons and mRNA stability that were previously challenging to assess. This approach provides new insights into the molecular mechanisms governing RNA interference and opens up new avenues for further exploration of the complex details involved in mRNA regulation and stability.

6. Self-Regulated Protein Expression via an Incoherrent Feed-Forward Loop Motif

In the previous chapter, the interplay between codon usage and mRNA stability was investigated. While understanding of mRNA degradation pathways and optimizing mRNA stability are crucial for efficient mRNA applications, these strategies alone are not sufficient to address the challenges of inherent variability and timing control associated with mRNA transfections. To enhance the precision and predictability of gene expression, artificial genetic circuits present a promising approach. In nature, one common regulatory motif is the incoherent feed-forward loop (icFFL), as introduced in Section 2.5.3 and illustrated in **Fig. 6.1a**. This network motif was shown to accelerate response time and to increase robustness against expression level fluctuations, which results in reduced output noise. Therefore, the aim of this work was to apply this network motif to mRNA transfections.

In this chapter, the concept of siRNA/mRNA-LNPs as a self-regulatory system for transient protein expression will be presented. Prior to application *in vitro*, simple regulation of mRNA transfections is explored, demonstrating that simple mRNA transfections are quantitative and predictable when delivered with LNPs instead of Lipofectamine (L2000). Building on this simple regulation, the dynamics and response times of icFFL-based transfections are analyzed. Further investigation into expression noise reveals a buffering capacity, leading to reduced variation in expression levels. A rate analysis, derived from fluorescence trajectory fitting, shows a dose-dependent degradation rate, resulting in a correlation between the expression and degradation rates in icFFL transfections. Finally, quantitative modeling captures of the observed ratio-dependent expression levels, providing deeper insights into the system's behavior.

6.1. Adaption of icFFL to RNA/LNPs

In this study, LNPs were employed to adapt the cargo from a simple mRNA-based transfection motif towards co-encapsulation of siRNA and mRNA within a single LNP, effectively reconstituting an icFFL (**Fig. 6.1b**). In terms of network theory (see **Fig. 6.1c**), this translates as following: the delivery of the LNP to the cytosol acts as an input signal, initiating the translation of mRNA (X) into protein (Y). The regulatory partner, the siRNA (Z), is co-delivered within the same LNP and is therefore activated by the same input signal. The indirect path of the icFFL involves siRNA assembling into the RISC, which degrades the mRNA, thus inhibiting protein production. The expected outcome, as predicted by classical network theory [197, 216], and previously discussed in **Fig. 2.14** and **2.15**, is illustrated in **Fig. 6.1d**. While reaching the same steady state level, the response time is faster and there is a certain buffering against fluctuations.

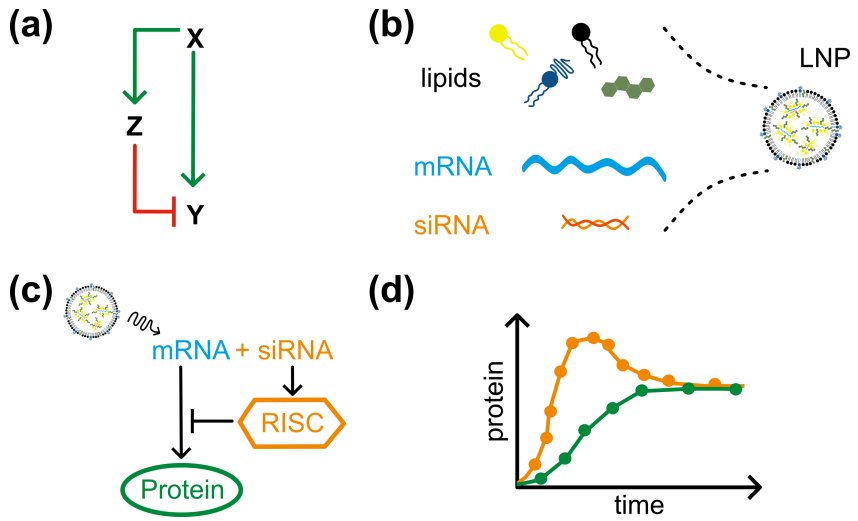

Figure 6.1.: Adaptation of icFFLs in RNA-LNP-transfections: (a) Structure of an icFFL type I (adapted from [197]). (b) LNPs are composed of four lipid species and can be loaded with different RNA species via microfluidic mixing. (c) The icFFL concept was applied to RNA-LNP transfections by co-delivering mRNA and a targeting siRNA. While the mRNA is translated into protein, the siRNA complexes with RISC proteins to target and degrade the mRNA, thereby inhibiting protein production. (d) A schematic comparison of transfection dynamics for classical mRNA transfection without siRNA (green) and with co-delivered siRNA (orange). Figure adapted from **[M1]**.

6.2. Simple Regulation of Protein Translation

A solid understanding of gene networks begins with describing the complex interplay between expression levels, mRNA dosage, and noise within simple systems. The single-

cell-based analysis used in this study generated hundreds of fluorescence trajectories, allowing for detailed studies of variability, distribution patterns, precise quantifications, and dynamic behavior. In a first step, GFP mRNA was transfected using either the commercially available *in-vitro* benchmark reagent L2000 or an in-house produced LNP (Appendix A.1.4 for more details). Based on the single-cell data, transfection efficiency (TE) - measured by the number of transfected cells - was determined, and the mean maximum expression levels were calculated along with their standard deviations and normalized standard deviations, represented by the coefficient of variation (CoV).

The first observation revealed that the transfection efficiency followed a Hill-function-shaped dose-response curve for both transfection reagents, although LNP transfections required higher doses (**Fig. 6.2a**, with 50% TE marked by dotted lines). The maximum expression level, which within the observed time frame approximates a steady-state level, also showed a dose-dependence for both transfection reagents (**Fig. 6.2b**). This dose-response exhibited near-linear behavior ($\sim x^{1.3}$) constrained by a stochastic limit at low doses (see also **Suppl. Fig. A.8**) and a saturation regime at high doses.

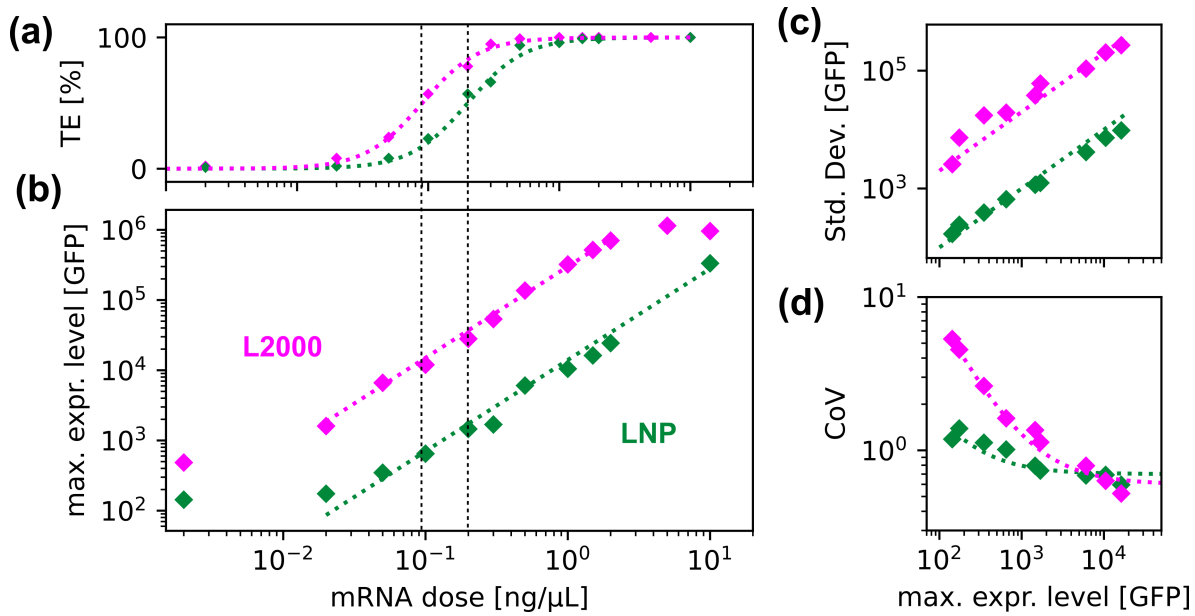

Figure 6.2.: Dose response in mRNA transfections: (a) Transfection efficiency, in terms of percentage of protein-expressing cells, after transfection with GFP mRNA using L2000 (magenta) or LNP (green). (b) The mean maximum expression level across all single-cells shows a clear dose dependence (SEM plotted, but smaller than the symbol). (c) Noise in the linear regime, described as the standard deviation between single-cell traces (dotted lines represent linear fit), and (d) noise normalized to the expression level and plotted as coefficient of variation (CoV) (dotted lines show ($\sim 1/x$) fit). Figure adapted from **[M1]**.

Additionally, noise in terms of standard deviation, increased linearly with expression level for both, L2000 and LNP transfections (**Fig. 6.2c**). The normalized standard deviation

(CoV, **Fig. 6.2d**) showed lower relative noise for LNP-based transfections, decreasing with $\sim$ (1/steady-state) consistent with the definition for a linear dose response of the expression level.
In summary, LNP-based transfections lead to lower expression levels but also reduce (relative) noise. Beyond changing the transfection reagent, the only tool available to regulate noise thus far has been adjusting the expression level.

6.3. Reduced Response Time in icFFL Regulated GFP Expression

Next, the dose-response experiments were repeated, this time including the co-delivery of siRNA. The molar co-encapsulation ratio of siRNA to mRNA (α) was defined as:

$$\alpha = \frac{s_0}{m_0} \tag{6.1}$$

where s_0 and m_0 represent the initial amounts of siRNA and mRNA, respectively. To prepare the LNPs, siRNA and mRNA were pre-mixed at the desired ratio in the aqueous phase before microfluidic mixing with the lipids. The amount of lipids was adjusted to maintain a constant N/P ratio. Single-cell traces from unregulated (no siRNA co-delivery) and regulated transfection experiments with varying α are shown in **Fig. 6.3a**. Clear differences were observed in these traces. While expression plateaued in all cases, higher levels of siRNA led to faster and more stable plateau formation. It is important to note here that the traces shown were selected for comparable expression levels, which required higher mRNA doses if siRNA was co-delivered.

Averaging the fluorescence trajectories from each experiment and normalizing them to their maximum expression level emphasizes the observed differences (**Fig. 6.3b**). As previously discussed in the three-stage translation model (**Fig. 2.9**), the initial incline of protein level primarily depends on the mRNA degradation. Since siRNA co-delivery enhances mRNA degradation, the observed sharper incline aligns well with theoretical predictions.
Normalization to the maximum expression level, P_{max}, further highlights the reduction in response time as the siRNA-to-mRNA ratio α increases. In **Fig. 6.3c**, the response times for different mRNA doses and siRNA ratios are plotted against the expression level. Regardless of siRNA co-delivery, a reduction in response time was observed with increasing

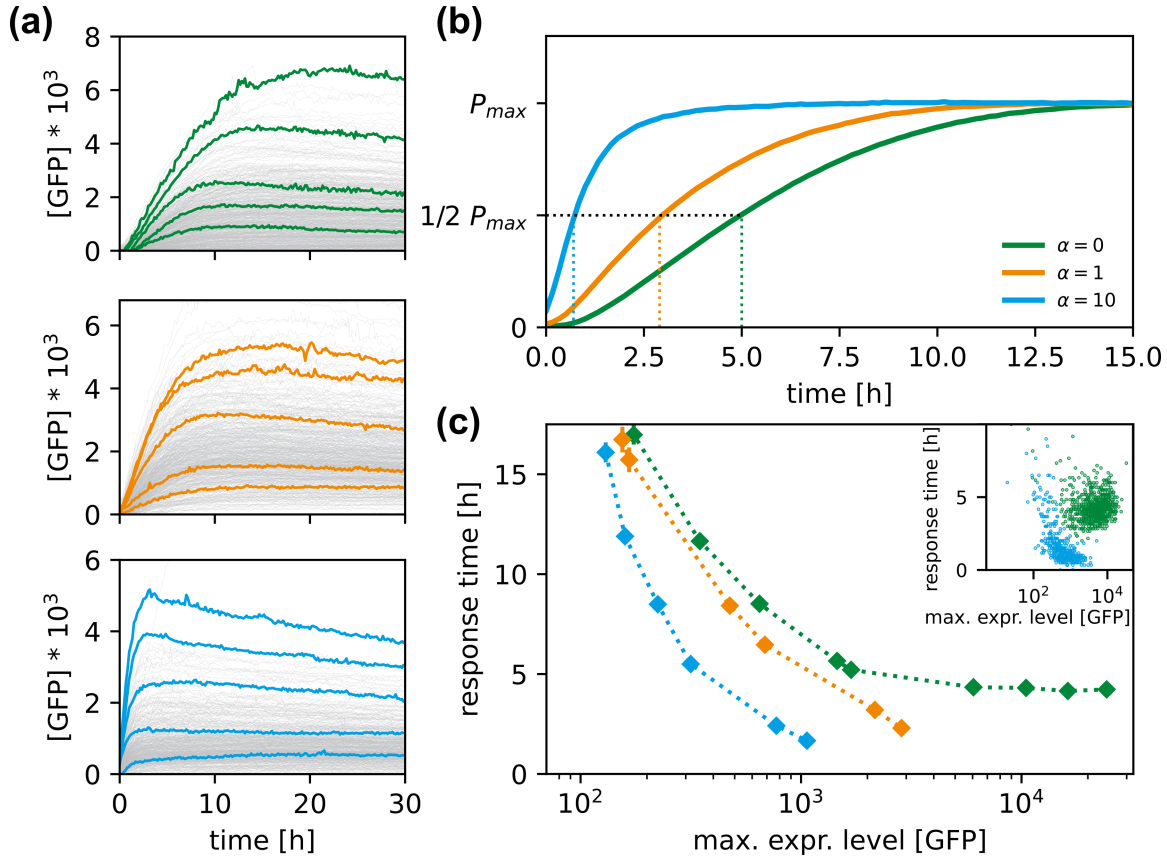

Figure 6.3.: icFFL LNPs allow control of response time: (a) Single-cell fluorescence trajectories. Green traces show unregulated transfection, while orange and blue traces represent regulated transfection kinetics with $\alpha = 1$ and $\alpha = 10$, respectively. (b) Mean fluorescence trajectories for the indicated siRNA-to-mRNA ratios α. Dotted lines indicate the time to half-maximum expression, which decreases with increasing α. Transfected mRNA doses in (a) and (b) were 10 ng, 25 ng and 50 ng, respectively. (c) Plot of response times versus maximum expression level shows reduced response times for regulated transfections at the same expression level. Introducing an icFFL allows achieving a lower response time with either a higher dose for the same expression level or the same dose for a lower expression level. Inset shows a scatter plot comparing $\alpha = 0$ and $\alpha = 10$. Figure adapted from [**M1**].

maximum expression level, and thus, increasing mRNA dose. At high expression levels, the response time approaches a mean of 5 hours, after which further increases in expression level do not result in further reduced response times. However, with siRNA co-delivery, the response time could be reduced further without altering expression level. The inset shows, that also the variability of the response times narrows at $\alpha = 10$.

Altogether, the data demonstrate, that co-delivery of functional siRNA results in faster and more stable protein expression, though at the cost of requiring a higher mRNA dose or yielding a lower expression level. The response time was found to depend on the expression level (**Fig. 6.3c**), but siRNA co-delivery provides an additional possibility to shorten response times while maintaining the expression level. This approach enables

a significant reduction in response times, even surpassing the 5-hour limit observed in simple mRNA-based regulation.

6.4. Reduced Dose Sensitivity of icFFL LNP Protein Expression

Beyond shortened response times, icFFL were shown to reduce noise of the output signal. In **Fig. 6.4a**, the dose-dependent expression levels are shown for simple regulation ($\alpha = 0$) and for icFFL systems with $\alpha = 1$ (equimolar siRNA and mRNA) and $\alpha = 10$ (a 10-fold excess of siRNA). The dose-response without siRNA can be approximated as linear within the displayed range. For siRNA-co-delivery, reduced dose-response exponents were found: $x^{0.7}$ for $\alpha = 1$ and $x^{0.4}$ for $\alpha = 10$. These lower exponents reflect a milder dose response, where variations in dose result in less dramatic changes in expression levels compared to unregulated transfections. The data suggest that this buffering capacity of input signal correlates with the amount of siRNA delivered.
The buffering also imparts another key property of regulated systems. **Fig. 6.4b** shows the relative noise (CoV) as a function of expression level. As observed for the response time, relative noise decreases with dose, regardless of α. However, the addition of siRNA narrows the distribution of expression levels for comparable mean expression level (inset), slightly reducing relative noise while maintaining a consistent expression level. This confirms that the noise-reducing property of icFFLs can indeed be transferred to mRNA transfections.

6.5. Model for icFFL Delivery

In the previous sections, control over both protein expression levels and timing was demonstrated for regulated mRNA transfections. To gain a deeper understanding of the underlying mechanisms, a theoretical model to describe the kinetics was developed.
To access key parameters such as mRNA degradation and expression rates, single-cell fluorescence traces were fitted to the three-stage maturation model for mRNA translation (**Fig. 2.9**). Unlike in unregulated transfections, a dose-dependent mRNA degradation was observed (**Fig. 6.5a**). The expression rate, $m_0 k_{tl}$, shown in **Fig. 6.5**, exhibited dose-dependency both with and without siRNA co-delivery, though it was slightly higher when siRNA was co-transfected, consistent with previous studies [91]. Interestingly, a correlation between the expression rate and mRNA degradation rate was found for $\alpha > 0$, as exemplary shown in **Fig. 6.5c**. This further underscores the dependency of mRNA

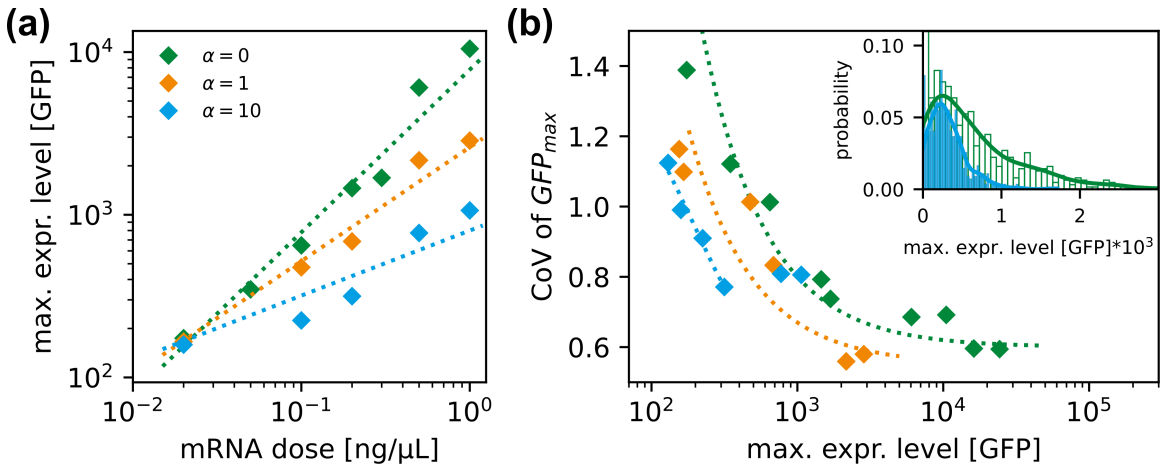

Figure 6.4.: Regulated dose-response of icFFL-LNPs: (a) Dose-response of unregulated transfections and regulated transfections at different siRNA-to-mRNA ratios α. Regulated transfections exhibit a milder dose-response. (b) Reduction in the coefficient of variation (CoV) shows a slight decrease in noise for the same expression levels. The inset shows a histogram illustrating the noise reduction of protein expression level. Figure adapted from [**M1**].

degradation on the amount of delivered mRNA m_0, and thereby siRNA, which is subject to fluctuations in cell culture experiments.

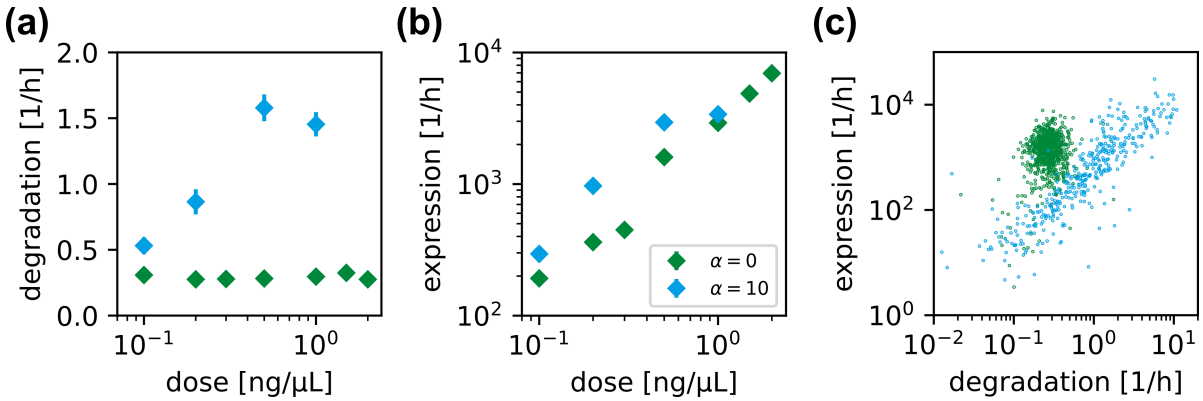

Figure 6.5.: Dose dependence of degradation and expression rates in regulated systems: (a) The degradation rate in regulated transfections was found to be dose-dependent. (b) The expression rate is slightly higher in co-transfections compared to simple regulation. Data shows mean values with standard error of the mean.(c) Single-cell correlation of expression rate and degradation rate in icFFL experiments. The transfected dose was 0.5 ng/µL in these experiments. Figure adapted from [**M1**].

The dynamics of mRNA translation without RNAi have been previously described using a simple set of ordinary differential equations (Equation 2.13 and 2.12, with the solution given in Equation 2.14). In simple mRNA transfections, all rates are assumed to remain constant, therefore, the only changing parameter with increasing mRNA dose is the initial

amount of mRNA (m_0). As a result, the protein levels are expected to increase linearly with dose, as observed.
When RNAi is introduced, an additional term for mRNA degradation must be included, modifying the total mRNA degradation rate δ to:

$$\delta = \delta_b + \delta_{RNAi} \tag{6.2}$$

This separates the mRNA degradation into a basal rate (δ_b) and an additional δ_{RNAi}, which accounts for siRNA-mediated mRNA cleavage. The new kinetic model is illustrated in **Fig. 6.6a**. A simple way to express the dependence of δ_{RNAi} on the co-delivered siRNA ratio is:

$$\delta_{RNAi} = \gamma * \alpha \tag{6.3}$$

where γ is a scaling factor. This linear relationship, together with the ODEs for mRNA translation (Equation 2.12 and 2.13), was implemented in Julia [230]. Expression levels at constant mRNA dose but varying siRNA ratios were plotted and compared to this simple model (**Fig. 6.6b**). The rates were estimated from previous literature [92] and are summarized in Table 6.1. While this estimation fits the data for low amounts of siRNA, it deviates at higher α. As previously described for ribosomal competition, also other resource limitations, such as saturation of RISC proteins, need to be considered. This saturation effect occurs when all available RISC proteins are bound to siRNA, leading to a plateau, which was also observed experimentally (**Fig. 6.6b**). Assuming stable siRNA-RISC binding, the kinetics were described using an enzymatic approach:

$$\delta_{RNAi} = \gamma * \frac{\alpha}{\alpha + k_M} \tag{6.4}$$

where k_M is a Michaelis-Menten-like reaction constant. This revised model captured the ratio dependence well, as shown in **Fig. 6.6b**.

Parameter	Description	Estimation	Source
k_{tl}	mRNA translation rate	1000 h^{-1}	experiment
δ_b	basal degradation rate	0.5 h^{-1}	experiment
β	GFP decay rate	5.22 * 10^{-3} h^{-1}	Krzyszton *et al.* [172]
m_0	initial mRNA level	30	experiment (with k_{tl})
γ	scaling factor	20	experiment and simulation
k_M	reaction constant	1	experiment and simulation
s_0	inital siRNA level	0 to 1500	experiment (with m_0)

Table 6.1.: Estimated parameter for RNAi modeling

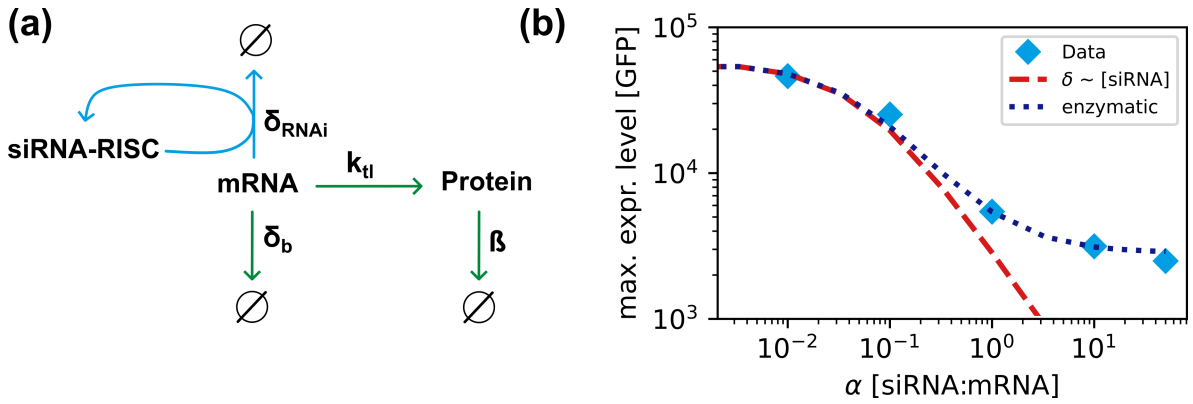

Figure 6.6.: Expression level control through siRNA molar ratio: (a) Kinetic model for icFFL-driven protein expression. (b) Expression level decreases as the siRNA ratio in the LNP increases. A simple linear relationship (red) does accurately represent the observed behavior for low *alpha*, while an enzymatic model for siRNA kinetics provides a better fit to the experimental data over the full tested range of α. Figure adapted from [**M1**].

6.6. Discussion

In this chapter, an incoherent feed-forward loop (icFFL) motif was implemented in LNP-mediated mRNA transfections based on the co-delivery of siRNA and mRNA. First, simple regulation was analyzed, and it was found that LNP-based transfections offered greater precision compared to L2000-mediated transfections, despite lower overall expression levels. This suggests that mRNA-LNP delivery behaves quantally, with the monodispersity of LNPs in size and encapsulation providing better control over the number of mRNAs delivered per *package*. The linearity observed in maximum expression levels during unregulated transfections aligns with theoretical predictions, assuming that all rates are constant. Consequently, the linearity of the standard deviation and the $\sim 1/x$ decrease in normalized standard deviation follow logically. Although both the L2000 and the LNP transfection follow this dependence, the controlled delivery of mRNA in LNPs exhibits a lower relative noise.

Interestingly, linearity in maximum expression level was observed despite transfection efficiencies being below 50% with the lower doses. Moreover, response time in unregulated transfections was found to decrease with increasing mRNA dose, likely due to the higher number of particles taken up by cells, which increases the likelihood of one escaping the endosome. However, the response time plateaus around 5 hours and does not accelerate further with higher doses. The introduction of icFFLs successfully reduced response time below this 5-hour threshold while maintaining the same expression levels. This provides a powerful tool for mRNA applications, where both the mRNA dose and siRNA can be adjusted to fine-tune response times and expression levels.

Additionally, the dose-response curve for protein expression in icFFL transfections showed reduced sensitivity, making the system less prone to variations in dose. The relative noise level was only slightly reduced. Fluorescence cross-correlation analysis of LNPs encapsulation labeled mRNA and siRNA revealed, that the siRNA:mRNA ratio that was prepared during mixing, was not the final ratio measured in the LNP, rather the results pointed towards an overloading with siRNA [304],**[M5]**. This underlines the assumption that the noise in expression levels could be reduced in theory but that the ratiometric mixing introduced a new source for fluctuations. Alternative approaches for the co-delivery should be explored to reduce this source of noise as far as possible. Those could be to encode both, mRNA and siRNA on one construct that will be seperated in the cytosol. This approach would require an carefully designed construct to provide efficient and reliable cleavage. An other approach could include labelling of both siRNA and mRNA and to determine their ratio via fluorescence intensity calibration for each single cell.
Further research is needed to explore cell-specific regulation, as described by Du and colleagues [55], and to investigate co-cooperativity, where multiple siRNAs bind to the same mRNA, which is of interest for the design of more complex regulatory networks [47].
In summary, single-cell analysis of LNP-mediated icFFL transfection systems presents a powerful tool to control noise and timing in gene expression. This control over natural variability in input signals, driven by the stochastic nature of LNP delivery, is particularly exciting. Beyond synthetic biology applications, where precision is essential for designing genetic switches [53], noise control is also relevant in therapeutic settings, where avoiding critical overexpression can be crucial.

7. Conclusion and Outlook

In this thesis, high-throughput live-cell imaging was employed to elucidate the kinetics of lipid-based RNA delivery. Specifically, mRNAs encoding fluorescence reporters were utilized to monitor protein expression following delivery via lipid-based carriers, with a particular focus on in-house produced lipid nanoparticles (LNPs). By additional mRNA labeling, the entire delivery process - from cellular uptake to endosomal escape and, ultimately, translation - was explored. To further investigate and modulate the underlying kinetics, exogenous RNA interference was integrated. The single-cell experimental setup generated fluorescence trajectories, which were analyzed using rate equations to quantify the dynamic processes.

To deliver RNA to a mammalian cell, a cascade of processes must be completed. After reaching the cell, the carrier must overcome the cell membrane, typically resulting in its engulfment and the formation of an endosome that is transported into the cell [112, 305]. As part of the natural endosomal pathway, this endosome is either recycled or undergoes acidification [126, 131, 132]. The acidification process ultimately leads to endosomal lysis unless the carrier and its cargo manage to escape [135, 143]. Delivery systems such as Lipofectamine (L2000) or LNPs are specifically designed to interact with the endosomal membrane upon acidification, triggering endosomal escape and releasing the cargo into the cytosol.
The kinetics of protein expression resulting from delivered mRNA cargo can provide insights into the dynamics leading to this protein production. Time-resolved single-cell expression trajectories enabled the characterization of distinct cell behavior. Initially, the influence of different vectors on delivery and protein expression dynamics was investigated. Despite its impaired functionality and toxicity *in vivo* [306], L2000 is frequently used for mRNA optimizations *in vitro*. In this work, the expression profiles of L2000 were compared with those of LNPs, which are the preferred non-viral delivery vector. LNPs exhibited lower overall expression levels, but showed distinct differences in their expression profiles compared of L2000 at low doses and the distribution of their onset times.
Endosomal escape is recognized as the primary bottleneck in lipid based nucleic acid delivery, yet reliable methods to study its kinetics are rare [27]. Therefore, single-cell

analysis using fluorescent reporters, alongside mRNA labeling to track processing, offers valuable insights into the dynamics of delivery with high statistical information. This revealed how the protein corona forming around LNPs influences not only cellular uptake but also intracellular processing, thereby affecting protein expression. a similar effect was observed for the bulk phase structure of LNPs, which can be altered by using different types of mixing buffers. This modification in the production process impacted uptake, and more importantly, the endosomal escape of the particles, enabling tuning of expression levels, onset, and kinetics. This technique could address additional topics in the field. For instance, LNP size was found to influence tissue-specific efficiency [84, 307, 308]. LISCA could reveal whether this is due to differences in payload, uptake, or endosomal escape. Since size changes can be achieved by varying the mixing conditions or altering the lipid composition, the specific impact of each modification on different trafficking parameters could be addressed. Furthermore, labeling of the corona lipids and the PEG could help determine whether protein interactions alter LNP affinity for cellular uptake or if endosomal escape is the key factor. The combination of buffers with varying pH and LNP lipid compositions may also contribute to these findings. Beyond uptake and endosomal escape, there is another understudied timeframe during delivery: the delay between endosomal escape and detectable protein expression, which is influenced by a delay of translation initiation potentially caused by the amount of lipid still adhering to the mRNA. The affinity between lipids and mRNA may further guide vector efficiency and impact expression timing. By selecting appropriate labels, this overlooked aspect could be explored in more detail.

However, protein expression is influenced not only by the vector but also by the cargo's composition. When two mRNAs were co-delivered, correlation analysis revealed an mRNA sequence-dependent ribosome competition, which can lead to unexpected effects on protein expression or be harnessed to regulate expression levels. A simple kinetic model was developed that qualitatively captured the dynamics. Nevertheless, more insights are required, such as those from partial translation inhibition experiments or further dose variations to improve this model and enable the prediction of competition scenarios. Co-encapsulation and co-delivery not only resulted in more uniform expression levels, but also improved the efficiency of exogenous RNAi. Single-cell analysis enabled the quantification of RNAi upon exogenous siRNA delivery and demonstrated that the knockdown efficiency is specific to both the binding site position and cell-type.

These results were applied to investigate the influence of ribosome density variations through manipulation of the GFP coding sequence using synonymous but slowly trans-

lated codons. Stochastic simulations indicated increased ribosome densities around these slow codons, and single-cell analysis revealed altered kinetics and expression levels. A more detailed investigation showed that mRNA degradation is particularly influenced by the position of the low-codon windows. Specifically, slow codons near the 5' end of the open reading frame (ORF) and the thereby increased ribosome density in this region positively correlated with mRNA degradation. In contrast, slow-codons near the 3' end had the opposite effect. Co-delivery of GFP-targeting siRNA revealed that an increased ribosome density due to slow codons could protect the mRNA from RNAi, an effect that was more pronounced in A459 cells than in HuH7 cells. This finding required precise determination of mRNA degradation rates, which was achieved through internal referencing against co-delivered CayRFP mRNA. As the position dependence was linked to the location of the slow codon window rather than the siRNA binding site, further research into the RISC binding mechanism, implications for protein folding, and cooperative effects is needed. Nevertheless, slow-codon windows offer a powerful strategy for tuning mRNA stability in transfection applications.

Finally, this work demonstrated that mRNA delivery can be controlled, although regulating noise and timing - without altering the carrier or cargo - can only be achieved through dose variations. However, the introduction of an incoherent feed-forward loop type I (icFFL) via ratiometric co-delivery of siRNA and mRNA enabled control over protein levels, noise, and timing. Kinetic modeling revealed that the relationship between the siRNA to mRNA ratio and mRNA degradation rate follows a Michaelis-Menten-like dependence on siRNA concentration. This predictability allows icFFL-LNPs to serve as precise tool for tuning the kinetics of mRNA delivery, which is highly valuable for future applications of complex combinatorial LNP-mRNA applications.

All these insights were enabled by the single-cell observation platform LISCA, which facilitated the investigation of the impact of carrier and cargo on the kinetics to develop tools for dynamic control of protein expression. The work presented herein provides the foundation for further studies aiming at improving the predictability of lipid-based mRNA delivery. For instance, encapsulating or attaching a pH dependent reporter, such as fluorescein, can provide information about the surrounding or inherent pH, thereby offering insights into the correlation between endosomal maturation, particle fate, and resulting protein expression. This approach becomes even more insightful when combined with the use of endosomal markers [161].
Additionally, in collaboration with two students, Carola W. Bartels and Bernhard Kirchmaier, the payload of LNPs was investigated using either surface-bound LNPs and fluores-

cence imaging [309] or fluorescence correlation spectroscopy [304]. Combining knowledge of LNP mRNA payload and quantal delivery - where only one particle is processed per cell - can yield further insights into translation dynamics.
Further information will be contributed through a collaboration with the *Hochschule München*, where advanced optical spectroscopy and imaging methods will be employed to track LNPs within cells together, alongside with recording of data regarding their diffusion coefficients and surrounding pH ([**M3**] and [**M6**]). Integrating this information with knowledge about carrier type could further enhance the understanding of the delivery process.
From a biological perspective, the complexity of single-cell cultures can be expanded. The use of proper markers would enable the co-culture of different cell species and co-transfection of various LNPs in parallel to investigate complex carrier and cell-type-specific behaviors. Additionally such an approach could allow for the parallel delivery of LNPs of different sizes, or prepared with different buffers loaded with different reporters, facilitating the study of concurrent behaviors. By placing multiple cells, spheroids, or even small organoids on the spots, collective protein expression could be analyzed in a single-cell manner to account for the impact of cell-cell contact on transfection.

All those findings can be combined to expand translational models, enabling quantification of the entire delivery process. This addresses a critical challenge in the development of lipid-based mRNA delivery: the lack of predictability in transferring results from cell culture to living organisms. Precise theoretical understanding will ultimately result in accurate reflections of the biological outcome. Therefore, this work contributes to the development of robust and complex combinatorial RNA-LNP tools for synthetic biology and therapeutic applications.

A. Appendix

A.1. Materials and Methods

A.1.1. Cell Culture

All cells used within this work were cultured at 37°C, 5 % CO_2. For single-cell transfection assays, they were seeded in growth medium according to Table A.2, as each cell line required a micropattern-specific cell density to ensure maximum spot occupancy together with a high single-cell percentage.

A549 Cell Line

The human lung carcinoma A549 cells were cultured in Gibco^{TM} RPMI Medium (RosswellPark Memorial Institute, ThermoFisher Scientific, #61870010) supplemented with 10 % (v/v) FCS (Fetal calf Serum, ThermoFisher Scientific, #10270106). At 70-90 % confluence, they were cleaved using T/E (Trypsin/EDTA, Gibco 15400-054).

HuH7 Cell Line

The HuH7 cell line originates from a human liver carcinoma. Cell culture was as described for the A549 cells, but the growth medium was further supplemented with 5 mM HEPES (GibcoTM, Thermofisher Scientific, #15630080) and 1 mM Na-Pyruvate (Gibco^{TM}, Thermofisher Scientific, #11360070). For cell cleavage, Acutase (invitrogen, 00-4555-56) was used.

HEK293 Cell Line

Human Embryonic Kidney cells (HEK293) were cultured in Gibco^{TM} DMEM (Dulbeccos Modified Eagle Medium, ThermoFisher Scientific, #10566016) supplemented with 10 % (v/v) FCS (Fetal calf Serum, ThermoFisher Scientific, #10270106). Cleavage was performed as described for HuH7 cells.

A.1.2. mRNA Production

Plasmids were ordered from Euorgentec. The production was carried out in three steps, including *in vito* transcription (IVT), dephosphorylation and post-polyadenylation. After each processstep, mRNA was purified.
For IVT, the respective nucleotide master mix was prepared containing 25 mM of each rATP (Jena Biosciences, NU-1010), rUTP (Jena Biosciences, NU-1013), rCTP (Jena Biosciences, NU-1011), and 5 mM rGTP (Jena Biosciences, NU-1012) together with 20 mM anti-reverse cap analog (ARCA) (Jena Biosciences, NU-855). Additionally, seperate mix of water (B.Braun, 3703444), Transcription buffer (ethris), RNAse inhibitor (ThermoFisher, EO038AFBXXX) and pyrophosphatase (ThermoFisher, EF022BXX) were mixed. This IVT mix was added to the rNTP mix together with the plasmid template. T7 polymerase (ThermoFisher, EPO11AFBXXX) was then added to start the transcription for 2 hours at 37°C, 300 rpm. Afterwards, DNAse (ThermoFisher, ENO52RAFBXXX) was added for another 45 min. Subsequently, precipitation and purification , using 5 M ammoniumacetate (SigmaAldrich, 9691), 70 % (v/v) ethanol (Roth, 5054.3).
Dephosphorolation was carried out using Quick CIP (NEB, 0041708) in MOPS buffer (pH 6.5) for 10 min at 37°C, followed by precipitation and purification as above. Polyadenylation was carried out by incubation of poly(A) polymerase buffer (ThermoFisher EP168B1 B001), ATP (Jena Biosciences, NU-1010), and DNAse (ThermoFisher, ENO52RAFBXXX) at 37°C for 5 minutes. Subsequently poly(a) polymerase (ThermoFisher, EP168B1B001) was added for 15 min at 37°C, again followed by precipitation and purification. Finally, ultrafiltration using Vivaspin 6 centrifugal concentrator (Merck) was performed to reach a concentration of 1 mg/mL, followed by sterile filtration with a 0.2 µM pore size filter (GE Healthcare, 6786-1302). mRNA was stored at -80°C.
Additionally, if available, mRNAs and siRNAs were purchased according to Table A.1

Name	Supplier	Cat. no.
CleanCap® EGFP mRNA	TriLink	L-7601
ARCA Cy5 EGFP mRNA	APExBIO	R1009
ARCA Cy3 EGFP mRNA (5-moUTP)	APExBIO	R1008
ARCA EGFP mRNA	APExBIO	R1001
GFP DuplexI siRNA	Horizon	P-002048-01-20

Table A.1.: Commercially available RNA constructs used in this thesis.

A.1.3. N/P Ratio Calculation

The N/P ratio is one of the central parameters when preparing LNPs as it describes the ratio of ionizable lipid to nucleic acid (NA) load. From there, the required amount of helper lipids automatically calculates from the intended lipid molar ratios. To calculate the N/P ratio, the number of available charges on the ionizable lipid and molecular weights of the components need to be taken into account. Simply spoken, the N/P ratio is:

$$\frac{N}{P} = \frac{\text{number of + charges on the amines of the ionizable lipid}}{\text{number of - charges from the phosphate backbone on the NA}} \tag{A.1}$$

The number of positive charges per mol is dependent on the type of lipid and thereby defined by its chemical structure. The nucleic acid has one negative charge per repeating unit with a defined molecular weight. Therefore, the N/P ratio can be described as:

$$\frac{N}{P} = \frac{\#_+ * n_{ionizable}}{\#_- * n_{NA}} = \frac{\#_+ * \frac{m_{ionizable}}{MW_{ionizable}}}{\#_- * \frac{m_{nA}}{MW_{NA}}} \tag{A.2}$$

with
$\#_+$ being the number of positive charges per molecule of the ionizable lipid
$\#_-$ being the number of negative charges of the nucleic acid repeating unit (= 1)
$MW_{ionizable}$ and MW_{NA} the respective molecular weights and
$m_{ionizable}$ and m_{NA} the masses.

The masses of nucleic acid and ionizable lipid can be expressed as:

$$m = c * V \tag{A.3}$$

with c being the concentration of the stock solution in mg/mL and V the corresponding volume. Inserting this in equation A.2 results in:

$$\frac{N}{P} = \frac{\#_+ * \frac{c_{ionizable} * V_{ionizable}}{MW_{ionizable}}}{\#_- * \frac{c_{NA} * V_{NA}}{MW_{NA}}} \tag{A.4}$$

A.1.4. LNP Production

Mixing of the LNPs was achieved through rapid mixing of the lipids in an organic phase (ethanol) with the aqueous phase containing nucleic acids and acidic buffer. Both phases

were prepared separately. If not indicated differently, lipids were prepared in the molar ratio 50:10:38.5:1.5 ionizable lipid, phospholipid, cholesterol and PEG lipid, respectively. mRNA mix was prepared to reach a final N/P ratio of 3 to 4 with a flow ratio of aqueous:organic 2:1. Microfluidic mixing was achieved using the NanoAssemblr® Spark™ (Precision NanoSystems).

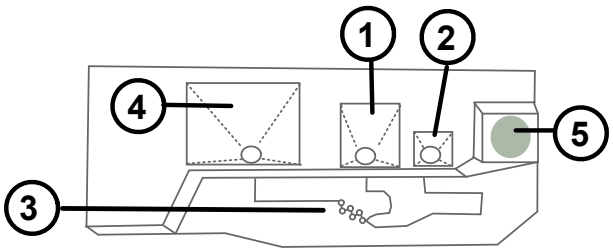

Figure A.1.: Illustration of the NanoAssemblr® Spark™ mixing cartridge: (1) Reservoir for the aqueous phase, (2) Reservoir for the organic phase. Both phases are mixed through microfluidic channels and a (3) bifurcating mixer and collected in the (4) sample reservoir that can be primed with buffer for in-line dilution. (5) The micro-chip controls that no cartridge is used more than once.

If no uniform size distribution was required, particles were mixed by rapid pipetting for the sake of costs. in this case, the aqueous phase was added rapidly and with constant mixing onto the lipid phase.

In case of microfluidic mixing, an inline-dilution with the respective LNP buffer was performed. After mixing, LNPs were kept for 15 minutes at room temperature to allow self-assembly.

Buffer exchange was performed using Slide-A-Lyzer™ 2,5 K MWCO Mini dialysis cups (ThermoFisher, 88403). Per 100 µL LNP, 1 L of buffer was used for dialysis over 18 hours.

Aggregate removal was performed by centrifugation at 20'000 g for 1 hour at room temperature and separation of aggregate pellet and supernatant containing the LNPs.

Additional concentration of the sample may be required, as the maximum mixing concentration within this set-up was 0.2 mg/mL. In this case, the LNP was dialysed into water (to avoid accumulation of salts) and the excess water was removed through vacuum evaporation at room temperature in an Eppendorf® centrifugal vacuum concentrator.

A.1.5. LNP Characterization

DLS

Dynamic light scattering was performed on the DynaPro® NanoStar™ (Wyatt) operating at 90° scattering angle. Disposable COC cuvettes were used with a sample volume of 10 µL. The measurement set-up is depicted in **Fig. A.2**

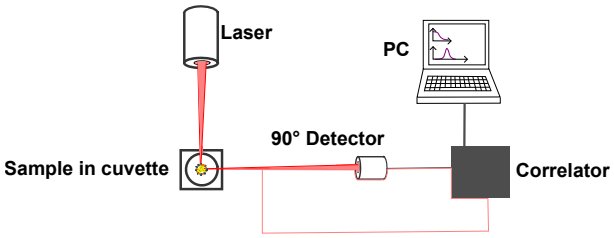

Figure A.2.: DLS Set-up: Laser is emitting light onto the sample in a microcuvette. Scattered light at 90° is collected and correlated for analysis.

UV/Vis Spectroscopy

To determine RNA concentration, absorbance at 260 nm (A_{260} was measured with the Nanodrop™ (ThermoFisher Scientific) was used [310]. Light from a xenon flash lamp was focused on the sample through an optical fiber. The sample droplet (2 µL) was placed between two optical fibers with a short and defined wavelength. A CCD detector collected the light after the sample, allowing to analyse the spectrum. The absorption at 260 nm was then directly calculated based on the Beer-Lambert law, predicting a linear correlation between absorbance and sample concentration:

$$A = \epsilon * c * I \tag{A.5}$$

with the absorbance A, the concentration c and the extinction coefficient ϵ.

Encapsulation Efficiency of Lipid Nanoparticles

To measure, which percentage of RNA is encapsulated in a lipid nanoparticle, an adapted protocol of the Quant-it™ RiboGreen RNA Assay was acquired. The RiboGreen reagent (Invitrogen) is an intercalating fluorescent dye. Binding to RNA increases it's fluorescence at 525 nm more then 1000-fold. As the dye can only bind to free mRNA, i.e. RNA that is not encapsulated within an LNP, it can be used to determine the ratio of free and total mRNA. To measure the free mRNA, the LNP was diluted to a concentration between 1 an 10 µg/mL. The dye was diluted 1:100 in TE-buffer and added to the LNP. To measure the

total amount of mRNA (free and encapsulated) at the same time, a sample of the same LNP is treated 1:1 with detergent (here, 2 % (v/v) Triton-X-100 (Roth)) for 15 minutes at 70°C and subsequently also mixed with the 1:100 dilution of dye. This completely de-complexes the LNP, allowing the RiboGreen dye to bind to the mRNA. Fluorescence readout was typically performed in a plate reader (Tecan Infinite Pro 200 M-Plex) in a black, flat bottom 96-well plate (Greiner). Fluorescence was measured in from the top with an excitation wavelength of 480 nm (bandwidth 9 nm) and emission was measured at 520 nm (bandwidth 20 nm). The encapsulation efficiency was then calculated as following:

$$EE = 1 - \frac{I_{LNP} - I_{blank}}{I_{LNP+detergent} - I_{blank+detergent}} \tag{A.6}$$

with the fluorescence intensities of the LNP alone (I_{LNP}) or treated with detergent mix ($I_{LNP+detergent}$). To account for background fluorescence, a blank with the corresponding buffers was measured.

Fluorecence Correlation Spectroscopy

FCS was performed using the LSM980 (Zeiss) confocal microscope. Sample was analyzed in a black 384-well plates with transparent bottom (Greiner, P8803-384) with a 60x magnification water-immersion objective (NA > 0.9, Plan-Apochromat: 420662-9970). Optimal measurement concentration for an LNP encapsulating EZ Cap™ Cy5 GFP mRNA (APExBIO, R1011) was determined to be at 1 µg/mL mRNA concentration. A schematic overview with the basic components is provided in **Fig. A.3**. Fluorescence intensity was captured using a GaAs detector. Aquisition was performed with the Zeiss Zen-blue software add-on *Counting and FCS*.

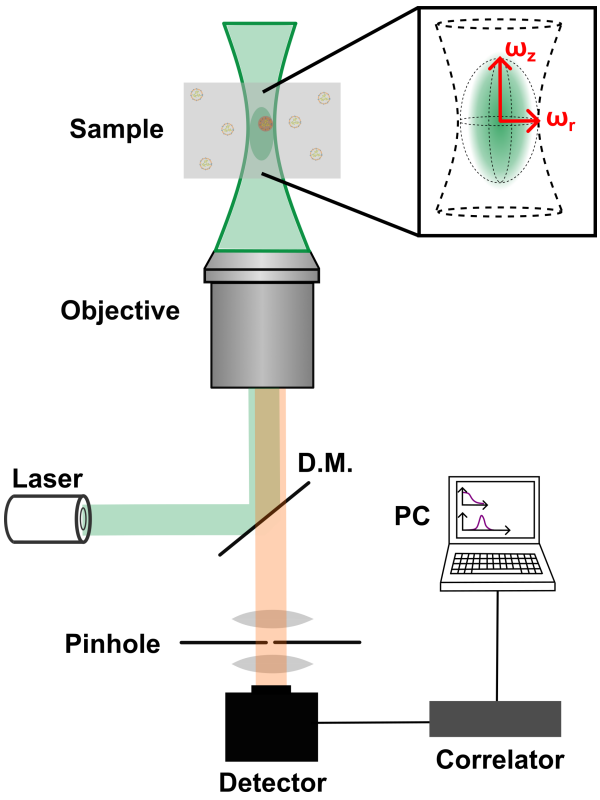

Figure A.3.: Basic optical setup for fluorescence correlation spectroscopy: With laser, dichroic mirror, objective, sample, lenses, pinhole, detector and correlator. Inset shows zoom on confocal and effective detection volume (green). Adapted from [311].

A.1.6. Micropatterning Techniques

Additive Approach

The additive single-cell pattern was prepared using a photo-induced $CuSO_4$ click reaction to selectively bind the cell-adhesive peptide cyclo-Arg-Gly-Asp (RGD) to a cell-repellent poly(vinyl alcohol) (PVA) surface. Hence, each channel of a bio-inert, PVA-coated µ-slide (ibidi, #80600) was filled with 33 µL of a 5 mM Diazirin (Enamine) solution in 10 % (v/v) DMSO (Thermofisher Scientific, #D12345). The slide was then exposed to UV light using an in-house built UV illumination lamp (Rapp, 365 nm) that allows even illumination over a 10 x 10 cm area. A silica-wafer-based photomask with 20 µm x 20 µm squares and 85 µm spacers was employed to achieve selective illumination. After a washing step 3 mL with MilliQ water per channel, a click reaction solution containing 10 mM BTTA (JenaBioscience, CLK-067-25), 2 mM CuSO4 (JenaBioscience, CLK-MI005), 0.1 mM cyclo-RGD-azide (Lumiprobe, A1330), and 100 mM vitamin C (JenaBioscience, CLK-MI005) in sodium phosphate buffer (JenaBioscience, #CLK-073) was applied and incubated for 1 hour at room temperature. Following incubation, the click reaction mix-

ture was removed, and the slide was washed several times with phosphate-buffered saline (PBS, Biochrom GmbH #L182). For schematic workflow, see **Fig. 2.6a**

Subtractive Approach

Here, single-cell microarrays were fabricated using the same 6-channel microscope slides coated with poly(vinyl alcohol) (PVA) as before (ibidi, #80600). A mixture of 100 mM PLPP (Enamine) and 2 % (w/v) super low-melt agarose (Roth, HP45.1) was prepared, and calcium peroxide was added to achieve a final concentration of 10 % (w/v) in ultra pure water (ThermoFisher, 1305-79-9). This solution was pipetted into the channels of the slide, which was then selectively exposed to 365 nm UV light as shown described before. The silica photomask, featuring 20 µm x 20 µm squares with 85 µm spacing, was used for illumination. After the UV exposure, the PLPP mixture was removed by repeatedly flushing the channels with MilliQ water. To eliminate any remaining agarose residues, the channels were further rinsed with 0.5 M HCl. The channels were then dried and sterilized through UV exposure for 20 minutes. For protein coating, as illustrated in the bottom row of Supplementary Figure Micropattern, the channels were pre-treated with PBS prior to the application of the desired protein in PBS. Unless otherwise specified, 20 µg/mL Laminin (BioLamina, 524 LN) was utilized. For illustration of the process, check **Fig. 2.6b**.

A.1.7. Single-cell Transfection Assay

To study protein expression, cells were cleaved as described above and seeded onto the micropatterns. Prior to cell seeding, the pattern was washed with 3 x 1 mL PBS and then primed with 2x150µL cell culture medium. For each cell-type and micropatterning approach, an optimal cell-density was determined according to **Table A.2**. To avoid cell-clutting, cell solution was transferred 5 times from the back to the front channel and mixed with the pipette. To allow self-assembly of the cells on the pattern, cells were then incubated for 45 min up to 2 hours, dependent on the cell type and pattern, until the first cells visibly flattened on the surface. The pattern was then gently washed with either OptiMEM in case of Lipofectamine transfections or cell culture medium in case of LNP transfections. This step was repeated again, one hour later.
mRNAs were typically transfected with 50 ng per channel in 50 µL, i.e. at a concentration of 1 ng/µL. For LNP transfections, LNPs (mixed as described previously) were pre-incubated in 10 % FCS for 45 minutes if not stated differently. L2000 was prepared according to the manufacturers protocol. A standard mixing protocol for an L2000 transfection would be:

Cell line	Photopattern (Bottom-up)	PVA removal (Top-down)
A549	$1*10^6$ cells/mL in 25 µL	$5*10^5$ cells/mL in 50 µL
HuH7	$5*10^5$ cells/mL in 25 µL	$5*10^5$ cells/mL in 50 µL
HEK293	$5*10^5$ cells/mL in 25 µL	$5*10^5$ cells/mL in 50 µL

Table A.2.: Cell type and micropattern specific cell densities

1. 0.25 µL L2000 + 49.75 µL OptiMEM, incubate 5 min at RT
2. 1 µL mRNA (at 0.1 µg/µL stock concentration) + 49 µL OptiMEM

Mix 50 µL solution (2) onto 50 µL solution (1) and incubate for 20 minutes at room temperature (RT).

For cell transfection, 50 µL of the transfection mix was applied to each channel and mixed three times. Cells were then incubated 45 min at 37°C for a standard transfection and subsequently washed with 2 x 150 µL L15 medium without phenol red (Gibco™, ThermoFisher Scientific, 21083027).

A.1.8. Live-cell Microscopy

Time-lapse microscopy was performed on an epifluorescent microscope. Here, an inverted Nikon Eclipse Ti microscope with a 10x objective was used. Physiologic conditions were created with an Okolabs incubation chamber. Each channel was scanned with up to 14 fields of view every 10 min up to 72 hours. For later cell segmentation, every experiment recorded bright field images. Additionally, fluorescence excitation was performed with an LED using combinations of the filters listed in **Table A.3**.

Filter	Excitation	Bandwidth	Emission	Bandwidth	Cat-no
GFP	470 nm	40 nm	525 nm	50 nm	AHF F46-002
dsRed	545 nm	30 nm	620 nm	60 nm	AHF F46-005
Cy5	628 nm	40 nm	692 nm	20 nm	AHF F36-523

Table A.3.: Filters used for fluorescence time-lapse imaging

A.1.9. Fluorescence Calibration

In fluorescence microscopy experiments, gray values are measured. For quantitative analysis, the calibration factor from gray value to GFP may be required. Therefore, purified

GFP protein was filled into polydimethylsiloxane (PDMS) calibration chips with defined channel heights (**Fig. A.4**). Channel height was low enough to be captured within one focus plane. Therefore, gray values per GFP molecule could be determined.

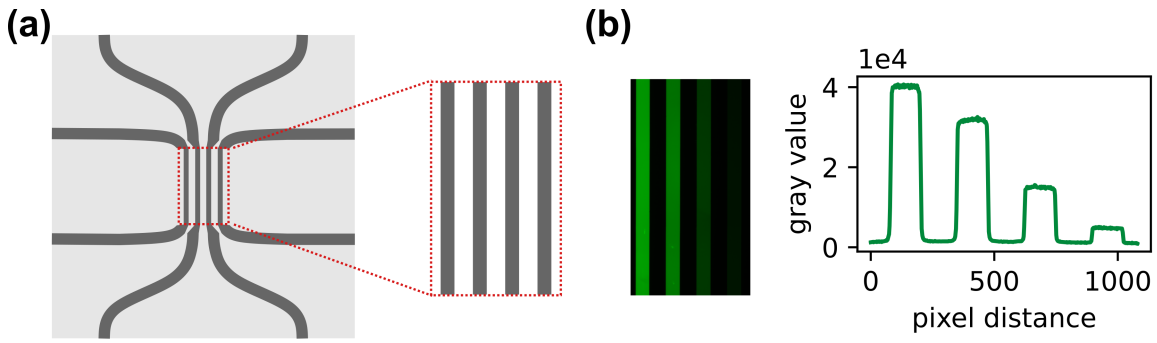

Figure A.4.: Calibration of fluorescence experiments: (a) Schematic representation of the calibration chip that was molded with PBS from an inverted silica wafer. Channels had a defined height of 17 µm. (b) Exemplary image with calibration chip filled with GFP in PBS at known concentrations. Grey values were measured to calculate back to gray value per GFP molecule.

A.1.10. Data Analysis

LISCA experiments performed in this work yielded data stored in *.nd2* file format. An in-house developed Python script was developed to export time-stacks for each field of view and channel as *.npz* file, which was then used to performed binarization and tracking of cells. Additionally, fluorescence channels were background corrected according to Schwarzfischer *et al.*.

As segmentation could also yield traces for double-occupied spots, dividing cells or dead cells, manual control of selections was performed with the PyAMA software, also available on GitHub [192]. If required, square ROIs were generated. Cell tracks together with fluorescence intensities of ROIs was saved as *.csv* file for further analysis.

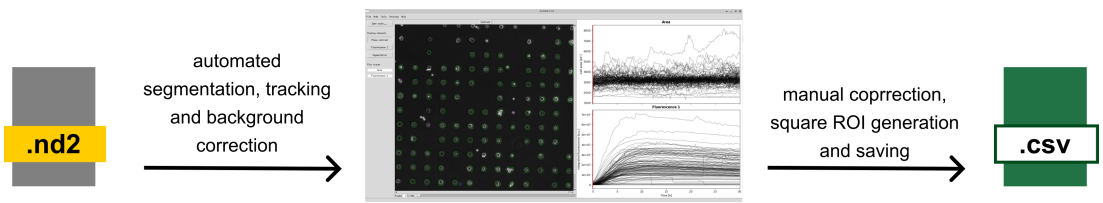

Figure A.5.: PyAMA data analysis pipeline

A.1.11. Data Fitting

Single-cell fluorescence trajectories were fitted to the three stage maturation model with a non-linear least square approach. Therefore, an automated python script was utilized [312].

Julia Simulations

Julia simulations were performed using the Package Catalyst.jl [313]. Kinetic equations were implemented as first-order reactions. Parameter estimations based on previous literature [47, 92] if not stated otherwise. The RodaS5P solver was used to solve the reactions.

A.2. Supplementary Figures

A.2.1. LNP characterization monitoring during protein adsorption

Transfection of cells with LNPs included dialysis after microfluidic mixing together with protein pre-incubation to allow formation of the protein corona. Therefore, hydrodynamic radius was determined after incubation with BSA and FCS through DLS. Results showed no changes in LNP size after incubation with different serum concentrations except for an outlier for the lowest BSA concentration (**Fig. A.6**

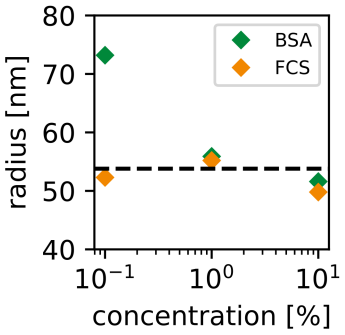

Figure A.6.: LNP size upon incubation with proteins: (a) Hydrodynamic radius (DLS measurement) was determined.

A.2.2. Mapping of Seed Binding on the ORF

In chapter 5.5, the interference of ribosomes and translation with RISC was investigated. As siRNA binding starts with scanning of the ORF for basepairing regions not of the full siRNA but with a seed region. This seed region is only a few nucleotides long. Therefore, in **Fig. A.7**, complementary sequences to the first three to eight nucleotides of both siRNA was mapped.

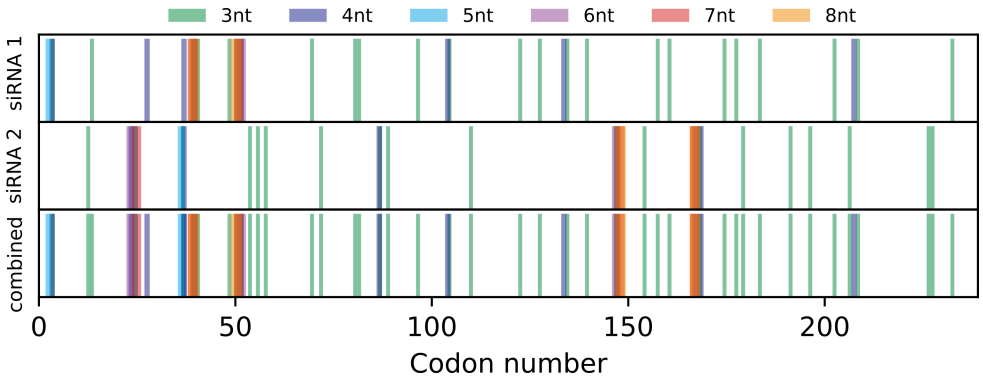

Figure A.7.: Seed binding regions on the ORF: Seed binding of the siRNA for different seed lengths (see legend) were mapped for siRNA 1 and 2 along the ORF. Bottom images shows overlay with increased density in the 5' end of the ORF

A.2.3. Quantal delivery of RNA-LNPs

At low mRNA transfection concentrations, only few cells showed protein expression. We assume that in this regime, quantal delivery, as shown in **Fig A.8**, can be observed.

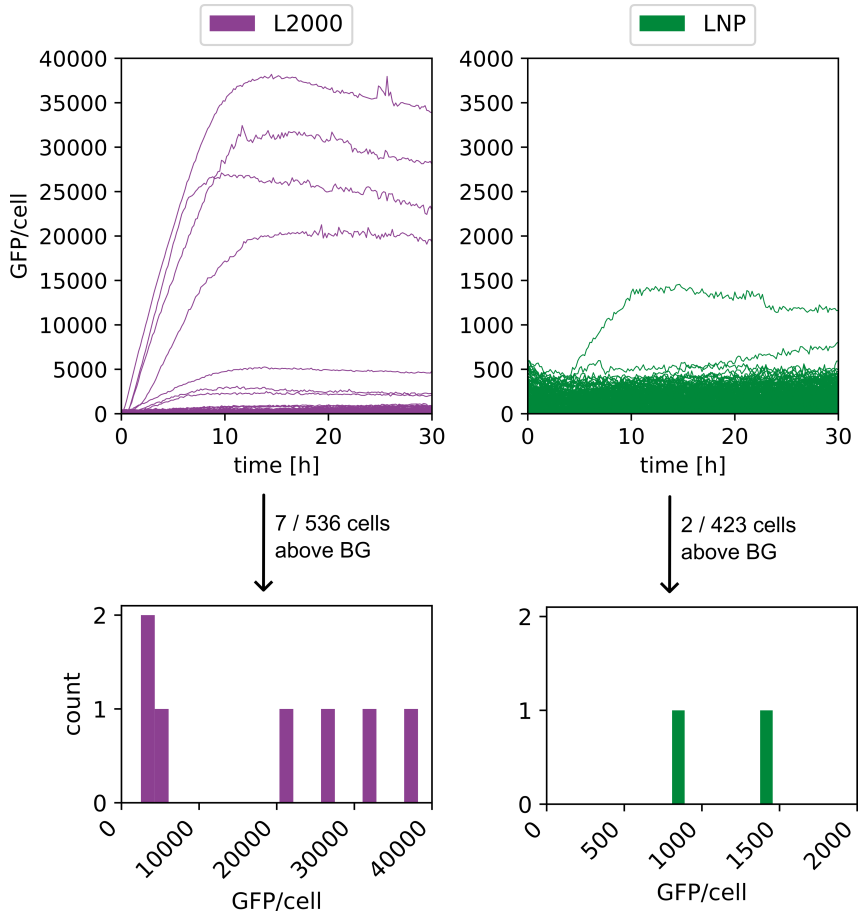

Figure A.8.: Quantal delivery of mRNA: At low concentrations, quantal delivery is observed: Top: Exemplary traces of a transfection experiment with 2 pg/µL mRNA encapsulated with either Lipofectamine2000 (L2000, purple) or a lipid nanoparticle (LNP, green). Only a low number of the totally observed cells showed protein expression above background level as indicated at the arrows. Plotting of the levels shows signs of quantal delivery.

A.3. Further Approaches

A collection of short descriptions of the approaches that were considered within the time period of this thesis but did not work within a proof of concept study.

A.3.1. Influence of LNP Composition on GFP Expression

Amongst other investigations, the influence of PEG content (and therefore LNP size) [74], the type of PEG lipid anchor and the preparation method was investigated. As this was only a proof of concept experiment, the data presented here arises from transfections in a 96-well plate and fluorescence was recorded with the Tecan plate reader. In **Fig. A.9a**, different molar ratios of PEG were prepared. To maintain total lipid ratio, the amount of cholesterol was adjusted accordingly. An inverse correlation of protein expression with

PEG content was observed here. Further, replacing DSPE-PEG2k with DMG-PEG2k (having a smaller anchor) led to increased transfection efficiency (**Fig. A.9b**). This may improve the exchange with proteins to form the protein corona and destabilize the particle towards favoured endosomal escape.
Also the mixing method was found be relevant, as the more controlled microfluidic mixing resulted in overall higher protein levels (**Fig. A.9c**), probably related to the more uniform size distribution and avoiding of aggregations.

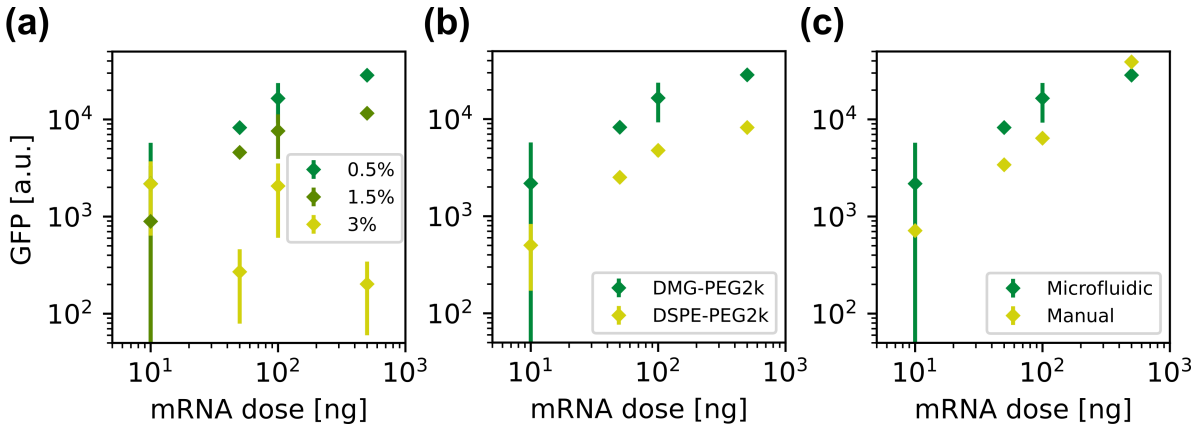

Figure A.9.: Plate reader experiment to investigate various LNP parameters on their influence on protein expression: Data shows GFP fluorescence of HuH7 cells 24 after transfection in a 96-well plate. (a) GFP expression for standard LNP with varying PEG content or (b) different types of PEG-lipid anchor or (c) preparation methods. Data shows mean of three replicates with standard deviation.

A.3.2. Expression Kinetics of Simple Codon Optimization Approaches

When we first started to investigate codon optimization, we aimed to study the impacts on several approaches on the protein expression kinetics. The unmutated GFP construct [182] was measured as positive control, a point mutation leading to a frame shift was induced as negative control (see figure A.10a first and last graph). As the GFP sequence is already fully optimized for maximal expression levels, we used a human wild-type GFP (hm-wt) sequence and tested full codon optimization based on OCTOPOS [275]. Further, we designed the UU/UA reduced construct as suggested by Al-Saif and Khabar in 2021 [244]. Lastly, we inserted a de-optimized codon window towards the end of the ORF to test the effect of ribosome jams on translation kinetics. Single cell traces of those constructs after Lipofectamine transfection in A549 cells are shown in figure A.10a. For a better comparison, mean traces are summarized in figure A.10b and mean plateau levels are shown in figure A.10c.

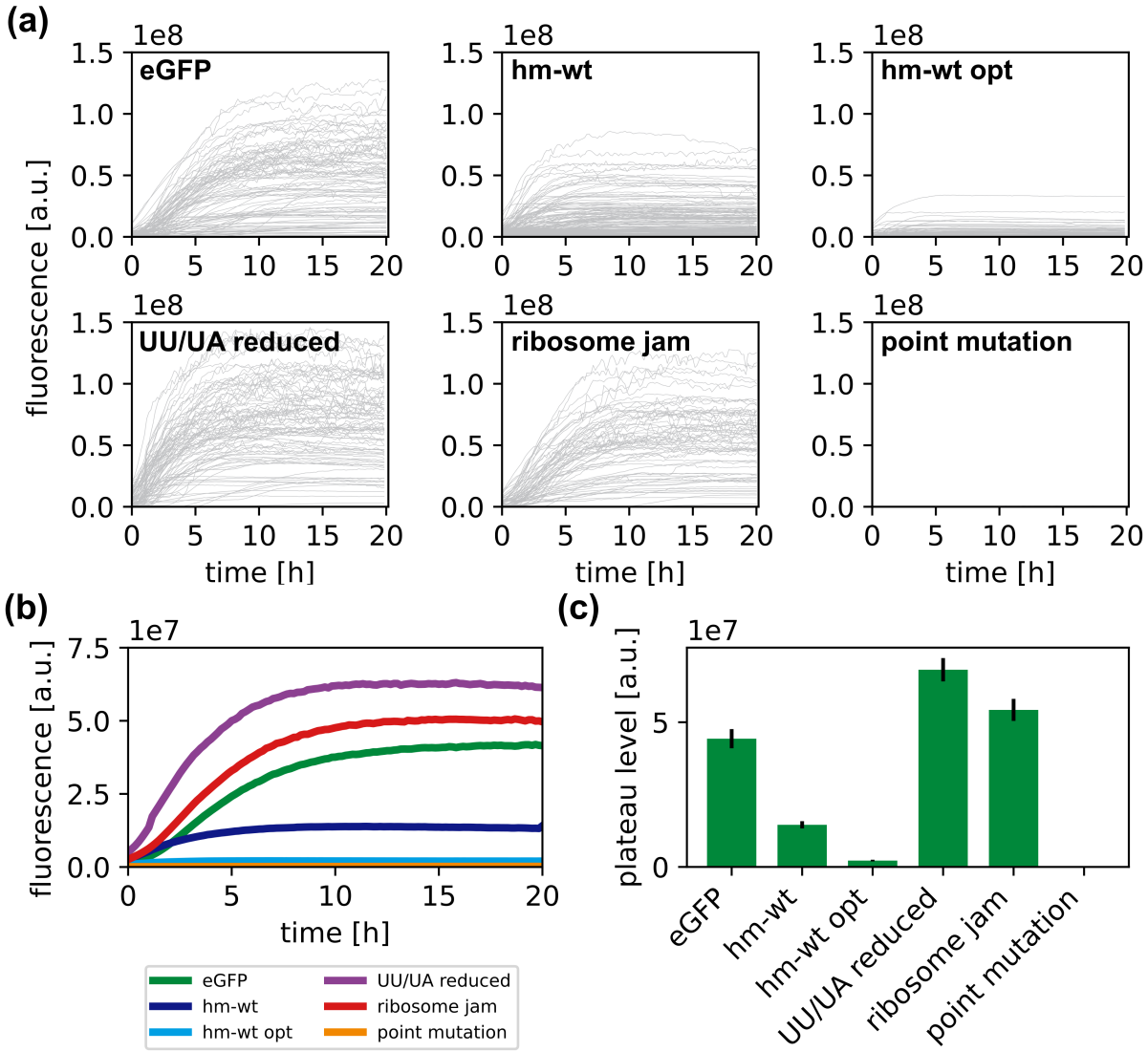

Figure A.10.: Initial Data from Codon optimization project: (a) Single cell traces of all tested conditions as indicated on the graphs. A549 cells were transfected with Lipofectamine and an mRNA dose of 1ng/µL. (b) Mean traces and (c) plateau expression level show high fluorescence levels for GFP, UU/UA reduced and ribosome jam construct, lower but still detectable levels for hm-wt and hm-wt optimized construct and no fluorescence for the point mutation construct. Bars show mean plateau level over every single cell trace with standard error of the mean.

We intuitively expected a higher expression level for the human wild-type optimized construct compared to the human wild-type construct that was not optimized. However, we found a clearly reduced expression level. This shows, that codon optimization is not a straight forward process. We hypothesized that the reduced expression level is related to protein miss-folding, as reported previously [263][269][232] resulting in reduced or no fluorescence. As the LISCA approach relies on correct protein folding and fluorescence,

protein miss-folding leads to a false-negative measurement.
The UU/UA reduced sequence showed an expression level, that was even higher than the one measured for GFP. But, analyzing the sequence reported in the original publication revealed, that the UU/UA content was not reduced at all and the changes that were made were not completely clear to us. Therefore, although this increase in fluorescence was interesting, we decided to not investigate here.
The ribosme jam construct was found to show a comparable output as the unmutated GFP sequence. We hypothesized that this was related to the ribosome jam towards the end of the construct. So we continued research on the position dependence of slow codon patches and interference with siRNA binding sites as described in the main text.

A.4. RNA sequences

siRNA 1 (Dharmacon, GFP Duplex I siRNA):
Target sequence: `GCAAGCUGACCCUGAAGUUC`

siRNA 2 (Dharmacon, custom production)
Target sequence: `GCCACAACGUCUAUAUCAUUUU`

For **CayRFP** refer to [311].

Slow codon Position 48

```
ATGGTGAGCAAGGGCGAGGAGCTGTTCACCGGGGTGGTGCCCATCCTGGTCGAGCTGGACGGCGACGTAAACG
GCCACAAGTTCAGCGTGTCCGGCGAGGGCGAGGGCGATGCCACCTACGGCAAGCTGACCCTGAAGTTCATATG
TACAACAGGGAAGCTACCGGTACCCTGGCCCACCCTCGTGACCACCCTGACCTACGGCGTGCAGTGCTTCAGC
CGCTACCCCGACCACATGAAGCAGCACGACTTCTTCAAGTCCGCCATGCCCGAAGGCTACGTCCAGGAGCGCA
CCATCTTCTTCAAGGACGACGGCAACTACAAGACCCGCGCCGAGGTGAAGTTCGAGGGCGACACCCTGGTGAA
CCGCATCGAGCTGAAGGGCATCGACTTCAAGGAGGACGGCAACATCCTGGGGCACAAGCTGGAGTACAACTAC
AACAGCCACAACGTCTATATCATGGCCGACAAGCAGAAGAACGGCATCAAGGTGAACTTCAAGATCCGCCACA
ACATCGAGGACGGCAGCGTGCAGCTCGCCGACCACTACCAGCAGAACACCCCCATCGGCGACGGCCCCGTGCT
GCTGCCCGACAACCACTACCTGAGCACCCAGTCCGCCCTGAGCAAAGACCCCAACGAGAAGCGCGATCACATG
GTCCTGCTGGAGTTCGTGACCGCCGCCGGGATCACTCTCGGCATGGACGAGCTGTACAAG
```

Slow codon Position 64

```
ATGGTGAGCAAGGGCGAGGAGCTGTTCACCGGGGTGGTGCCCATCCTGGTCGAGCTGGACGGCGACGTAAACG
GCCACAAGTTCAGCGTGTCCGGCGAGGGCGAGGGCGATGCCACCTACGGCAAGCTGACCCTGAAGTTCATCTG
```

CACCACCGGCAAGCTGCCCGTGCCCTGGCCCACCCTCGTGACCACCCTAACATACGGGGTACAATGTTTCTCG
CGGTACCCCGACCACATGAAGCAGCACGACTTCTTCAAGTCCGCCATGCCCGAAGGCTACGTCCAGGAGCGCA
CCATCTTCTTCAAGGACGACGGCAACTACAAGACCCGCGCCGAGGTGAAGTTCGAGGGCGACACCCTGGTGAA
CCGCATCGAGCTGAAGGGCATCGACTTCAAGGAGGACGGCAACATCCTGGGGCACAAGCTGGAGTACAACTAC
AACAGCCACAACGTCTATATCATGGCCGACAAGCAGAAGAACGGCATCAAGGTGAACTTCAAGATCCGCCACA
ACATCGAGGACGGCAGCGTGCAGCTCGCCGACCACTACCAGCAGAACACCCCCATCGGCGACGGCCCCGTGCT
GCTGCCCGACAACCACTACCTGAGCACCCAGTCCGCCCTGAGCAAAGACCCCAACGAGAAGCGCGATCACATG
GTCCTGCTGGAGTTCGTGACCGCCGCCGGGATCACTCTCGGCATGGACGAGCTGTACAAG

Slow codon Position 119

ATGGTGAGCAAGGGCGAGGAGCTGTTCACCGGGGTGGTGCCCATCCTGGTCGAGCTGGACGGCGACGTAAACG
GCCACAAGTTCAGCGTGTCCGGCGAGGGCGAGGGCGATGCCACCTACGGCAAGCTGACCCTGAAGTTCATCTG
CACCACCGGCAAGCTGCCCGTGCCCTGGCCCACCCTCGTGACCACCCTGACCTACGGCGTGCAGTGCTTCAGC
CGCTACCCCGACCACATGAAGCAGCACGACTTCTTCAAGTCCGCCATGCCCGAAGGCTACGTCCAGGAGCGCA
CCATCTTCTTCAAGGACGACGGCAACTACAAGACCCGCGCCGAGGTGAAGTTCGAGGGCGACACCCTAGTAAA
CCGGATAGAGCTAAAGGGGATAGACTTCAAGGAGGACGGCAACATCCTGGGGCACAAGCTGGAGTACAACTAC
AACAGCCACAACGTCTATATCATGGCCGACAAGCAGAAGAACGGCATCAAGGTGAACTTCAAGATCCGCCACA
ACATCGAGGACGGCAGCGTGCAGCTCGCCGACCACTACCAGCAGAACACCCCCATCGGCGACGGCCCCGTGCT
GCTGCCCGACAACCACTACCTGAGCACCCAGTCCGCCCTGAGCAAAGACCCCAACGAGAAGCGCGATCACATG
GTCCTGCTGGAGTTCGTGACCGCCGCCGGGATCACTCTCGGCATGGACGAGCTGTACAAG

Slow codon Position 187

ATGGTGAGCAAGGGCGAGGAGCTGTTCACCGGGGTGGTGCCCATCCTGGTCGAGCTGGACGGCGACGTAAACG
GCCACAAGTTCAGCGTGTCCGGCGAGGGCGAGGGCGATGCCACCTACGGCAAGCTGACCCTGAAGTTCATCTG
CACCACCGGCAAGCTGCCCGTGCCCTGGCCCACCCTCGTGACCACCCTGACCTACGGCGTGCAGTGCTTCAGC
CGCTACCCCGACCACATGAAGCAGCACGACTTCTTCAAGTCCGCCATGCCCGAAGGCTACGTCCAGGAGCGCA
CCATCTTCTTCAAGGACGACGGCAACTACAAGACCCGCGCCGAGGTGAAGTTCGAGGGCGACACCCTGGTGAA
CCGCATCGAGCTGAAGGGCATCGACTTCAAGGAGGACGGCAACATCCTGGGGCACAAGCTGGAGTACAACTAC
AACAGCCACAACGTCTATATCATGGCCGACAAGCAGAAGAACGGCATCAAGGTGAACTTCAAGATCCGCCACA
ACATCGAGGACGGCAGCGTGCAGCTCGCCGACCACTACCAGCAGAACACCCCGATAGGGGATGGGCCGGTACT
ACTACCGGACAACCACTACCTGAGCACCCAGTCCGCCCTGAGCAAAGACCCCAACGAGAAGCGCGATCACATG
GTCCTGCTGGAGTTCGTGACCGCCGCCGGGATCACTCTCGGCATGGACGAGCTGTACAAG

Slow codon Position 229

ATGGTGAGCAAGGGCGAGGAGCTGTTCACCGGGGTGGTGCCCATCCTGGTCGAGCTGGACGGCGACGTAAACG
GCCACAAGTTCAGCGTGTCCGGCGAGGGCGAGGGCGATGCCACCTACGGCAAGCTGACCCTGAAGTTCATCTG
CACCACCGGCAAGCTGCCCGTGCCCTGGCCCACCCTCGTGACCACCCTGACCTACGGCGTGCAGTGCTTCAGC

CGCTACCCCGATCATATGAAGCAACATGATTTCTTCAAGTCCGCCATGCCCGAAGGCTACGTCCAGGAGCGCA
CCATCTTCTTCAAGGACGACGGCAACTACAAGACCCGCGCCGAGGTGAAGTTCGAGGGCGACACCCTGGTGAA
CCGCATCGAGCTGAAGGGCATCGACTTCAAGGAGGACGGCAACATCCTGGGGCACAAGCTGGAGTACAACTAC
AACAGCCACAACGTCTATATCATGGCCGACAAGCAGAAGAACGGCATCAAGGTGAACTTCAAGATCCGCCACA
ACATCGAGGACGGCAGCGTGCAGCTCGCCGACCACTACCAGCAGAACACCCCCATCGGCGACGGCCCCGTGCT
GCTGCCCGACAACCACTACCTGAGCACCCAGTCCGCCCTGAGCAAAGACCCCAACGAGAAGCGCGATCACATG
GTCCTGCTGGAGTTCGTGACCGCCGCCGGGATCACTCTCGGCATGGACGAGCTGTACAAG

List of Figures

List of Tables

B. Abbreviations

ACF	auto-correlation function
Ago2	argonaute protein 2
ApoE	apolipoprotein E
ARCA	anti-reverse cap analog
CAR-T	chimeric antigen receptor T-cell
CayRFP	cayenne red fluorescence protein
CME	clathrin-mediated endocytosis
COSEM	codon-specific elongation model
CoV	coefficient of variation
cRGD	cyclo-Arg-Gly-Asp
CryoTEM	cryogenic transmission electron cryomicroscopy
Cy3	cyanine 3
Cy5	cyanine 5
DLS	dynamic light scattering
DNA	desoxy ribonucleic acid
DODAP	1,2-dioleoyl-3-dimethylammonium propane
ECM	extracellular matrix
EMT	epithelial-mesenchymal transition
FCS	fetal calf serum
GFP	green fluorescent protein
FFL	feed-forward loop
icFFL	incoherent feed-forward loop
IVT	*in vito* transcription
L2000	Lipofectamine^{TM} 2000, Invitrogen^{TM}

LISCA live-cell imaging on single-cell arrays

LNP lipid nanoparticle

MAD median absolute deviation

MC3 DLin-MC3-DMA

miRNA micro RNA

mRNA messenger ribonucleic acid

NAR negative autoregulation

NGD no-go decay

N/P nitrogen to phosphate

OCTOPOS optimized codon translation for protein synthesis

ODE ordinary differential equation

ORF open reading frame

PAR positive autoregulation

PBAE poly(ß-Aminoesters)

PC phosphatidylcholine

PdI polydispersity index

PDMS polydimethylsiloxane

pDNA plasmid DNA

PEG polyethylene glycol

PEI polyethyleneamine

PKR protein kinase R

PVA poly(vinyl alcohol)

PyAMA python-based automated microscopy analysis

RISC RNA-induced silencing complex

RNAi RNA interference

ROI region of interest

RT room temperature

SAXS small angle X-ray scattering

sgRNA single guide RNA

siRNA	small interferring RNA
TE	transfection efficiency
TFF	tangential flow filtration
tRNA	transfer RNA
µPiPP	microscale plasma-initiated protein patterning
UTR	untranslated region

Bibliography

[1] Fernando P. Polack, Stephen J. Thomas, Nicholas Kitchin, Judith Absalon, Alejandra Gurtman, Stephen Lockhart, John L. Perez, Gonzalo Pérez Marc, Edson D. Moreira, Cristiano Zerbini, Ruth Bailey, Kena A. Swanson, Satrajit Roychoudhury, Kenneth Koury, Ping Li, Warren V. Kalina, David Cooper, Robert W. Frenck, Laura L. Hammitt, Özlem Türeci, Haylene Nell, Axel Schaefer, Serhat Ünal, Dina B. Tresnan, Susan Mather, Philip R. Dormitzer, Uğur Şahin, Kathrin U. Jansen, and William C. Gruber. "Safety and Efficacy of the BNT162b2 mRNA Covid-19 Vaccine". en. In: *New England Journal of Medicine* 383.27 (Dec. 2020), pp. 2603–2615. ISSN: 0028-4793, 1533-4406. DOI: 10.1056/NEJMoa2034577. URL: http://www.nejm.org/doi/10.1056/NEJMoa2034577 (visited on 10/04/2024).

[2] Ugur Sahin, Katalin Karikó, and Özlem Türeci. "mRNA-based therapeutics — developing a new class of drugs". en. In: *Nature Reviews Drug Discovery* 13.10 (Oct. 2014), pp. 759–780. ISSN: 1474-1776, 1474-1784. DOI: 10.1038/nrd4278. URL: https://www.nature.com/articles/nrd4278 (visited on 01/22/2024).

[3] Luis A. Rojas, Zachary Sethna, Kevin C. Soares, Cristina Olcese, Nan Pang, Erin Patterson, Jayon Lihm, Nicholas Ceglia, Pablo Guasp, Alexander Chu, Rebecca Yu, Adrienne Kaya Chandra, Theresa Waters, Jennifer Ruan, Masataka Amisaki, Abderezak Zebboudj, Zagaa Odgerel, George Payne, Evelyna Derhovanessian, Felicitas Müller, Ina Rhee, Mahesh Yadav, Anton Dobrin, Michel Sadelain, Marta Łuksza, Noah Cohen, Laura Tang, Olca Basturk, Mithat Gönen, Seth Katz, Richard Kinh Do, Andrew S. Epstein, Parisa Momtaz, Wungki Park, Ryan Sugarman, Anna M. Varghese, Elizabeth Won, Avni Desai, Alice C. Wei, Michael I. D'Angelica, T. Peter Kingham, Ira Mellman, Taha Merghoub, Jedd D. Wolchok, Ugur Sahin, Özlem Türeci, Benjamin D. Greenbaum, William R. Jarnagin, Jeffrey Drebin, Eileen M. O'Reilly, and Vinod P. Balachandran. "Personalized RNA neoantigen vaccines stimulate T cells in pancreatic cancer". en. In: *Nature* 618.7963 (June 2023), pp. 144–150. ISSN: 0028-0836, 1476-4687. DOI: 10.1038/s41586-023-06063-y. URL: https://www.nature.com/articles/s41586-023-06063-y (visited on 10/04/2024).

[4] Norbert Pardi, Michael J. Hogan, Frederick W. Porter, and Drew Weissman. "mRNA vaccines — a new era in vaccinology". en. In: *Nature Reviews Drug Discovery* 17.4 (Apr. 2018), pp. 261–279. ISSN: 1474-1776, 1474-1784. DOI: 10.1038/nrd.2017.243. URL: https://www.nature.com/articles/nrd.2017.243 (visited on 10/06/2024).

[5] Jayesh A. Kulkarni, Dominik Witzigmann, Sam Chen, Pieter R. Cullis, and Roy Van Der Meel. "Lipid Nanoparticle Technology for Clinical Translation of siRNA Therapeutics". en. In: *Accounts of Chemical Research* 52.9 (Sept. 2019), pp. 2435–2444. ISSN: 0001-4842, 1520-4898. DOI: 10.1021/acs.accounts.9b00368. URL: https://pubs.acs.org/doi/10.1021/acs.accounts.9b00368 (visited on 10/17/2024).

[6] Jason B Miller, Shuyuan Zhang, Petra Kos, Hu Xiong, Kejin Zhou, Sofya S Perelman, Hao Zhu, and Daniel J Siegwart. "Non-viral CRISPR/Cas gene editing in vitro and in vivo enabled by synthetic nanoparticle co-delivery of Cas9 mRNA and sgRNA". en. In: (2018).

[7] Daniel Rosenblum, Anna Gutkin, Ranit Kedmi, Srinivas Ramishetti, Nuphar Veiga, Ashley M. Jacobi, Mollie S. Schubert, Dinorah Friedmann-Morvinski, Zvi R. Cohen, Mark A. Behlke, Judy Lieberman, and Dan Peer. "CRISPR-Cas9 genome editing using targeted lipid nanoparticles for cancer therapy". en. In: *Science Advances* 6.47 (Nov. 2020), eabc9450. ISSN: 2375-2548. DOI: 10.1126/sciadv.abc9450. URL: https://www.science.org/doi/10.1126/sciadv.abc9450 (visited on 10/20/2023).

[8] Peter B. Dykstra, Matias Kaplan, and Christina D. Smolke. "Engineering synthetic RNA devices for cell control". en. In: *Nature Reviews Genetics* 23.4 (Apr. 2022), pp. 215–228. ISSN: 1471-0056, 1471-0064. DOI: 10.1038/s41576-021-00436-7. URL: https://www.nature.com/articles/s41576-021-00436-7 (visited on 10/06/2024).

[9] Yueyi Li, Anibal Arce, Tyler Lucci, Rebecca A. Rasmussen, and Julius B. Lucks. "Dynamic RNA synthetic biology: new principles, practices and potential". en. In: *RNA Biology* 20.1 (Dec. 2023), pp. 817–829. ISSN: 1547-6286, 1555-8584. DOI: 10.1080/15476286.2023.2269508. URL: https://www.tandfonline.com/doi/full/10.1080/15476286.2023.2269508 (visited on 10/06/2024).

[10] James Chappell, Kyle E Watters, Melissa K Takahashi, and Julius B Lucks. "A renaissance in RNA synthetic biology: new mechanisms, applications and tools for the future". en. In: *Current Opinion in Chemical Biology* 28 (Oct. 2015), pp. 47–56. ISSN: 13675931. DOI: 10.1016/j.cbpa.2015.05.018. URL: https://linkinghub.elsevier.com/retrieve/pii/S1367593115000514 (visited on 10/06/2024).

[11] L. Porosk, J. Nebogatova, I. Gaidutšik, and Ü. Langel. "Endpoint and Kinetic Approaches for Assessing Transfection Efficacy in Mammalian Cell Culture". In: *Cell Penetrating Peptides. Methods in Molecular Biology.* 2383. Humana, New York. ISBN: 978-1-07-161752-6.

[12] Pieter R. Cullis and Michael J. Hope. "Lipid Nanoparticle Systems for Enabling Gene Therapies". en. In: *Molecular Therapy* 25.7 (July 2017), pp. 1467–1475. ISSN: 15250016. DOI: 10.1016/j.ymthe.2017.03.013. URL: https://linkinghub.elsevier.com/retrieve/pii/S1525001617301119 (visited on 10/20/2023).

[13] Xucheng Hou, Tal Zaks, Robert Langer, and Yizhou Dong. "Lipid nanoparticles for mRNA delivery". en. In: *Nature Reviews Materials* 6.12 (Aug. 2021), pp. 1078–1094. ISSN: 2058-8437. DOI: 10.1038/s41578-021-00358-0. URL: https://www.nature.com/articles/s41578-021-00358-0 (visited on 07/09/2023).

[14] Giuseppe Ronzitti, David-Alexandre Gross, and Federico Mingozzi. "Human Immune Responses to Adeno-Associated Virus (AAV) Vectors". en. In: *Frontiers in Immunology* 11 (Apr. 2020), p. 670. ISSN: 1664-3224. DOI: 10.3389/fimmu.2020.00670. URL: https://www.frontiersin.org/article/10.3389/fimmu.2020.00670/full (visited on 11/13/2023).

[15] Hui Zu and Danchen Gao. "Non-viral Vectors in Gene Therapy: Recent Development, Challenges, and Prospects". en. In: *The AAPS Journal* 23.4 (June 2021), p. 78. ISSN: 1550-7416. DOI: 10.1208/s12248-021-00608-7. URL: https://link.springer.com/10.1208/s12248-021-00608-7 (visited on 10/17/2024).

[16] Sumit Ghosh, Alex M. Brown, Chris Jenkins, and Katie Campbell. "Viral Vector Systems for Gene Therapy: A Comprehensive Literature Review of Progress and Biosafety Challenges". en. In: *Applied Biosafety* 25.1 (Mar. 2020), pp. 7–18. ISSN: 1535-6760, 2470-1246. DOI: 10.1177/1535676019899502. URL: https://www.liebertpub.com/doi/10.1177/1535676019899502 (visited on 10/17/2024).

[17] Erwin Schrödinger. *What Is Life? The Physical Aspect of the Living Cell*. English. Cambridge University Press, 1944. ISBN: 0-521-42708-8.

[18] Michael Elowitz and Wendell A. Lim. "Build life to understand it". en. In: *Nature* 468.7326 (Dec. 2010), pp. 889–890. ISSN: 0028-0836, 1476-4687. DOI: 10.1038/468889a. URL: https://www.nature.com/articles/468889a (visited on 10/03/2024).

[19] Ahmad S. Khalil and James J. Collins. "Synthetic biology: applications come of age". en. In: *Nature Reviews Genetics* 11.5 (May 2010), pp. 367–379. ISSN: 1471-0056, 1471-0064. DOI: 10.1038/nrg2775. URL: https://www.nature.com/articles/nrg2775 (visited on 10/03/2024).

[20] Thomas S. Ligon, Carolin Leonhardt, and Joachim O. Rädler. "Multi-Level Kinetic Model of mRNA Delivery via Transfection of Lipoplexes". en. In: *PLoS ONE* 9.9 (Sept. 2014). Ed. by Roeland M.H. Merks, e107148. ISSN: 1932-6203. DOI: 10.1371/journal.pone.0107148. URL: https://dx.plos.org/10.1371/journal.pone.0107148 (visited on 06/19/2023).

[21] Carolin Leonhardt, Gerlinde Schwake, Tobias R. Stögbauer, Susanne Rappl, Jan-Timm Kuhr, Thomas S. Ligon, and Joachim O. Rädler. "Single-cell mRNA transfection studies: Delivery, kinetics and statistics by numbers". en. In: *Nanomedicine: Nanotechnology, Biology and Medicine* 10.4 (May 2014), pp. 679–688. ISSN: 15499634. DOI: 10.1016/j.nano.2013.11.008. URL: https://linkinghub.elsevier.com/retrieve/pii/S1549963413006734 (visited on 06/19/2023).

[22] Valentina Francia, Raymond M. Schiffelers, Pieter R. Cullis, and Dominik Witzigmann. "The Biomolecular Corona of Lipid Nanoparticles for Gene Therapy". en. In: *Bioconjugate Chemistry* 31.9 (Sept. 2020), pp. 2046–2059. ISSN: 1043-1802, 1520-4812. DOI: 10.1021/acs.bioconjchem.0c00366. URL: https://pubs.acs.org/doi/10.1021/acs.bioconjchem.0c00366 (visited on 10/19/2023).

[23] Akin Akinc, William Querbes, Soma De, June Qin, Maria Frank-Kamenetsky, K. Narayanannair Jayaprakash, Muthusamy Jayaraman, Kallanthottathil G Rajeev, William L Cantley, J Robert Dorkin, James S Butler, LiuLiang Qin, Timothy Racie, Andrew Sprague, Eugenio Fava, Anja Zeigerer, Michael J Hope, Marino Zerial, Dinah Wy Sah, Kevin Fitzgerald, Mark A Tracy, Muthiah Manoharan, Victor Koteliansky, Antonin De Fougerolles, and Martin A Maier. "Targeted Delivery of RNAi Therapeutics With Endogenous and Exogenous Ligand-Based Mechanisms". en. In: *Molecular Therapy* 18.7 (July 2010), pp. 1357–1364. ISSN: 15250016. DOI: 10.1038/mt.2010.85. URL: https://linkinghub.elsevier.com/retrieve/pii/S1525001616310814 (visited on 06/21/2023).

[24] Nima Aliakbarinodehi, Audrey Gallud, Mokhtar Mapar, Emelie Wesén, Sahar Heydari, Yujia Jing, Gustav Emilsson, Kai Liu, Alan Sabirsh, Vladimir P. Zhdanov, Lennart Lindfors, Elin K. Esbjörner, and Fredrik Höök. "Interaction Kinetics of Individual mRNA-Containing Lipid Nanoparticles with an Endosomal Membrane Mimic: Dependence on pH, Protein Corona Formation, and Lipoprotein Depletion". en. In: *ACS Nano* 16.12 (Dec. 2022), pp. 20163–20173. ISSN: 1936-0851, 1936-086X. DOI: 10.1021/acsnano.2c04829. URL: https://pubs.acs.org/doi/10.1021/acsnano.2c04829 (visited on 06/21/2023).

[25] Lei Miao, Jiaqi Lin, Yuxuan Huang, Linxian Li, Derfogail Delcassian, Yifan Ge, Yunhua Shi, and Daniel G. Anderson. "Synergistic lipid compositions for albumin receptor mediated delivery of mRNA to the liver". en. In: *Nature Communications* 11.1 (May 2020), p. 2424. ISSN: 2041-1723. DOI: 10.1038/s41467-020-16248-y. URL: https://www.nature.com/articles/s41467-020-16248-y (visited on 07/11/2023).

[26] Joanna Rejman, Alessandra Bragonzi, and Massimo Conese. "Role of clathrin- and caveolae-mediated endocytosis in gene transfer mediated by lipo- and polyplexes". en. In: *Molecular Therapy* 12.3 (Sept. 2005), pp. 468–474. ISSN: 15250016. DOI: 10.1016/j.ymthe.2005.03.038. URL: https://linkinghub.elsevier.com/retrieve/pii/S1525001605001875 (visited on 09/13/2023).

[27] Sushmita Chatterjee, Edo Kon, Preeti Sharma, and Dan Peer. "Endosomal escape: A bottleneck for LNP-mediated therapeutics". en. In: *Proceedings of the National Academy of Sciences* 121.11 (Mar. 2024), e2307800120. ISSN: 0027-8424, 1091-6490. DOI: 10.1073/pnas.2307800120. URL: https://pnas.org/doi/10.1073/pnas.2307800120 (visited on 10/06/2024).

[28] Ludwig Von Bertalanffy. "The Theory of Open Systems in Physics and Biology". en. In: *Science* 111.2872 (Jan. 1950), pp. 23–29. ISSN: 0036-8075, 1095-9203. DOI: 10.1126/science.111.2872.23. URL: https://www.science.org/doi/10.1126/science.111.2872.23 (visited on 10/03/2024).

[29] Dale Muzzey and Alexander Van Oudenaarden. "Quantitative Time-Lapse Fluorescence Microscopy in Single Cells". en. In: *Annual Review of Cell and Developmental Biology* 25.1 (Nov. 2009), pp. 301–327. ISSN: 1081-0706, 1530-8995. DOI: 10.1146/annurev.cellbio.042308.113408. URL: https://www.annualreviews.org/doi/10.1146/annurev.cellbio.042308.113408 (visited on 10/03/2024).

[30] Anita Reiser, Daniel Woschée, Simon Maximilian Kempe, and J O Rädler. "Live-cell Imaging of Single-Cell Arrays (LISCA) - a Versatile Technique to Quantify Cellular Kinetics". In: *J Vis Exp* (2021). DOI: 10.3791/62025.

[31] S. Brenner, F. Jacob, and M. Meselson. "An Unstable Intermediate Carrying Information from Genes to Ribosomes for Protein Synthesis". en. In: *Nature* 190.4776 (May 1961), pp. 576–581. ISSN: 0028-0836, 1476-4687. DOI: 10.1038/190576a0. URL: https://www.nature.com/articles/190576a0 (visited on 10/18/2024).

[32] RamaRao Malla, Mundla Srilatha, Batoul Farran, and Ganji Purnachandra Nagaraju. "mRNA vaccines and their delivery strategies: A journey from infectious diseases to cancer". en. In: *Molecular Therapy* 32.1 (Jan. 2024), pp. 13–31. ISSN: 15250016. DOI: 10.1016/j.ymthe.2023.10.024. URL: https://linkinghub.elsevier.com/retrieve/pii/S1525001623006019 (visited on 08/28/2024).

[33] Namit Chaudhary, Drew Weissman, and Kathryn A. Whitehead. "mRNA vaccines for infectious diseases: principles, delivery and clinical translation". en. In: *Nature Reviews Drug Discovery* 20.11 (Nov. 2021), pp. 817–838. ISSN: 1474-1776, 1474-1784. DOI: 10.1038/s41573-021-00283-5. URL: https://www.nature.com/articles/s41573-021-00283-5 (visited on 09/06/2024).

[34] Michael S D Kormann, Günther Hasenpusch, Manish K Aneja, Gabriela Nica, Andreas W Flemmer, Susanne Herber-Jonat, Marceline Huppmann, Lauren E Mays, Marta Illenyi, Andrea Schams, Matthias Griese, Iris Bittmann, Rupert Handgretinger, Dominik Hartl, Joseph Rosenecker, and Carsten Rudolph. "Expression of therapeutic proteins after delivery of chemically modified mRNA in mice". en. In: *Nature Biotechnology* 29.2 (Feb. 2011), pp. 154–157. ISSN: 1087-0156, 1546-1696. DOI: 10.1038/nbt.1733. URL: https://www.nature.com/articles/nbt.1733 (visited on 09/06/2024).

[35] Katalin Karikó, Hiromi Muramatsu, Jason M Keller, and Drew Weissman. "Increased Erythropoiesis in Mice Injected With Submicrogram Quantities of Pseudouridine-containing mRNA Encoding Erythropoietin". en. In: *Molecular Therapy* 20.5 (May 2012), pp. 948–953. ISSN: 15250016. DOI: 10.1038/mt.2012.7. URL: https://linkinghub.elsevier.com/retrieve/pii/S1525001616319347 (visited on 09/06/2024).

[36] Lior Zangi, Kathy O Lui, Alexander Von Gise, Qing Ma, Wataru Ebina, Leon M Ptaszek, Daniela Später, Huansheng Xu, Mohammadsharif Tabebordbar, Rostic Gorbatov, Brena Sena, Matthias Nahrendorf, David M Briscoe, Ronald A Li, Amy J Wagers, Derrick J Rossi, William T Pu, and Kenneth R Chien. "Modified mRNA directs the fate of heart progenitor cells and induces vascular regeneration after myocardial infarction". en. In: *Nature Biotechnology* 31.10 (Oct. 2013), pp. 898–907. ISSN: 1087-0156, 1546-1696. DOI: 10.1038/nbt.2682. URL: https://www.nature.com/articles/nbt.2682 (visited on 09/06/2024).

[37] Juan A. Bernal. "RNA-Based Tools for Nuclear Reprogramming and Lineage-Conversion: Towards Clinical Applications". en. In: *Journal of Cardiovascular Translational Research* 6.6 (Dec. 2013), pp. 956–968. ISSN: 1937-5387, 1937-5395. DOI: 10.1007/s12265-013-9494-8. URL: http://link.springer.com/10.1007/s12265-013-9494-8 (visited on 10/18/2024).

[38] Andreas N. Kuhn, Tim Beißert, Petra Simon, Britta Vallazza, Janina Buck, Brian P. Davies, Ozlem Tureci, and Ugur Sahin. "mRNA as a Versatile Tool for Exogenous Protein Expression". In: Volume 12.Issue 5 (2012). DOI: 10.2174/156652312802762536.

[39] Sebastian Kreiter, Mustafa Diken, Abderraouf Selmi, Özlem Türeci, and Ugur Sahin. "Tumor vaccination using messenger RNA: prospects of a future therapy". en. In: *Current Opinion in Immunology* 23.3 (June 2011), pp. 399–406. ISSN: 09527915. DOI: 10.1016/j.coi.2011.03.007. URL: https://linkinghub.elsevier.com/retrieve/pii/S095279151100032X (visited on 11/29/2023).

[40] Andrew Fire, SiQun Xu, Mary K Montgomery, Steven A Kostas, Samuel E Driver, and Craig C Mello. "Potent and specific genetic interference by double-stranded RNA in". en. In: 391 (1998).

[41] Richard W. Carthew and Erik J. Sontheimer. "Origins and Mechanisms of miRNAs and siRNAs". en. In: *Cell* 136.4 (Feb. 2009), pp. 642–655. ISSN: 00928674. DOI: 10.1016/j.cell.2009.01.035. URL: https://linkinghub.elsevier.com/retrieve/pii/S009286740900083X (visited on 08/08/2024).

[42] Vasant Jadhav, Akshay Vaishnaw, Kevin Fitzgerald, and Martin A. Maier. "RNA interference in the era of nucleic acid therapeutics". en. In: *Nature Biotechnology* 42.3 (Mar. 2024), pp. 394–405. ISSN: 1087-0156, 1546-1696. DOI: 10.1038/s41587-023-02105-y. URL: https://www.nature.com/articles/s41587-023-02105-y (visited on 09/09/2024).

[43] Robin C. Friedman, Kyle Kai-How Farh, Christopher B. Burge, and David P. Bartel. "Most mammalian mRNAs are conserved targets of microRNAs". en. In: *Genome Research* 19.1 (Jan. 2009), pp. 92–105. ISSN: 1088-9051. DOI: 10.1101/gr.082701.108. URL: http://genome.cshlp.org/lookup/doi/10.1101/gr.082701.108 (visited on 09/03/2024).

[44] David P. Bartel. "MicroRNAs: Target Recognition and Regulatory Functions". en. In: *Cell* 136.2 (Jan. 2009), pp. 215–233. ISSN: 00928674. DOI: 10.1016/j.cell.2009.01.002. URL: https://linkinghub.elsevier.com/retrieve/pii/S0092867409000087 (visited on 09/03/2024).

[45] Kathryn A. Whitehead, Robert Langer, and Daniel G. Anderson. "Knocking down barriers: advances in siRNA delivery". en. In: *Nature Reviews Drug Discovery* 8.2 (Feb. 2009), pp. 129–138. ISSN: 1474-1776, 1474-1784. DOI: 10.1038/nrd2742. URL: https://www.nature.com/articles/nrd2742 (visited on 08/25/2024).

[46] Sayda M. Elbashir, Jens Harborth, Winfried Lendeckel, Abdullah Yalcin, Klaus Weber, and Thomas Tuschl. "Duplexes of 21-nucleotide RNAs mediate RNA interference in cultured mammalian cells". en. In: *Nature* 411.6836 (May 2001), pp. 494–498. ISSN: 0028-0836, 1476-4687. DOI: 10.1038/35078107. URL: https://www.nature.com/articles/35078107 (visited on 08/08/2024).

[47] Giulia Cuccato, Athanasios Polynikis, Velia Siciliano, Mafalda Graziano, Mario Di Bernardo, and Diego Di Bernardo. "Modeling RNA interference in mammalian cells". en. In: *BMC Systems Biology* 5.1 (Dec. 2011), p. 19. ISSN: 1752-0509. DOI: 10.1186/1752-0509-5-19. URL: https://bmcsystbiol.biomedcentral.com/articles/10.1186/1752-0509-5-19 (visited on 08/08/2024).

[48] György Hutvágner and Phillip D. Zamore. "A microRNA in a Multiple-Turnover RNAi Enzyme Complex". en. In: *Science* 297.5589 (Sept. 2002), pp. 2056–2060. ISSN: 0036-8075, 1095-9203. DOI: 10.1126/science.1073827. URL: https://www.science.org/doi/10.1126/science.1073827 (visited on 08/25/2024).

[49] Anton P. McCaffrey, Lepnard Meuse, Thu-Thao T. Pham, Doughlas S. Conklin, Gregory J. Hannon, and Mark A. Kay. "RNA interference in adult mice". In: *Nature* 418 (2002), pp. 38–39. DOI: doi.org/10.1038/418038a.

[50] David Adams, Alejandra Gonzalez-Duarte, William D. O'Riordan, Chih-Chao Yang, Mitsuharu Ueda, Arnt V. Kristen, Ivailo Tournev, Hartmut H. Schmidt, Teresa Coelho, John L. Berk, Kon-Ping Lin, Giuseppe Vita, Shahram Attarian, Violaine Planté-Bordeneuve, Michelle M. Mezei, Josep M. Campistol, Juan Buades, Thomas H. Brannagan, Byoung J. Kim, Jeeyoung Oh, Yesim Parman, Yoshiki Sekijima, Philip N. Hawkins, Scott D. Solomon, Michael Polydefkis, Peter J. Dyck, Pritesh J. Gandhi, Sunita Goyal, Jihong Chen, Andrew L. Strahs, Saraswathy V. Nochur, Marianne T. Sweetser, Pushkal P. Garg, Akshay K. Vaishnaw, Jared A. Gollob, and Ole B. Suhr. "Patisiran, an RNAi Therapeutic, for Hereditary Transthyretin Amyloidosis". en. In: *New England Journal of Medicine* 379.1 (July 2018), pp. 11–21. ISSN: 0028-4793, 1533-4406. DOI: 10.1056/NEJMoa1716153. URL: http://www.nejm.org/doi/10.1056/NEJMoa1716153 (visited on 11/27/2023).

[51] Marcel Tigges, Tatiana T. Marquez-Lago, Jörg Stelling, and Martin Fussenegger. "A tunable synthetic mammalian oscillator". en. In: *Nature* 457.7227 (Jan. 2009), pp. 309–312. ISSN: 0028-0836, 1476-4687. DOI: 10.1038/nature07616. URL: https://www.nature.com/articles/nature07616 (visited on 09/09/2024).

[52] Bianca Köhler, Emily Brieger, Tom Brandstätter, Elisa Hörterer, Ulrich Wilk, Jana Pöhmerer, Anna Jötten, Philipp Paulitschke, Chase P Broedersz, Stefan Zahler, Joachim O Rädler, Ernst Wagner, and Andreas Roidl. *Unravelling the metastasis-preventing effect of miR-200c in vitro and in vivo*. en. Nov. 2023. DOI: 10.1101/2023.11.14.566527. URL: http://biorxiv.org/lookup/doi/10.1101/2023.11.14.566527 (visited on 09/03/2024).

[53] Tara L. Deans, Charles R. Cantor, and James J. Collins. "A Tunable Genetic Switch Based on RNAi and Repressor Proteins for Regulating Gene Expression in Mammalian Cells". en. In: *Cell* 130.2 (July 2007), pp. 363–372. ISSN: 00928674. DOI: 10.1016/j.cell.2007.05.045. URL: https://linkinghub.elsevier.com/retrieve/pii/S0092867407006848 (visited on 09/09/2024).

[54] Timothy J. Strovas, Alexander B. Rosenberg, Brianna E. Kuypers, Richard A. Muscat, and Georg Seelig. "MicroRNA-Based Single-Gene Circuits Buffer Protein Synthesis Rates against Perturbations". en. In: *ACS Synthetic Biology* 3.5 (May 2014), pp. 324–331. ISSN: 2161-5063, 2161-5063. DOI: 10.1021/sb4001867. URL: https://pubs.acs.org/doi/10.1021/sb4001867 (visited on 09/03/2024).

[55] Rongrong Du, Michael J. Flynn, Monique Honsa, Ralf Jungmann, and Michael B. Elowitz. *miRNA circuit modules for precise, tunable control of gene expression*. en. Mar. 2024. DOI: 10.1101/2024.03.12.583048. URL: http://biorxiv.org/lookup/doi/10.1101/2024.03.12.583048 (visited on 09/03/2024).

[56] Andrew G. Bowie and Leonie Unterholzner. "Viral evasion and subversion of pattern-recognition receptor signalling". en. In: *Nature Reviews Immunology* 8.12 (Dec. 2008), pp. 911–922. ISSN: 1474-1733, 1474-1741. DOI: 10.1038/nri2436. URL: https://www.nature.com/articles/nri2436 (visited on 08/28/2024).

[57] J. Gehl. "Electroporation: theory and methods, perspectives for drug delivery, gene therapy and research". en. In: *Acta Physiologica Scandinavica* 177.4 (Apr. 2003), pp. 437–447. ISSN: 0001-6772, 1365-201X. DOI: 10.1046/j.1365-201X.2003.01093.x. URL: https://onlinelibrary.wiley.com/doi/10.1046/j.1365-201X.2003.01093.x (visited on 08/28/2024).

[58] Jamie L. Shirley, Ype P. De Jong, Cox Terhorst, and Roland W. Herzog. "Immune Responses to Viral Gene Therapy Vectors". en. In: *Molecular Therapy* 28.3 (Mar. 2020), pp. 709–722. ISSN: 15250016. DOI: 10.1016/j.ymthe.2020.01.001. URL: https://linkinghub.elsevier.com/retrieve/pii/S1525001620300022 (visited on 08/28/2024).

[59] Yuan Rui, David R. Wilson, Stephany Y. Tzeng, Hannah M. Yamagata, Deepti Sudhakar, Marranne Conge, Cynthia A. Berlinicke, Donald J. Zack, Anthony Tuesca, and Jordan J. Green. "High-throughput and high-content bioassay enables tuning of polyester nanoparticles for cellular uptake, endosomal escape, and systemic in vivo delivery of mRNA". en. In: *Science Advances* 8.1 (Jan. 2022), eabk2855. ISSN: 2375-2548. DOI: 10.1126/sciadv.abk2855. URL: https://www.science.org/doi/10.1126/sciadv.abk2855 (visited on 08/28/2024).

[60] Wenqian Yang, Lucas Mixich, Eger Boonstra, and Horacio Cabral. "Polymer-Based mRNA Delivery Strategies for Advanced Therapies". en. In: *Advanced Healthcare Materials* 12.15 (June 2023), p. 2202688. ISSN: 2192-2640, 2192-2659. DOI: 10.1002/adhm.202202688. URL: https://onlinelibrary.wiley.com/doi/10.1002/adhm.202202688 (visited on 08/28/2024).

[61] Hongtao Lv, Shubiao Zhang, Bing Wang, Shaohui Cui, and Jie Yan. "Toxicity of cationic lipids and cationic polymers in gene delivery". en. In: *Journal of Controlled Release* 114.1 (Aug. 2006), pp. 100–109. ISSN: 01683659. DOI: 10.1016/j.jconrel.2006.04.014. URL: https://linkinghub.elsevier.com/retrieve/pii/S0168365906002045 (visited on 08/28/2024).

[62] P.R. Cullis and B. De Kruijff. "Lipid polymorphism and the functional roles of lipids in biological membranes". en. In: *Biochimica et Biophysica Acta (BBA) - Reviews on Biomembranes* 559.4 (Dec. 1979), pp. 399–420. ISSN: 03044157. DOI: 10.1016/0304-4157(79)90012-1. URL: https://linkinghub.elsevier.com/retrieve/pii/0304415779900121 (visited on 08/28/2024).

[63] P L Felgner, T R Gadek, M Holm, R Roman, H W Chan, M Wenz, J P Northrop, G M Ringold, and M Danielsen. "Lipofection: a highly efficient, lipid-mediated DNA-transfection procedure." en. In: *Proceedings of the National Academy of Sciences* 84.21 (Nov. 1987), pp. 7413–7417. ISSN: 0027-8424, 1091-6490. DOI: 10.1073/pnas.84.21.7413. URL: https://pnas.org/doi/full/10.1073/pnas.84.21.7413 (visited on 08/28/2024).

[64] J-P Yang and L Huang. "Time-dependent maturation of cationic liposome–DNA complex for serum resistance". en. In: *Gene Therapy* 5.3 (Mar. 1998), pp. 380–387. ISSN: 0969-7128, 1476-5462. DOI: 10.1038/sj.gt.3300596. URL: https://www.nature.com/articles/3300596 (visited on 08/28/2024).

[65] Sean C Semple, Sandra K Klimuk, Troy O Harasym, Nancy Dos Santos, Steven M Ansell, Kim F Wong, Norbert Maurer, Holger Stark, Pieter R Cullis, Michael J Hope, and Peter Scherrer. "Efficient encapsulation of antisense oligonucleotides in lipid vesicles using ionizable aminolipids: formation of novel small multilamellar vesicle structures". en. In: *Biochimica et Biophysica Acta* (2001).

[66] Akin Akinc, Martin A. Maier, Muthiah Manoharan, Kevin Fitzgerald, Muthusamy Jayaraman, Scott Barros, Steven Ansell, Xinyao Du, Michael J. Hope, Thomas D. Madden, Barbara L. Mui, Sean C. Semple, Ying K. Tam, Marco Ciufolini, Dominik Witzigmann, Jayesh A. Kulkarni, Roy Van Der Meel, and Pieter R. Cullis. "The Onpattro story and the clinical translation of nanomedicines containing nucleic acid-based drugs". en. In: *Nature Nanotechnology* 14.12 (Dec. 2019), pp. 1084–1087. ISSN: 1748-3387, 1748-3395. DOI: 10.1038/s41565-019-0591-y. URL: https://www.nature.com/articles/s41565-019-0591-y (visited on 10/18/2024).

[67] Mark J. Mulligan, Kirsten E. Lyke, Nicholas Kitchin, Judith Absalon, Alejandra Gurtman, Stephen Lockhart, Kathleen Neuzil, Vanessa Raabe, Ruth Bailey, Kena A. Swanson, Ping Li, Kenneth Koury, Warren Kalina, David Cooper, Camila Fontes-Garfias, Pei-Yong Shi, Özlem Türeci, Kristin R. Tompkins, Edward E. Walsh, Robert Frenck, Ann R. Falsey, Philip R. Dormitzer, William C. Gruber, Uğur Şahin, and Kathrin U. Jansen. "Phase I/II study of COVID-19 RNA vaccine BNT162b1 in adults". en. In: *Nature* 586.7830 (Oct. 2020), pp. 589–593. ISSN: 0028-0836, 1476-4687. DOI: 10.1038/s41586-020-2639-4. URL: https://www.nature.com/articles/s41586-020-2639-4 (visited on 08/28/2024).

[68] Sean C. Semple, Robert Leone, Christopher J. Barbosa, Ying K. Tam, and Paulo J. C. Lin. "Lipid Nanoparticle Delivery Systems to Enable mRNA-Based Therapeutics". en. In: *Pharmaceutics* 14.2 (Feb. 2022), p. 398. ISSN: 1999-4923. DOI: 10.3390/pharmaceutics14020398. URL: https://www.mdpi.com/1999-4923/14/2/398 (visited on 08/30/2024).

[69] Jinjin Chen, Zhongfeng Ye, Changfeng Huang, Min Qiu, Donghui Song, Yamin Li, and Qiaobing Xu. "Lipid nanoparticle-mediated lymph node–targeting delivery of mRNA cancer vaccine elicits robust CD8 $^+$ T cell response". en. In: *Proceedings of the National Academy of Sciences* 119.34 (Aug. 2022), e2207841119. ISSN: 0027-8424, 1091-6490. DOI: 10.1073/pnas.2207841119. URL: https://pnas.org/doi/full/10.1073/pnas.2207841119 (visited on 10/07/2024).

[70] Youhuai Li, Mina Wang, Xueqiang Peng, Yingying Yang, Qishuang Chen, Jiaxing Liu, Qing She, Jichao Tan, Chuyuan Lou, Zehuan Liao, and Xuexin Li. "mRNA vaccine in cancer therapy: Current advance and future outlook". en. In: *Clinical and Translational Medicine* 13.8 (Aug. 2023), e1384. ISSN: 2001-1326, 2001-1326. DOI: 10.1002/ctm2.1384. URL: https://onlinelibrary.wiley.com/doi/10.1002/ctm2.1384 (visited on 10/07/2024).

[71] Alex K. K. Leung, Ismail M. Hafez, Svetlana Baoukina, Nathan M. Belliveau, Igor V. Zhigaltsev, Elham Afshinmanesh, D. Peter Tieleman, Carl L. Hansen, Michael J. Hope, and Pieter R. Cullis. "Lipid Nanoparticles Containing siRNA Synthesized by Microfluidic Mixing Exhibit an Electron-Dense Nanostructured Core". en. In: *The Journal of Physical Chemistry C* 116.34 (Aug. 2012), pp. 18440–18450. ISSN: 1932-7447, 1932-7455. DOI: 10.1021/jp303267y. URL: https://pubs.acs.org/doi/10.1021/jp303267y (visited on 07/31/2023).

[72] James C. W. Locke and Michael B. Elowitz. "Using movies to analyse gene circuit dynamics in single cells". en. In: *Nature Reviews Microbiology* 7.5 (May 2009), pp. 383–392. ISSN: 1740-1526, 1740-1534. DOI: 10.1038/nrmicro2056. URL: https://www.nature.com/articles/nrmicro2056 (visited on 07/08/2023).

[73] Julian Philipp, Aleksandra Dabkowska, Anita Reiser, Kilian Frank, Rafal Krzysztoń, Christiane Brummer, Bert Nickel, Clement E. Blanchet, Akhil Sudarsan, Mohd Ibrahim, Svante Johansson, Pia Skantze, Urban Skantze, Sofia Östman, Marie Johansson, Neil Henderson, Kjetil Elvevold, Bård Smedsrød, Nadine Schwierz, Lennart Lindfors, and Joachim O. Rädler. "pH-dependent structural transitions in cationic ionizable lipid mesophases are critical for lipid nanoparticle function". In: *PNAS* (2023).

[74] Marianna Yanez Arteta, Tomas Kjellman, Stefano Bartesaghi, Simonetta Wallin, Xiaoqiu Wu, Alexander J. Kvist, Aleksandra Dabkowska, Noémi Székely, Aurel Radulescu, Johan Bergenholtz, and Lennart Lindfors. "Successful reprogramming of cellular protein production through mRNA delivered by functionalized lipid nanoparticles". en. In: *Proceedings of the National Academy of Sciences* 115.15 (Apr. 2018). ISSN: 0027-8424, 1091-6490. DOI: 10.1073/pnas.1720542115. URL: https://pnas.org/doi/full/10.1073/pnas.1720542115 (visited on 10/19/2023).

[75] Muthusamy Jayaraman, Steven M. Ansell, Barbara L. Mui, Ying K. Tam, Jianxin Chen, Xinyao Du, David Butler, Laxman Eltepu, Shigeo Matsuda, Jayaprakash K. Narayanannair, Kallanthottathil G. Rajeev, Ismail M. Hafez, Akin Akinc, Martin A. Maier, Mark A. Tracy, Pieter R. Cullis, Thomas D. Madden, Muthiah Manoharan, and Michael J. Hope. "Maximizing the Potency of siRNA Lipid Nanoparticles for Hepatic Gene Silencing In Vivo**". en. In: *Angewandte Chemie International Edition* 51.34 (Aug. 2012), pp. 8529–8533. ISSN: 1433-7851, 1521-3773. DOI: 10.1002/anie.201203263. URL: https://onlinelibrary.wiley.com/doi/10.1002/anie.201203263 (visited on 08/28/2024).

[76] Sean C Semple, Akin Akinc, Jianxin Chen, Ammen P Sandhu, Barbara L Mui, Connie K Cho, Dinah W Y Sah, Derrick Stebbing, Erin J Crosley, Ed Yaworski, Ismail M Hafez, J Robert Dorkin, June Qin, Kieu Lam, Kallanthottathil G Rajeev, Kim F Wong, Lloyd B Jeffs, Lubomir Nechev, Merete L Eisenhardt, Muthusamy Jayaraman, Mikameh Kazem, Martin A Maier, Masuna Srinivasulu, Michael J Weinstein, Qingmin Chen, Rene Alvarez, Scott A Barros, Soma De, Sandra K Klimuk, Todd Borland, Verbena Kosovrasti, William L Cantley, Ying K Tam, Muthiah Manoharan, Marco A Ciufolini, Mark A Tracy, Antonin De Fougerolles, Ian MacLachlan, Pieter R Cullis, Thomas D Madden, and Michael J Hope. "Rational design of cationic lipids for siRNA delivery". en. In: *Nature Biotechnology* 28.2 (Feb. 2010), pp. 172–176. ISSN: 1087-0156, 1546-1696. DOI: 10.1038/nbt.1602. URL: https://www.nature.com/articles/nbt.1602 (visited on 11/27/2023).

[77] Ester Álvarez-Benedicto, Lukas Farbiak, Martha Márquez Ramírez, Xu Wang, Lindsay T. Johnson, Osamah Mian, Erick D. Guerrero, and Daniel J. Siegwart. "Optimization of phospholipid chemistry for improved lipid nanoparticle (LNP) delivery of messenger RNA (mRNA)". en. In: *Biomaterials Science* 10.2 (2022), pp. 549–559. ISSN: 2047-4830, 2047-4849. DOI: 10.1039/D1BM01454D. URL: https://xlink.rsc.org/?DOI=D1BM01454D (visited on 08/28/2024).

[78] Nisha Chander, Genc Basha, Miffy Hok Yan Cheng, Dominik Witzigmann, and Pieter R. Cullis. "Lipid nanoparticle mRNA systems containing high levels of sphingomyelin engender higher protein expression in hepatic and extra-hepatic tissues". en. In: *Molecular Therapy - Methods & Clinical Development* 30 (Sept. 2023), pp. 235–245. ISSN: 23290501. DOI: 10.1016/j.omtm.2023.06.005. URL: https://linkinghub.elsevier.com/retrieve/pii/S2329050123000955 (visited on 10/06/2024).

[79] Yulia Eygeris, Mohit Gupta, Jeonghwan Kim, and Gaurav Sahay. "Chemistry of Lipid Nanoparticles for RNA Delivery". en. In: *Accounts of Chemical Research* 55.1 (Jan. 2022), pp. 2–12. ISSN: 0001-4842, 1520-4898. DOI: 10.1021/acs.accounts.1c00544. URL: https://pubs.acs.org/doi/10.1021/acs.accounts.1c00544 (visited on 08/28/2024).

[80] Siddharth Patel, N. Ashwanikumar, Ema Robinson, Yan Xia, Cosmin Mihai, Joseph P. Griffith, Shangguo Hou, Adam A. Esposito, Tatiana Ketova, Kevin Welsher, John L. Joyal, Örn Almarsson, and Gaurav Sahay. "Naturally-occurring cholesterol analogues in lipid nanoparticles induce polymorphic shape and enhance intracellular delivery of mRNA". en. In: *Nature Communications* 11.1 (Feb. 2020), p. 983. ISSN: 2041-1723. DOI: 10.1038/s41467-020-14527-2. URL: https://www.nature.com/articles/s41467-020-14527-2 (visited on 07/08/2023).

[81] Jung Soo Suk, Qingguo Xu, Namho Kim, Justin Hanes, and Laura M. Ensign. "PEGylation as a strategy for improving nanoparticle-based drug and gene delivery". en. In: *Advanced Drug Delivery Reviews* 99 (Apr. 2016), pp. 28–51. ISSN: 0169409X. DOI: 10.1016/j.addr.2015.09.012. URL: https://linkinghub.elsevier.com/retrieve/pii/S0169409X15002173 (visited on 10/07/2024).

[82] Xi Zhu, Wei Tao, Danny Liu, Jun Wu, Zilei Guo, Xiaoyuan Ji, Zameer Bharwani, Lili Zhao, Xiaoping Zhao, Omid C. Farokhzad, and Jinjun Shi. "Surface De-PEGylation Controls Nanoparticle-Mediated siRNA Delivery *In Vitro* and *In Vivo*". en. In: *Theranostics* 7.7 (2017), pp. 1990–2002. ISSN: 1838-7640. DOI: 10.7150/thno.18136. URL: http://www.thno.org/v07p1990.htm (visited on 10/07/2024).

[83] Barbara L Mui, Ying K Tam, Muthusamy Jayaraman, Steven M Ansell, Xinyao Du, Yuen Yi C Tam, Paulo Jc Lin, Sam Chen, Jayaprakash K Narayanannair, Kallanthottathil G Rajeev, Muthiah Manoharan, Akin Akinc, Martin A Maier, Pieter Cullis, Thomas D Madden, and Michael J Hope. "Influence of Polyethylene Glycol Lipid Desorption Rates on Pharmacokinetics and Pharmacodynamics of siRNA Lipid Nanoparticles". en. In: *Molecular Therapy - Nucleic Acids* 2 (2013), e139. ISSN: 21622531. DOI: 10.1038/mtna.2013.66. URL: https://linkinghub.elsevier.com/retrieve/pii/S2162253116301974 (visited on 08/28/2024).

[84] Sam Chen, Yuen Yi C. Tam, Paulo J.C. Lin, Molly M.H. Sung, Ying K. Tam, and Pieter R. Cullis. "Influence of particle size on the in vivo potency of lipid nanoparticle formulations of siRNA". en. In: *Journal of Controlled Release* 235 (Aug. 2016), pp. 236–244. ISSN: 01683659. DOI: 10.1016/j.jconrel.2016.05.059. URL: https://linkinghub.elsevier.com/retrieve/pii/S0168365916303492 (visited on 08/28/2024).

[85] A. Gallud, M. J. Munson, K. Liu, A. Idström, H. M. G. Barriga, S. R. Tabaei, N. Aliakbarinodehi, M. Ojansivu, Q. Lubart, J. J. Doutch, M. N. Holme, L. Evenäs, L. Lindfors, M. M. Stevens, A. Collén, A. Sabirsh, F. Höök, and E. K. Esbjörner. *Time evolution of PEG-shedding and serum protein coronation determines the cell uptake kinetics and delivery of lipid nanoparticle formulated mRNA*. en. preprint. Biophysics, Aug. 2021. DOI: 10.1101/2021.08.20.457104. URL: http://biorxiv.org/lookup/doi/10.1101/2021.08.20.457104 (visited on 08/30/2023).

[86] Nathan M Belliveau, Jens Huft, Paulo Jc Lin, Sam Chen, Alex Kk Leung, Timothy J Leaver, Andre W Wild, Justin B Lee, Robert J Taylor, Ying K Tam, Carl L Hansen, and Pieter R Cullis. "Microfluidic Synthesis of Highly Potent Limit-size Lipid Nanoparticles for In Vivo Delivery of siRNA". en. In: *Molecular Therapy - Nucleic Acids* 1 (2012), e37. ISSN: 21622531. DOI: 10.1038/mtna.2012.28. URL: https://linkinghub.elsevier.com/retrieve/pii/S2162253116300932 (visited on 08/28/2024).

[87] Xu Wang, Shuai Liu, Yehui Sun, Xueliang Yu, Sang M. Lee, Qiang Cheng, Tuo Wei, Junyu Gong, Joshua Robinson, Di Zhang, Xizhen Lian, Pratima Basak, and Daniel J. Siegwart. "Preparation of selective organ-targeting (SORT) lipid nanoparticles (LNPs) using multiple technical methods for tissue-specific mRNA delivery". en. In: *Nature Protocols* 18.1 (Jan. 2023), pp. 265–291. ISSN: 1754-2189, 1750-2799. DOI: 10.1038/s41596-022-00755-x. URL: https://www.nature.com/articles/s41596-022-00755-x (visited on 08/28/2024).

[88] Ester Álvarez-Benedicto, Zeru Tian, Sumanta Chatterjee, Domenico Orlando, Minjeong Kim, Erick D. Guerrero, Xu Wang, and Daniel J. Siegwart. "Spleen SORT LNP Generated in situ CAR T Cells Extend Survival in a Mouse Model of Lymphoreplete B Cell Lymphoma". en. In: *Angewandte Chemie International Edition* 62.44 (Oct. 2023), e202310395. ISSN: 1433-7851, 1521-3773. DOI: 10.1002/anie.202310395. URL: https://onlinelibrary.wiley.com/doi/10.1002/anie.202310395 (visited on 10/20/2023).

[89] Amy E. Pasquinelli, Brenda J. Reinhart, Frank Slack, Mark Q. Martindale, Mitzi I. Kuroda, Betsy Maller, David C. Hayward, Eldon E. Ball, Bernard Degnan, Peter Müller, Jürg Spring, Ashok Srinivasan, Mark Fishman, John Finnerty, Joseph Corbo, Michael Levine, Patrick Leahy, Eric Davidson, and Gary Ruvkun. "Conservation of the sequence and temporal expression of let-7 heterochronic regulatory RNA". en. In: *Nature* 408.6808 (Nov. 2000), pp. 86–89. ISSN: 0028-0836, 1476-4687. DOI: 10.1038/35040556. URL: https://www.nature.com/articles/35040556 (visited on 10/07/2024).

[90] J.D. Watson and F.H.C. Crick. "Molecular Structure of Nucleic Acids: A Structure for Deoxyribose Nucleic Acid". In: *Nature* 171 (1953), pp. 737–738. DOI: 10.1038/171737a0.

[91] Rebecca L. Ball, Khalid A. Hajj, Jamie Vizelman, Palak Bajaj, and Kathryn A. Whitehead. "Lipid Nanoparticle Formulations for Enhanced Co-delivery of siRNA and mRNA". en. In: *Nano Letters* 18.6 (June 2018), pp. 3814–3822. ISSN: 1530-6984, 1530-6992. DOI: 10.1021/acs.nanolett.8b01101. URL: https://pubs.acs.org/doi/10.1021/acs.nanolett.8b01101 (visited on 07/09/2023).

[92] R. Krzysztoń, B. Salem, D. J. Lee, G. Schwake, E. Wagner, and J. O. Rädler. "Microfluidic self-assembly of folate-targeted monomolecular siRNA-lipid nanoparticles". en. In: *Nanoscale* 9.22 (2017), pp. 7442–7453. ISSN: 2040-3364, 2040-3372. DOI: 10.1039/C7NR01593C. URL: http://xlink.rsc.org/?DOI=C7NR01593C (visited on 06/19/2023).

[93] Maria L. Guevara, Francesca Persano, and Stefano Persano. "Advances in Lipid Nanoparticles for mRNA-Based Cancer Immunotherapy". en. In: *Frontiers in Chemistry* 8 (Oct. 2020), p. 589959. ISSN: 2296-2646. DOI: 10.3389/fchem.2020.589959. URL: https://www.frontiersin.org/articles/10.3389/fchem.2020.589959/full (visited on 10/07/2024).

[94] Kyle J. M. Bishop, Christopher E. Wilmer, Siowling Soh, and Bartosz A. Grzybowski. "Nanoscale Forces and Their Uses in Self-Assembly". en. In: *Small* 5.14 (July 2009), pp. 1600–1630. ISSN: 1613-6810, 1613-6829. DOI: 10.1002/smll.200900358. URL: https://onlinelibrary.wiley.com/doi/10.1002/smll.200900358 (visited on 09/06/2024).

[95] Sarah J. Shepherd, David Issadore, and Michael J. Mitchell. "Microfluidic formulation of nanoparticles for biomedical applications". en. In: *Biomaterials* 274 (July 2021), p. 120826. ISSN: 01429612. DOI: 10.1016/j.biomaterials.2021.120826. URL: https://linkinghub.elsevier.com/retrieve/pii/S0142961221001824 (visited on 09/06/2024).

[96] Manon Ripoll, Elian Martin, Mathilde Enot, Oscar Robbe, Chiara Rapisarda, Marie-Claire Nicolai, Aurélie Deliot, Patrick Tabeling, Jean-René Authelin, Mostafa Nakach, and Pierre Wils. "Optimal self-assembly of lipid nanoparticles (LNP) in a ring micromixer". en. In: *Scientific Reports* 12.1 (June 2022), p. 9483. ISSN: 2045-2322. DOI: 10.1038/s41598-022-13112-5. URL: https://www.nature.com/articles/s41598-022-13112-5 (visited on 10/07/2024).

[97] Marco Maugeri, Muhammad Nawaz, Alexandros Papadimitriou, Annelie Angerfors, Alessandro Camponeschi, Manli Na, Mikko Hölttä, Pia Skantze, Svante Johansson, Martina Sundqvist, Johnny Lindquist, Tomas Kjellman, Inga-Lill Mårtensson, Tao Jin, Per Sunnerhagen, Sofia Östman, Lennart Lindfors, and Hadi Valadi. "Linkage between endosomal escape of LNP-mRNA and loading into EVs for transport to other cells". en. In: *Nature Communications* 10.1 (Sept. 2019), p. 4333. ISSN: 2041-1723. DOI: 10.1038/s41467-019-12275-6. URL: https://www.nature.com/articles/s41467-019-12275-6 (visited on 07/10/2023).

[98] Andre Wild, Timothy Leaver, Robert James Taylor, Euan Ramsay, Nicolas Klaassen, Shao Fang Shannon Chang, and Keara Marshall. "Smart Micofluidic mixing instrument and cartridges". US 11,059,039 B2 (Vancouver).

[99] Suzanne Saffie-Siebert, Nissim Torabi-Pour, Andrew Gibson, Flavia Maria Sutera, Ashkan Dehsorkhi, Paulina Baran-Rachwalska, and Skye Quinn. "Toward a large-batch manufacturing process for silicon-stabilized lipid nanoparticles: A highly customizable RNA delivery platform". en. In: *Molecular Therapy - Methods & Clinical Development* 32.3 (Sept. 2024), p. 101299. ISSN: 23290501. DOI: 10.1016/j.omtm.2024.101299. URL: https://linkinghub.elsevier.com/retrieve/pii/S2329050124001153 (visited on 09/06/2024).

[100] Jörg Stetefeld, Sean A. McKenna, and Trushar R. Patel. "Dynamic light scattering: a practical guide and applications in biomedical sciences". en. In: *Biophysical Reviews* 8.4 (Dec. 2016), pp. 409–427. ISSN: 1867-2450, 1867-2469. DOI: 10.1007/s12551-016-0218-6. URL: http://link.springer.com/10.1007/s12551-016-0218-6 (visited on 08/21/2023).

[101] Jonas Ries and Petra Schwille. "Fluorescence correlation spectroscopy". en. In: *BioEssays* 34.5 (May 2012), pp. 361–368. ISSN: 0265-9247, 1521-1878. DOI: 10.1002/bies.201100111. URL: https://onlinelibrary.wiley.com/doi/10.1002/bies.201100111 (visited on 10/19/2023).

[102] Sixuan Li, Yizong Hu, Jinghan Lin, Zachary Schneiderman, Fangchi Shao, Lai Wei, Andrew Li, Kuangwen Hsieh, Efrosini Kokkoli, Tine Curk, Hai-Quan Mao, and Tza-Huei Wang. "Single-Particle Spectroscopic Chromatography Reveals Heterogeneous RNA Loading and Size Correlations in Lipid Nanoparticles". en. In: *ACS Nano* 18.24 (June 2024), pp. 15729–15743. ISSN: 1936-0851, 1936-086X. DOI: 10.1021/acsnano.4c02341. URL: https://pubs.acs.org/doi/10.1021/acsnano.4c02341 (visited on 09/16/2024).

[103] Ana I. Gómez-Varela, Ricardo Gaspar, Adelaide Miranda, Juliane L. Assis, Rafael H.F. Valverde, Marcelo Einicker-Lamas, Bruno F. B. Silva, and Pieter A.A. De Beule. "Fluorescence cross-correlation spectroscopy as a valuable tool to characterize cationic liposome-DNA nanoparticle assembly". In: *J. Biophotonics* 14.1 (2021). DOI: https://doi.org/10.1002/jbio.202000200.

[104] Oriol Vilanova, Judith J. Mittag, Philip M. Kelly, Silvia Milani, Kenneth A. Dawson, Joachim O. Rädler, and Giancarlo Franzese. "Understanding the Kinetics of Protein–Nanoparticle Corona Formation". en. In: *ACS Nano* 10.12 (Dec. 2016), pp. 10842–10850. ISSN: 1936-0851, 1936-086X. DOI: 10.1021/acsnano.6b04858. URL: https://pubs.acs.org/doi/10.1021/acsnano.6b04858 (visited on 09/16/2024).

[105] J.W. Strutt. "On the scattering of light by small particles". en. In: *The London, Edinburgh, and Dublin Philosophical Magazine and Journal of Science* 41.275 (June 1871), pp. 447–454. ISSN: 1941-5982, 1941-5990. DOI: 10.1080/14786447108640507. URL: https://www.tandfonline.com/doi/full/10.1080/14786447108640507 (visited on 10/08/2024).

[106] Gustav Mie. "Beiträge zur Optik trüber Medien, speziell kolloidaler Metallösungen". de. In: *Annalen der Physik* 330.3 (Jan. 1908), pp. 377–445. ISSN: 0003-3804, 1521-3889. DOI: 10.1002/andp.19083300302. URL: https://onlinelibrary.wiley.com/doi/10.1002/andp.19083300302 (visited on 10/08/2024).

[107] Judith A. Müller, Nathalie Schäffler, Thomas Kellerer, Gerlinde Schwake, Thomas S. Ligon, and Joachim O. Rädler. "Kinetics of RNA-LNP delivery and protein expression". en. In: *European Journal of Pharmaceutics and Biopharmaceutics* 197 (Apr. 2024), p. 114222. ISSN: 09396411. DOI: 10.1016/j.ejpb.2024.114222. URL: https://linkinghub.elsevier.com/retrieve/pii/S0939641124000481 (visited on 07/30/2024).

[108] Katharina Von Gersdorff, Niek N. Sanders, Roosmarijn Vandenbroucke, Stefaan C. De Smedt, Ernst Wagner, and Manfred Ogris. "The Internalization Route Resulting in Successful Gene Expression Depends on both Cell Line and Polyethylenimine Polyplex Type". en. In: *Molecular Therapy* 14.5 (Nov. 2006), pp. 745–753. ISSN: 15250016. DOI: 10.1016/j.ymthe.2006.07.006. URL: https://linkinghub.elsevier.com/retrieve/pii/S1525001606002620 (visited on 11/14/2023).

[109] Jerome Gilleron, William Querbes, Anja Zeigerer, Anna Borodovsky, Giovanni Marsico, Undine Schubert, Kevin Manygoats, Sarah Seifert, Cordula Andree, Martin Stöter, Hila Epstein-Barash, Ligang Zhang, Victor Koteliansky, Kevin Fitzgerald, Eugenio Fava, Marc Bickle, Yannis Kalaidzidis, Akin Akinc, Martin Maier, and Marino Zerial. "Image-based analysis of lipid nanoparticle–mediated siRNA delivery, intracellular trafficking and endosomal escape". en. In: *Nature Biotechnology* 31.7 (July 2013), pp. 638–646. ISSN: 1087-0156, 1546-1696. DOI: 10.1038/nbt.2612. URL: https://www.nature.com/articles/nbt.2612 (visited on 06/21/2023).

[110] Darío Manzanares and Valentín Ceña. "Endocytosis: The Nanoparticle and Submicron Nanocompounds Gateway into the Cell". en. In: *Pharmaceutics* 12.4 (Apr. 2020), p. 371. ISSN: 1999-4923. DOI: 10.3390/pharmaceutics12040371. URL: https://www.mdpi.com/1999-4923/12/4/371 (visited on 07/11/2023).

[111] Joshua J. Rennick, Angus P. R. Johnston, and Robert G. Parton. "Key principles and methods for studying the endocytosis of biological and nanoparticle therapeutics". en. In: *Nature Nanotechnology* 16.3 (Mar. 2021), pp. 266–276. ISSN: 1748-3387, 1748-3395. DOI: 10.1038/s41565-021-00858-8. URL: https://www.nature.com/articles/s41565-021-00858-8 (visited on 07/11/2023).

[112] Christina Lorenz, Mariola Fotin-Mleczek, Günter Roth, Christina Becker, Thanh Chau Dam, Wouter P. R. Verdurmen, Roland Brock, Jochen Probst, and Thomas Schlake. "Protein expression from exogenous mRNA: Uptake by receptor-mediated endocytosis and trafficking via the lysosomal pathway". en. In: *RNA Biology* 8.4 (July 2011), pp. 627–636. ISSN: 1547-6286, 1555-8584. DOI: 10.4161/rna.8.4.15394. URL: http://www.tandfonline.com/doi/abs/10.4161/rna.8.4.15394 (visited on 10/20/2023).

[113] Kai Liu, Ralf Nilsson, Elisa Lázaro-Ibáñez, Hanna Duàn, Tasso Miliotis, Marie Strimfors, Michael Lerche, Ana Rita Salgado Ribeiro, Johan Ulander, Daniel Lindén, Anna Salvati, and Alan Sabirsh. "Multiomics analysis of naturally efficacious lipid nanoparticle coronas reveals high-density lipoprotein is necessary for their function". en. In: *Nature Communications* 14.1 (July 2023), p. 4007. ISSN: 2041-1723. DOI: 10.1038/s41467-023-39768-9. URL: https://www.nature.com/articles/s41467-023-39768-9 (visited on 07/08/2023).

[114] Prasath Paramasivam, Christian Franke, Martin Stöter, Andreas Höijer, Stefano Bartesaghi, Alan Sabirsh, Lennart Lindfors, Marianna Yanez Arteta, Anders Dahlén, Annette Bak, Shalini Andersson, Yannis Kalaidzidis, Marc Bickle, and Marino Zerial. "Endosomal escape of delivered mRNA from endosomal recycling tubules visualized at the nanoscale". en. In: *Journal of Cell Biology* 221.2 (Feb. 2022), e202110137. ISSN: 0021-9525, 1540-8140. DOI: 10.1083/jcb.202110137. URL: https://rupress.org/jcb/article/221/2/e202110137/212896/Endosomal-escape-of-delivered-mRNA-from-endosomal (visited on 06/21/2023).

[115] Joel G Rurik, István Tombácz, Amir Yadegari, Pedro O Méndez Fernández, Swapnil V Shewale, Li Li, Toru Kimura, Ousamah Younoss Soliman, Tyler E Papp, Ying K Tam, Barbara L Mui, Steven M Albelda, Ellen Puré, Carl H June, Haig Aghajanian, Drew Weissman, Hamideh Parhiz, and Jonathan A Epstein. "CAR T cells produced in vivo to treat cardiac injury". en. In: (2022).

[116] István Tombácz, Dorottya Laczkó, Hamna Shahnawaz, Hiromi Muramatsu, Ambika Natesan, Amir Yadegari, Tyler E. Papp, Mohamad-Gabriel Alameh, Vladimir Shuvaev, Barbara L. Mui, Ying K. Tam, Vladimir Muzykantov, Norbert Pardi, Drew Weissman, and Hamideh Parhiz. "Highly efficient CD4+ T cell targeting and genetic recombination using engineered CD4+ cell-homing mRNA-LNPs". en. In: *Molecular Therapy* 29.11 (Nov. 2021), pp. 3293–3304. ISSN: 15250016. DOI: 10.1016/j.ymthe.2021.06.004. URL: https://linkinghub.elsevier.com/retrieve/pii/S1525001621003105 (visited on 10/20/2023).

[117] Hamideh Parhiz, Vladimir V. Shuvaev, Norbert Pardi, Makan Khoshnejad, Raisa Yu Kiseleva, Jacob S. Brenner, Thomas Uhler, Steven Tuyishime, Barbara L. Mui, Ying K. Tam, Thomas D. Madden, Michael J. Hope, Drew Weissman, and Vladimir R. Muzykantov. "PECAM-1 directed re-targeting of exogenous mRNA providing two orders of magnitude enhancement of vascular delivery and expression in lungs independent of apolipoprotein E-mediated uptake". en. In: *Journal of Controlled Release* 291 (Dec. 2018), pp. 106–115. ISSN: 01683659. DOI: 10.1016/j.jconrel.2018.10.015. URL: https://linkinghub.elsevier.com/retrieve/pii/S0168365918305868 (visited on 10/20/2023).

[118] Stephanie E. A. Gratton, Patricia A. Ropp, Patrick D. Pohlhaus, J. Christopher Luft, Victoria J. Madden, Mary E. Napier, and Joseph M. DeSimone. "The effect of particle design on cellular internalization pathways". en. In: *Proceedings of the National Academy of Sciences* 105.33 (Aug. 2008), pp. 11613–11618. ISSN: 0027-8424, 1091-6490. DOI: 10.1073/pnas.0801763105. URL: https://pnas.org/doi/full/10.1073/pnas.0801763105 (visited on 11/13/2023).

[119] Hongyan Yuan, Ju Li, Gang Bao, and Sulin Zhang. "Variable Nanoparticle-Cell Adhesion Strength Regulates Cellular Uptake". en. In: *Physical Review Letters* 105.13 (Sept. 2010), p. 138101. ISSN: 0031-9007, 1079-7114. DOI: 10.1103/PhysRevLett.105.138101. URL: https://link.aps.org/doi/10.1103/PhysRevLett.105.138101 (visited on 11/13/2023).

[120] Joanna Rejman, Volker Oberle, Inge S. Zuhorn, and Dick Hoekstra. "Size-dependent internalization of particles via the pathways of clathrin- and caveolae-mediated endocytosis". en. In: *Biochemical Journal* 377.1 (Jan. 2004), pp. 159–169. ISSN: 0264-6021, 1470-8728. DOI: 10.1042/bj20031253. URL: https://portlandpress.com/biochemj/article/377/1/159/43138/Size-dependent-internalization-of-particles-via (visited on 11/13/2023).

[121] Shahed Behzadi, Vahid Serpooshan, Wei Tao, Majd A. Hamaly, Mahmoud Y. Alkawareek, Erik C. Dreaden, Dennis Brown, Alaaldin M. Alkilany, Omid C. Farokhzad, and Morteza Mahmoudi. "Cellular uptake of nanoparticles: journey inside the cell". en. In: *Chemical Society Reviews* 46.14 (2017), pp. 4218–4244. ISSN: 0306-0012, 1460-4744. DOI: 10.1039/C6CS00636A. URL: http://xlink.rsc.org/?DOI=C6CS00636A (visited on 08/21/2023).

[122] Nadia Ruthardt, Don C Lamb, and Christoph Bräuchle. "Single-particle Tracking as a Quantitative Microscopy-based Approach to Unravel Cell Entry Mechanisms of Viruses and Pharmaceutical Nanoparticles". en. In: *Molecular Therapy* 19.7 (July 2011), pp. 1199–1211. ISSN: 15250016. DOI: 10.1038/mt.2011.102. URL: https://linkinghub.elsevier.com/retrieve/pii/S1525001616324868 (visited on 08/21/2023).

[123] James E. Dahlman, Kevin J. Kauffman, Yiping Xing, Taylor E. Shaw, Faryal F. Mir, Chloe C. Dlott, Robert Langer, Daniel G. Anderson, and Eric T. Wang. "Barcoded nanoparticles for high throughput in vivo discovery of targeted therapeutics". en. In: *Proceedings of the National Academy of Sciences* 114.8 (Feb. 2017), pp. 2060–2065. ISSN: 0027-8424, 1091-6490. DOI: 10.1073/pnas.1620874114. URL: https://pnas.org/doi/full/10.1073/pnas.1620874114 (visited on 08/02/2023).

[124] Michael J. Munson, Gwen O'Driscoll, Andreia M. Silva, Elisa Lázaro-Ibáñez, Audrey Gallud, John T. Wilson, Anna Collén, Elin K. Esbjörner, and Alan Sabirsh. "A high-throughput Galectin-9 imaging assay for quantifying nanoparticle uptake, endosomal escape and functional RNA delivery". en. In: *Communications Biology* 4.1 (Feb. 2021), p. 211. ISSN: 2399-3642. DOI: 10.1038/s42003-021-01728-8. URL: https://www.nature.com/articles/s42003-021-01728-8 (visited on 07/11/2023).

[125] Serena Omo-Lamai, Yufei Wang, Manthan N. Patel, Eno-Obong Essien, Mengwen Shen, Aparajeeta Majumdar, Carolann Espy, Jichuan Wu, Breana Channer, Michael Tobin, Shruthi Murali, Tyler E. Papp, Rhea Maheshwari, Liuqian Wang, Liam S. Chase, Marco E. Zamora, Mariah L. Arral, Oscar A. Marcos-Contreras, Jacob W. Myerson, Christopher A. Hunter, Andrew Tsourkas, Vladimir Muzykantov, Igor Brodsky, Sunny Shin, Kathryn A. Whitehead, Peter Gaskill, Dennis Discher, Hamideh Parhiz, and Jacob S. Brenner. *Lipid Nanoparticle-Associated Inflammation is Triggered by Sensing of Endosomal Damage: Engineering Endosomal Escape Without Side Effects*. en. Apr. 2024. DOI: 10.1101/2024.04.16.589801. URL: http://biorxiv.org/lookup/doi/10.1101/2024.04.16.589801 (visited on 08/25/2024).

[126] Anders Wittrup, Angela Ai, Xing Liu, Peter Hamar, Radiana Trifonova, Klaus Charisse, Muthiah Manoharan, Tomas Kirchhausen, and Judy Lieberman. "Visualizing lipid-formulated siRNA release from endosomes and target gene knockdown". en. In: *Nature Biotechnology* 33.8 (Aug. 2015), pp. 870–876. ISSN: 1087-0156, 1546-1696. DOI: 10.1038/nbt.3298. URL: https://www.nature.com/articles/nbt.3298 (visited on 09/13/2023).

[127] Kameron V. Kilchrist, Somtochukwu C. Dimobi, Meredith A. Jackson, Brian C. Evans, Thomas A. Werfel, Eric A. Dailing, Sean K. Bedingfield, Isom B. Kelly, and Craig L. Duvall. "Gal8 Visualization of Endosome Disruption Predicts Carrier-Mediated Biologic Drug Intracellular Bioavailability". en. In: *ACS Nano* (Jan. 2019), acsnano.8b05482. ISSN: 1936-0851, 1936-086X. DOI: 10.1021/acsnano.8b05482. URL: https://pubs.acs.org/doi/10.1021/acsnano.8b05482 (visited on 10/19/2023).

[128] Staci Sabnis, E. Sathyajith Kumarasinghe, Timothy Salerno, Cosmin Mihai, Tatiana Ketova, Joseph J. Senn, Andy Lynn, Alex Bulychev, Iain McFadyen, Joyce Chan, Örn Almarsson, Matthew G. Stanton, and Kerry E. Benenato. "A Novel Amino Lipid Series for mRNA Delivery: Improved Endosomal Escape and Sustained Pharmacology and Safety in Non-human Primates". en. In: *Molecular Therapy* 26.6 (June 2018), pp. 1509–1519. ISSN: 15250016. DOI: 10.1016/j.ymthe.2018.03.010. URL: https://linkinghub.elsevier.com/retrieve/pii/S1525001618301187 (visited on 06/21/2023).

[129] Heyang Zhang, Jeroen Bussmann, Florian H. Huhnke, Joke Devoldere, An-Katrien Minnaert, Wim Jiskoot, Friedhelm Serwane, Joachim Spatz, Magnus Röding, Stefaan C. De Smedt, Kevin Braeckmans, and Katrien Remaut. "Together is Better: mRNA Co-Encapsulation in Lipoplexes is Required to Obtain Ratiometric Co-Delivery and Protein Expression on the Single Cell Level". en. In: *Advanced Science* 9.4 (Feb. 2022), p. 2102072. ISSN: 2198-3844, 2198-3844. DOI: 10.1002/advs.202102072. URL: https://onlinelibrary.wiley.com/doi/10.1002/advs.202102072 (visited on 07/31/2023).

[130] Gaurav Sahay, William Querbes, Christopher Alabi, Ahmed Eltoukhy, Sovan Sarkar, Christopher Zurenko, Emmanouil Karagiannis, Kevin Love, Delai Chen, Roberto Zoncu, Yosef Buganim, Avi Schroeder, Robert Langer, and Daniel G Anderson. "Efficiency of siRNA delivery by lipid nanoparticles is limited by endocytic recycling". en. In: *Nature Biotechnology* 31.7 (July 2013), pp. 653–658. ISSN: 1087-0156, 1546-1696. DOI: 10.1038/nbt.2614. URL: https://www.nature.com/articles/nbt.2614 (visited on 07/26/2023).

[131] Alessandro Parodi, Claudia Corbo, Armando Cevenini, Roberto Molinaro, Roberto Palomba, Laura Pandolfi, Marco Agostini, Francesco Salvatore, and Ennio Tasciotti. "Enabling cytoplasmic delivery and organelle targeting by surface modification of nanocarriers". en. In: *Nanomedicine* 10.12 (July 2015), pp. 1923–1940. ISSN: 1743-5889, 1748-6963. DOI: 10.2217/nnm.15.39. URL: https://www.futuremedicine.com/doi/10.2217/nnm.15.39 (visited on 10/19/2023).

[132] Isabelle M. S. Degors, Cuifeng Wang, Zia Ur Rehman, and Inge S. Zuhorn. "Carriers Break Barriers in Drug Delivery: Endocytosis and Endosomal Escape of Gene Delivery Vectors". en. In: *Accounts of Chemical Research* 52.7 (July 2019), pp. 1750–1760. ISSN: 0001-4842, 1520-4898. DOI: 10.1021/acs.accounts.9b00177. URL: https://pubs.acs.org/doi/10.1021/acs.accounts.9b00177 (visited on 07/09/2023).

[133] Maria Pamela Dobay, Alexandra Schmidt, Eduardo Mendoza, Thomas Bein, and Joachim O. Rädler. "Cell Type Determines the Light-Induced Endosomal Escape Kinetics of Multifunctional Mesoporous Silica Nanoparticles". en. In: *Nano Letters* 13.3 (Mar. 2013), pp. 1047–1052. ISSN: 1530-6984, 1530-6992. DOI: 10.1021/nl304273u. URL: https://pubs.acs.org/doi/10.1021/nl304273u (visited on 07/12/2023).

[134] Edward J. Sayers, Samantha E. Peel, Anna Schantz, Richard M. England, Maya Beano, Stephanie M. Bates, Arpan S. Desai, Sanyogitta Puri, Marianne B. Ashford, and Arwyn T. Jones. "Endocytic Profiling of Cancer Cell Models Reveals Critical Factors Influencing LNP-Mediated mRNA Delivery and Protein Expression". en. In: *Molecular Therapy* 27.11 (Nov. 2019), pp. 1950–1962. ISSN: 15250016. DOI: 10.1016/j.ymthe.2019.07.018. URL: https://linkinghub.elsevier.com/retrieve/pii/S1525001619303570 (visited on 07/10/2023).

[135] Zongyi Li, Jessica Carter, Luis Santos, Carl Webster, Christopher F. Van Der Walle, Peixun Li, Sarah E. Rogers, and Jian Ren Lu. "Acidification-Induced Structure Evolution of Lipid Nanoparticles Correlates with Their *In Vitro* Gene Transfections". en. In: *ACS Nano* 17.2 (Jan. 2023), pp. 979–990. ISSN: 1936-0851, 1936-086X. DOI: 10.1021/acsnano.2c06213. URL: https://pubs.acs.org/doi/10.1021/acsnano.2c06213 (visited on 11/13/2023).

[136] Haitao Yu, Angelina Angelova, Borislav Angelov, Brendan Dyett, Lauren Matthews, Yiran Zhang, Mohamad El Mohamad, Xudong Cai, Sepideh Valimehr, Calum J. Drummond, and Jiali Zhai. "Real-Time pH-Dependent Self-Assembly of Ionisable Lipids from COVID-19 Vaccines and *In Situ* Nucleic Acid Complexation". en. In: *Angewandte Chemie International Edition* 62.35 (Aug. 2023), e202304977. ISSN: 1433-7851, 1521-3773. DOI: 10.1002/anie.202304977. URL: https://onlinelibrary.wiley.com/doi/10.1002/anie.202304977 (visited on 11/13/2023).

[137] Hiroyuki Kamiya, Hidetaka Akita, and Hideyoshi Harashima. "Pharmacokinetic and pharmacodynamic considerations in gene therapy". en. In: *Drug Discovery Today* 8.21 (Nov. 2003), pp. 990–996. ISSN: 13596446. DOI: 10.1016/S1359-6446(03)02889-7. URL: https://linkinghub.elsevier.com/retrieve/pii/S1359644603028897 (visited on 10/19/2023).

[138] Xiaoping Zhang, Varun Goel, and Gabriel J. Robbie. "Pharmacokinetics of Patisiran, the First Approved RNA Interference Therapy in Patients With Hereditary Transthyretin-Mediated Amyloidosis". en. In: *The Journal of Clinical Pharmacology* 60.5 (May 2020), pp. 573–585. ISSN: 0091-2700, 1552-4604. DOI: 10.1002/jcph.1553. URL: https://accp1.onlinelibrary.wiley.com/doi/10.1002/jcph.1553 (visited on 10/20/2023).

[139] Roy Pattipeiluhu, Ye Zeng, Marco M.R.M. Hendrix, Ilja K. Voets, Alexander Kros, and Thomas H. Sharp. "Liquid crystalline inverted lipid phases encapsulating siRNA enhance lipid nanoparticle mediated transfection". en. In: *Nature Communications* 15.1 (Feb. 2024), p. 1303. ISSN: 2041-1723. DOI: 10.1038/s41467-024-45666-5. URL: https://www.nature.com/articles/s41467-024-45666-5 (visited on 09/02/2024).

[140] Dingcheng Zhu, Huijie Yan, Zhuxian Zhou, Jianbin Tang, Xiangrui Liu, Raimo Hartmann, Wolfgang J. Parak, Neus Feliu, and Youqing Shen. "Detailed investigation on how the protein corona modulates the physicochemical properties and gene delivery of polyethylenimine (PEI) polyplexes". en. In: *Biomaterials Science* 6.7 (2018), pp. 1800–1817. ISSN: 2047-4830, 2047-4849. DOI: 10.1039/C8BM00128F. URL: http://xlink.rsc.org/?DOI=C8BM00128F (visited on 08/02/2023).

[141] Morag Rose Hunter, Lili Cui, Benjamin Thomas Porebski, Sara Pereira, Silvia Sonzini, Uchechukwu Odunze, Preeti Iyer, Ola Engkvist, Rebecca Louise Lloyd, Samantha Peel, Alan Sabirsh, Douglas Ross-Thriepland, Arwyn Tomos Jones, and Arpan Shailesh Desai. "Understanding Intracellular Biology to Improve mRNA Delivery by Lipid Nanoparticles". en. In: *Small Methods* (June 2023), p. 2201695. ISSN: 2366-9608, 2366-9608. DOI: 10.1002/smtd.202201695. URL: https://onlinelibrary.wiley.com/doi/10.1002/smtd.202201695 (visited on 06/21/2023).

[142] Bin Li, Xiao Luo, Binbin Deng, Junfeng Wang, David W. McComb, Yimin Shi, Karin M. L. Gaensler, Xu Tan, Amy L. Dunn, Bryce A. Kerlin, and Yizhou Dong. "An Orthogonal Array Optimization of Lipid-like Nanoparticles for mRNA Delivery in Vivo". en. In: *Nano Letters* 15.12 (Dec. 2015), pp. 8099–8107. ISSN: 1530-6984, 1530-6992. DOI: 10.1021/acs.nanolett.5b03528. URL: https://pubs.acs.org/doi/10.1021/acs.nanolett.5b03528 (visited on 07/08/2023).

[143] Siddharth Patel, N. Ashwanikumar, Emily Robinson, Allison DuRoss, Conroy Sun, Kerry E. Murphy-Benenato, Cosmin Mihai, Örn Almarsson, and Gaurav Sahay. "Boosting Intracellular Delivery of Lipid Nanoparticle-Encapsulated mRNA". en. In: *Nano Letters* 17.9 (Sept. 2017), pp. 5711–5718. ISSN: 1530-6984, 1530-6992. DOI: 10.1021/acs.nanolett.7b02664. URL: https://pubs.acs.org/doi/10.1021/acs.nanolett.7b02664 (visited on 07/25/2023).

[144] Jing Zhang, Renhao Xue, Wei-Yi Ong, and Peng Chen. "Roles of Cholesterol in Vesicle Fusion and Motion". en. In: *Biophysical Journal* 97.5 (Sept. 2009), pp. 1371–1380. ISSN: 00063495. DOI: 10.1016/j.bpj.2009.06.025. URL: https://linkinghub.elsevier.com/retrieve/pii/S0006349509011643 (visited on 07/09/2023).

[145] Juliane Nguyen and Francis C. Szoka. "Nucleic Acid Delivery: The Missing Pieces of the Puzzle?" en. In: *Accounts of Chemical Research* 45.7 (July 2012), pp. 1153–1162. ISSN: 0001-4842, 1520-4898. DOI: 10.1021/ar3000162. URL: https://pubs.acs.org/doi/10.1021/ar3000162 (visited on 07/08/2023).

[146] Wei Leong Chew, Mohammadsharif Tabebordbar, Jason K W Cheng, Prashant Mali, Elizabeth Y Wu, Alex H M Ng, Kexian Zhu, Amy J Wagers, and George M Church. "A multifunctional AAV–CRISPR–Cas9 and its host response". en. In: *Nature Methods* 13.10 (Oct. 2016), pp. 868–874. ISSN: 1548-7091, 1548-7105. DOI: 10.1038/nmeth.3993. URL: https://www.nature.com/articles/nmeth.3993 (visited on 10/19/2023).

[147] Alex G. Hamilton, Kelsey L. Swingle, Ryann A. Joseph, David Mai, Ningqiang Gong, Margaret M. Billingsley, Mohamad-Gabriel Alameh, Drew Weissman, Neil C. Sheppard, Carl H. June, and Michael J. Mitchell. "Ionizable Lipid Nanoparticles with Integrated Immune Checkpoint Inhibition for mRNA CAR T Cell Engineering". en. In: *Advanced Healthcare Materials* (Aug. 2023), p. 2301515. ISSN: 2192-2640, 2192-2659. DOI: 10.1002/adhm.202301515. URL: https://onlinelibrary.wiley.com/doi/10.1002/adhm.202301515 (visited on 10/20/2023).

[148] Tuo Wei, Qiang Cheng, Yi-Li Min, Eric N. Olson, and Daniel J. Siegwart. "Systemic nanoparticle delivery of CRISPR-Cas9 ribonucleoproteins for effective tissue specific genome editing". en. In: *Nature Communications* 11.1 (June 2020), p. 3232. ISSN: 2041-1723. DOI: 10.1038/s41467-020-17029-3. URL: https://www.nature.com/articles/s41467-020-17029-3 (visited on 10/19/2023).

[149] Jeong Pil Han, MinJeong Kim, Beom Seok Choi, Jeong Hyeon Lee, Geon Seong Lee, Michaela Jeong, Yeji Lee, Eun-Ah Kim, Hye-Kyung Oh, Nanyeong Go, Hyerim Lee, Kyu Jun Lee, Un Gi Kim, Jae Young Lee, Seokjoong Kim, Jun Chang, Hyukjin Lee, Dong Woo Song, and Su Cheong Yeom. "In vivo delivery of CRISPR-Cas9 using lipid nanoparticles enables antithrombin gene editing for sustainable hemophilia A and B therapy". en. In: *Science Advances* 8.3 (Jan. 2022), eabj6901. ISSN: 2375-2548. DOI: 10.1126/sciadv.abj6901. URL: https://www.science.org/doi/10.1126/sciadv.abj6901 (visited on 10/20/2023).

[150] Kunwoo Lee, Michael Conboy, Hyo Min Park, Fuguo Jiang, Hyun Jin Kim, Mark A. Dewitt, Vanessa A. Mackley, Kevin Chang, Anirudh Rao, Colin Skinner, Tamanna Shobha, Melod Mehdipour, Hui Liu, Wen-chin Huang, Freeman Lan, Nicolas L. Bray, Song Li, Jacob E. Corn, Kazunori Kataoka, Jennifer A. Doudna, Irina Conboy, and Niren Murthy. "Nanoparticle delivery of Cas9 ribonucleoprotein and donor DNA in vivo induces homology-directed DNA repair". en. In: *Nature Biomedical Engineering* 1.11 (Oct. 2017), pp. 889–901. ISSN: 2157-846X. DOI: 10.1038/s41551-017-0137-2. URL: https://www.nature.com/articles/s41551-017-0137-2 (visited on 08/02/2023).

[151] Gerlinde Schwake, Simon Youssef, Jan-Timm Kuhr, Sebastian Gude, Maria Pamela David, Eduardo Mendoza, Erwin Frey, and Joachim O. RÃ¤dler. "Predictive modeling of non-viral gene transfer". en. In: *Biotechnology and Bioengineering* (2010), n/a–n/a. ISSN: 00063592, 10970290. DOI: 10.1002/bit.22604. URL: https://onlinelibrary.wiley.com/doi/10.1002/bit.22604 (visited on 07/31/2023).

[152] Hanieh Moradian, Andreas Lendlein, and Manfred Gossen. "Strategies for simultaneous and successive delivery of RNA". en. In: *Journal of Molecular Medicine* 98.12 (Dec. 2020), pp. 1767–1779. ISSN: 0946-2716, 1432-1440. DOI: 10.1007/s00109-020-01956-1. URL: http://link.springer.com/10.1007/s00109-020-01956-1 (visited on 04/18/2024).

[153] Steven J. Altschuler and Lani F. Wu. "Cellular Heterogeneity: Do Differences Make a Difference?" en. In: *Cell* 141.4 (May 2010), pp. 559–563. ISSN: 00928674. DOI: 10.1016/j.cell.2010.04.033. URL: https://linkinghub.elsevier.com/retrieve/pii/S0092867410004873 (visited on 07/08/2023).

[154] Berend Snijder and Lucas Pelkmans. "Origins of regulated cell-to-cell variability". en. In: *Nature Reviews Molecular Cell Biology* 12.2 (Feb. 2011), pp. 119–125. ISSN: 1471-0072, 1471-0080. DOI: 10.1038/nrm3044. URL: https://www.nature.com/articles/nrm3044 (visited on 08/19/2024).

[155] Richard Losick and Claude Desplan. "Stochasticity and Cell Fate". en. In: *Science* 320.5872 (Apr. 2008), pp. 65–68. ISSN: 0036-8075, 1095-9203. DOI: 10.1126/science.1147888. URL: https://www.science.org/doi/10.1126/science.1147888 (visited on 08/19/2024).

[156] Johan Paulsson. "Summing up the noise in gene networks". en. In: *Nature* 427.6973 (Jan. 2004), pp. 415–418. ISSN: 0028-0836, 1476-4687. DOI: 10.1038/nature02257. URL: https://www.nature.com/articles/nature02257 (visited on 10/08/2024).

[157] Michael L. Simpson, Chris D. Cox, Michael S. Allen, James M. McCollum, Roy D. Dar, David K. Karig, and John F. Cooke. "Noise in biological circuits". en. In: *WIREs Nanomedicine and Nanobiotechnology* 1.2 (Mar. 2009), pp. 214–225. ISSN: 1939-5116, 1939-0041. DOI: 10.1002/wnan.22. URL: https://wires.onlinelibrary.wiley.com/doi/10.1002/wnan.22 (visited on 10/08/2024).

[158] Arjun Raj and Alexander van Oudenaarden. "Stochastic gene expression and its consequences". en. In: (2011).

[159] Ioannis Lestas, Glenn Vinnicombe, and Johan Paulsson. "Fundamental limits on the suppression of molecular fluctuations". en. In: *Nature* 467.7312 (Sept. 2010), pp. 174–178. ISSN: 0028-0836, 1476-4687. DOI: 10.1038/nature09333. URL: https://www.nature.com/articles/nature09333 (visited on 08/20/2024).

[160] Karen Sachs, Omar Perez, Dana Pe'er, Douglas A. Lauffenburger, and Garry P. Nolan. "Causal Protein-Signaling Networks Derived from Multiparameter Single-Cell Data". en. In: *Science* 308.5721 (Apr. 2005), pp. 523–529. ISSN: 0036-8075, 1095-9203. DOI: 10.1126/science.1105809. URL: https://www.science.org/doi/10.1126/science.1105809 (visited on 08/19/2024).

[161] Alexandra Murschhauser, Peter J. F. Röttgermann, Daniel Woschée, Martina F. Ober, Yan Yan, Kenneth A. Dawson, and Joachim O. Rädler. "A high-throughput microscopy method for single-cell analysis of event-time correlations in nanoparticle-induced cell death". en. In: *Communications Biology* 2.1 (Jan. 2019), p. 35. ISSN: 2399-3642. DOI: 10.1038/s42003-019-0282-0. URL: https://www.nature.com/articles/s42003-019-0282-0 (visited on 07/08/2023).

[162] Yaron Shav-Tal, Robert H. Singer, and Xavier Darzacq. "Imaging gene expression in single living cells". en. In: *Nature Reviews Molecular Cell Biology* 5.10 (Oct. 2004), pp. 855–862. ISSN: 1471-0072, 1471-0080. DOI: 10.1038/nrm1494. URL: https://www.nature.com/articles/nrm1494 (visited on 08/19/2024).

[163] Nickolay Korabel, Alessandro Taloni, Gianni Pagnini, Viki Allan, Sergei Fedotov, and Thomas Andrew Waigh. "Ensemble heterogeneity mimics ageing for endosomal dynamics within eukaryotic cells". en. In: *Scientific Reports* 13.1 (May 2023), p. 8789. ISSN: 2045-2322. DOI: 10.1038/s41598-023-35903-0. URL: https://www.nature.com/articles/s41598-023-35903-0 (visited on 08/21/2023).

[164] Sanaa Ben Djemaa, Katel Hervé-Aubert, Laurie Lajoie, Annarita Falanga, Stefania Galdiero, Steven Nedellec, Martin Soucé, Emilie Munnier, Igor Chourpa, Stéphanie David, and Emilie Allard-Vannier. "gH625 Cell-Penetrating Peptide Promotes the Endosomal Escape of Nanovectorized siRNA in a Triple-Negative Breast Cancer Cell Line". en. In: *Biomacromolecules* 20.8 (Aug. 2019), pp. 3076–3086. ISSN: 1525-7797, 1526-4602. DOI: 10.1021/acs.biomac.9b00637. URL: https://pubs.acs.org/doi/10.1021/acs.biomac.9b00637 (visited on 09/13/2023).

[165] Li Shang, Peng Gao, Haixia Wang, Radian Popescu, Dagmar Gerthsen, and Gerd Ulrich Nienhaus. "Protein-based fluorescent nanoparticles for super-resolution STED imaging of live cells". en. In: *Chemical Science* 8.3 (2017), pp. 2396–2400. ISSN: 2041-6520, 2041-6539. DOI: 10.1039/C6SC04664A. URL: http://xlink.rsc.org/?DOI=C6SC04664A (visited on 09/13/2023).

[166] Mikhail Y. Berezin and Samuel Achilefu. "Fluorescence Lifetime Measurements and Biological Imaging". en. In: *Chemical Reviews* 110.5 (May 2010), pp. 2641–2684. ISSN: 0009-2665, 1520-6890. DOI: 10.1021/cr900343z. URL: https://pubs.acs.org/doi/10.1021/cr900343z (visited on 08/21/2023).

[167] Thomas Kellerer, Janko Janusch, Christian Freymüller, Adrian Rühm, Ronald Sroka, and Thomas Hellerer. "Comprehensive Investigation of Parameters Influencing Fluorescence Lifetime Imaging Microscopy in Frequency- and Time-Domain Illustrated by Phasor Plot Analysis". en. In: *International Journal of Molecular Sciences* 23.24 (Dec. 2022), p. 15885. ISSN: 1422-0067. DOI: 10.3390/ijms232415885. URL: https://www.mdpi.com/1422-0067/23/24/15885 (visited on 08/21/2023).

[168] Rupsa Datta, Tiffany M. Heaster, Joe T. Sharick, Amani A. Gillette, and Melissa C. Skala. "Fluorescence lifetime imaging microscopy: fundamentals and advances in instrumentation, analysis, and applications". en. In: *Journal of Biomedical Optics* 25.07 (May 2020), p. 1. ISSN: 1083-3668. DOI: 10.1117/1.JBO.25.7.071203. URL: https://www.spiedigitallibrary.org/journals/journal-of-biomedical-optics/volume-25/issue-07/071203/Fluorescence-lifetime-imaging-microscopy--fundamentals-and-advances-in-instrumentation/10.1117/1.JBO.25.7.071203.full (visited on 08/21/2023).

[169] Th. Förster. "Zwischenmolekulare Energiewanderung und Fluoreszenz". en. In: *Annalen der Physik* 437.1-2 (Jan. 1948), pp. 55–75. ISSN: 0003-3804, 1521-3889. DOI: 10.1002/andp.19484370105. URL: https://onlinelibrary.wiley.com/doi/10.1002/andp.19484370105 (visited on 08/21/2023).

[170] Tongkai Chen, Bing He, Jingsong Tao, Yuan He, Hailiang Deng, Xueqing Wang, and Ying Zheng. "Application of Förster Resonance Energy Transfer (FRET) technique to elucidate intracellular and In Vivo biofate of nanomedicines". In: *Advanced Drug Delivery Reviews* 143 (Mar. 2019), pp. 177–205. DOI: https://doi.org/10.1016/j.addr.2019.04.009.

[171] Luís Loura. "FRET in membrane biophysics: an overview". en. In: *Frontiers in Physiology* 2 (2011). ISSN: 1664042X. DOI: 10.3389/fphys.2011.00082. URL: http://journal.frontiersin.org/article/10.3389/fphys.2011.00082/abstract (visited on 01/05/2024).

[172] Rafał Krzysztoń, Daniel Woschée, Anita Reiser, Gerlinde Schwake, Helmut H. Strey, and Joachim O. Rädler. "Single-cell kinetics of siRNA-mediated mRNA degradation". en. In: *Nanomedicine: Nanotechnology, Biology and Medicine* 21 (Oct. 2019), p. 102077. ISSN: 15499634. DOI: 10.1016/j.nano.2019.102077. URL: https://linkinghub.elsevier.com/retrieve/pii/S1549963419301613 (visited on 06/19/2023).

[173] A Reiser, D Woschée, N Mehrotra, R Krzysztoń, H H Strey, and J O Rädler. "Correlation of mRNA delivery timing and protein expression in lipid-based transfection". en. In: *Integrative Biology* 11.9 (Dec. 2019), pp. 362–371. ISSN: 1757-9708. DOI: 10.1093/intbio/zyz030. URL: https://academic.oup.com/ib/article/11/9/362/5673747 (visited on 06/19/2023).

[174] Judith A. Müller, Gerlinde Schwake, and Joachim O. Rädler. "Einzelzellmikroskopie im Hochdurchsatz auf Mikrostrukturen". de. In: *BIOspektrum* 28.7 (Nov. 2022), pp. 723–725. ISSN: 0947-0867, 1868-6249. DOI: 10.1007/s12268-022-1857-8. URL: https://link.springer.com/10.1007/s12268-022-1857-8 (visited on 06/19/2023).

[175] A. Reiser, M. L. Zorn, A. Murschhauser, and Joachim O. Rädler. "Chapter 4: Single Cell Microarrays Fabricated by Microscale Plasma-Initiated Protein Patterning (µPiPP) in Cell-Based Microarrays: Methods and Protocols". In: *Springer New York* (2018), pp. 41–54.

[176] Jürgen Stephan, Felix Keber, Valentin Stierle, Joachim O Rädler, and Philipp Paulitschke. "Single-Cell Optical Distortion Correction and Label-Free 3D Cell Shape Reconstruction on Lattices of Nanostructures". en. In: *Nano Lett.* (2017).

[177] Mirjam Ochsner, Marc R Dusseiller, H Michelle Grandin, Sheila Luna-Morris, Marcus Textor, Viola Vogel, and Michael L Smith. "Micro-well arrays for 3D shape control and high resolution analysis of single cells{". en. In: (2007).

[178] Farzad Sekhavati. "Marker-free detection of progenitor cell differentiation by analysis of Brownian motion in micro-wells". en. In: *Integrative Biology* (2015).

[179] Kurt Thorn. "A quick guide to light microscopy in cell biology". en. In: *Molecular Biology of the Cell* 27 (2016).

[180] Jeff W Lichtman and José-Angel Conchello. "Fluorescence microscopy". In: *Nature Methods* 2 (2005), pp. 910–919. DOI: 10.1038/nmeth817.

[181] Osamu Shimomura, Frank H. Johnson, and Yo Saiga. "Extraction, Purification and Properties of Aequorin, a Bioluminescent Protein from the Luminous Hydromedusan, *Aequorea*". en. In: *Journal of Cellular and Comparative Physiology* 59.3 (June 1962), pp. 223–239. ISSN: 0095-9898, 1553-0809. DOI: 10.1002/jcp.1030590302. URL: https://onlinelibrary.wiley.com/doi/10.1002/jcp.1030590302 (visited on 08/20/2024).

[182] Roger Y. Tsien. "THE GREEN FLUORESCENT PROTEIN". en. In: *Annual Review of Biochemistry* 67.1 (June 1998), pp. 509–544. ISSN: 0066-4154, 1545-4509. DOI: 10.1146/annurev.biochem.67.1.509. URL: https://www.annualreviews.org/doi/10.1146/annurev.biochem.67.1.509 (visited on 06/19/2023).

[183] Martin Chalfie, Yuan Tu, Ghia Euskirchen, William W. Ward, and Douglas C. Prasher. "Green Fluorescent Protein as a Marker for Gene Expression". en. In: *Science* 263.5148 (1994), pp. 802–805. ISSN: 0036-8075.

[184] Roger Heim and Roger Y Tsien. "Engineering green fluorescent protein for improved brightness, longer wavelengths and fluorescence resonance energy transfer". en. In: *Current Biology* 6.2 (Feb. 1996), pp. 178–182. ISSN: 09609822. DOI: 10.1016/S0960-9822(02)00450-5. URL: https://linkinghub.elsevier.com/retrieve/pii/S0960982202004505 (visited on 11/17/2023).

[185] Theodorus W. J. Gadella, Laura Van Weeren, Jente Stouthamer, Mark A. Hink, Anouk H. G. Wolters, Ben N. G. Giepmans, Sylvain Aumonier, Jérôme Dupuy, and Antoine Royant. "mScarlet3: a brilliant and fast-maturing red fluorescent protein". en. In: *Nature Methods* 20.4 (Apr. 2023), pp. 541–545. ISSN: 1548-7091, 1548-7105. DOI: 10.1038/s41592-023-01809-y. URL: https://www.nature.com/articles/s41592-023-01809-y (visited on 08/20/2024).

[186] Benjamin C. Campbell, Maria G. Paez-Segala, Loren L. Looger, Gregory A. Petsko, and Ce Feng Liu. "Chemically stable fluorescent proteins for advanced microscopy". en. In: *Nature Methods* 19.12 (Dec. 2022), pp. 1612–1621. ISSN: 1548-7091, 1548-7105. DOI: 10.1038/s41592-022-01660-7. URL: https://www.nature.com/articles/s41592-022-01660-7 (visited on 10/19/2023).

[187] Annaig J. Rozo, Megan H. Cox, Andrew Devitt, Alice J. Rothnie, and Alan D. Goddard. "Biophysical analysis of lipidic nanoparticles". In: *Methods* 180 (Aug. 2020), pp. 45–55. DOI: https://doi.org/10.1016/j.ymeth.2020.05.001.

[188] Pavel G. Pronkin and Alexander S. Tatikolov. "Photonics of Trimethine Cyanine Dyes as Probes for Biomolecules". en. In: *Molecules* 27.19 (Sept. 2022), p. 6367. ISSN: 1420-3049. DOI: 10.3390/molecules27196367. URL: https://www.mdpi.com/1420-3049/27/19/6367 (visited on 10/09/2024).

[189] Xiaoying Ma, Lei Shi, Buyue Zhang, Lu Liu, Yao Fu, and Xiufeng Zhang. "Recent advances in bioprobes and biolabels based on cyanine dyes". en. In: *Analytical and Bioanalytical Chemistry* 414.16 (July 2022), pp. 4551–4573. ISSN: 1618-2642, 1618-2650. DOI: 10.1007/s00216-022-03995-8. URL: https://link.springer.com/10.1007/s00216-022-03995-8 (visited on 10/09/2024).

[190] Jonathan L. Kirschman, Sushma Bhosle, Daryll Vanover, Emmeline L. Blanchard, Kristin H. Loomis, Chiara Zurla, Kathryn Murray, Blaine C. Lam, and Philip J. Santangelo. "Characterizing exogenous mRNA delivery, trafficking, cytoplasmic release and RNA–protein correlations at the level of single cells". en. In: *Nucleic Acids Research* 45.12 (July 2017), e113–e113. ISSN: 0305-1048, 1362-4962. DOI: 10.1093/nar/gkx290. URL: https://academic.oup.com/nar/article/45/12/e113/3760188 (visited on 07/11/2023).

[191] K. Rombouts, K. Braeckmans, and K. Remaut. "Fluorescent Labeling of Plasmid DNA and mRNA: Gains and Losses of Current Labeling Strategies". en. In: *Bioconjugate Chemistry* 27.2 (Feb. 2016), pp. 280–297. ISSN: 1043-1802, 1520-4812. DOI: 10.1021/acs.bioconjchem.5b00579. URL: https://pubs.acs.org/doi/10.1021/acs.bioconjchem.5b00579 (visited on 01/04/2024).

[192] Daniel Woschée. *PyAMA*. 2020. URL: https://github.com/SoftmatterLMURaedlerGroup/pyama.

[193] Michael Schwarzfischer, Carsten Marr, Jan Krumsiek, Philipp S Hoppe, Timm Schroeder, and Fabian J Theis. "Efficient fluorescence image normalization for time lapse movies". en. In: ().

[194] Carsen Stringer and Marius Pachitariu. *Cellpose3: one-click image restoration for improved cellular segmentation*. en. Feb. 2024. DOI: 10.1101/2024.02.10.579780. URL: http://biorxiv.org/lookup/doi/10.1101/2024.02.10.579780 (visited on 08/22/2024).

[195] Anh-Tuan Dinh, Chinmay Pangarkar, Theo Theofanous, and Samir Mitragotri. "Understanding Intracellular Transport Processes Pertinent to Synthetic Gene Delivery via Stochastic Simulations and Sensitivity Analyses". en. In: *Biophysical Journal* 92.3 (Feb. 2007), pp. 831–846. ISSN: 00063495. DOI: 10.1529/biophysj.106.095521. URL: https://linkinghub.elsevier.com/retrieve/pii/S0006349507708913 (visited on 10/18/2023).

[196] Csanad M. Varga, Klaudyne Hong, and Douglas A. Lauffenburger. "Quantitative Analysis of Synthetic Gene Delivery Vector Design Properties". en. In: *Molecular Therapy* 4.5 (Nov. 2001), pp. 438–446. ISSN: 15250016. DOI: 10.1006/mthe.2001.0475. URL: https://linkinghub.elsevier.com/retrieve/pii/S1525001601904757 (visited on 10/19/2023).

[197] Uri Alon. "Network motifs: theory and experimental approaches". en. In: *Nature Reviews Genetics* 8.6 (June 2007), pp. 450–461. ISSN: 1471-0056, 1471-0064. DOI: 10.1038/nrg2102. URL: https://www.nature.com/articles/nrg2102 (visited on 05/02/2024).

[198] Erel Levine, Zhongge Zhang, Thomas Kuhlman, and Terence Hwa. "Quantitative Characteristics of Gene Regulation by Small RNA". en. In: *PLoS Biology* 5.9 (Aug. 2007). Ed. by Mikhail S Gelfand, e229. ISSN: 1545-7885. DOI: 10.1371/journal.pbio.0050229. URL: https://dx.plos.org/10.1371/journal.pbio.0050229 (visited on 09/09/2024).

[199] Laetitia Malphettes and Martin Fussenegger. "Impact of RNA interference on gene networks". en. In: *Metabolic Engineering* 8.6 (Nov. 2006), pp. 672–683. ISSN: 10967176. DOI: 10.1016/j.ymben.2006.07.005. URL: https://linkinghub.elsevier.com/retrieve/pii/S1096717606000681 (visited on 09/09/2024).

[200] Benjamin Haley and Phillip D Zamore. "Kinetic analysis of the RNAi enzyme complex". en. In: *Nature Structural & Molecular Biology* 11.7 (July 2004), pp. 599–606. ISSN: 1545-9993, 1545-9985. DOI: 10.1038/nsmb780. URL: https://www.nature.com/articles/nsmb780 (visited on 09/09/2024).

[201] Rudolf Gesztelyi, Judit Zsuga, Adam Kemeny-Beke, Balazs Varga, Bela Juhasz, and Arpad Tosaki. "The Hill equation and the origin of quantitative pharmacology". en. In: *Archive for History of Exact Sciences* 66.4 (July 2012), pp. 427–438. ISSN: 0003-9519, 1432-0657. DOI: 10.1007/s00407-012-0098-5. URL: http://link.springer.com/10.1007/s00407-012-0098-5 (visited on 09/10/2024).

[202] Shankar Mukherji, Margaret S Ebert, Grace X Y Zheng, John S Tsang, Phillip A Sharp, and Alexander Van Oudenaarden. "MicroRNAs can generate thresholds in target gene expression". en. In: *Nature Genetics* 43.9 (Sept. 2011), pp. 854–859. ISSN: 1061-4036, 1546-1718. DOI: 10.1038/ng.905. URL: https://www.nature.com/articles/ng.905 (visited on 09/03/2024).

[203] Eshel Ben-Jacob, Inon Cohen, and Herbert Levine. "Cooperative self-organization of microorganisms". en. In: *Advances in Physics* 49.4 (June 2000), pp. 395–554. ISSN: 0001-8732, 1460-6976. DOI: 10.1080/000187300405228. URL: http://www.tandfonline.com/doi/abs/10.1080/000187300405228 (visited on 09/12/2024).

[204] Avigdor Eldar and Michael B. Elowitz. "Functional roles for noise in genetic circuits". en. In: *Nature* 467.7312 (Sept. 2010), pp. 167–173. ISSN: 0028-0836, 1476-4687. DOI: 10.1038/nature09326. URL: https://www.nature.com/articles/nature09326 (visited on 09/12/2024).

[205] Zakary S. Singer, John Yong, Julia Tischler, Jamie A. Hackett, Alphan Altinok, M. Azim Surani, Long Cai, and Michael B. Elowitz. "Dynamic Heterogeneity and DNA Methylation in Embryonic Stem Cells". en. In: *Molecular Cell* 55.2 (July 2014), pp. 319–331. ISSN: 10972765. DOI: 10.1016/j.molcel.2014.06.029. URL: https://linkinghub.elsevier.com/retrieve/pii/S1097276514005632 (visited on 09/10/2024).

[206] Ertugrul M. Ozbudak, Mukund Thattai, Iren Kurtser, Alan D. Grossman, and Alexander Van Oudenaarden. "Regulation of noise in the expression of a single gene". en. In: *Nature Genetics* 31.1 (May 2002), pp. 69–73. ISSN: 1061-4036, 1546-1718. DOI: 10.1038/ng869. URL: https://www.nature.com/articles/ng869z (visited on 09/10/2024).

[207] Cameron P. Bracken, Philip A. Gregory, Natasha Kolesnikoff, Andrew G. Bert, Jun Wang, M. Frances Shannon, and Gregory J. Goodall. "A Double-Negative Feedback Loop between ZEB1-SIP1 and the microRNA-200 Family Regulates Epithelial-Mesenchymal Transition". en. In: *Cancer Research* 68.19 (Oct. 2008), pp. 7846–7854. ISSN: 0008-5472, 1538-7445. DOI: 10.1158/0008-5472.CAN-08-1942. URL: https://aacrjournals.org/cancerres/article/68/19/7846/541234/A-Double-Negative-Feedback-Loop-between-ZEB1-SIP1 (visited on 09/03/2024).

[208] Bojan Ljepoja, Jonathan García-Roman, Ann-Katrin Sommer, Thomas Fröhlich, Georg J. Arnold, Ernst Wagner, and Andreas Roidl. "A proteomic analysis of an in vitro knock-out of miR-200c". en. In: *Scientific Reports* 8.1 (May 2018), p. 6927. ISSN: 2045-2322. DOI: 10.1038/s41598-018-25240-y. URL: https://www.nature.com/articles/s41598-018-25240-y (visited on 10/11/2024).

[209] Shai S. Shen-Orr, Ron Milo, Shmoolik Mangan, and Uri Alon. "Network motifs in the transcriptional regulation network of Escherichia coli". en. In: *Nature Genetics* 31.1 (May 2002), pp. 64–68. ISSN: 1061-4036, 1546-1718. DOI: 10.1038/ng881. URL: https://www.nature.com/articles/ng881z (visited on 09/12/2024).

[210] R Milo, S Shen-Orr, S Itzkovitz, N Kashtan, D Chklovskii, and U Alon. "Network Motifs: Simple Building Blocks of Complex Networks". en. In: 298 (2002).

[211] Denis Thieffry, Araceli M. Huerta, Ernesto Pérez-Rueda, and Julio Collado-Vides. "From specific gene regulation to genomic networks: a global analysis of transcriptional regulation in Escherichia coli". en. In: *BioEssays* 20.5 (Dec. 1998), pp. 433–440. ISSN: 02659247. DOI: 10.1002/(SICI)1521-1878(199805)20:5<433::AID-BIES10>3.0.CO;2-2. URL: https://onlinelibrary.wiley.com/doi/10.1002/(SICI)1521-1878(199805)20:5%3C433::AID-BIES10%3E3.0.CO;2-2 (visited on 09/10/2024).

[212] H.-W. Ma. "An extended transcriptional regulatory network of Escherichia coli and analysis of its hierarchical structure and network motifs". en. In: *Nucleic Acids Research* 32.22 (Dec. 2004), pp. 6643–6649. ISSN: 1362-4962. DOI: 10.1093/nar/gkh1009. URL: https://academic.oup.com/nar/article-lookup/doi/10.1093/nar/gkh1009 (visited on 09/10/2024).

[213] Jörn M. Schmiedel, Sandy L. Klemm, Yannan Zheng, Apratim Sahay, Nils Blüthgen, Debora S. Marks, and Alexander Van Oudenaarden. "MicroRNA control of protein expression noise". en. In: *Science* 348.6230 (Apr. 2015), pp. 128–132. ISSN: 0036-8075, 1095-9203. DOI: 10.1126/science.aaa1738. URL: https://www.science.org/doi/10.1126/science.aaa1738 (visited on 09/03/2024).

[214] Elsi Ferro, Chiara Enrico Bena, Silvia Grigolon, and Carla Bosia. "From Endogenous to Synthetic microRNA-Mediated Regulatory Circuits: An Overview". en. In: *Cells* 8.12 (Nov. 2019), p. 1540. ISSN: 2073-4409. DOI: 10.3390/cells8121540. URL: https://www.mdpi.com/2073-4409/8/12/1540 (visited on 09/03/2024).

[215] Cora Davide, Re Angela, Caselle Michele, and Bussolino Federico. "MicroRNA-mediated regulatory circuits: outlook and perspectives". In: *Phiysical Biology* 14 (2017). DOI: 10.1088/1478-3975/aa6f21.

[216] Uri Alon. *An Introduction to Systems Biology: Design Principles of Biological Circuits*. Chapman & Hall / CRC, 2006.

[217] Leonidas Bleris, Zhen Xie, David Glass, Asa Adadey, Eduardo Sontag, and Yaakov Benenson. "Synthetic incoherent feedforward circuits show adaptation to the amount of their genetic template". en. In: *Molecular Systems Biology* 7.1 (Jan. 2011), p. 519. ISSN: 1744-4292, 1744-4292. DOI: 10.1038/msb.2011.49. URL: https://www.embopress.org/doi/10.1038/msb.2011.49 (visited on 09/03/2024).

[218] Vinay Shimoga, Jacob T White, Yi Li, Eduardo Sontag, and Leonidas Bleris. "Synthetic mammalian transgene negative autoregulation". en. In: *Molecular Systems Biology* 9.1 (Jan. 2013), p. 670. ISSN: 1744-4292, 1744-4292. DOI: 10.1038/msb.2013.27. URL: https://www.embopress.org/doi/10.1038/msb.2013.27 (visited on 09/03/2024).

[219] A Chonn, S.C. Semple, and P.R. Cullis. "Association of blood proteins with large unilamellar liposomes in vivo. Relation to circulation lifetimes." en. In: *Journal of Biological Chemistry* 267.26 (Sept. 1992), pp. 18759–18765. ISSN: 00219258. DOI: 10.1016/S0021-9258(19)37026-7. URL: https://linkinghub.elsevier.com/retrieve/pii/S0021925819370267 (visited on 08/28/2024).

[220] Shuai Liu, Wei Yang, Yunlei Li, and Changqing Sun. "Fetal bovine serum, an important factor affecting the reproducibility of cell experiments". en. In: *Scientific Reports* 13.1 (Feb. 2023), p. 1942. ISSN: 2045-2322. DOI: 10.1038/s41598-023-29060-7. URL: https://www.nature.com/articles/s41598-023-29060-7 (visited on 10/01/2024).

[221] Christiane Brummer. *Mobility of Nucleic Acids in Lipidic Mesophases*. Master thesis. Munich: LMU, 2023.

[222] Xi Chen, Jiwei Cui, Huanli Sun, Markus Müllner, Yan Yan, Ka Fung Noi, Yuan Ping, and Frank Caruso. "Analysing intracellular deformation of polymer capsules using structured illumination microscopy". en. In: *Nanoscale* 8.23 (2016), pp. 11924–11931. ISSN: 2040-3364, 2040-3372. DOI: 10.1039/C6NR02151D. URL: http://xlink.rsc.org/?DOI=C6NR02151D (visited on 09/13/2023).

[223] H.-K. Kim, E. Tuite, B. Nordén, and B.W. Ninham. "Co-ion dependence of DNA nuclease activity suggests hydrophobic cavitation as a potential source of activation energy". en. In: *The European Physical Journal E* 4.4 (Apr. 2001), pp. 411–417. ISSN: 12928941. DOI: 10.1007/s101890170096. URL: http://link.springer.com/10.1007/s101890170096 (visited on 08/30/2024).

[224] Andrea Salis, Luca Cappai, Cristina Carucci, Drew F. Parsons, and Maura Monduzzi. "Specific Buffer Effects on the Intermolecular Interactions among Protein Molecules at Physiological pH". en. In: *The Journal of Physical Chemistry Letters* 11.16 (Aug. 2020), pp. 6805–6811. ISSN: 1948-7185, 1948-7185. DOI: 10.1021/acs.jpclett.0c01900. URL: https://pubs.acs.org/doi/10.1021/acs.jpclett.0c01900 (visited on 08/30/2024).

[225] Monica Mura, Ben Humphreys, Jennifer Gilbert, Andrea Salis, and Tommy Nylander. "Cation and buffer specific effects on the DNA-lipid interaction". en. In: *Colloids and Surfaces B: Biointerfaces* 223 (Mar. 2023), p. 113187. ISSN: 09277765. DOI: 10.1016/j.colsurfb.2023.113187. URL: https://linkinghub.elsevier.com/retrieve/pii/S0927776523000656 (visited on 08/30/2024).

[226] Pierandrea Lo Nostro and Barry W. Ninham. "Hofmeister Phenomena: An Update on Ion Specificity in Biology". en. In: *Chemical Reviews* 112.4 (Apr. 2012), pp. 2286–2322. ISSN: 0009-2665, 1520-6890. DOI: 10.1021/cr200271j. URL: https://pubs.acs.org/doi/10.1021/cr200271j (visited on 08/30/2024).

[227] Michele Schlich, Roberto Palomba, Gabriella Costabile, Shoshy Mizrahy, Martina Pannuzzo, Dan Peer, and Paolo Decuzzi. "Cytosolic delivery of nucleic acids: The case of ionizable lipid nanoparticles". en. In: *Bioengineering & Translational Medicine* 6.2 (May 2021). ISSN: 2380-6761, 2380-6761. DOI: 10.1002/btm2.10213. URL: https://onlinelibrary.wiley.com/doi/10.1002/btm2.10213 (visited on 07/10/2023).

[228] Alon Raveh, Michael Margaliot, Eduardo D. Sontag, and Tamir Tuller. "A model for competition for ribosomes in the cell". en. In: *Journal of The Royal Society Interface* 13.116 (Mar. 2016), p. 20151062. ISSN: 1742-5689, 1742-5662. DOI: 10.1098/rsif.2015.1062. URL: https://royalsocietypublishing.org/doi/10.1098/rsif.2015.1062 (visited on 09/18/2024).

[229] Kevin C. Cassidy, Roni M. Lahr, Jesse C. Kaminsky, Stephanie Mack, Bruno D. Fonseca, Subha R. Das, Andrea J. Berman, and Jacob D. Durrant. "Capturing the Mechanism Underlying TOP mRNA Binding to LARP1". en. In: *Structure* 27.12 (Dec. 2019), 1771–1781.e5. ISSN: 09692126. DOI: 10.1016/j.str.2019.10.006. URL: https://linkinghub.elsevier.com/retrieve/pii/S0969212619303478 (visited on 08/28/2024).

[230] Jeff Bezanson, Stefan Karpinski, and Viral B. Shah. *The Julia Programming Language*. URL: https://julialang.org/ (visited on 10/19/2023).

[231] Shlomi Reuveni, Isaac Meilijson, Martin Kupiec, Eytan Ruppin, and Tamir Tuller. "Genome-Scale Analysis of Translation Elongation with a Ribosome Flow Model". en. In: *PLoS Computational Biology* 7.9 (Sept. 2011). Ed. by Wyeth W. Wasserman, e1002127. ISSN: 1553-7358. DOI: 10.1371/journal.pcbi.1002127. URL: https://dx.plos.org/10.1371/journal.pcbi.1002127 (visited on 09/20/2024).

[232] Sebastian Pechmann and Judith Frydman. "Evolutionary conservation of codon optimality reveals hidden signatures of cotranslational folding". en. In: *Nature Structural & Molecular Biology* 20.2 (Feb. 2013), pp. 237–243. ISSN: 1545-9993, 1545-9985. DOI: 10.1038/nsmb.2466. URL: https://www.nature.com/articles/nsmb.2466 (visited on 03/11/2024).

[233] Suzan Ruijtenberg, Stijn Sonneveld, Tao Ju Cui, Ive Logister, Dion De Steenwinkel, Yao Xiao, Ian J. MacRae, Chirlmin Joo, and Marvin E. Tanenbaum. "mRNA structural dynamics shape Argonaute-target interactions". en. In: *Nature Structural & Molecular Biology* 27.9 (Sept. 2020), pp. 790–801. ISSN: 1545-9993, 1545-9985. DOI: 10.1038/s41594-020-0461-1. URL: https://www.nature.com/articles/s41594-020-0461-1 (visited on 11/07/2023).

[234] Yuriko Harigaya and Roy Parker. "No-go decay: a quality control mechanism for RNA in translation". en. In: *WIREs RNA* 1.1 (July 2010), pp. 132–141. ISSN: 1757-7004, 1757-7012. DOI: 10.1002/wrna.17. URL: https://wires.onlinelibrary.wiley.com/doi/10.1002/wrna.17 (visited on 03/11/2024).

[235] Ramona Weber, Lara Wohlbold, and Chung-Te Chang. *Human DDX6 regulates translation and decay of inefficiently translated mRNAs*. en. preprint. Jan. 2024. DOI: 10.7554/eLife.92426.1. URL: https://elifesciences.org/reviewed-preprints/92426v1 (visited on 03/12/2024).

[236] Katalin Karikó and Drew Weissman. "Naturally occurring nucleoside modifications suppress the immunostimulatory activity of RNA: Implication for therapeutic RNA development". en. In: (2007).

[237] Hyewon Youn and June-Key Chung. "Modified mRNA as an alternative to plasmid DNA (pDNA) for transcript replacement and vaccination therapy". en. In: *Expert Opinion on Biological Therapy* 15.9 (Sept. 2015), pp. 1337–1348. ISSN: 1471-2598, 1744-7682. DOI: 10.1517/14712598.2015.1057563. URL: http://www.tandfonline.com/doi/full/10.1517/14712598.2015.1057563 (visited on 06/19/2023).

[238] Mehrije Ferizi, Carolin Leonhardt, Christian Meggle, Manish K. Aneja, Carsten Rudolph, Christian Plank, and Joachim O. Rädler. "Stability analysis of chemically modified mRNA using micropattern-based single-cell arrays". en. In: *Lab on a Chip* 15.17 (2015), pp. 3561–3571. ISSN: 1473-0197, 1473-0189. DOI: 10.1039/C5LC00749F. URL: http://xlink.rsc.org/?DOI=C5LC00749F (visited on 06/19/2023).

[239] Carol J. Wilusz, Michael Wormington, and Stuart W. Peltz. "The cap-to-tail guide to mRNA turnover". en. In: *Nature Reviews Molecular Cell Biology* 2.4 (Apr. 2001), pp. 237–246. ISSN: 1471-0072, 1471-0080. DOI: 10.1038/35067025. URL: https://www.nature.com/articles/35067025 (visited on 06/19/2023).

[240] Silke Holtkamp, Sebastian Kreiter, Abderraouf Selmi, Petra Simon, Michael Koslowski, Christoph Huber, Özlem Türeci, and Ugur Sahin. "Modification of antigen-encoding RNA increases stability, translational efficacy, and T-cell stimulatory capacity of dendritic cells". en. In: *Blood* 108.13 (Dec. 2006), pp. 4009–4017. ISSN: 0006-4971, 1528-0020. DOI: 10.1182/blood-2006-04-015024. URL: https://ashpublications.org/blood/article/108/13/4009/6595/Modification-of-antigenencoding-RNA-increases (visited on 06/19/2023).

[241] Alexandra E Grier, Stephen Burleigh, Jaya Sahni, Courtnee A Clough, Victoire Cardot, Dongwook C Choe, Michelle C Krutein, David J Rawlings, Michael C Jensen, Andrew M Scharenberg, and Kyle Jacoby. "pEVL: A Linear Plasmid for Generating mRNA IVT Templates With Extended Encoded Poly(A) Sequences". en. In: *Molecular Therapy - Nucleic Acids* 5 (2016), e306. ISSN: 21622531. DOI: 10.1038/mtna.2016.21. URL: https://linkinghub.elsevier.com/retrieve/pii/S2162253117300355 (visited on 06/19/2023).

[242] Lori A. Passmore and Jeff Coller. "Roles of mRNA poly(A) tails in regulation of eukaryotic gene expression". en. In: *Nature Reviews Molecular Cell Biology* 23.2 (Feb. 2022), pp. 93–106. ISSN: 1471-0072, 1471-0080. DOI: 10.1038/s41580-021-00417-y. URL: https://www.nature.com/articles/s41580-021-00417-y (visited on 06/19/2023).

[243] Bin Li, Xiao Luo, and Yizhou Dong. "Effects of Chemically Modified Messenger RNA on Protein Expression". en. In: *Bioconjugate Chemistry* 27.3 (Mar. 2016), pp. 849–853. ISSN: 1043-1802, 1520-4812. DOI: 10.1021/acs.bioconjchem.6b00090. URL: https://pubs.acs.org/doi/10.1021/acs.bioconjchem.6b00090 (visited on 06/19/2023).

[244] Maher Al-Saif and Khalid Sa Khabar. "UU/UA Dinucleotide Frequency Reduction in Coding Regions Results in Increased mRNA Stability and Protein Expression". en. In: *Molecular Therapy* 20.5 (May 2012), pp. 954–959. ISSN: 15250016. DOI: 10.1038/mt.2012.29. URL: https://linkinghub.elsevier.com/retrieve/pii/S1525001616319359 (visited on 06/19/2023).

[245] Carl D. Novina and Phillip A. Sharp. "The RNAi revolution". en. In: *Nature* 430.6996 (July 2004), pp. 161–164. ISSN: 0028-0836, 1476-4687. DOI: 10.1038/430161a. URL: https://www.nature.com/articles/430161a (visited on 06/19/2023).

[246] Kazuki Saito, Hanna Kratzat, Annabelle Campbell, Robert Buschauer, A. Maxwell Burroughs, Otto Berninghausen, L. Aravind, Rachel Green, Roland Beckmann, and Allen R. Buskirk. "Ribosome collisions induce mRNA cleavage and ribosome rescue in bacteria". en. In: *Nature* 603.7901 (Mar. 2022), pp. 503–508. ISSN: 0028-0836, 1476-4687. DOI: 10.1038/s41586-022-04416-7. URL: https://www.nature.com/articles/s41586-022-04416-7 (visited on 06/19/2023).

[247] Ashrut Narula, James Ellis, J. Matthew Taliaferro, and Olivia S. Rissland. "Coding regions affect mRNA stability in human cells". en. In: *RNA* 25.12 (Dec. 2019), pp. 1751–1764. ISSN: 1355-8382, 1469-9001. DOI: 10.1261/rna.073239.119. URL: http://rnajournal.cshlp.org/lookup/doi/10.1261/rna.073239.119 (visited on 03/11/2024).

[248] Yuichiro Mishima, Peixun Han, Kota Ishibashi, Seisuke Kimura, and Shintaro Iwasaki. "Ribosome slowdown triggers codon-mediated mRNA decay independently of ribosome quality control". en. In: *The EMBO Journal* 41.5 (Mar. 2022), e109256. ISSN: 0261-4189, 1460-2075. DOI: 10.15252/embj.2021109256. URL: https://www.embopress.org/doi/10.15252/embj.2021109256 (visited on 06/19/2023).

[249] Sarah M. Richardson, Sarah J. Wheelan, Robert M. Yarrington, and Jef D. Boeke. "GeneDesign: Rapid, automated design of multikilobase synthetic genes". en. In: *Genome Research* 16.4 (Apr. 2006), pp. 550–556. ISSN: 1088-9051. DOI: 10.1101/gr.4431306. URL: http://genome.cshlp.org/lookup/doi/10.1101/gr.4431306 (visited on 03/11/2024).

[250] Wenfeng Qian, Jian-Rong Yang, Nathaniel M. Pearson, Calum Maclean, and Jianzhi Zhang. "Balanced Codon Usage Optimizes Eukaryotic Translational Efficiency". en. In: *PLoS Genetics* 8.3 (Mar. 2012). Ed. by Harmit S. Malik, e1002603. ISSN: 1553-7404. DOI: 10.1371/journal.pgen.1002603. URL: https://dx.plos.org/10.1371/journal.pgen.1002603 (visited on 03/11/2024).

[251] Vincent P. Mauro and Stephen A. Chappell. "A critical analysis of codon optimization in human therapeutics". en. In: *Trends in Molecular Medicine* 20.11 (Nov. 2014), pp. 604–613. ISSN: 14714914. DOI: 10.1016/j.molmed.2014.09.003. URL: https://linkinghub.elsevier.com/retrieve/pii/S1471491414001403 (visited on 03/11/2024).

[252] Vladimir Presnyak, Najwa Alhusaini, Ying-Hsin Chen, Sophie Martin, Nathan Morris, Nicholas Kline, Sara Olson, David Weinberg, Kristian E. Baker, Brenton R. Graveley, and Jeff Coller. "Codon Optimality Is a Major Determinant of mRNA Stability". en. In: *Cell* 160.6 (Mar. 2015), pp. 1111–1124. ISSN: 00928674. DOI: 10.1016/j.cell.2015.02.029. URL: https://linkinghub.elsevier.com/retrieve/pii/S0092867415001956 (visited on 06/19/2023).

[253] Elysia M Hollams, Keith M Giles, Andrew M Thomson, and Peter J Leedman. "mRNA Stability and the Control of Gene Expression: Implications for Human Disease". en. In: *Protein Interactions* ().

[254] Siv G E Andersson and C G Kurland. "Codon Preferences in Free-Living Microorganisms". en. In: *MICROBIOL. REV.* 54 (1990).

[255] Christina E. Brule and Elizabeth J. Grayhack. "Synonymous Codons: Choose Wisely for Expression". en. In: *Trends in Genetics* 33.4 (Apr. 2017), pp. 283–297. ISSN: 01689525. DOI: 10.1016/j.tig.2017.02.001. URL: https://linkinghub.elsevier.com/retrieve/pii/S0168952517300227 (visited on 06/19/2023).

[256] Joshua B. Plotkin and Grzegorz Kudla. "Synonymous but not the same: the causes and consequences of codon bias". en. In: *Nature Reviews Genetics* 12.1 (Jan. 2011), pp. 32–42. ISSN: 1471-0056, 1471-0064. DOI: 10.1038/nrg2899. URL: https://www.nature.com/articles/nrg2899 (visited on 03/04/2024).

[257] Gavin Hanson and Jeff Coller. "Codon optimality, bias and usage in translation and mRNA decay". en. In: *Nature Reviews Molecular Cell Biology* 19.1 (Jan. 2018), pp. 20–30. ISSN: 1471-0072, 1471-0080. DOI: 10.1038/nrm.2017.91. URL: https://www.nature.com/articles/nrm.2017.91 (visited on 06/19/2023).

[258] H Akashi. "Synonymous codon usage in Drosophila melanogaster: natural selection and translational accuracy." en. In: *Genetics* 136.3 (Mar. 1994), pp. 927–935. ISSN: 1943-2631. DOI: 10.1093/genetics/136.3.927. URL: https://academic.oup.com/genetics/article/136/3/927/6012271 (visited on 06/19/2023).

[259] D. Allan Drummond and Claus O. Wilke. "Mistranslation-Induced Protein Misfolding as a Dominant Constraint on Coding-Sequence Evolution". en. In: *Cell* 134.2 (July 2008), pp. 341–352. ISSN: 00928674. DOI: 10.1016/j.cell.2008.05.042. URL: https://linkinghub.elsevier.com/retrieve/pii/S0092867408007058 (visited on 06/19/2023).

[260] Gene-Wei Li, Eugene Oh, and Jonathan S. Weissman. "The anti-Shine–Dalgarno sequence drives translational pausing and codon choice in bacteria". en. In: *Nature* 484.7395 (Apr. 2012), pp. 538–541. ISSN: 0028-0836, 1476-4687. DOI: 10.1038/nature10965. URL: https://www.nature.com/articles/nature10965 (visited on 03/04/2024).

[261] Tessa E.F. Quax, Yuri I. Wolf, Jasper J. Koehorst, Omri Wurtzel, Richard van der Oost, Wenqi Ran, Fabian Blombach, Kira S. Makarova, Stan J.J. Brouns, Anthony C. Forster, E. Gerhart H. Wagner, Rotem Sorek, Eugene V. Koonin, and John van der Oost. "Differential Translation Tunes Uneven Production of Operon-Encoded Proteins". en. In: *Cell Reports* 4.5 (Sept. 2013), pp. 938–944. ISSN: 22111247. DOI: 10.1016/j.celrep.2013.07.049. URL: https://linkinghub.elsevier.com/retrieve/pii/S2211124713004117 (visited on 03/04/2024).

[262] Shiping Zhang, Emanuel Goldman, and Geoffrey Zubay. "Clustering of Low Usage Codons and Ribosome Movement". en. In: *Journal of Theoretical Biology* 170.4 (Oct. 1994), pp. 339–354. ISSN: 00225193. DOI: 10.1006/jtbi.1994.1196. URL: https://linkinghub.elsevier.com/retrieve/pii/S0022519384711969 (visited on 03/11/2024).

[263] Chien-Hung Yu, Yunkun Dang, Zhipeng Zhou, Cheng Wu, Fangzhou Zhao, Matthew S. Sachs, and Yi Liu. "Codon Usage Influences the Local Rate of Translation Elongation to Regulate Co-translational Protein Folding". en. In: *Molecular Cell* 59.5 (Sept. 2015), pp. 744–754. ISSN: 10972765. DOI: 10.1016/j.molcel.2015.07.018. URL: https://linkinghub.elsevier.com/retrieve/pii/S1097276515005766 (visited on 03/11/2024).

[264] Aditya Radhakrishnan, Ying-Hsin Chen, Sophie Martin, Najwa Alhusaini, Rachel Green, and Jeff Coller. "The DEAD-Box Protein Dhh1p Couples mRNA Decay and Translation by Monitoring Codon Optimality". en. In: *Cell* 167.1 (Sept. 2016), 122–132.e9. ISSN: 00928674. DOI: 10.1016/j.cell.2016.08.053. URL: https://linkinghub.elsevier.com/retrieve/pii/S0092867416311503 (visited on 02/06/2024).

[265] Daniel Tarrant and Tobias Von Der Haar. "Synonymous codons, ribosome speed, and eukaryotic gene expression regulation". en. In: *Cellular and Molecular Life Sciences* 71.21 (Nov. 2014), pp. 4195–4206. ISSN: 1420-682X, 1420-9071. DOI: 10.1007/s00018-014-1684-2. URL: http://link.springer.com/10.1007/s00018-014-1684-2 (visited on 04/15/2024).

[266] Paul M. Sharp, Therese M.F. Tuohy, and Krzysztof R. Mosurski. "Codon usage in yeast: cluster analysis clearly differentiates highly and lowly expressed genes". en. In: *Nucleic Acids Research* 14.13 (1986), pp. 5125–5143. ISSN: 0305-1048, 1362-4962. DOI: 10.1093/nar/14.13.5125. URL: https://academic.oup.com/nar/article-lookup/doi/10.1093/nar/14.13.5125 (visited on 03/04/2024).

[267] Orna Man and Yitzhak Pilpel. "Differential translation efficiency of orthologous genes is involved in phenotypic divergence of yeast species". en. In: *Nature Genetics* 39.3 (Mar. 2007), pp. 415–421. ISSN: 1061-4036, 1546-1718. DOI: 10.1038/ng1967. URL: https://www.nature.com/articles/ng1967 (visited on 03/04/2024).

[268] Tamir Tuller, Yedael Y. Waldman, Martin Kupiec, and Eytan Ruppin. "Translation efficiency is determined by both codon bias and folding energy". en. In: *Proceedings of the National Academy of Sciences* 107.8 (Feb. 2010), pp. 3645–3650. ISSN: 0027-8424, 1091-6490. DOI: 10.1073/pnas.0909910107. URL: https://pnas.org/doi/full/10.1073/pnas.0909910107 (visited on 03/04/2024).

[269] Chung-Jung Tsai, Zuben E. Sauna, Chava Kimchi-Sarfaty, Suresh V. Ambudkar, Michael M. Gottesman, and Ruth Nussinov. "Synonymous Mutations and Ribosome Stalling Can Lead to Altered Folding Pathways and Distinct Minima". In: *J Mol Biol.* 383(2) (2008). DOI: 10.1016/j.jmb.2008.08.012.

[270] Paul M. Sharp and Wen-Hsiung Li. "The codon adaptation index-a measure of directional synonymous codon usage bias, and its potential applications". en. In: *Nucleic Acids Research* 15.3 (1987), pp. 1281–1295. ISSN: 0305-1048, 1362-4962. DOI: 10.1093/nar/15.3.1281. URL: https://academic.oup.com/nar/article-lookup/doi/10.1093/nar/15.3.1281 (visited on 03/11/2024).

[271] Anabel Rodriguez, Gabriel Wright, Scott Emrich, and Patricia L. Clark. "%MinMax: A versatile tool for calculating and comparing synonymous codon usage and its impact on protein folding". en. In: *Protein Science* 27.1 (Jan. 2018), pp. 356–362. ISSN: 0961-8368, 1469-896X. DOI: 10.1002/pro.3336. URL: https://onlinelibrary.wiley.com/doi/10.1002/pro.3336 (visited on 03/11/2024).

[272] Janaina De Freitas Nascimento, Steven Kelly, Jack Sunter, and Mark Carrington. "Codon choice directs constitutive mRNA levels in trypanosomes". en. In: *eLife* 7 (Mar. 2018), e32467. ISSN: 2050-084X. DOI: 10.7554/eLife.32467. URL: https://elifesciences.org/articles/32467 (visited on 03/11/2024).

[273] Michay Diez, Santiago Gerardo Medina-Muñoz, Luciana Andrea Castellano, Gabriel Da Silva Pescador, Qiushuang Wu, and Ariel Alejandro Bazzini. "iCodon customizes gene expression based on the codon composition". en. In: *Scientific Reports* 12.1 (July 2022), p. 12126. ISSN: 2045-2322. DOI: 10.1038/s41598-022-15526-7. URL: https://www.nature.com/articles/s41598-022-15526-7 (visited on 03/11/2024).

[274] He Zhang, Liang Zhang, Ang Lin, Congcong Xu, Ziyu Li, Kaibo Liu, Boxiang Liu, Xiaopin Ma, Fanfan Zhao, Huiling Jiang, Chunxiu Chen, Haifa Shen, Hangwen Li, David H. Mathews, Yujian Zhang, and Liang Huang. "Algorithm for optimized mRNA design improves stability and immunogenicity". en. In: *Nature* 621.7978 (Sept. 2023), pp. 396–403. ISSN: 0028-0836, 1476-4687. DOI: 10.1038/s41586-023-06127-z. URL: https://www.nature.com/articles/s41586-023-06127-z (visited on 03/11/2024).

[275] Jan-Hendrik Trösemeier, Sophia Rudorf, Holger Loessner, Benjamin Hofner, Andreas Reuter, Thomas Schulenborg, Ina Koch, Isabelle Bekeredjian-Ding, Reinhard Lipowsky, and Christel Kamp. "Optimizing the dynamics of protein expression". en. In: *Scientific Reports* 9.1 (May 2019), p. 7511. ISSN: 2045-2322. DOI: 10.1038/s41598-019-43857-5. URL: https://www.nature.com/articles/s41598-019-43857-5 (visited on 06/19/2023).

[276] Namiko Mitarai, Kim Sneppen, and Steen Pedersen. "Ribosome Collisions and Translation Efficiency: Optimization by Codon Usage and mRNA Destabilization". en. In: *Journal of Molecular Biology* 382.1 (Sept. 2008), pp. 236–245. ISSN: 00222836. DOI: 10.1016/j.jmb.2008.06.068. URL: https://linkinghub.elsevier.com/retrieve/pii/S002228360800795X (visited on 02/28/2024).

[277] Karole N. D'Orazio and Rachel Green. "Ribosome states signal RNA quality control". en. In: *Molecular Cell* 81.7 (Apr. 2021), pp. 1372–1383. ISSN: 10972765. DOI: 10.1016/j.molcel.2021.02.022. URL: https://linkinghub.elsevier.com/retrieve/pii/S1097276521001325 (visited on 02/28/2024).

[278] Christopher J Shoemaker and Rachel Green. "Translation drives mRNA quality control". en. In: *Nature Structural & Molecular Biology* 19.6 (June 2012), pp. 594–601. ISSN: 1545-9993, 1545-9985. DOI: 10.1038/nsmb.2301. URL: https://www.nature.com/articles/nsmb.2301 (visited on 09/20/2023).

[279] Sophia Rudorf and Reinhard Lipowsky. "Protein Synthesis in E. coli: Dependence of Codon-Specific Elongation on tRNA Concentration and Codon Usage". en. In: *PLOS ONE* 10.8 (Aug. 2015). Ed. by Hans-Joachim Wieden, e0134994. ISSN: 1932-6203. DOI: 10.1371/journal.pone.0134994. URL: https://dx.plos.org/10.1371/journal.pone.0134994 (visited on 06/19/2023).

[280] M.A. García, E.F. Meurs, and M. Esteban. "The dsRNA protein kinase PKR: Virus and cell control". en. In: *Biochimie* 89.6-7 (June 2007), pp. 799–811. ISSN: 03009084. DOI: 10.1016/j.biochi.2007.03.001. URL: https://linkinghub.elsevier.com/retrieve/pii/S030090840700051X (visited on 10/04/2024).

[281] Chuncheng Hao, Ruping Shao, Uma Raju, Bingliang Fang, Stephen G. Swisher, and Apar Pataer. "Accumulation of RNA-dependent protein kinase (PKR) in the nuclei of lung cancer cells mediates radiation resistance". en. In: *Oncotarget* 7.25 (June 2016), pp. 38235–38242. ISSN: 1949-2553. DOI: 10.18632/oncotarget.9428. URL: https://www.oncotarget.com/lookup/doi/10.18632/oncotarget.9428 (visited on 10/04/2024).

[282] Anthony J Veltri, Karole N D'Orazio, Laura N Lessen, Raphael Loll-Krippleber, Grant W Brown, and Rachel Green. "Distinct elongation stalls during translation are linked with distinct pathways for mRNA degradation". en. In: *eLife* 11 (July 2022), e76038. ISSN: 2050-084X. DOI: 10.7554/eLife.76038. URL: https://elifesciences.org/articles/76038 (visited on 06/19/2023).

[283] Carrie L. Simms, Liewei L. Yan, and Hani S. Zaher. "Ribosome Collision Is Critical for Quality Control during No-Go Decay". en. In: *Molecular Cell* 68.2 (Oct. 2017), 361–373.e5. ISSN: 10972765. DOI: 10.1016/j.molcel.2017.08.019. URL: https://linkinghub.elsevier.com/retrieve/pii/S1097276517306160 (visited on 03/11/2024).

[284] Daniel H. Goldman, Nathan M. Livingston, Jonathan Movsik, Bin Wu, and Rachel Green. "Live-cell imaging reveals kinetic determinants of quality control triggered by ribosome stalling". en. In: *Molecular Cell* 81.8 (Apr. 2021), 1830–1840.e8. ISSN: 10972765. DOI: 10.1016/j.molcel.2021.01.029. URL: https://linkinghub.elsevier.com/retrieve/pii/S1097276521000496 (visited on 06/19/2023).

[285] Toshifumi Inada and Roland Beckmann. "Mechanisms of Translation-coupled Quality Control". en. In: *Journal of Molecular Biology* 436.6 (Mar. 2024), p. 168496. ISSN: 00222836. DOI: 10.1016/j.jmb.2024.168496. URL: https://linkinghub.elsevier.com/retrieve/pii/S0022283624000688 (visited on 03/11/2024).

[286] Tamir Tuller and Hadas Zur. "Multiple roles of the coding sequence 5 end in gene expression regulation". en. In: *Nucleic Acids Research* 43.1 (Jan. 2015), pp. 13–28. ISSN: 1362-4962, 0305-1048. DOI: 10.1093/nar/gku1313. URL: http://academic.oup.com/nar/article/43/1/13/2903398/Multiple-roles-of-the-coding-sequence-5-end-in (visited on 10/04/2024).

[287] D H Bechhofer and K H Zen. "Mechanism of erythromycin-induced ermC mRNA stability in Bacillus subtilis". en. In: *Journal of Bacteriology* 171.11 (Nov. 1989), pp. 5803–5811. ISSN: 0021-9193, 1098-5530. DOI: 10.1128/jb.171.11.5803-5811.1989. URL: https://journals.asm.org/doi/10.1128/jb.171.11.5803-5811.1989 (visited on 03/11/2024).

[288] F. Braun. "Ribosomes inhibit an RNase E cleavage which induces the decay of the rpsO mRNA of Escherichia-coli". en. In: *The EMBO Journal* 17.16 (Aug. 1998), pp. 4790–4797. ISSN: 14602075. DOI: 10.1093/emboj/17.16.4790. URL: http://emboj.embopress.org/cgi/doi/10.1093/emboj/17.16.4790 (visited on 06/19/2023).

[289] Atilio Deana and Joel G Belasco. "Lost in translation: the influence of ribosomes on bacterial mRNA decay". en. In: *GENES & DEVELOPMENT* 19 (2005), pp. 2526–2533. ISSN: 0890-9369/05.

[290] Roula Daou-Chabo, Nathalie Mathy, Lionel Bénard, and Ciarán Condon. "Ribosomes initiating translation of the *hbs* mRNA protect it from 5-to-3 exoribonucleolytic degradation by RNase J1". en. In: *Molecular Microbiology* 71.6 (Mar. 2009), pp. 1538–1550. ISSN: 0950-382X, 1365-2958. DOI: 10.1111/j.1365-2958.2009.06620.x. URL: https://onlinelibrary.wiley.com/doi/10.1111/j.1365-2958.2009.06620.x (visited on 03/12/2024).

[291] Margit Pedersen, Søren Nissen, Namiko Mitarai, Sine Lo Svenningsen, Kim Sneppen, and Steen Pedersen. "The Functional Half-Life of an mRNA Depends on the Ribosome Spacing in an Early Coding Region". en. In: *Journal of Molecular Biology* 407.1 (Mar. 2011), pp. 35–44. ISSN: 00222836. DOI: 10.1016/j.jmb.2011.01.025. URL: https://linkinghub.elsevier.com/retrieve/pii/S0022283611000544 (visited on 06/19/2023).

[292] Carlus Deneke, Reinhard Lipowsky, and Angelo Valleriani. "Effect of ribosome shielding on mRNA stability". en. In: *Physical Biology* 10.4 (July 2013), p. 046008. ISSN: 1478-3967, 1478-3975. DOI: 10.1088/1478-3975/10/4/046008. URL: https://iopscience.iop.org/article/10.1088/1478-3975/10/4/046008 (visited on 06/19/2023).

[293] Ajeet K. Sharma, Johannes Venezian, Ayala Shiber, Günter Kramer, Bernd Bukau, and Edward P. O'Brien. "Combinations of slow-translating codon clusters can increase mRNA half-life in *Saccharomyces cerevisiae*". en. In: *Proceedings of the National Academy of Sciences* 118.51 (Dec. 2021), e2026362118. ISSN: 0027-8424, 1091-6490. DOI: 10.1073/pnas.2026362118. URL: https://pnas.org/doi/full/10.1073/pnas.2026362118 (visited on 06/19/2023).

[294] Stefan Ludwig Ameres, Javier Martinez, and Renée Schroeder. "Molecular Basis for Target RNA Recognition and Cleavage by Human RISC". en. In: *Cell* 130.1 (July 2007), pp. 101–112. ISSN: 00928674. DOI: 10.1016/j.cell.2007.04.037. URL: https://linkinghub.elsevier.com/retrieve/pii/S0092867407005831 (visited on 11/07/2023).

[295] Kirk M Brown, Chia-ying Chu, and Tariq M Rana. "Target accessibility dictates the potency of human RISC". en. In: *Nature Structural & Molecular Biology* 12.5 (May 2005), pp. 469–470. ISSN: 1545-9993, 1545-9985. DOI: 10.1038/nsmb931. URL: https://www.nature.com/articles/nsmb931 (visited on 11/06/2023).

[296] Institute for Theoretical Chemistry — University of Vienna. *RNAfold*. 2023. URL: http://rna.tbi.univie.ac.at/cgi-bin/RNAWebSuite/RNAfold.cgi.

[297] Daniel B. Goodman, George M. Church, and Sriram Kosuri. "Causes and Effects of N-Terminal Codon Bias in Bacterial Genes". en. In: *Science* 342.6157 (Oct. 2013), pp. 475–479. ISSN: 0036-8075, 1095-9203. DOI: 10.1126/science.1241934. URL: https://www.science.org/doi/10.1126/science.1241934 (visited on 10/04/2024).

[298] Marilyn Kozak. "Regulation of translation via mRNA structure in prokaryotes and eukaryotes". en. In: *Gene* 361 (Nov. 2005), pp. 13–37. ISSN: 03781119. DOI: 10.1016/j.gene.2005.06.037. URL: https://linkinghub.elsevier.com/retrieve/pii/S0378111905004348 (visited on 10/04/2024).

[299] Grzegorz Kudla, Andrew W. Murray, David Tollervey, and Joshua B. Plotkin. "Coding-Sequence Determinants of Gene Expression in *Escherichia coli*". en. In: *Science* 324.5924 (Apr. 2009), pp. 255–258. ISSN: 0036-8075, 1095-9203. DOI: 10.1126/science.1170160. URL: https://www.science.org/doi/10.1126/science.1170160 (visited on 10/04/2024).

[300] Tamir Tuller, Isana Veksler-Lublinsky, Nir Gazit, Martin Kupiec, Eytan Ruppin, and Michal Ziv-Ukelson. "Composite effects of gene determinants on the translation speed and density of ribosomes". en. In: *Genome Biology* 12.11 (2011), R110. ISSN: 1465-6906. DOI: 10.1186/gb-2011-12-11-r110. URL: http://genomebiology.biomedcentral.com/articles/10.1186/gb-2011-12-11-r110 (visited on 10/04/2024).

[301] M Kozak. "Downstream secondary structure facilitates recognition of initiator codons by eukaryotic ribosomes." en. In: *Proceedings of the National Academy of Sciences* 87.21 (Nov. 1990), pp. 8301–8305. ISSN: 0027-8424, 1091-6490. DOI: 10.1073/pnas.87.21.8301. URL: https://pnas.org/doi/full/10.1073/pnas.87.21.8301 (visited on 10/04/2024).

[302] Hiro-oki Iwakawa and Yukihide Tomari. "Life of RISC: Formation, action, and degradation of RNA-induced silencing complex". en. In: *Molecular Cell* 82.1 (Jan. 2022), pp. 30–43. ISSN: 10972765. DOI: 10.1016/j.molcel.2021.11.026. URL: https://linkinghub.elsevier.com/retrieve/pii/S1097276521010285 (visited on 10/25/2023).

[303] Ashley J. Pratt and Ian J. MacRae. "The RNA-induced Silencing Complex: A Versatile Gene-silencing Machine". en. In: *Journal of Biological Chemistry* 284.27 (July 2009), pp. 17897–17901. ISSN: 00219258. DOI: 10.1074/jbc.R900012200. URL: https://linkinghub.elsevier.com/retrieve/pii/S002192582055549X (visited on 11/07/2023).

[304] Bernhard Kirchmair. *RNA Quantification in Lipid Nanoparticles Using Fluorescence Correlation Spectroscopy*. en. Master thesis. LMU Munich, 2024.

[305] Gaurav Sahay, Daria Y. Alakhova, and Alexander V. Kabanov. "Endocytosis of nanomedicines". en. In: *Journal of Controlled Release* 145.3 (Aug. 2010), pp. 182–195. ISSN: 01683659. DOI: 10.1016/j.jconrel.2010.01.036. URL: https://linkinghub.elsevier.com/retrieve/pii/S0168365910002075 (visited on 07/26/2023).

[306] John C. Burnett and John J. Rossi. "RNA-Based Therapeutics: Current Progress and Future Prospects". en. In: *Chemistry & Biology* 19.1 (Jan. 2012), pp. 60–71. ISSN: 10745521. DOI: 10.1016/j.chembiol.2011.12.008. URL: https://linkinghub.elsevier.com/retrieve/pii/S1074552111004595 (visited on 10/17/2024).

[307] Takashi Nakamura, Minori Kawai, Yusuke Sato, Masatoshi Maeki, Manabu Tokeshi, and Hideyoshi Harashima. "The Effect of Size and Charge of Lipid Nanoparticles Prepared by Microfluidic Mixing on Their Lymph Node Transitivity and Distribution". en. In: *Molecular Pharmaceutics* 17.3 (Mar. 2020), pp. 944–953. ISSN: 1543-8384, 1543-8392. DOI: 10.1021/acs.molpharmaceut.9b01182. URL: https://pubs.acs.org/doi/10.1021/acs.molpharmaceut.9b01182 (visited on 10/17/2024).

[308] Ruvanthi N. Kularatne, Rachael M. Crist, and Stephan T. Stern. "The Future of Tissue-Targeted Lipid Nanoparticle-Mediated Nucleic Acid Delivery". en. In: *Pharmaceuticals* 15.7 (July 2022), p. 897. ISSN: 1424-8247. DOI: 10.3390/ph15070897. URL: https://www.mdpi.com/1424-8247/15/7/897 (visited on 10/17/2024).

[309] Carola Wanja Bartels. *mRNA Quantifizierung in Lipid-Nanopartikeln mittels Fluoreszenzanalyse*. Bachelorarbeit. München: LMU, 2022.

[310] Philippe Desjardins and Deborah Conklin. "NanoDrop Microvolume Quantitation of Nucleic Acids". In: *J. Vis. Exp.* 45 (2010). DOI: 10.3791/2565.

[311] Rafal Stanislaw Krzyszton. "Towards efficient siRNA delivery and gene silencing kinetics on the single-cell level". en. Dissertation. Munich: Ludwig-Maximilians-Universität, 2018.

[312] Daniel Woschée. *Fluorescence Trajectory Fitting*. 2022. URL: https://gitlab.physik.uni-muenchen.de/transfection-analysis/py_fit_fluorescence.

[313] Torkel E. Loman and James C. W. Locke. "The B alternative sigma factor circuit modulates noise to generate different types of pulsing dynamics". en. In: *PLOS Computational Biology* 19.8 (Aug. 2023). Ed. by Tobias Bollenbach, e1011265. ISSN: 1553-7358. DOI: 10.1371/journal.pcbi.1011265. URL: https://dx.plos.org/10.1371/journal.pcbi.1011265 (visited on 09/24/2024).

Danksagung

Lieber Joachim, ich möchte dir danken, dafür, dass du mein Doktorvater warst, mein Mentor und mein Freund während der letzten dreinhalb Jahre. Danke, dass du mir den Spaß am neugierigen Forschen ermöglicht, mich ermutigt und gefördert hast. Ich werde die Arbeit mit dir sehr vermissen!
Sophia, auch wenn es gedauert hat, bis wir uns nicht mehr nur über Zoom, sondern auch live kennen gelernt haben, so warst du doch von Anfang an dabei und hast mit mir unermüdlich Ribosomenstaus (oder nicht-Staus) erkundet. Danke für deinen Optimismus, der mich so manches Mal aus einem Tief gezogen hat und für deine Liebe zum Detail!
Während der ganzen gut dreieinhalb Jahre am Lehrstuhl, hatte ich das Glück in einer tollen Gruppe gelandet zu sein. Daher Danke an die ganze Rädlergruppe, vorallem für Antholz, Wanderausflüge, Wiesnbesuche, Schneeballschlachten, Schlauchbootaction und was nicht noch alles.
Emily, du hast die Doktorarbeitszeit zu etwas ganz Besonderem gemacht, warst meine Freundin in allen Höhen und Tiefen und hast immer zu mir gehalten. Mit dir haben das Arbeiten im Labor, die Wochenendsessions, die Konferenzen und gegen Ende sogar das Handballspielen Spaß gemacht. Und für alles andere gab es ja den Wein.
Nathalie und Stefan, von Anfang bis (fast) Ende vereint als Kellerkinder. Gemeinsam haben wir Corona und was danach kam gemeistert, haben uns gegenseitig aufgefangen, wenn mal alles nicht so gut lief und konnten uns immer aufeinander verlassen.
Chris, wenn auch nur inoffiziel einer von den Rädlers, ohne dich wäre die Zeit am Lehrstuhl nur halb so lustig gewesen. Du warst immer da, um mich auf den Boden der Tatsachen zurück zu holen und für die entspannte Sicht der Dinge.
Gerlinde, Danke für deinen warmen Empfang, es gibt vieles zu sagen aber am wichtigsten ist: Ohne dich läuft hier nix!
Thomas, egal wie verrückt die Fragestellung auch war, du hast fix was gebaut oder programmiert und es wie nichts aussehen lassen. Beeindruckender war nur dein Repertoire an Wortwitzen.
Danke auch an meine Studenten Aylin, Vinzenz, Carola, Manu und Bernhard. Ihr habt mich geduldig das Lehren gelehrt und ich durfte euch auf euren Wegen zu Bachelor-

und Masterarbeit begleiten.
Danke an die Turn-Omis vom TSV Großhadern, an vorderster Front Dino, Aylin und Fuzi, ihr habt mich auf dem ganzen Weg begleitet. Was hätte ich nur ohne euch gemacht? Egal wie der Tag war, nachdem ich mit euch in der Turnhalle war, ging es mir gut.
Ganz besonderen Dank an meine Famile, die unverrückbar immer für mich da ist, mich unterstützt und vorallem dahin gebracht hat, wo ich heute bin.
Und - last, but not least - Tim: Du verleihst mir Flügel, Partner.